Imperial College
London

Experimental and Numerical Analysis of Creep Cracking under Secondary and Combined Loading

A Thesis submitted for the Degree of Doctor in Engineering (EngD) of
Imperial College London
and
Diploma of Imperial College

by
Priyesh Kapadia

December 2014

Department of Mechanical Engineering
Imperial College London
SW7 2AZ

ABSTRACT

The UK's advanced gas-cooled reactor power plants contain welded components which were not stress relieved following fabrication. The presence of weld induced residual stresses, in combination with the plant operating under creep conditions and the material's low creep ductility has caused cracks to form during service due to a process known as reheat cracking. To investigate this cracking process and to develop assessment procedures to evaluate the structural integrity of such components in operation, fracture specimens are required to simulate this loading condition and subsequently perform crack growth studies in laboratory controlled conditions.

Two new fracture mechanics specimen designs were proposed in this study: an electron beam (EB) welded compact tension, C(T), specimen and a wedge-loaded C(T) specimen. EB welding had previously been used as a fabrication process to manufacture C(T) specimens reconstituted from ex-service components. However in this study, this weld process was used specifically to introduce residual stresses in the specimens. Both specimen designs were fabricated using ex-service Type 316H austenitic stainless steel.

Extensive residual stress measurements were made using the neutron diffraction, contour method and slitting techniques on EB welded and wedge-loaded C(T) specimens. This data was used to develop and validate numerical simulations of the fabrication processes enabling residual stress predictions to be made and stress intensity factors, which define the crack driving force, to be determined. Large initial stress intensity factors due to the residual stresses were determined as up to 22.2 $MPam^{1/2}$ and 43.6 $MPam^{1/2}$ for the EB welded and wedge-loaded C(T) specimens respectively. Accurate estimates of the weld residual stresses in the EB welded C(T) specimen required detailed weld simulations to be developed. These were created by following guidelines recently published in the R6 fracture assessment procedure for modelling arc welding processes. The stress predictions made by the weld simulations were in close agreement with the experimental measurements, which showed the advice in the R6 guidelines may be followed to produce accurate numerical simulations of EB welding.

Creep crack growth (CCG) tests were conducted using these new specimen designs at 550°C for up to 1,300 h, under secondary and combined loading conditions, where large crack extensions of up to 5.4 mm occurred. Such large crack growth was achieved by pre-conditioning the material by uniform pre-compression prior to specimen fabrication. This

process reduced the creep ductility of the material enabling CCG to occur during relaxation of the residual stresses. It was shown that this pre-conditioning process was necessary to perform such experiments, as the creep ductility in ex-service Type 316H stainless steel in the as-received condition can be high.

The experimental measurements were used to validate crack growth predictions using the new revision of the R5 assessment procedure. Crack extensions were predicted using $C(t)$ estimated using a reference stress based approach under secondary and combined loading conditions. This assessment was shown to be very conservative where no plastic deformation was assumed, as predicted crack lengths were up to 10 times larger than experimental measurements. By including the effects of crack tip plasticity in the assessment, estimates of the crack extensions were in close agreement with the experimental data. The creep crack growth rates were sensitive to the material's creep ductility, which differed between the test specimens due to weld induced plasticity and variability of the microstructure in the ex-service material. Use of the upper bound crack growth properties is recommended to ensure conservative assessments are made. Damage models developed using the ductility exhaustion approach were also used to predict CCG. Crack length predictions in the wedge-loaded C(T) specimens were generally in good agreement with the numerical models. However non-conservative crack growth predictions were made in the EB welded C(T) specimens which was due to the presence of plasticity.

DECLARATION OF ORIGINALITY

I, Priyesh Kapadia, declare that the work presented in this thesis has been undertaken by myself, except where explicit reference and acknowledgement is made to the contribution of others. No portion of the work in this thesis has been submitted in support of an application for another degree or qualification in this or any other university or other institute of learning.

COPYRIGHT DECLARATION

The copyright of this thesis rests with the author and is made available under a Creative Commons Attribution Non-Commercial No Derivatives licence. Researchers are free to copy, distribute or transmit the thesis on the condition that they attribute it, that they do not use it for commercial purposes and that they do not alter, transform or build upon it. For any reuse or redistribution, researchers must make clear to others the licence terms of this work.

ACKNOWLEDGEMENTS

I would like to express my thanks to my academic supervisors Prof. Kamran Nikbin, and Dr Catrin Davies from Imperial College London, and industrial supervisor Prof. David Dean from EDF Energy Nuclear Generation Ltd for providing me with the opportunity to work on this project and their invaluable guidance and technical support throughout.

In this project I have been fortunate to work with many experts who have kindly offered their time for technical discussions and assistance in obtaining experimental measurements. I would like to thank Prof. George Webster from Imperial College London for sharing his vast knowledge of high temperature fracture mechanics throughout the project, Prof. Mike Smith from the University of Manchester for guidance in the development of weld simulations and Dr Yuebao Lei for his advice in evaluating fracture mechanics parameters from numerical simulations. I am indebted to the engineers and instrument scientists who helped me measure residual stresses throughout this project: Dr Thilo Pirling from the ILL, Dr Michael Hofmann from FRM II, Dr Robert Wimpory from HZB, and Dr Foroogh Hosseinzadeh and Peter Ledgard from the Open University. Thank you to staff at Electron Beam Processes Ltd who welded my specimens and Amit Choda from Imperial College London for his guidance in manufacturing using wire EDM. I'd like to express my gratitude to current and former colleagues Dr Ali Mehmanparast, Dr Leonard Wanigasooriya and Keith Tarnowski for many helpful discussions and assistance in performing experimental testing. Furthermore I'd like to express my thanks to former colleagues at AMEC as all the skills I developed, especially in performing FE analyses, have been invaluable for me to complete this project.

Financial support was provided by the Engineering and Physical Sciences Research Council (EPSRC) and EDF Energy who are gratefully acknowledged. This project has also received funding from the European Union's 7th Framework Programme for research, technological development and demonstration under the NMI3-II Grant number 283883.

Personally, I would like to thank my family and friends who have provided me with encouragement throughout this project. Most importantly, thank you to my mother for her love and support throughout my life, and the sacrifices she has made to allow me the achieve all that I have. I would like to extend my heartfelt thanks to my girlfriend, Dharmini, for her love and friendship, and constant words of encouragement. Finally, I would like say thank you to my nieces and nephews for making me smile.

TABLE OF CONTENTS

1 Introduction 1

1.1 Background 1

1.2 Aims and Objectives 2

1.3 Structure of the Thesis 3

2 Literature Review 4

2.1 Introduction 4

2.2 Type 316H Stainless Steel and its Material Properties 4
2.2.1 Material Description 4
2.2.2 Tensile Properties 5
2.2.3 Creep Deformation Models 7
2.2.4 Creep Damage Models 14
2.2.5 Uniform Pre-Compression to Reduce the Creep Ductility 15

2.3 Fracture Mechanics Concepts 15
2.3.1 Linear Elastic Fracture Mechanics 15
2.3.2 Elastic-Plastic Fracture Mechanics 16
2.3.3 Creep Fracture Mechanics 18

2.4 Review of Methods to Induce Residual Stresses in Fracture Specimens 20
2.4.1 Overview of Residual Stresses 20
2.4.2 Pre-Compressed C(T) Specimens 21
2.4.3 Side Punched C(T) Specimens 22
2.4.4 Residual Stresses from EB Welds 23
2.4.5 Load Application using a Three Bar Structure 24
2.4.6 Creep Crack Growth Studies under Secondary Loads 25

2.5 Stress Intensity Factor under Secondary Loading Conditions, K^S 27
2.5.1 Through Thickness Variation of K^S 27
2.5.2 The J-Integral with Initial Strains 27
2.5.3 K^S Using the Principle of Superposition 31

2.6 Experimental Evaluation of Residual Stresses 32
2.6.1 Overview 32
2.6.2 Neutron Diffraction 33
2.6.3 Slitting 35
2.6.4 The Contour Method 37
2.6.5 Digital Image Correlation 38

2.7 Discussion 39

2.8 Summary 41

3 Measurement of Residual Stresses in EB Welded C(T) Specimens 42

3.1 Introduction 42

3.2 Generation of Residual Stresses by Welding 43

3.3 Specimen Design and Manufacture 45
3.3.1 Specimen Design 45

3.3.2 Specimen Manufacture 47
3.4 Temperature Measurements 49
3.5 Weld Images and Hardness Testing 51
3.6 Residual Strains and Stresses Measured by Neutron Diffraction 54
3.6.1 Measurement Locations 54
3.6.2 Measurement of the Reference Scattering Angle 56
3.6.3 Residual Strains 58
3.6.4 Residual Stresses 62
3.7 SIF and Residual Stress Measured by the Slitting Method 66
3.7.1 Cutting Procedure 66
3.7.2 Stress Intensity Factor 68
3.7.3 Residual Stress 68
3.8 Residual Stresses Measured by the Contour Method 69
3.8.1 Cutting and Surface Measurement 69
3.8.2 Stress Evaluation 71
3.9 Comparison of Experimental Residual Stress Measurements 75
3.10 Summary 76
4 Prediction of Residual Stresses in EB Welded C(T) Specimens 78
4.1 Introduction 78
4.2 Description of the FE Models 78
4.3 Heat Source Model 80
4.4 Thermal Analysis 82
4.4.1 Model Description 82
4.4.2 Time Incrementation 85
4.4.3 Comparison of Temperature Data 86
4.4.4 Comparison of Weld Fusion Boundaries 89
4.5 Mechanical Analysis 89
4.5.1 Model Description 89
4.5.2 Material Model 92
4.5.3 Comparison of FE with ND Strain Measurements 95
4.5.4 Comparison of Longitudinal Stresses with Experimental Measurements 97
4.6 Discussion 99
4.7 Crack Driving Force due to Secondary Loads 101
4.7.1 Redistributed Stresses at 550°C 101
4.7.2 Stress Intensity Factor 106
4.8 Summary 110
5 Residual Stresses in Wedge-Loaded C(T) Specimens 112
5.1 Introduction 112
5.2 Specimen Design and Manufacture 113
5.2.1 Specimen Design 113
5.2.2 Specimen Fabrication 114

5.3 Experimental Measurements 115
5.3.1 Mouth Opening Displacement 115
5.3.2 Surface Strain Measurements 116
5.3.3 Residual Strain and Stress Measurements 117
5.4 Numerical Analysis 119
5.4.1 Model Description 119
5.4.2 Validation of the FE Predictions 121
5.5 Crack Driving Force due to Secondary Loads 125
5.5.1 Redistributed Stresses at 550°C 125
5.5.2 Stress Intensity Factor 128
5.6 Summary 130

6 CCG Testing of Specimens with Residual Stresses 131

6.1 Introduction 131
6.2 Test Specimens 131
6.3 Test Procedure 132
6.4 Results 134
6.4.1 Thermocouple, DCPD and Capacitance Gauge Measurements 134
6.4.2 Metallography 139
6.5 Discussion 143
6.6 Summary 147

7 Assessment of Stress Relaxation and Crack Growth 148

7.1 Introduction 148
7.2 Relaxation of Residual Stresses 148
7.2.1 Estimation of Stress Relaxation 148
7.2.2 Stress Relaxation in Uniaxial Specimens 149
7.2.3 Stress Relaxation in C(T) Specimens 153
7.2.4 Assessment of Creep Deformation Models in Predicting Stress Relaxation 155
7.3 Crack Growth Predictions using $C(t)$ during Stress Relaxation 155
7.3.1 The $C(t)$-integral 155
7.3.2 Evaluating The $C(t)$-Integral using FE Analyses 156
7.3.3 $C(t)$ Definition in the R5 Procedure 157
7.3.4 $C(t)$ Estimation using Reference Stresses 160
7.3.5 Comparison of $C(t)$ determined using FE and the R5 Procedure 167
7.3.6 Estimates of CCG using the R5 Procedure 170
7.4 CCG Predictions using Damage Modelling in FE Simulations 173
7.4.1 Finite Element Model 173
7.4.2 Crack Growth Predictions 175
7.4.3 Sensitivity Studies 179
7.5 Discussion 180
7.6 Summary 182

8 Conclusions and Future Work 183
8.1 Conclusions 183
8.2 Future Work 186
9 References 188

Appendices

A Validation of Methods to Evaluate K^s 196

LIST OF FIGURES

Figure 2.1 Change in yield stress due to (a) non-linear kinematic hardening, (b) isotropic hardening and (c) translation of yield surface due to mixed hardening 6
Figure 2.2 Accumulation of creep strain for a typical stainless steel 7
Figure 2.3 Deformation mechanism map for Type 316 stainless steel of grain size 50 μm (image from [8, p65]) 8
Figure 2.4 Accumulation of creep strain for varying stress and temperature conditions due to strain and time hardening laws 13
Figure 2.5 The J-integral along a path around a crack tip 17
Figure 2.6 Pre-compression of a C(T) specimen showing the plastic zone ahead of the notch 21
Figure 2.7 C(T) specimen indented using (a) single punch and (b) double punch tools to generate residual stresses (images from [35]) 22
Figure 2.8 (a) Illustration of a C(T) blank containing MMA and EB welds (b) Residual stress distribution across C(T) blank along HAZ in MMA and EB welded block (data from [42]) 23
Figure 2.9 (a) Residual stress component normal to the crack plane and (b) equivalent plastic strain, along the ligament and at mid-thickness of secondary loaded C(T) specimens, data from [3, 31, 38] 25
Figure 2.10 Contour integral within a region A (image from [50]) 28
Figure 2.11 Applied loads on (a) a cracked body and (b) an uncracked body to determine K^s using the superposition approach 31
Figure 2.12 Superposition of boundary loads on crack plate to determine K (a) remotely loaded crack body, (b) remotely loaded crack body with compressive crack face tractions to cause crack closure and (c) crack body with tensile crack face tractions 32

Figure 2.13 (a) Illustration of a diffractometer instrument for measuring strain using a monochromatic neutron beam (b) Peak shift in measured scattering angle caused by lattice strain 33

Figure 2.14 The contour method described by the superposition principle (a) body with residual stresses, σ_{yy} (b) deformed body after cutting and (c) loading on stress free deformed body to create flat cut surface 37

Figure 3.1 Schematic representation of (a) isotherms around a weld pool, (b) stresses across the weld pool at various stages of welding and (c) a typical stress-strain curve for the HAZ 43

Figure 3.2 (a) Isometric view and (b) dimensions of the EB welded C(T) specimen 45

Figure 3.3 EB welded C(T) blank with sacrificial blocks 46

Figure 3.4 Clamping arrangement of specimens welded at Electron Beam Processes Ltd 47

Figure 3.5 Location of thermocouples on EB weld specimens 48

Figure 3.6 Temperatures measured during welding specimens (a) EBW3, (b) EBW4, (c) EBW5, (d) EBW6 and (e) EBW7, and (f) thermocouple colour legend 49

Figure 3.7 Weld micrograph of specimen (a) EBW3 and (b) EBW4 52

Figure 3.8 Weld micrograph of specimen EBW3 52

Figure 3.9 Profile of Vickers hardness values measured across EBW3 53

Figure 3.10 ND measurement lines on (a) EB welded specimen, (b) C(T) blank and (c) C(T) specimen 54

Figure 3.11 Geometry of toothcomb specimens used for reference measurements at the instrument (a) SALSA and (b) Stress-Spec 56

Figure 3.12 Scattering angles measured across toothcomb specimens using (a) $2 \times 2 \times 2$ mm^3 and (b) $0.5 \times 10 \times 2$ mm^3 gauge volumes 57

Figure 3.13 Residual strains measured using ND along line AB in specimens (a) EBW3, (b) EBW4 and (c) EBW5 after welding 59

Figure 3.14 Residual strains measured using ND along line CD in specimens (a) EBW4 and (b) EBW5 after machining into a C(T) blank 60

Figure 3.15 Residual strains measured using ND in specimens (a) EBW3 along line EF and (b) EBW5 along lines EF and GH, after machining into a C(T) specimen 61

Figure 3.16 Residual stresses measured in as-welded specimens (a) EBW3 and EBW4, and (b) EBW5 along line AB 62

Figure 3.17 Redistribution of residual stresses in specimen EBW3 when machining C(T) specimen (line EF) from as-welded specimen (line AB) 64

Figure 3.18 Redistribution of residual stresses in specimen EBW4 when machining C(T) blank (line CD) from as-welded specimen (line AB) 64

Figure 3.19 (a) Redistribution of residual stresses in specimen EBW5 when machining C(T) blank (line CD) from as-welded specimen (line AB) and (b) residual stresses in crack plane of C(T) specimen machined from EBW5 65

Figure 3.20 EBW4 C(T) blank showing strain gauge locations for slitting 66
Figure 3.21 EBW4 C(T) blank during cutting for residual stress measurement by slitting 67
Figure 3.22 Back face strain measurements during slitting of C(T) blank from EBW4 67
Figure 3.23 Stress intensity factor for EBW4 C(T) blank determined by slitting 67
Figure 3.24 Longitudinal stress, σ_{yy}, for C(T) blank (EBW4) determined from the slitting method 69
Figure 3.25 Deformation of cut faces of EBW4 C(T) blank for the contour method on (a) side A and (b) side B 70
Figure 3.26 Averaged and smoothed displacements evaluated at nodal positions of the contour FE model for EBW4 C(T) blank 70
Figure 3.27 Longitudinal weld residual stresses, σ_{yy}, in EBW4 C(T) blank determined by the contour method (a) initial estimate (b) updated to take into account cut tip deformations 73
Figure 3.28 Longitudinal weld residual stresses, σ_{yy}, along mid-thickness of EBW4 C(T) blank determined by the contour method, cut direction from left to right 73
Figure 3.29 Simulating cutting of EBW4 C(T) blank to determine the deformation of the cut tip 73
Figure 3.30 Displacement of cut tip at nodal positions of the contour FE model for EBW4 C(T) blank 74
Figure 3.31 Comparison of longitudinal weld residual stresses in C(T) blank made from EBW4 using different measurement techniques (a) at mid-thickness and (b) averaged across thickness 75
Figure 4.1 Heat flux distribution profiles in (a) double ellipsoidal, (b) conical and (c) combined heat source models, for a weld arc positioned along the z-axis moving in the y-direction 80
Figure 4.2 Thermal model of the EB weld specimen 83
Figure 4.3 Temperature distribution in thermal analysis near weld pool 86
Figure 4.4 Comparison of FE temperature predictions at thermocouple locations with averaged experimental measurements for (a) a single pass weld and (b) a two pass weld 87
Figure 4.5 Comparison of weld fusion boundaries predicted by FE model with macrographs (a) EBW3 and (b) EBW4 89
Figure 4.6 Mechanical model of the EB weld specimen 90
Figure 4.7 Mechanical models used to simulate fabrication of the EB welded C(T) specimen: (a) half model of EB welded specimen, (b) half model of C(T) blank, (c) full model of C(T) blank and (d) quarter model of C(T) specimen 91
Figure 4.8 Lemaitre-Chaboche (LC) model fitted to monotonic uniaxial tensile test data for Type 316H in as-received (AR) and 8% pre-compressed (8PC) material conditions at (a) room temperature and (b) 550°C 94

Figure 4.9 Comparison of residual strains predicted by FE analyses to ND measurements (a) EBW3 – as-welded, (b) EBW4 – as-welded, (c) EBW4 – C(T) blank, (d) EBW5 – as-weld and (e) EBW5 – C(T) blank 96

Figure 4.10 Comparison of residual strains predicted by FE analyses to ND measurements in C(T) specimens (a) EBW3 along line EF and (b) EBW5 along lines EF and GH 97

Figure 4.11 Comparison of longitudinal weld residual stress measurements in the C(T) blank made from EBW4 with FE predictions (a) at mid-thickness and (b) averaged across thickness 98

Figure 4.12 Contour plots of longitudinal weld residual stress, σ_{yy}, in C(T) blank made from EBW4 (a) measured by the contour method and (b) predicted by weld simulation 98

Figure 4.13 Mesh of EB welded C(T) specimen (a) without side groove, (b) with side groove and (c) focused mesh at crack tip 101

Figure 4.14 Stress components in EB welded C(T) blank at 550°C (a) FE model, (b) σ_{xx}, (c) σ_{yy} and (d) σ_{zz} on the z-symmetry plane, and (e) σ_{xx}, (f) σ_{yy} and (g) σ_{zz} on the y-symmetry plane 103

Figure 4.15 Stress components in EB welded C(T) specimen with pre-crack only at 550°C (a) FE model, (b) σ_{xx}, (c) σ_{yy} and (d) σ_{zz} on the z-symmetry plane, and (e) σ_{xx}, (f) σ_{yy} and (g) σ_{zz} on the y-symmetry plane 103

Figure 4.16 Stress components in EB welded C(T) specimen with pre-crack and pin holes at 550°C (a) FE model, (b) σ_{xx}, (c) σ_{yy} and (d) σ_{zz} on the z-symmetry plane, and (e) σ_{xx}, (f) σ_{yy} and (g) σ_{zz} on the y-symmetry plane 104

Figure 4.17 Stress components in EB welded C(T) specimen with pre-crack, pin holes and side grooves at 550°C (a) FE model, (b) σ_{xx}, (c) σ_{yy} and (d) σ_{zz} on the z-symmetry plane, and (e) σ_{xx}, (f) σ_{yy} and (g) σ_{zz} on the y-symmetry plane 104

Figure 4.18 Stress components along line CD for the C(T) blank and line EF for the C(T) specimen at 550°C 105

Figure 4.19 Equivalent plastic strain ε_{pl} along line CD for the C(T) blank and line EF for the C(T) specimen EBW5 105

Figure 4.20 Hydrostatic stress, σ_h, equivalent stress, σ_{eq}, and triaxiality, σ_h/σ_{eq}, along line EF in C(T) specimen EBW5 at 550°C 106

Figure 4.21 (a) Node regions for three contour integrals in C(T) specimen EBW5, (b) J-integral determined for the three node planes and (c) converged values of K_J^S across the thickness of the specimen 107

Figure 4.22 (a) The crack face region of the C(T) specimen EBW5 (b) the distributed pressure, in MPa, at the integration points on the crack face 108

Figure 4.23 (a) K^S in C(T) specimen EBW5 through three node planes determined using the superposition method (b) K^S across the thickness of C(T) specimen EBW5 109

Figure 4.24 Comparison of stress intensity factors, K_J^S, determined by two different approaches for C(T) specimen EBW5 at 550°C 109

Figure 4.25 Comparison of stress intensity factors, K_J^s, determined for two EB welded C(T) specimen configurations at 550°C 110
Figure 4.26 Comparison of stress intensity factors, K_J^s, determined for C(T) specimens EBW3 and EBW5 at 550°C 110
Figure 5.1 Wedge-loaded C(T) specimen (a) isometric view, (b) dimensions of the modified C(T) specimen and (c) dimensions of the wedge 113
Figure 5.2 Wedge-loaded C(T) specimen in during wedge insertion using an Instron testing machine 114
Figure 5.3 Speckle pattern on wedge-loaded C(T) specimen, WC(T)5, showing a typical facet used in the DIC measurement technique 115
Figure 5.4 (a) Mouth opening displacement in wedge-loaded C(T) specimens measured by clip gauge (b) Clip gauge attachment points 116
Figure 5.5 (a) Mouth opening displacement in wedge-loaded C(T) specimens measured by DIC (b) Initial position of facets used to measure mouth opening displacement with DIC 116
Figure 5.6 Measurement line AB in wedge-loaded C(T) specimens sampled during ND tests 117
Figure 5.7 Residual strain components measured by ND in the wedge-loaded C(T) specimens 118
Figure 5.8 Residual stress components determined from ND measurements in the wedge-loaded C(T) specimens 118
Figure 5.9 FE model of wedge-loaded C(T) specimen 120
Figure 5.10 FE predictions of strain component ε_{xx} on the side face of specimens (a) WC(T)3, (b) WC(T)4 and (c) WC(T)5 compared to DIC measurements 122
Figure 5.11 FE predictions of strain component ε_{yy} on the side face of specimens (a) WC(T)3, (b) WC(T)4 and (c) WC(T)5 compared to DIC measurements 122
Figure 5.12 Comparison of residual strains in the wedge-loaded C(T) specimen predicted by FE simulation to ND measurements (a) ε_{xx}^e, (b) ε_{yy}^e and (c) ε_{zz}^e 124
Figure 5.13 Stress components on the crack plane of the wedge-loaded C(T) specimens at 550°C 125
Figure 5.14 FE predictions of stress and plasticity along the ligament of the wedge C(T) specimens at 550°C (a) σ_{xx}, (b) σ_{yy}, (c) σ_{zz}, (d) σ_h, (e) σ_{eq}, (f) σ_h/σ_{eq} and (g) ε^{pl} 127
Figure 5.15 Contact stresses between wedge and modified C(T) specimen at 550°C in WC(T)5 129
Figure 5.16 (a) Node regions for three contour integrals in the wedge-loaded C(T) specimen, (b) K^s through three node planes in WC(T)5 and (c) K^s across the thickness of the wedge-loaded C(T) specimens 129
Figure 6.1 (a) Temperature measurements for specimen WC(T)3 and WC(T)4 (b) DCPD voltage measurements for specimen WC(T)3 134

Figure 6.2 (a) Temperature measurements and (b) DCPD voltage measurements for specimen WC(T)5 135
Figure 6.3 (a) Temperature, (b) DCPD voltage for specimen EBW3 135
Figure 6.4 (a) Temperature, (b) DCPD voltage, (c) DCPD reference voltage and (d) relative DCPD voltage measurements for specimen EBW5 136
Figure 6.5 (a) Temperature, (b) DCPD voltage and (c) mouth opening displacement measurements for specimen EBW6 137
Figure 6.6 (a) Temperature, (b) DCPD voltage and (c) relative DCPD voltage measurements for specimen EBW7 138
Figure 6.7 Location of planes used to image crack micrographs and fracture surfaces in (a) wedge-loaded C(T) specimens and (b) EB welded C(T) specimens 139
Figure 6.8 (a) Crack micrograph and (b) fracture surface of specimen WC(T)3 140
Figure 6.9 (a) Crack micrograph and (b) fracture surface of specimen WC(T)4 140
Figure 6.10 (a) Crack micrograph and (b) fracture surface of specimen WC(T)5 140
Figure 6.11 Crack micrograph of specimen EBW3 141
Figure 6.12 (a) Crack micrograph and (b) fracture surface of specimen EBW5 141
Figure 6.13 (a) Crack micrograph and (b) fracture surface of specimen EBW6 141
Figure 6.14 (a) Crack micrograph and (b) fracture surface of specimen EBW7 142
Figure 6.15 (a) Maximum and (b) average crack length during CCG testing of wedge-loaded C(T) specimens determined using PD data 143
Figure 6.16 (a) Maximum and (b) average crack length during CCG testing of EB welded C(T) specimens determined using PD data 143
Figure 6.17 Comparison of (a) stress normal to crack plane and (b) ε^{pl} for C(T) specimens under secondary loading conditions (data from [33] and [38]) 145
Figure 7.1 Stress relaxation measured from constant-displacement creep tests of Type 316H stainless steel at 550°C (data from [13]) 150
Figure 7.2 Comparison of stress relaxation predicted by creep deformation laws with uniaxial constant-displacement creep tests at 550°C: (a) σ_0 = 230 MPa (R0395), (b) σ_0 = 190 MPa (FLZ002) and (c) σ_0 = 125 MPa (R0394); (i) log-linear plot and (ii) linear-linear plot. 152
Figure 7.3 Comparison of residual stress measurements in secondary loaded C(T) specimens before and after thermal soaking with FE predictions using various creep deformation models (a) WC(T)3, (b) WC(T)4 and (c) EBW5 154
Figure 7.4 Relaxation of reference stress in wedge-loaded C(T) specimens 161
Figure 7.5 Relaxation of reference stress in EB welded C(T) specimens 161
Figure 7.6 Stress relaxation in specimen EBW6 determined using reference stress approach 162
Figure 7.7 $C(t)$ estimation in wedge-loaded C(T) specimens using reference stress approaches 163

Figure 7.8 $C(t)$ estimation in EB welded C(T) specimens using reference stress approaches 164
Figure 7.9 True stress vs. plastic strain from uniaxial tensile test of 8% pre-compressed Type 316H stainless steel at 550°C compared to Ramberg-Osgood models (data from [18]) 165
Figure 7.10 Sensitivity of $C(t)$ estimation in WC(T)5 to plastic strain 165
Figure 7.11 Sensitivity of $C(t)$ estimation in WC(T)5 to elastic follow up factor, Z 166
Figure 7.12 Sensitivity of $C(t)$ estimation in WC(T)5 to the parameter $\phi(t)$ 166
Figure 7.13 $C(t)$ determined from a FE model of WC(T)5 where the creep deformation model assumes an average creep strain rate 168
Figure 7.14 Comparison of $C(t)$ estimation in WC(T)5 using R5 to FE analyses 169
Figure 7.15 Comparison of $C(t)$ estimation in EBW5 using R5 to FE analyses 169
Figure 7.16 Comparison of crack growth predictions from $C(t)$ with experimentally measured crack length in wedge-loaded C(T) specimens: (a) WC(T)3 (b) WC(T)4 and (c) WC(T)5 for (i) elastic-creep and (ii) elastic-plastic-creep deformations 171
Figure 7.17 Comparison of crack growth predictions from $C(t)$ with experimentally measured crack length in EB welded C(T) specimens: (a) EBW5 (b) EBW6 and (c) EBW7 for (i) elastic-creep and (ii) elastic-plastic-creep deformations 172
Figure 7.18 Finite element mesh for CCG analyses of (a) wedge-loaded and (b) EB welded C(T) specimens 173
Figure 7.19 Comparison of multiaxial creep ductilities predicted by various void growth models 174
Figure 7.20 Comparison of crack growth predictions from FE simulations with experimental measurements in wedge-loaded C(T) specimens: (a) WC(T)3 (b) WC(T)4 and (c) WC(T)5 176
Figure 7.21 Comparison of crack growth predictions from FE simulations with experimental measurements in EB welded C(T) specimens: (a) EBW5 (b) EBW6 and (c) EBW7 176
Figure 7.22 Comparison of crack profiles measured experimentally in wedge-loaded C(T) specimens with predictions using damage modelling (a) WC(T)3, (b) WC(T)4 and (c) WC(T)5 177
Figure 7.23 Comparison of crack profiles measured experimentally in EB welded C(T) specimens with predictions using damage modelling (a) EBW5, (b) EBW6 and (c) EBW7 178
Figure 7.24 Comparison of crack extension prediction in specimen WC(T)3 using different void growth models 179
Figure 7.25 Comparison of crack length prediction in specimen WC(T)3 using different mesh densities and integration schemes 180

LIST OF TABLES

Table 2.1	Constants characterising a mixed hardening model for Type 316H stainless steel (data from [6]) as implemented in ABAQUS	6
Table 2.2	RCC-MR creep deformation model constants for Type 316H stainless steel at 550°C	10
Table 2.3	Constants to determine the maximum primary creep strain in the modified Garofalo model for Type 316H stainless steel defined by Douglas et al. [13]	12
Table 2.4	Constants for the secondary creep strain rate in the modified Garofalo model for Type 316H stainless steel defined by Douglas et al. [13]	12
Table 2.5	hkl specific material constants for austenitic stainless steel [59, pp222-230]	35
Table 2.6	Coefficients of A_{kl} used to determine the weight function for a C(T) specimen [63]	36
Table 3.1	List of EB welded specimens	46
Table 3.2	Beam parameters used during EB welding	48
Table 3.3	Maximum temperature measured during EB welding	51
Table 3.4	Position of thermocouples measured after EB welding	51
Table 3.5	Instruments used to make ND measurements in EB welded C(T) specimens	55
Table 4.1	Thermo physical properties for Type 316H stainless steel [6, 32]	84
Table 4.2	Constants used in the heat source model	84
Table 4.3	FE temperature predictions and averaged experimental measurements for an EB weld specimen with a single pass weld	88
Table 4.4	FE temperature predictions and averaged experimental measurements for the second weld pass of an EB weld specimen with a two pass weld	88
Table 4.5	Elastic properties for Type 316H stainless steel [6, 32]	93
Table 4.6	Constants for the Lemaitre-Chaboche formulation of the mixed hardening model for Type 316H stainless steel in the 8% pre-compressed condition	94
Table 5.1	List of wedge-loaded C(T) specimens fabricated	114
Table 5.2	Comparison of Δ_{MOD} predicted by FE analyses to experimental data	121
Table 5.3	Peak and average K^s for wedge-loaded C(T) specimens at 550°C	130
Table 6.1	List of specimens with residual stresses used to conduct CCG testing	131
Table 6.2	Maximum crack length, average crack length and grain diameter in C(T) specimens	142
Table 7.1	Reference stress estimates for C(T) specimens with secondary and combined loads	160
Table 7.2	Redistribution time, t_{red}, for C(T) specimens tested under combined loads	162

Table 7.3 C_0^* determined for the C(T) specimens 163
Table 7.4 Constants for different fits of the Ramberg-Osgood model to 8% pre-compressed Type 316H stainless steel (for σ in MPa and ε in mm/mm) 164
Table 7.5 Creep crack growth rate properties for 8% pre-compressed Type 316H stainless steel at 550°C (for a in mm/h and $C(t)$ in MPam/h) 170

1 INTRODUCTION

1.1 BACKGROUND

Residual stresses are commonly induced in engineering components during fabrication, by forming processes such as quenching, bending and welding. Residual stresses may exist inherently in structures when no external loading is applied and occasionally are inserted into components deliberately to improve their performance, e.g. by shot peening or the autofrettage of cylinders. However, they often have a detrimental effect on performance where these stresses combined with applied loading can cause unexpected failure. When the magnitudes of residual stresses are large relative to the applied stresses, they must be taken into account when performing structural integrity assessments. Post weld heat treatment (PWHT) is a fabrication process commonly used to reduce the magnitude of residual stresses. However, it is often impractical to do so for components welded in-situ and furthermore, this process changes the microstructure of the material which can also detrimentally affect the material's mechanical properties.

Components in the UK's advanced gas-cooled reactor (AGR) plants contain welds in AISI Type 316H austenitic stainless steel that are in-service and that have not been stress relieved. During operation at 510-550°C, within the materials creep regime, the relaxation of the weld residual stresses combined with the material's low creep ductility causes creep damage to occur and cracks to grow [1]. This cracking mechanism, called reheat cracking, occurs in the heat affected zone (HAZ) and such cracks have been found after 10,000 to 50,000 h of operation.

AGR plants are now operating beyond the original design life, for continued operation a safety case must be made to demonstrate the structural integrity of the plant and to show that risks have been reduced as low as reasonably practicable. The R5 document [2] contains a high temperature fracture assessment procedure used to make such justifications. This procedure is developed and validated using test data from laboratory specimens performed under carefully controlled conditions. In the recently issued revision, the guidance in R5 Volume 4/5 Appendix A3 to assess crack growth under combined load conditions was updated. Combined load conditions exist where both residual stresses and applied stresses act on a structure or component. Validation of the crack growth predictions for combined loading conditions using this new methodology is required.

For this, fracture specimens need to be tested in laboratories at high temperature under secondary loading conditions, where crack growth is due to residual stresses only, and also under combined loading conditions, where an additional applied load is imposed. Such studies have been previously conducted by Turski et al. [3] where compact tension, C(T), specimens were pre-compressed to generate residual stresses and then heated to 550°C for extended time periods. Crack growth occurred at high temperature due to the residual stresses. However, the plasticity introduced during compression reduced the material's creep ductility making it more susceptible to cracking at high temperature. In the pre-compressed C(T) specimen it was difficult to distinguish between the influence of residual stresses and plasticity. Therefore to validate the assessment methodology presented in the R5 procedure, a fracture specimen was required which could be used to perform experimental creep crack growth (CCG) studies under secondary and combined loading conditions, without the influence of prior plasticity.

1.2 AIMS AND OBJECTIVES

The aim of this study was to develop novel fracture mechanics specimens that could be used to validate CCG predictions made using the numerical and analytical models presented in the R5 procedure for residual stress dominated loadings. Ideally this would allow the residual stresses to be introduced in a controlled manner without affecting the underlying creep properties of the material. The objectives of the work were to:

1. Review and appraise existing experimental methods employed to examine crack growth under the influence of residual stresses
2. Design and fabricate new fracture test specimens where the effect of residual stresses on CCG may be investigated without the influence of prior plasticity
3. Perform measurements to evaluate the magnitude and distribution of the residual stresses induced in these specimens
4. Develop numerical simulations of the fabrication processes to predict the residual stresses induced and validate the simulations using experimental measurements
5. Conduct CCG testing on Type 316H stainless steel specimens, at 550°C, under secondary and combined loading conditions for a range of loads
6. Determine the extent of crack growth in these tests using the R5 procedure to validate the assessment methodology under secondary and combined loading conditions

1.3 STRUCTURE OF THE THESIS

The constitutive material laws and fracture mechanics parameters that are relevant to this study are presented in Chapter 2. This chapter also includes a review of previous studies to investigate the influence of residual stresses on CCG that have been published in literature. Extensive residual stress measurements were performed on fracture specimens throughout this study hence the principles of these measurement techniques are also described in Chapter 2.

Two specimen designs were developed: the electron beam (EB) welded C(T) specimen and the wedge-loaded C(T) specimen. A few specimens for each design were manufactured whilst strain measurements were performed during and after fabrication to determine the extent of deformation in the specimens and the residual stresses that remained. Chapter 3 presents the fabrication processes and experimental assessments of the residual stresses in the EB welded C(T) specimens. This includes stress measurements using the neutron diffraction (ND), contour method and slitting techniques. Numerical predictions of the residual stresses in the EB welded C(T) specimens, which include weld simulations, are presented in Chapter 4. Chapter 5 details the fabrication of the wedge-loaded C(T) specimens, and also presents residual stress measurements made using ND and numerical predictions of the stresses induced.

Specimens of each design were then used to perform CCG tests under secondary and combined loading conditions where large cracks were successfully grown. Chapter 6 includes details of the testing procedure and the accompanying experimental results. Residual stresses were experimentally measured after CCG testing. Chapter 7 presents assessments of stress relaxation in the fracture specimens using various creep deformation models and comparisons with the residual stress test data. Crack growth assessments following the methodology in the R5 procedure are also presented in Chapter 7. Crack extensions were estimated using a reference stress based approach to determine the fracture mechanics parameter, $C(t)$, and also using numerical simulations which incorporated damage modelling. The conclusions and future work are detailed in Chapter 8.

Appendix A contains details of a validation study performed to determine the crack driving force from numerical simulations. The recommendations from this study were used to determine relevant fracture mechanics parameters from the simulations presented Chapter 4 and Chapter 5.

2 LITERATURE REVIEW

2.1 INTRODUCTION

In solid mechanics the deformation of materials in response to applied loads is described by constitutive laws. Material models that define elastic, plastic and creep deformations of Type 316H stainless steel are presented in this chapter. This review focuses on material hardening models, due to their relevance for weld modelling, and creep deformation and damage models.

Fracture mechanics parameters are used to describe the stress and deformation fields around a crack tip, failure is predicted when such parameters reach a critical value. In this chapter a review of fracture mechanics and creep principles for cracked bodies, relevant to this study, is presented. Methods of determining fracture mechanics parameters specific to cracked bodies under secondary loading conditions are also detailed.

This chapter includes a review of relevant experiments that have been published in literature, where residual stresses have been induced in fracture specimens and CCG studies have been carried out. In this study, specimens were manufactured using material that was pre-strained hence the effects of this preconditioning process on material behaviour is described. Furthermore, the residual stress measurement techniques that were performed as part of this investigation are detailed.

2.2 TYPE 316H STAINLESS STEEL AND ITS MATERIAL PROPERTIES

2.2.1 MATERIAL DESCRIPTION

The material tested in this study was Type 316H austenitic stainless steel. This creep resistant steel is used in steam header components in AGR plants which operate at high temperatures. This alloy has a relatively high amount of carbon in comparison to other grades in the 300 series as the high carbon content improves the creep resistance of the alloy. The material has a high chromium content which improves the corrosion resistance of the material and a high nickel content to allow the austenite phase to be retained at room temperature. Austenitic steels have a face-centre-cubic (FCC) lattice structure which makes the material ductile [4, pp273-274].

2.2.2 TENSILE PROPERTIES

Constitutive models are used to describe material deformation. Such models vary in complexity from simple power-law relationships such as the Ramberg-Osgood plasticity model to mixed isotropic-kinematic hardening models where the deformation is dependent on the loading history. A review of material laws to define plastic deformation is presented in this section.

The Ramberg-Osgood model describes the stress-strain behaviour as a power-law relationship. The elastic and plastic strains are summed to determine the total strain, ε, using:

$$\varepsilon = \frac{\sigma}{E} + A\sigma^N \tag{2.1}$$

where E is Young's modulus and, A and N are constants that are fitted to experimental uniaxial tensile test data. At large stresses where plastic strains are larger than elastic strains the second term in (2.1) dominates. At small stresses the plastic contribution is low and hence the response is almost linear.

Constitutive models which describe the cyclic hardening behaviour are required to accurately predict the deformation of bodies where the material undergoes reverse loading. The hardening behaviour can be described by isotropic, kinematic or mixed isotropic-kinematic models. The hardening models define how the yield stress, σ_y, changes when the material yields due to deformation in the opposing direction, e.g. how the compressive yield stress is changed by yielding in tension.

For kinematic hardening models, the difference between the tensile and compressive yield stresses of a material upon load reversal is $2\sigma_y$ as shown in Figure 2.1(a), hence as σ_y increases in one direction, e.g. in tension, σ_y in the opposing direction is reduced, e.g. in compression. The material's reduction in yield strength due to plastic deformation in the opposite direction is known as the Bauschinger effect [5, p110]. Kinematic hardening represents a translation of the yield surface as shown in Figure 2.1(c). Isotropic hardening models define the same yield stress in tension and compression during load reversal. Figure 2.1(b) shows the isotropic hardening behaviour where load reversal occurring on a material which yields in tension with a stress of σ_A causes compressive yielding to occur at $-\sigma_A$. Isotropic hardening causes expansion or contraction of the yield surface, as shown in Figure 2.1(c).

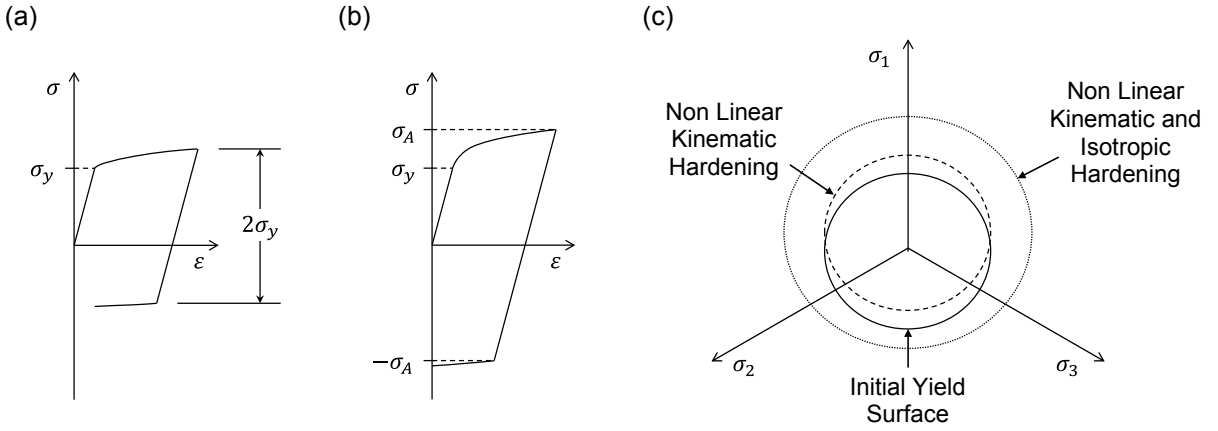


Figure 2.1 Change in yield stress due to (a) non-linear kinematic hardening, (b) isotropic hardening and (c) translation of yield surface due to mixed hardening

The mixed non-linear isotropic kinematic hardening model is implemented in the commercial finite element (FE) software, ABAQUS, using the formulation by Lemaitre and Chaboche [5, pp195-240]. Each of the hardening components are determined separately. The size of the yield surface in the isotropic hardening model changes according to:

$$\sigma_y = \sigma_{y0} + Q_\infty \left(1 - e^{-b\varepsilon^{pl}}\right) \tag{2.2}$$

where σ_{y0} is the initial size of σ_y and ε^{pl} is the equivalent plastic strain. The constants Q_∞ and b are experimentally fitted constants which define the expansion of the yield surface. The non-linear kinematic hardening law is defined by:

$$\sigma_y = \sigma_{y0} + \sum_i \left[\frac{C_{LC_i}}{\gamma_i}\left(1 - e^{-\gamma_i \varepsilon^{pl}}\right)\right] \tag{2.3}$$

where C_{LC} and γ are constants fitted to experimental data which define how the yield surface translates as the material plastically deforms. Multiple, i, pairs of constants can be defined to improve the fit to the experimental data.

Table 2.1 Constants characterising a mixed hardening model for Type 316H stainless steel (data from [6]) as implemented in ABAQUS

T (°C)	σ_{y0} (MPa)	C_{LC_1} (MPa)	γ_1	C_{LC_2} (MPa)	γ_2	Q_∞ (MPa)	b
20	216.5	156,435.0	1,410.85	6,134.0	47.19	62.5	6.9
275	165.6	100,631.0	1,410.85	5,568.0	47.19	86.7	6.9
550	147.7	64,341.0	1,410.85	5,227.0	47.19	93.8	6.9
750	117.3	56,232.0	1,410.85	4,108.0	47.19	12.0	6.9
900	114.1	49,588.0	1,410.85	292.1	47.19	0.0	6.9
1,000	54.9	0.0	1,410.85	0.0	47.19	0.0	6.9
1,100	34.0	0.0	1,410.85	0.0	47.19	0.0	6.9
1,400	3.7	0.0	1,410.85	0.0	47.19	0.0	6.9

Constants for the mixed hardening law have been fitted by Aird et al. [6] to Type 316H stainless steel and are shown in Table 2.1 for a range of temperatures, T. Further detail on fitting these constants is presented in Section 4.5.2 which focuses on weld modelling.

2.2.3 CREEP DEFORMATION MODELS

OVERVIEW OF CREEP DEFORMATION

Components operating at high temperature can permanently deform due to the accumulation of creep strains, ε^c. Creep is the time dependent strain which occurs when a material is subjected to stresses at high temperatures for an extended period of time, t. It is caused by the thermally activated movement of dislocations and voids within a materials microstructure. Creep becomes significant at approximately half the absolute melting temperature, T_m, of a material [7, p10].

Time dependant creep behaviour can typically be described by four stages: incubation, primary, secondary and tertiary, as shown in Figure 2.2, when a component is loaded under a constant stress at constant temperature. The incubation period is associated with the gradual accumulation of mobile dislocations. In primary creep early rapid elongation occurs and the creep strain rate decreases. In this initial stage there are many mobile dislocations randomly distributed throughout the grains which become pinned and the material work hardens. In the secondary creep regime the creep strain rate, $\dot{\varepsilon}^c$, becomes constant where the work hardening is balanced by generation of new mobile dislocations. The secondary stage of creep is generally the dominant form of creep during the life of engineering materials. Finally tertiary creep occurs where the creep strain rate accelerates and rupture occurs. During tertiary creep the load carrying capacity of a material is reduced. Typical polycrystalline materials, such as steels, exhibit creep deformation behaviour that is described by the primary, secondary and tertiary regimes [7, pp10-14].

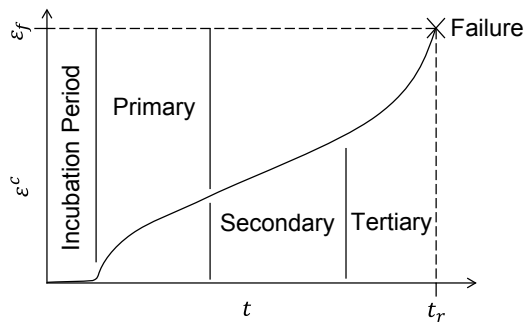


Figure 2.2 Accumulation of creep strain for a typical stainless steel

Various creep mechanisms can occur in metals which are commonly shown in deformation maps. Such diagrams show the relationship between shear stress, temperature and strain rate in a material. The deformation map for Type 316 stainless steel is shown in Figure 2.3. At a temperature of 550°C, which is relevant to this study, the creep deformation mechanism that is prevalent in Type 316 stainless steel is known as power-law creep which is associated with the glide and climb of dislocations. The creep strain rate has a power-law dependence with stress. At low stresses, creep strains accumulate due to the diffusion of atoms and the creep strain rate is approximately proportional to the stress. This deformation mechanism is known as diffusional flow [7, pp14-16].

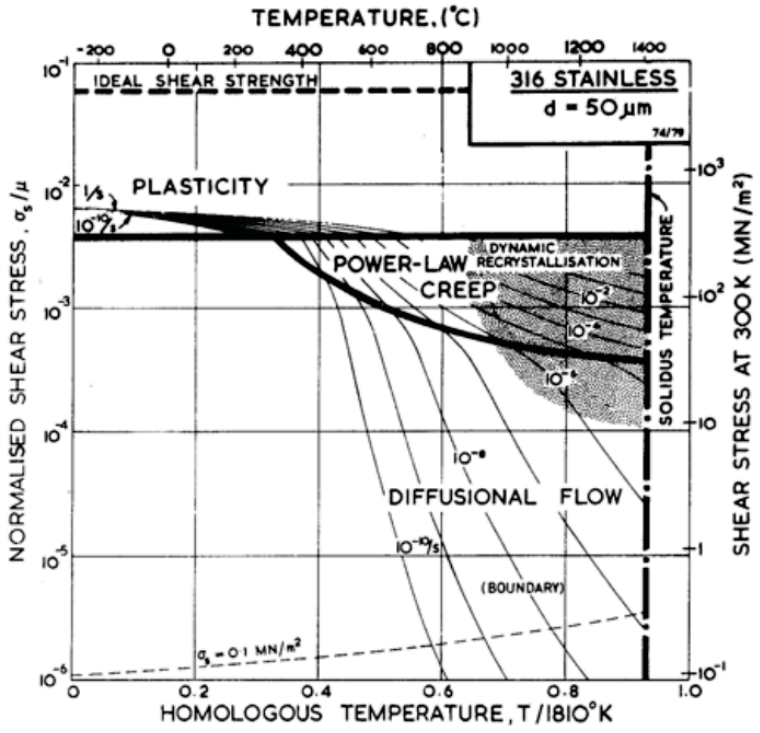


Figure 2.3 Deformation mechanism map for Type 316 stainless steel of grain size 50 μm (image from [8, p65])

Constitutive equations are used to determine ε^c when carrying out assessments or performing numerical analyses. A general expression of $\dot{\varepsilon}^c$ for a uniaxial creep curve, as shown in Figure 2.2, is given by (2.4) where creep strains are dependent on the stress, temperature and time.

$$\dot{\varepsilon}^c = f_1(\sigma, T, t) \tag{2.4}$$

The temperature dependence is defined by:

$$\dot{\varepsilon}^c = f_2(\sigma, t)e^{-Q/RT} \tag{2.5}$$

where Q is the activation energy, R is Boltzmann's constant and T is the absolute temperature. Equation (2.5) includes the Arrhenius rate equation which shows creep is controlled by diffusion processes.

The stress dependence of creep is commonly defined using a power-law relationship such as the Norton creep law where $\dot{\varepsilon}_c$ for constant stress and temperature is defined by:

$$\dot{\varepsilon}^c = C\sigma^n \tag{2.6}$$

where C and n are material constants. The Norton creep law describes the steady state creep strain rate during the secondary creep regime. A similar expression is obtained for the average creep strain rate, $\dot{\varepsilon}_A^c$, where a constant creep strain rate is assumed throughout a components life at a given stress and temperature. It is defined as the ratio of the uniaxial failure strain, ε_f, to the rupture time in a uniaxial creep test, t_r:

$$\dot{\varepsilon}_A^c = \frac{\varepsilon_f}{t_r} = C_A\sigma^{n_A} \tag{2.7}$$

where C_A and n_A are temperature dependent material constants. For Type 316H stainless steel, this law was empirically fitted to test data from 87 constant-load creep tests conducted at 550°C by Webster et al. [9]. The constants C_A and n_A were determined as 1.05×10^{-25} and 8.45 respectively, which define ε^c in mm/mm where σ and t are in units of MPa and h respectively.

The average creep strain rate tends to underestimate the extent of creep deformation at short times and over-estimate creep strains at long times. More accurate creep deformation models can be defined using a power-law or exponential dependence with time, as shown in the following sub-sections. Such models may be used in FE analyses to predict creep deformations, as presented in Chapter 7. Whilst $\dot{\varepsilon}_A^c$ may be less accurate in comparison to these time dependent deformation models, an average creep strain rate is still often assumed for analytical assessments as it is simple to calculate and may be defined when the availability of creep deformation material data is limited.

THE RCC-MR CREEP DEFORMATION MODEL

The RCC-MR design code [10] defines a creep law which separates the primary and secondary creep regimes:

$$\varepsilon^c = \begin{cases} C_1 t^{C_2} \sigma^{n_1}, & t \leq t_{fp} \\ {C_1 t_{fp}}^{C_2} \sigma^{n_1} + C\sigma^n (t - t_{fp}), & t > t_{fp} \end{cases} \quad (2.8)$$

where C_1, C_2, C, n and n_1 are material constants defined in the RCC-MR design code and t is time (in h). The primary creep strain has a power-law relationship with stress and time. The secondary creep strain is in the form of (2.6) in addition to a maximum primary creep strain which is evaluated at the transition time, t_{fp}. This is defined as the time that the primary creep strain rate and secondary creep strain rate are equal and is calculated by differentiating (2.8) with respect to time and equating the resulting expressions.

$$t_{fp} = C_3 \sigma^{n_3} \quad (2.9)$$

where the constants C_3 and n_3 are:

$$C_3 = \left(\frac{C}{C_1 C_2}\right)^{\frac{1}{C_2 - 1}} \quad (2.10)$$

$$n_3 = \frac{n - n_1}{C_2 - 1} \quad (2.11)$$

The RCC-MR code states these expressions are valid up to 1% creep strain. The primary creep formula applies for temperatures between 425°C and 700°C and the secondary creep formula for temperatures between 480°C and 700°C. The constants for the RCC-MR model at 550°C for Type 316H are shown in Table 2.2, which define ε^c in mm/mm where σ and t are in units of MPa and h respectively [11].

Table 2.2 RCC-MR creep deformation model constants for Type 316H stainless steel at 550°C

C_1	C_2	n_1	C	n
2.96×10^{-14}	0.42	4.18	5.29×10^{-26}	8.20

EXPONENTIAL CREEP DEFORMATION MODELS

Garofalo et al. [12] presented a creep law where the primary creep strain has an exponential relationship with time. Authors have presented different versions of this expression to provide the best empirical fit to experimental data for Type 316H stainless steel.

Douglas et al. [13] present:

$$\varepsilon^c = \varepsilon^{cp}_{max}(\sigma, T)[1 - e^{-rt^{\mu}}] + \dot{\varepsilon}^{cs}t \tag{2.12}$$

where ε^{cp}_{max} is the maximum primary creep strain which is a function of stress and temperature, and r and μ are constants which are defined as 0.8 and 0.6 respectively. Chen et al. [11] present the expression:

$$\varepsilon^c = \varepsilon^{cp}_{max}[1 - e^{-\frac{t}{\tau(\sigma)}}] + \dot{\varepsilon}^{cs}t \tag{2.13}$$

where τ is a stress dependent function. At large times the first terms in (2.12) and (2.13) which defines the primary creep strain tend towards $\varepsilon^{cp}_{max}(\sigma, T)$. Chen et al. defined ε^{cp}_{max} as a constant, 6.98 × 10^{-3} mm/mm at 550°C, whereas Douglas et al. used an expression with a stress dependence:

$$\varepsilon^{cp}_{max} = B(\sigma - \sigma_i)^m e^{-q/RT} \tag{2.14}$$

where B, q, R and m are material constants, σ_i is a term representing the internal stress and T is the temperature (in Kelvin). The internal stress takes into account the initial plastic loading on the specimen and is defined as:

$$\sigma_i = \begin{cases} 0.95(\sigma_L - 139) & \sigma > 139 \\ 0 & \sigma \leq 139 \end{cases} \tag{2.15}$$

where σ_L is the loading stress in MPa. The constants for (2.14) are defined in Table 2.3 which define ε^{cp}_{max} in mm/mm where σ is in MPa [13].

In (2.12) and (2.13), $\dot{\varepsilon}^{cs}$ is defined by the Norton creep law, however Douglas et al. include an additional back stress, β, term:

$$\dot{\varepsilon}^{cs} = A(\sigma - \beta)^n e^{-Q/RT} \tag{2.16}$$

where A, n, Q and R are material constants which are shown in Table 2.4 for Type 316H stainless steel [13].

Table 2.3 Constants to determine the maximum primary creep strain in the modified Garofalo model for Type 316H stainless steel defined by Douglas et al. [13]

B	m	q (J/mol)	R (J/mol K)
4	3	158,153	8.314

Table 2.4 Constants for the secondary creep strain rate in the modified Garofalo model for Type 316H stainless steel defined by Douglas et al. [13]

A	n	Q (J/mol)	R (J/mol K)	β
581,315	6.0	392,020	8.314	25

For the exponential creep law fitted by Chen et al. for Type 316H stainless steel at 550°C, the constants C and n to define $\dot{\varepsilon}^{cs}$, using (2.6), are $10^{-32.45}$ and 11.59 respectively. The function τ in (2.13) is defined as:

$$\tau = 1.997 \times 10^{14}(\sigma - \sigma_i)^{-5.129} \tag{2.17}$$

where σ is in MPa and t in (2.13) is in h to determine ε_c, in mm/mm.

Both of these exponential creep laws include internal stress terms which have been empirically determined to improve stress relaxation predictions. Further detail of stress relaxation is given in Chapter 7.

CREEP HARDENING LAWS

The creep models described in the previous sub-sections define $\dot{\varepsilon}^{c}$ for constant σ and constant T. To determine the creep strain rate for variable stress and/or temperature the creep deformation history must be taken into account by hardening laws [7, pp27-29]. Creep strain rates are assumed to be dependent on the exposed time or current creep strain in the material, which are commonly known as time hardening and strain hardening laws respectively.

To illustrate the significance of the hardening law, consider a material where the loading conditions change from σ_1, T_1 to σ_2, T_2 and finally to σ_3, T_3 as shown in Figure 2.4. If time hardening is assumed, at point A where the loading conditions change to σ_2, T_2 the creep strain rate is defined at point B' on the creep strain curve. In this case the transition between the isothermal constant-stress creep curves is made at constant time. Conversely for the strain hardening assumption, the transition between creep curves is made at constant strain and therefore the creep strain rate is defined by point B as the loading conditions change to σ_2, T_2. The effect of using these assumptions is shown in Figure 2.4(b) where the

accumulated creep strain using the various hardening laws differ. In the example shown where $\varepsilon_1^c(\sigma_1, T_1) < \varepsilon_2^c(\sigma_2, T_2) < \varepsilon_3^c(\sigma_3, T_3)$ and in the primary creep regime, the strain hardening law predicts more creep strain. However, if the stress in the component was decreasing or the material was undergoing tertiary creep the time hardening law would estimate greater creep strains [7, pp27-29].

Creep strain rates may be defined for the material models with each of the hardening laws by defining $\dot{\varepsilon}^c$ as a function of time or strain. Differentiating the RCC-MR creep model for the primary regime with respect to time gives:

$$\dot{\varepsilon}^c = C_1 \sigma^{n_1} C_2 t^{C_2 - 1} \tag{2.18}$$

Substituting (2.8) into (2.18) gives the strain hardening formulation:

$$\dot{\varepsilon}^c = (C_1 \sigma^{n_1})^{\frac{1}{C_2}} C_2 \, \varepsilon_c^{\frac{C_2 - 1}{C_2}} \tag{2.19}$$

For the RCC-MR secondary creep law the creep strain has a linear time dependence. Therefore $\dot{\varepsilon}^c$ for time and strain hardening is given by the Norton creep law (2.6).

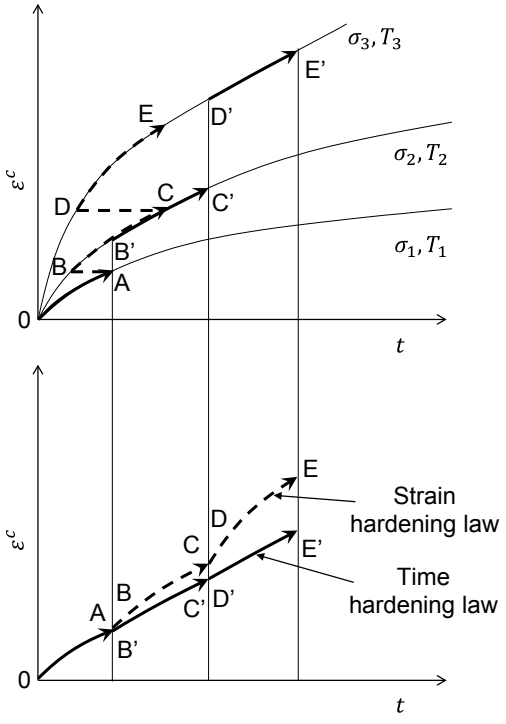


Figure 2.4 Accumulation of creep strain for varying stress and temperature conditions due to strain and time hardening laws

2.2.4 CREEP DAMAGE MODELS

The creep constitutive models detailed in Section 2.2.3 describe the time dependent deformation of materials at high temperature. Eventually, failure of the material occurs as the maximum creep strain or the rupture life is reached, as shown in Figure 2.2. In polycrystalline materials operating in the creep regime, the diffusion of atoms within grains allows pinned dislocations to become mobile. These dislocations propagate through the grain and pile up on grain boundaries causing voids to nucleate and grow. Eventually these voids coalesce to form cracks which leads to material failure.

Failure can be predicted using a ductility exhaustion model where a parameter, D_c, is a measure of the extent of material damage and defined by:

$$D_c = \int_0^t \frac{\dot{\varepsilon}^c}{\varepsilon_f^*} dt \tag{2.20}$$

where ε_f^* is the multiaxial failure strain, or creep ductility. In such a model, failure occurs when the accumulated creep strains reach the multiaxial failure strain, i.e. when the parameter D_c reaches a value of unity. The multiaxial creep ductility can be defined using models based on physical processes such as the void growth model developed by Cocks and Ashby (2.21) [14] or using empirical equations as shown in the R5 procedure (2.22) [2].

$$\frac{\varepsilon_f^*}{\varepsilon_f} = sinh\left[\frac{2}{3}\left(\frac{n-\frac{1}{2}}{n+\frac{1}{2}}\right)\right] \Big/ sinh\left[2\left(\frac{n-\frac{1}{2}}{n+\frac{1}{2}}\right)\frac{\sigma_h}{\sigma_{eq}}\right] \tag{2.21}$$

$$\frac{\varepsilon_f^*}{\varepsilon_f} = exp\left[p\left(1-\frac{\sigma_1}{\sigma_{eq}}\right) + q\left(\frac{1}{2}-\frac{3}{2}\frac{\sigma_h}{\sigma_{eq}}\right)\right] \tag{2.22}$$

where n is the creep strain exponent, σ_1 is the principal stress, σ_h is the hydrostatic stress, σ_{eq} is the equivalent stress and ε_f is the uniaxial creep ductility which is determined experimentally from uniaxial creep tests.

Spindler [15] shows void growth can occur due to different mechanisms, which are identified as diffusion-controlled cavity growth and constrained-cavity growth. The constants p and q in (2.22) are dependent on which of these mechanisms is prevalent for the material and creep strain rate. In Type 316 stainless steel operating at 593°C, Spindler found the creep ductility was independent of the creep strain rate and the void growth mechanism was identified as constrained-cavity growth. The constants p and q were defined as 0.15 and 1.25 respectively.

The uniaxial creep ductility for Type 316H stainless steel at 550°C is found to be 11.3% [9]. However significant scatter exists in test data where upper and lower bound fits to the data were determined as 46.4% and 2.7% respectively. Cast to cast variability has been found to cause a significant contribution to this scatter, where small changes in the chemical composition of the material can have a large impact on the creep ductility [16]. For Type 316H stainless steel in the HAZ, the creep ductility is reduced due to thermo-mechanical cycling experienced during welding. In such regions ε_f has been found to be 0.9% [17].

2.2.5 UNIFORM PRE-COMPRESSION TO REDUCE THE CREEP DUCTILITY

The effect of pre-conditioning Type 316H stainless steel on creep deformation and failure was studied by Mehmanparast et al. [18, 19] where Type 316H stainless steel was uniformly pre-compressed to 8% plastic strain before conducting uniaxial tensile, uniaxial creep and CCG tests. The uniaxial creep tests showed that the pre-compression process had little effect on the minimum and average creep strain rates of the material however the creep ductility was significantly reduced, ε_f = 2.1%. CCG testing was performed using compact tension, C(T), specimens machined from uniformly pre-compressed blocks where the pre-compression direction was aligned normal to the specimen's crack plane. Due to the reduced ductility, faster crack growth rates were observed in CCG tests in comparison to material in the as-received condition [19].

The test specimens developed in this study, which are presented in the following chapters, also used this pre-conditioning process. The reduced creep ductility ensured crack growth occurred during CCG testing. The need to use such material is discussed in Section 2.7.

2.3 FRACTURE MECHANICS CONCEPTS

2.3.1 LINEAR ELASTIC FRACTURE MECHANICS

In linear elastic fracture mechanics (LEFM) the stress intensity factor, K, is used to describe the magnitude of the stress field surrounding a crack tip*. For a cracked body under an applied stress, σ, with a flaw size, a, K is determined by:

$$K = Y\sigma\sqrt{a} \tag{2.23}$$

* The parameter K_I is specific to Mode I conditions where the loads cause the crack mouth to open in the direction normal to the crack faces. Only Mode I conditions are considered in this study so K_I is denoted as K throughout.

where Y is a non-dimensional constant that is dependent on the geometry. For simple geometries and common fracture test specimens values for Y have been published by Tada et al. [20]. For a compact tension, C(T), specimen Y is defined as:

$$Y = \sqrt{\frac{W}{a}}\left[\frac{2+\frac{a}{W}}{\left(1-\frac{a}{W}\right)^{\frac{3}{2}}}\right]\left[0.886 + 4.64\left(\frac{a}{W}\right) - 13.32\left(\frac{a}{W}\right)^{2} + 14.72\left(\frac{a}{W}\right)^{3} - 5.60\left(\frac{a}{W}\right)^{4}\right] \quad (2.24)$$

where W is the distance from the back face of the specimen to the load line.

Directly ahead of the crack tip, the stress component normal to the crack plane, σ_{yy}, is given by:

$$\sigma_{yy} = \frac{K}{\sqrt{2\pi r}} \quad (2.25)$$

where r is the distance from the crack tip. The expression shows a $1/\sqrt{r}$ singularity where stresses reach infinite magnitude towards the crack tip (as $r \to 0$). Local failure of the body occurs, i.e. the crack propagates through the body, when K reaches a critical value called the fracture toughness, K_c.

2.3.2 ELASTIC-PLASTIC FRACTURE MECHANICS

In the LEFM approach the stresses near the crack tip approach infinity as shown by (2.25). For elastic-plastic materials, inelastic deformation occurs at the crack tip as the equivalent stresses, σ_{eq}, reach yield magnitude. In such cases the LEFM solution becomes invalid. If the plastic deformation is confined to a local region around the crack tip a small scale yielding approximation can be made as detailed by Anderson [21, pp61-63]. However when the size of the plastic zone becomes significant, the stress and deformation fields surrounding the crack tip can no longer be characterised by K.

The fracture mechanics parameter J has been shown by Rice [22] to be identical to the energy release rate, G, for linear elastic materials which defines the energy released from a body, per unit area of crack growth. For a homogeneous uncracked body in a state of equilibrium and made of a non-linear elastic material, a line integral can be defined around any closed path that is equal to zero. If a crack is introduced into the body such that it intersects the path, the contour is no longer closed and the line integral takes a finite value. Rice showed that under certain conditions this line integral has a constant value which is independent of the path taken around the crack faces. Like K it is a measure of the stress

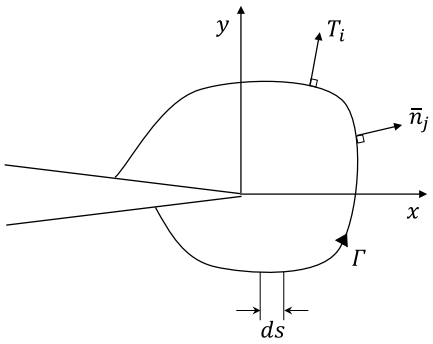


Figure 2.5 The J-integral along a path around a crack tip

field surrounding a crack tip, however unlike K the J-integral is not limited to LEFM. It can be defined for an elastic-plastic material providing no unloading occurs, i.e. where loading is monotonic, and where proportional loading is assumed, i.e. where all stress components increase in proportion. Therefore the material can be assumed to be non-linear elastic.

The mathematical definition of the J-integral was derived by Rice [22] as:

$$J = \int_{\Gamma} \left(W_{SED} dy - T_i \frac{\partial u_i}{\partial x} ds \right) \tag{2.26}$$

where W_{SED} is the strain energy density and T_i, u_i and ds are the traction vector, displacement vector and distance along the contour Γ respectively, as shown in Figure 2.5. The strain energy density, or the elastic-plastic work per unit volume, for a non-linear elastic material is defined as:

$$W_{SED} = \int_0^{\varepsilon_{ij}} \sigma_{ij} d\varepsilon_{ij} \tag{2.27}$$

where σ_{ij} and ε_{ij} are the stress and strain matrices in index notation. The traction vector, T_i, is evaluated by:

$$T_i = \sigma_{ij} \bar{n}_j \tag{2.28}$$

where $\bar{n}_j$ is the unit normal vector at a given plane.

The stress and strain fields around a crack tip under elastic-plastic conditions can be described by the HRR solution presented by Hutchinson [23] and Rice and Rosengren [24]. This solution applies for a material that has a power-law relationship between stress and plastic strain and hence where the behaviour can be described by the Ramberg-Osgood material model (2.1). The stress and strain fields determined using a (r,θ) polar co-ordinate system with origin at the crack tip are determined by (2.29) and (2.30) respectively.

$$\sigma_{ij} = \sigma_0 \left(\frac{J}{\alpha \varepsilon_0 \sigma_0 I_N r} \right)^{\frac{1}{N+1}} \tilde{\sigma}_{ij}(N, \theta) \tag{2.29}$$

$$\varepsilon_{ij} = \alpha \varepsilon_0 \left(\frac{J}{\alpha \varepsilon_0 \sigma_0 I_N r} \right)^{\frac{N}{N+1}} \tilde{\varepsilon}_{ij}(N, \theta) \tag{2.30}$$

where $\tilde{\sigma}_{ij}(N, \theta)$ and $\tilde{\varepsilon}_{ij}(N, \theta)$ are non-dimensionless functions of N and θ, and I_N is a non-dimensionless function of N.

The parameter J defines the magnitude of the stress singularity in a similar way to K for linear elastic conditions. In general, the stresses ahead of a crack tip in elastic-plastic materials can be defined by three zones. At very short distances, the HRR solution predicts infinite stresses. However, crack tip blunting occurs to limit the stresses and hence an alternate large strain analysis is required to define the stresses. At distances greater than twice the crack tip opening displacement, the HRR solutions define the stress field in the plastic zone. If the plastic zone is less than the size of the specimen a region will exist where the stresses are defined by LEFM [21, pp111-114].

2.3.3 CREEP FRACTURE MECHANICS

When cracked bodies operate in the creep regime, creep strains accumulate rapidly around the crack tip due to its stress concentration effect. The parameters K and J describe the stress fields in elastic and elastic-plastic conditions respectively, however when creep conditions are prevalent neither are able to characterise the crack tip stresses. At short times a creep process zone grows around the crack tip, where the stresses relax. Due to this, stress redistribution occurs across the specimen to maintain equilibrium. For constant loading the creep zone eventually becomes widespread and the stress field becomes constant, which is known as the steady state condition. Here the stress and strain fields can be described by a fracture mechanics parameter called C^*.

The parameter C^* may be determined by a contour integral analogous to (2.26) which defined the J-integral:

$$C^* = \int_{\Gamma} \left(\dot{W}_{SED} dy - T_i \frac{\partial \dot{u}_i}{\partial x} ds \right) \tag{2.31}$$

where $\dot{u}$ is the displacement rate vector and $\dot{W}_{SED}$ is the strain energy rate density determined by (2.32).

$$\dot{W}_{SED} = \int_0^{\dot{\varepsilon}_{ij}^c} \sigma_{ij} d\dot{\varepsilon}_{ij}^c \tag{2.32}$$

where $\dot{\varepsilon}_{ij}^c$ is the creep strain rate matrix in index notation.

The C^* parameter describes the stress field at long times where the creep process zone is widespread. Whilst at very short times the creep process zones extends just beyond the crack tip and the stress field is defined by K or J, depending on the extent of crack tip plasticity. However as the creep zone continues to grow, there is a transition region where the stresses are in between that defined by K or J and C^*. At such times the stress field is defined by the parameter $C(t)$. Like C^* this parameter is defined by a contour integral:

$$C(t) = \int_{\Gamma \to 0} \left(\dot{W}_{SED} dy - T_i \frac{\partial \dot{u}_i}{\partial x} ds \right) \tag{2.33}$$

However the parameter $C(t)$ is path dependent and must be evaluated close to the crack tip where creep strains dominate [7, pp111-117].

The RR stress and strain fields in the crack tip region were derived by Riedel and Rice [25] using an elastic-creep material model, where creep strains are determined by the Norton creep law (2.6):

$$\sigma_{ij} = \sigma_0 \left(\frac{C(t)}{I_n \sigma_0 \dot{\varepsilon}_0 r} \right)^{\frac{1}{n+1}} \tilde{\sigma}_{ij}(n, \theta) \tag{2.34}$$

$$\varepsilon_{ij} = \varepsilon_0 \left(\frac{C(t)}{I_n \sigma_0 \dot{\varepsilon}_0 r} \right)^{\frac{n}{n+1}} \tilde{\varepsilon}_{ij}(n, \theta) \tag{2.35}$$

which is analogous to the HRR field solutions shown by (2.29) and (2.30). At long times when creep becomes widespread $C(t) \to C^*$ and therefore the stress and strain fields may be obtained by replacing $C(t)$ with C^* in (2.34) and (2.35) respectively.

The R5 assessment procedure [2] presents methods to estimate the parameters C^* and $C(t)$ using the reference stress concept. This allows conservative estimates of these parameters to be obtained without the use of contour integrals. These methods are detailed in Chapter 7.

2.4 REVIEW OF METHODS TO INDUCE RESIDUAL STRESSES IN FRACTURE SPECIMENS

2.4.1 OVERVIEW OF RESIDUAL STRESSES

Residual stresses are those which remain in a specimen or component once all applied loads have been removed. Such stresses are self-equilibrating across the body and are caused by geometrical misfits between different regions within the specimen or component [26]. Residual stresses are often classed by the length scale over which they self-equilibrate. Those on a micro-scale (type III) exist within grains where there is a misfit of point defects such as solute atoms. Meso-stresses (type II) occur between grains and can arise due to the variation of material properties between grains, such as the presence of different phases in the microstructure or the random orientation of grains in a polycrystalline material. Macro-scale residual stresses (type I) act over large distances, typically over the dimensions of the body. They can arise when the misfit of a plastically deformed region is accommodated by elastic deformation elsewhere in the body.

In assessment procedures, such as R6 [27], the stresses are categorised as primary or secondary. Secondary stresses are those which do not contribute to plastic collapse. Such stresses arise to accommodate a strain mismatch which could be induced from local distortions or thermal gradients. Secondary stresses are self-equilibrating across the structure and at high temperature tend to relax due to creep deformation. Primary stresses are generated by applied loads such as bending or pressure which could lead to plastic collapse of the structure. Combined loading conditions occur where both primary and secondary stresses exist.

When components with residual stresses operate in the creep regime, relaxation of the residual stresses occurs. In such cases creep strains accumulate over time which replaces the elastic strains that were initially present. This reduces the effect of the misfit and therefore the magnitude of the stresses reduce.

Methods to induce residual stresses in fracture specimens to conduct CCG tests under secondary and combined loading conditions were investigated in this study. The magnitudes of residual stresses induced in such specimens and the amount of crack growth measured in subsequent CCG tests are compared in the following sub-sections.

2.4.2 PRE-COMPRESSED C(T) SPECIMENS

The test specimen design which has been frequently used to study the effects of residual stresses on CCG is the pre-compressed C(T) specimen [3, 28-31]. Compressive loads were applied along the load line of C(T) specimens (without a pre-crack and pin holes), as shown in Figure 2.6, where the stress concentration effect of the notch caused local yielding. Upon unloading the tendency of the undeformed material to elastically return to its original shape induced tensile stresses in the plastic region ahead of the notch.

The variation of residual stress along the ligament of a pre-compressed C(T) specimen at mid-thickness is shown as CT3 in Figure 2.9(a). The specimen was made from ex-service Type 316H stainless steel and the stress component normal to the crack plane, σ_{yy}, is shown, (data from [3]). Tensile stresses existed ahead of the notch that were far in excess of yield magnitude (σ_y = 264.6 MPa at room temperature [32])) which drive crack growth in fracture tests. A pre-crack was inserted into the notch after pre-compression where the stress concentration increased the magnitude of crack tip stresses, shown as CT1 in Figure 2.9(a). The stress intensity factor due to the secondary loads, K^s, was determined as 37.6 MPam$^{1/2}$ in specimen CT1 at 550°C [33]. In these specimens significant local plastic strains were induced ahead of the notch and pre-crack, as shown in Figure 2.9(b), where ε^{pl} = 3% near the pre-crack in CT1.

Dai et al. [34] developed a modified design for a pre-compressed C(T) specimen, also made from ex-service Type 316H stainless steel, where a second pair of arms on the back face were used to compress the sample. The rationale of this design is to confine the plastically deformed region to the back of the specimen. After pre-compression these additional arms were removed. However the tensile residual stress ahead of the notch was only 100 MPa which is low relative to σ_y.

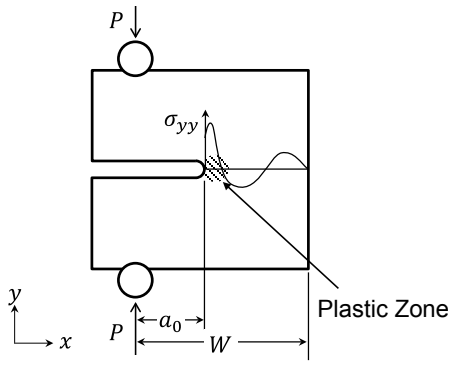


Figure 2.6 Pre-compression of a C(T) specimen showing the plastic zone ahead of the notch

2.4.3 SIDE PUNCHED C(T) SPECIMENS

Mahmoudi et al. [35-37] and Hossain et al. [38] induced residual stresses in C(T) specimens using local out-of-plane compression (LOPC), where the sides of the C(T) specimens were indented with cylindrical punches, as shown in Figure 2.7. The stresses ahead of the pre-crack were tensile and highly triaxial. Triaxiality is defined as the hydrostatic stress, σ_h, divided by the equivalent stress, σ_{eq}. By changing the size and shape of the punch tool and the punch location relative to the crack tip, the distribution of the residual stresses and the extent of plastic deformation could be varied. The LOPC technique was also used by Leggatt and Kamath [39] to mechanically stress relieve weld residual stresses in C(T) specimens.

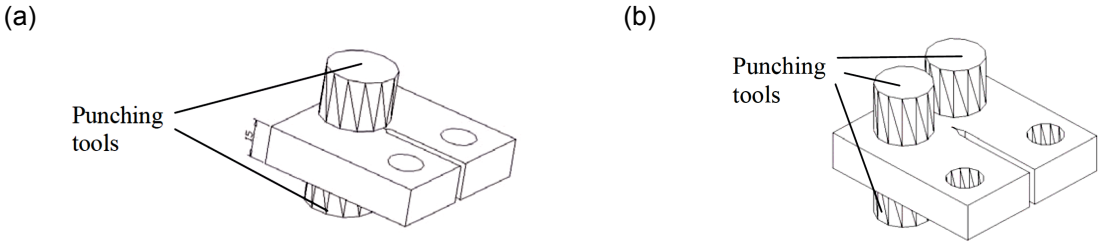


Figure 2.7 C(T) specimen indented using (a) single punch and (b) double punch tools to generate residual stresses (images from [35])

The residual stresses induced in three specimens, with different punch tools, were predicted by Hossain et al. [38] using FE models which were validated using ND measurements, and are shown as SP, FoE and DP in Figure 2.9(a). These specimens were made from ex-service Type 316H stainless steel. Tensile residual stresses between 500 MPa to 900 MPa were generated ahead of the crack tip for the various tools, which were far in excess of σ_y. The tensile region extended 3 to 7 mm from the pre-crack. Triaxial stresses were generated ahead of the crack tip in all specimens, where triaxiality was largest for the DP tool shape (σ_h/σ_{eq} = 2.3). This tool shape inhibited plastic deformation during compression and the equivalent plastic strain, ε^{pl}, was 1.3% at 0.3 mm ahead of the crack tip which increased to 5% at 10 mm from the crack tip, as shown in Figure 2.9(b). For the other two side punched specimens, ε^{pl} was greater than 4% throughout the ligament. The stress intensity factors have not been published for these test specimens.

2.4.4 RESIDUAL STRESSES FROM EB WELDS

Leggatt [40] and Sharples et al. [41] induced residual stresses in aluminium plates by using multiple electron beam (EB) weld passes. The specimens were created with the purpose of assessing ductile tearing behaviour in accordance with the R6 procedure [27].

Pre-cracks were located parallel to and in between two EB welds such that the transverse weld residual stresses provided the crack driving force. Residual stresses were measured using biaxial strain gauges. Tensile residual stresses of up to 100 MPa were generated in the transverse direction, which was less than a third of the material's yield stress (σ_y = 355 MPa).

EB welding was used by Davies et al. [42] to fabricate C(T) specimens containing Manual Metal Arc (MMA) weldments from an ex-service stainless steel header made of Type 316H stainless steel. Extension blocks were EB welded to the weldment blocks, as shown in Figure 2.8(a), to manufacture C(T) blanks. Pre-cracks and pin-holes were then machined into the C(T) blanks to create C(T) specimens.

ND measurements were made at mid-thickness through the centre of the specimen. The residual stresses are shown in Figure 2.8(b), the stress directions are based on the co-ordinate system shown in Figure 2.8(a). Large residual stresses were present in the

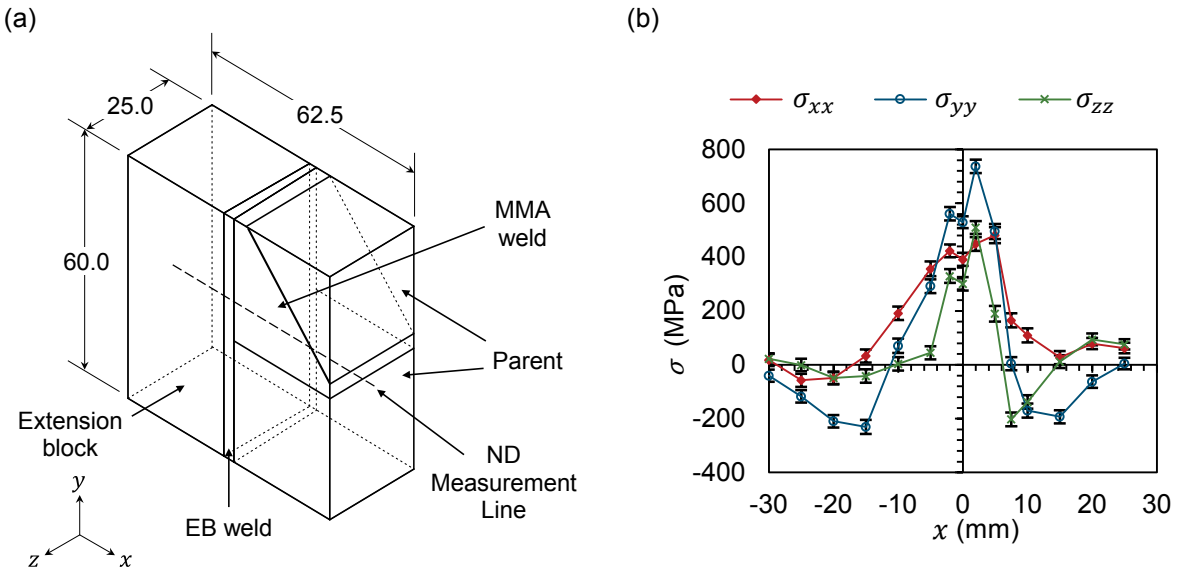


Figure 2.8 (a) Illustration of a C(T) blank containing MMA and EB welds (b) Residual stress distribution across C(T) blank along HAZ in MMA and EB welded block (data from [42])

centre of the specimen, close to the EB weld line, in all three of the measured directions. The longitudinal residual stresses, σ_{yy}, were the greatest with the peak magnitude measured to be 740 MPa. The transverse, σ_{xx}, and normal, σ_{zz}, residual stresses were 500 MPa near the weld line. The tensile residual stress region extended to approximately 10 mm from the weld line. Compressive stresses towards the outer edges of the specimen balanced those at the centre.

2.4.5 LOAD APPLICATION USING A THREE BAR STRUCTURE

A system to apply loads to C(T) specimens which relax during a creep test has been developed by Shirahatti el al. [43, 44]. The authors describe the imposed stresses as long range residual stresses which can arise in plant components during the fit up of a pipework assembly. This test rig was designed to investigate the role of elastic follow up on CCG.

At high temperature elastic follow up can occur when part of a structure accumulates creep strains and stress relaxation takes place. If the overall structure is compliant, i.e. has low stiffness, it will deform elastically to accommodate an inelastically deforming local region. Hence high elastic follow up occurs and any loads which the structure exerts on the creeping component remain. Conversely if the overall structure is stiff, deformation only occurs in that local region and due to this the local stresses relax.

A C(T) specimen was mounted in a test rig consisting of three bars: one attached in series and two in parallel. During fit up, the C(T) specimen and the bar attached in series were loaded in tension which was balanced by compression in two outer bars connected in parallel. Hence the residual stresses equilibrated across the structure rather than the specimen. The rig with the C(T) specimen was placed in a furnace. During creep testing, inelastic deformation occurred in the C(T) specimen and subsequently the test rig changed to accommodate the deformation. When the stiffness of the outer bars were relatively low, significant elastic follow up occurred and the bars extended. Therefore the structure continued to apply a large tensile load on the C(T) specimen. Conversely when the bars were stiff the loading condition was similar to a displacement controlled test and the load relaxed in the C(T) specimen. The extent of stress relaxation was dependent on the relative stiffness of the three bar structure.

This recently developed test method has the advantage that the effect of residual stresses may be studied in laboratory environments without changing the microstructure of the material, which occurs for residual stresses induced as a result of plastic deformation.

However, this test rig is complex relative to the pre-compression and welded specimens where the stresses are self-contained. The three bar structure must be carefully fabricated to minimise displacements at the fixtures and in-situ strain measurements must be accurately made to determine the relative stiffness of the bars.

2.4.6 CREEP CRACK GROWTH STUDIES UNDER SECONDARY LOADS

Creep crack growth tests were conducted on the pre-compressed [3, 31] and LOPC C(T) specimens [38] to study the effect of secondary loads on crack growth. These specimens were thermally soaked at 550°C to allow creep damage to accumulate during stress relaxation. All of these specimens were made using ex-service Type 316H stainless steel.

Turski et al. [3] thermally soaked two pre-compressed C(T) specimens, CT1 and CT3, which had a 3.5 mm pre-crack and no pre-crack respectively for 4,500 h. Nezhad [31] thermally soaked a pre-compressed C(T) specimen with a pre-crack (A1B4) for 1,025 h. Three LOPC C(T) specimens (SP, DP and FoE) were tested by Hossain et al. [38] at 550°C for 2,100 h. Each of these specimens had been punched using a different tool shape to generate various residual stress distributions.

The residual stresses normal to the crack plane, σ_{yy}, along the ligament and at mid-thickness for each specimen are shown in Figure 2.9(a). These were determined by the

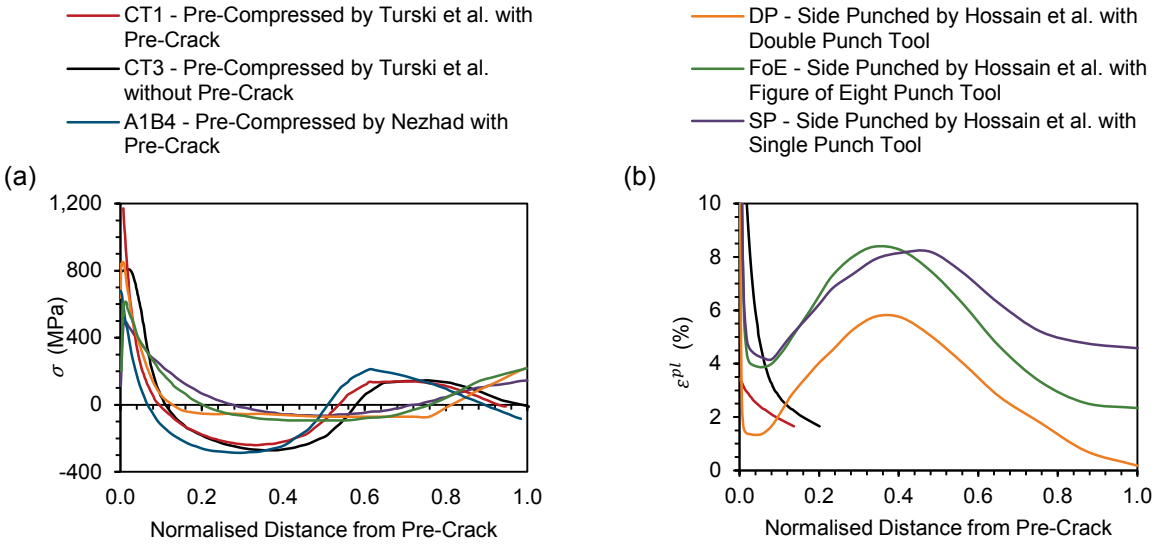


Figure 2.9 (a) Residual stress component normal to the crack plane and (b) equivalent plastic strain, along the ligament and at mid-thickness of secondary loaded C(T) specimens, data from [3, 31, 38]

authors using three dimensional FE simulations of the compression processes at room temperature, which were validated using ND residual stress measurements [3, 31, 38]. All of these simulations assumed isotropic hardening. The equivalent plastic strain, ε^{pl} along the ligament at mid-thickness is shown in Figure 2.9(b). For specimen A1B4, ε^{pl} was not reported by Nezhad.

In specimen CT3, tensile stresses of approximately 800 MPa existed ahead of the notch. The stress concentration effect of the pre-crack in CT1 caused these stresses to increase further. The stress magnitude in A1B4, which was also pre-cracked, was less than CT1. The side punched C(T) specimen DP had large tensile residual stresses which were comparable to those in the pre-compressed C(T) specimens. Specimens FoE and SP had decreasing magnitudes of peak tensile stress although these were still large relative to the room temperature yield stress (σ_y = 264.6 MPa [32]) of the material.

Following thermal soaking, CT1 had maximum and average crack extensions of 2.0 and 1.4 mm respectively. The crack was deepest at mid-thickness where the stresses were highly triaxial, little crack growth was observed near the side faces. Specimen CT3, which had no pre-crack, had a crack which had a maximum depth of 2.1 mm. However this crack was discontinuous through the thickness of the specimen and had an average depth of 0.9 mm. In specimen A1B4, no crack growth was observed after 1,025 h of testing. Specimen DP and FoE had approximately 0.4 mm of crack growth in the central region of the specimen and specimen SP had no crack growth.

The extent of crack growth does not appear to be consistent with the magnitude of tensile residual stresses ahead of the pre-crack. Specimen CT1 had higher residual stress than CT3 yet the amount of crack growth was the same. Similarly the tensile residual stresses in specimen DP were greater than specimen FoE yet the amount of crack growth was the same. Specimen A1B4 had similar magnitude of residual stresses to the side-punched C(T) specimens however no crack growth was observed.

Creep testing of uniformly pre-compressed material, detailed in Section 2.2.5, has shown plasticity significantly reduces the material's creep ductility and therefore increases crack growth rates in CCG tests. During plastic deformation, dislocations are generated and pile up on grain boundaries to form voids. These provide favourable sites for cavity nucleation and growth during creep, hence the presence of plastic deformation causes a reduction in creep ductility.

The specimens with large cracks have a combination of high residual stresses and plasticity. During CCG tests it is difficult to distinguish between the effects of the tensile residual stresses and the changes in creep ductility due to plasticity. To investigate the effects of residual stresses on CCG the plasticity, and therefore the creep ductility, must be constant across the ligament of the specimen.

2.5 STRESS INTENSITY FACTOR UNDER SECONDARY LOADING CONDITIONS, K^s

2.5.1 DEFINITION OF K^s

The stress intensity factor, K, defines the crack driving force, as described in Section 2.3.1. Distinction between the stress intensity factor due to the primary and secondary load is made using the notation K^p and K^s. Under primary loading conditions K^p is routinely found using analytical solutions, e.g. by (2.23) and (2.24), or determined numerically in FE analyses. For secondary loading conditions, K^s is generally difficult to analyse analytically due to the complicated and often unknown residual stress distributions. Some guidance to determine K^s is given in the R6 procedure or under certain loading conditions it may be obtained from handbook solutions [20] (an example is included in Appendix A).

A modified J-integral approach was developed by Lei et al. [45] which allowed the crack driving force under residual stresses to be determined. This approach is implemented in FE post-processing software, such as JEDI [46, 47], and has been frequently used to determine J [47, 48]. The FE software, ABAQUS, has recently been updated to include this modified approach. In this section methods to determine K^s from FE analyses where residual stresses are present are explored.

2.5.2 THE J-INTEGRAL WITH INITIAL STRAINS

In the presence of residual stresses, the definition of the J contour integral defined by Rice [22] is no longer valid as the loading history to induce the residual stress cannot be assumed to be monotonic. The definition of the contour integral was extended to include the effects of residual stresses by Lei et al. The J-integral is commonly evaluated numerically using FE analyses and recently the FE software ABAQUS (version 6.11) was updated to include this modified J-integral [49].

The general expression for the J-integral is presented by Shih et al. [50] and is shown in (2.36), where the kinetic energy term is omitted as quasi-static conditions are assumed.

$$J = \lim_{\Gamma \to 0} \int_{\Gamma} \left(W_{SED} \delta_{1i} - \sigma_{ij} \frac{\partial u_j}{\partial x_1} \right) \bar{n}_i ds \tag{2.36}$$

where the parameters are as described in Section 2.3.2 and Figure 2.5. In the general expression the value of the J-integral is obtained in the limiting case where the contour approaches the size of the crack tip. When there are no body forces, residual strains and crack face tractions (2.36) reduces to (2.26) which is the path independent form derived by Rice [50]. Lei et al. showed this general expression can be solved to determine a path independent J under secondary load conditions.

In FE analyses the stresses and strains are calculated at integration points within elements and it is more accurate to evaluate J over an area instead of computing line integrals. The divergence theorem is used to convert (2.36) into an area integral. An area integral is evaluated over the region A, shown in Figure 2.10, that is enclosed by the contours $C_I + C^+ - \Gamma + C^-$. To evaluate this integral, Li et al. [51] introduced a parameter q_1 which defines a smooth function within the integral region A that has the value of one and zero at the inner, C_I, and outer, Γ, contours respectively. This approach is similar to the virtual crack extension method presented by DeLorenzi [52].

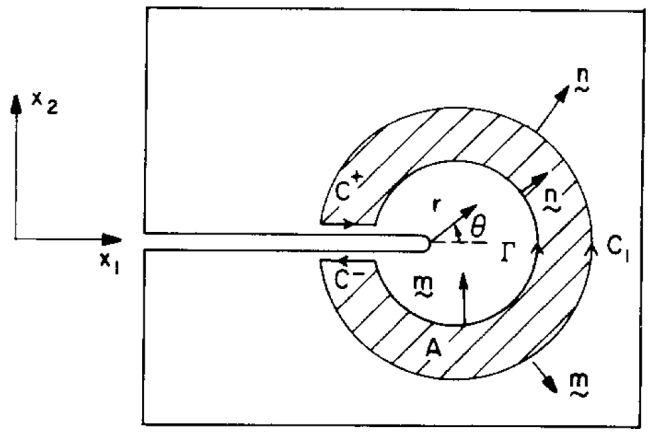


Figure 2.10 Contour integral within a region A (image from [50])

Applying the divergence theorem to (2.36) and assuming no body forces and crack face tractions, the J-integral is expressed as [50]:

$$J = \int_A \frac{\partial}{\partial x_1}\left[\left(\sigma_{ij}\frac{\partial u_j}{\partial x_1} - W_{SED}\delta_{1i}\right)q_1\right]dA$$
$$= \int_A \left[\sigma_{ij}\frac{\partial u_j}{\partial x_1} - W_{SED}\delta_{1i}\right]\frac{\partial q_1}{\partial x_1}\,dA + \int_A \left[\frac{\partial}{\partial x_i}\left(\sigma_{ij}\frac{\partial u_j}{\partial x_1}\right) - \frac{\partial W_{SED}}{\partial x_1}\right]q\,dA \tag{2.37}$$

Equation (2.37) remains valid where residual or thermal stresses are present, however the inner contour of the area integral domain must tend towards the crack tip region [50].

The general expression shown in (2.37) was modified to evaluate path independent J-integrals from load conditions with initial strain fields generated by thermal loads [50, 53] and later extended to load conditions with residual stresses [45]. Where pre-strains exist, the total strain consists of the mechanical strain, ε_{ij}^m, and the initial strain ε_{ij}^0:

$$\varepsilon_{ij} = \varepsilon_{ij}^m + \varepsilon_{ij}^0 \tag{2.38}$$

where ε_{ij}^0 equals the thermal strain, ε_{ij}^{th}, under conditions with thermal stresses and ε_{ij}^0 equals the initial plastic strain, ε_{ij}^{pl0}, for residual stresses generated by plastic deformation in an uncracked body [54].

The definition of the strain energy density, W_{SED}, is modified from (2.27) to take into account the mechanical strain field only [49]:

$$W_{SED} = \int_0^{\varepsilon^m} \sigma_{ij}\,d\varepsilon_{ij}^m \tag{2.39}$$

which is equal to the total strain energy density less the inelastic strain energy density at the initial state.

$$W_{SED} = W_{SED}^{Total} - W_{SED}^{initial\ state} \tag{2.40}$$

The plastic strains in the body due to the residual stresses are considered as part of the initial state. As long as any further loading in the specimen is monotonic and proportional, the J-integral is path independent [54].

Using the chain rule, the derivative of the strain energy density can be expressed as:

$$\begin{aligned}\frac{\partial W_{SED}}{\partial x_1} &= \frac{\partial W_{SED}}{\partial \varepsilon_{ij}^m}\frac{\partial \varepsilon_{ij}^m}{\partial x_1} \\ &= \sigma_{ij}\frac{\partial \varepsilon_{ij}^m}{\partial x_1} \\ &= \sigma_{ij}\frac{\partial \varepsilon_{ij}}{\partial x_1} - \sigma_{ij}\frac{\partial \varepsilon_{ij}^0}{\partial x_1}\end{aligned} \tag{2.41}$$

Also the equilibrium equation provides:

$$\frac{\partial \sigma_{ij}}{\partial x_j} = 0 \tag{2.42}$$

From this the first term in the second integral in (2.37) can be simplified to:

$$\frac{\partial}{\partial x_i}\left(\sigma_{ij}\frac{\partial u_j}{\partial x_1}\right) = \sigma_{ij}\frac{\partial \varepsilon_{ij}}{\partial x_1} \tag{2.43}$$

Substitution of (2.41) and (2.43) into (2.37) provides a path independent expression for the J-integral assuming no body forces, no crack face tractions and equilibrium conditions:

$$J = \int_A \left[\sigma_{ij}\frac{\partial u_j}{\partial x_1} - W_{SED}\delta_{1i}\right]\frac{\partial q_1}{\partial x_i}dA + \int_A \sigma_{ij}\frac{\partial \varepsilon_{ij}^0}{\partial x_1}qdA \tag{2.44}$$

This expression allows J to be evaluated using area integrals for 2D FE analyses and can be extended to perform volume integrals to determine J in 3D simulations [49]. The commercial FE software ABAQUS was recently updated to include this modified J-integral expression to determine J under residual stress conditions. ABAQUS calculates J for area or volume domains for models in two or three dimensions respectively, which are specified during model development. It is common to choose many domains of increasing size to verify J is path independent.

From J the effective stress intensity factor, K_J^s, may be estimated by:

$$K_J^s = \sqrt{JE'} \tag{2.45}$$

where $E' = E/(1-\nu^2)$ and $E' = E$ under plane strain and plane stress conditions respectively as defined in R6 Section II.6.5. The subscript J is used to denote the stress intensity factor has been determined from the J integral. If secondary stresses are low and elastic follow up is not significant, $K_J^s \approx K^s$ [27].

2.5.3 K^s USING THE PRINCIPLE OF SUPERPOSITION

An alternate method to determine K^s has been used by various authors [28, 33, 45, 55] using the principle of superposition. This principle states that for a cracked body subject to various applied loads under linear elastic conditions, K can be determined by the summation of the K solutions when considering each of these applied loads individually, provided the mode of crack loading is consistent, e.g. Mode I loading [21]. Using this principle, it can be shown that K for a cracked body under remote stresses can be determined by considering the same geometry where the remote stress is replaced by tractions on the crack face [52, 56].

Consider a cracked body with applied loads that are symmetric through the crack plane as shown in Figure 2.11(a). An equivalent problem for an uncracked body, as shown in Figure 2.11(b), can be solved to determine the stresses in the region corresponding to the crack plane, $p(x)$.

Using the principle of superposition, the value of K can be determined by considering the sum of the bodies shown in Figure 2.12. Figure 2.12(b) shows the cracked body under the original load conditions and also with the stress distribution $p(x)$, which is found from Figure 2.11(b) and is applied in compression on the crack face. The applied stress distribution $-p(x)$ is such that the crack mouth closes exactly. In the uncracked body shown in (c), only the tractions $p(x)$ are applied to the crack face. The summation of the loads acting on the boundaries in (b) and (c) results in the original load condition shown in (a).

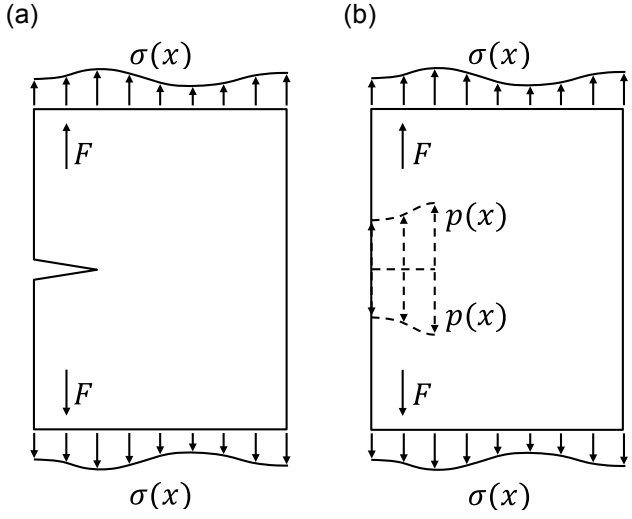


Figure 2.11 Applied loads on (a) a cracked body and (b) an uncracked body to determine K^s using the superposition approach

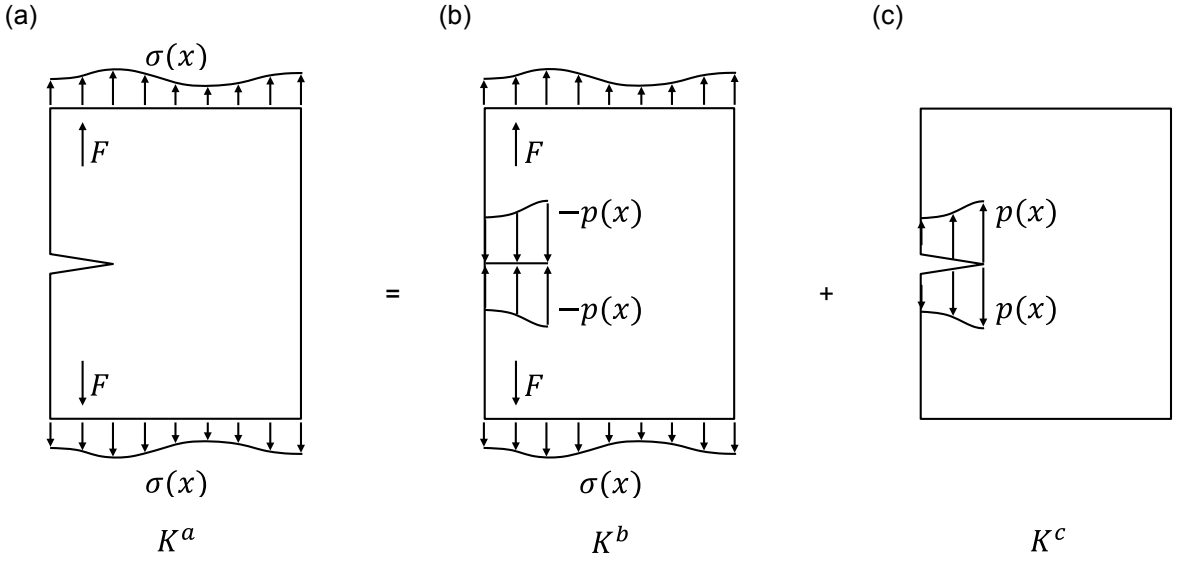


Figure 2.12 Superposition of boundary loads on crack plate to determine K (a) remotely loaded crack body, (b) remotely loaded crack body with compressive crack face tractions to cause crack closure and (c) crack body with tensile crack face tractions

Using the principle of superposition, the sum of the K solutions is also equivalent:

$$K^a = K^b + K^c \tag{2.46}$$

However in Figure 2.12(b) the crack mouth is closed and a stress singularity at the crack tip is not present, therefore K^b = 0. Following this, K for the crack face loaded geometry is the same as the original remotely loaded problem, i.e. $K^c = K^a$.

Using this approach, K in a cracked body due to residual stresses can be determined by considering the residual stresses for the equivalent uncracked body as a stress distribution across the crack face. The value of K^s can be evaluated using numerical simulations where the residual stress field in the uncracked body is determined from an elastic-plastic FE analysis and mapped onto a linear elastic model of the cracked body.

2.6 EXPERIMENTAL EVALUATION OF RESIDUAL STRESSES

2.6.1 OVERVIEW

Many measurement techniques are available to measure sub-surface residual stresses in specimens and components. Non-destructive methods include neutron and X-ray diffraction where the atomic spacing of the material is used as a strain gauge. Destructive techniques include hole drilling and the contour method where residual stresses are inferred from distortions caused by stress redistribution following cutting of the sample. The number

of stress components that can be evaluated vary between each technique. There are also limitations to the size of the sample and spatial resolution of the measurement region for each measurement method. The ND, contour method and slitting techniques were used in this study which are detailed in this section. In-situ surface strain measurements were additionally made whilst fabricating C(T) specimens using the digital image correlation (DIC) optical technique which is also described.

2.6.2 NEUTRON DIFFRACTION

In the ND technique, residual stresses are calculated from measurements of the spacing between crystal lattice planes. Testing is performed using diffractometer instruments located at neutron generating facilities, which is shown schematically in Figure 2.13(a) for a monochromatic beam produced by a reactor source. A beam of neutrons directed into a specimen is scattered at various angles by each of the material's crystallographic planes.

The scattering angle is defined by Bragg's Law [57]:

$$d_{hkl} = \frac{\lambda}{2\,sin\,\theta_{hkl}} \tag{2.47}$$

where λ is the wavelength of the incident beam, θ is the Bragg angle of the diffraction peak, d_{hkl} is the lattice spacing and $\{hkl\}$ denotes the crystallographic plane.

For a monochromatic beam, a detector is positioned such that the number of neutrons scattered by one of these planes is counted. Residual stresses in the specimen cause small changes in the lattice spacing and hence there are small variations in the scattering angle

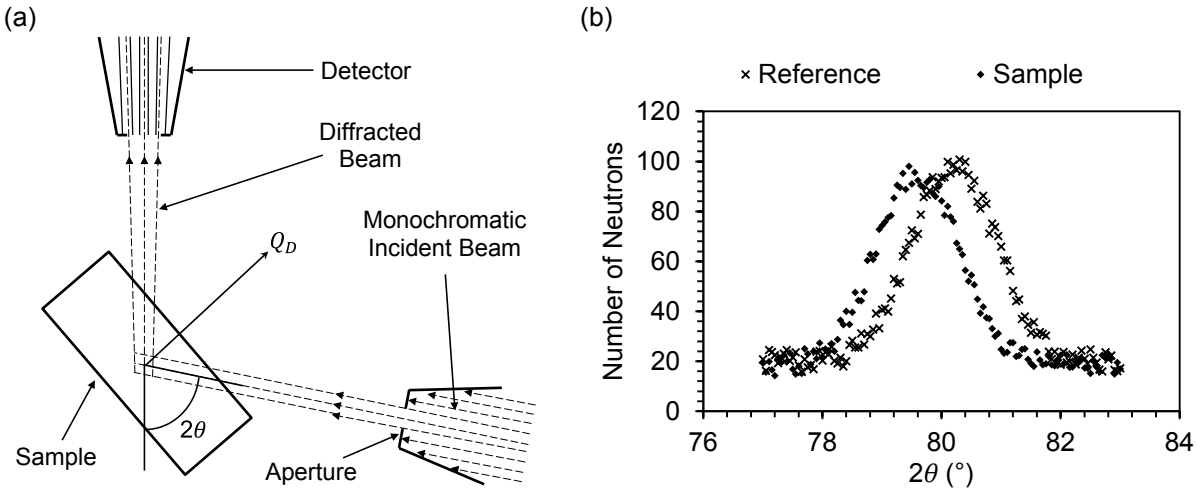


Figure 2.13 (a) Illustration of a diffractometer instrument for measuring strain using a monochromatic neutron beam (b) Peak shift in measured scattering angle caused by lattice strain

measured. The detector counts neutrons over a small range of angles. Scattering in a particular direction is favoured depending on the lattice strain as shown in Figure 2.13(b). A Gaussian profile is fitted to each data set to find 2θ at the peak position of the scattering angle. Elastic strain is calculated by comparing θ to that of a strain free sample using [58]:

$$\varepsilon_{hkl} = \frac{d_{hkl} - d_{0,hkl}}{d_{0,hkl}} = -\left(\theta_{hkl} - \theta_{0,hkl}\right) cot\, \theta_{0,hkl} \tag{2.48}$$

where ε_{hkl} is the lattice strain, d_0 is the reference lattice spacing and θ_0 is the reference scattering angle which are measured from a strain free sample. The strain is measured in the direction Q_D as shown in Figure 2.13(a) and the gauge volume is described by the intersection of the incident beam and the diffracted beam. By moving and rotating the specimen relative to the incident beam and detector other measurement points and strain components in the specimen can be sampled. Changing apertures for the incident beam and the detector allows the size of the gauge volume to be varied.

The deformation of some crystallographic planes remain elastic after the bulk material undergoes plastic deformation as shown by Hutchings et al. [59, pp149-151]. Therefore measuring the lattice spacing for such planes allows strains to be measured for material which has undergone macroscopic yielding. For austenitic stainless steel the $\{311\}$ plane is recommended as the stress-strain response of this plane remains linear for large applied stresses [59, pp210-215].

Residual stresses may be calculated providing the strains have been measured in three mutually orthogonal directions using:

$$\sigma_i = \frac{E_{hkl}}{1 + \nu_{hkl}} \varepsilon_i + \frac{\nu_{hkl} E_{hkl}}{(1 + \nu_{hkl})(1 - 2\nu_{khl})} (\varepsilon_1 + \varepsilon_2 + \varepsilon_3) \tag{2.49}$$

where E_{hkl} and ν_{hkl} are the Young's modulus and Poisson's ratio respectively of the crystallographic plane $\{hkl\}$.

The Voigt, Reuss or Kröner models may be used to determine the values of the $\{hkl\}$ specific material constants. Each of these models are based on different assumptions for the stress and strain distributions through grains in the material. The ND technique measures the strain in the crystal lattice. Lattice strains are favoured in particular directions and therefore in a polycrystalline material, where grains are randomly orientated, intergranular stresses occur [59, pp210-215]. The strains measured using the ND technique are a combination of type I

macrostresses, acting over length scales of the order of the specimen geometry, and type II intergranular stresses, which occur between grains.

In the Voigt model it is assumed all the grains within a polycrystalline aggregate experience the same uniform strain under an applied uniaxial stress. Whereas the Reuss model assumes grains experience the same uniform stress. The Reuss model does not ensure compatibility of strains at the grain boundaries. The Kröner model allows the stress and strain to vary between the grains in a polycrystalline aggregate. The values of E_{hkl} and ν_{hkl} for austenitic stainless steel are shown in Table 2.5. The Voigt and Reuss model provide upper and lower bounds of the $\{hkl\}$ specific material constants whilst the Kröner model is considered the most accurate [59, pp222-230].

Table 2.5 $\{hkl\}$ specific material constants for austenitic stainless steel [59, pp222-230]

	Voigt Model	**Reuss Model**	**Kröner Model**
E_{311} (GPa)	225.5	138.3	183.5
ν_{311}	0.27	0.35	0.31

2.6.3 SLITTING

The slitting technique is commonly used to experimentally determine K^s and a single component of residual stress in components or specimens [60]. A sample containing residual stresses is incrementally cut using wire electrical discharge machining (EDM) whilst the deformation of the specimen is measured using strain gauges usually located at the back face of the cut profile.

The stress intensity factor due to secondary loads, K^s, can be determined from back face residual strains using [61]:

$$K^s(a) = \frac{E'}{Z(a)}\frac{d\varepsilon}{da} \tag{2.50}$$

where ε is the back face strain, a is the crack length, i.e. cut distance, E', is the plane stress or plane strain Young's modulus and $Z(a)$ is the influence function which is dependent on the geometry and strain measurement location. Schindler and Bertschinger [62] present analytical expressions for $Z(a)$ for a rectangular plate with length, L, width, W and crack length, a:

For $a/W < 1 - 0.4L/W$:

$$Z(a) = \frac{-2.532}{(W-a)^{3/2}} \sqrt{1 - \frac{\left(\frac{a}{W} - 1 + \frac{0.4L}{W}\right)^2}{\left(1 - \frac{0.4L}{W}\right)^2}}\, \xi(a) \tag{2.51}$$

where:

$$\xi(a) = \left[1 + \left(-3.268 + \frac{4.597L}{W}\right)\left(1 - \frac{0.4L}{W} - \frac{a}{W}\right)^2 - \left(-0.028 + \frac{0.316L}{W}\right)\left(1 - \frac{0.4L}{W} - \frac{a}{W}\right)\right]$$

For $1 - 0.4L/W < a/W < 1$:

$$Z(a) = \frac{-2.532}{(W-a)^{3/2}} \tag{2.52}$$

The residual stresses are calculated using a weight function solution which is a geometry dependent expression that relates K^s to an arbitrary loading condition for the same mode of fracture [21, pp56-58]. The weight function solution for a C(T) specimen is [61]:

$$K^s(a_i) = \sum_{j=1}^{i} \sigma_j \int_{a_{j-1}}^{a_j} h(x, a_i)\ dx \tag{2.53}$$

where:

$$h(x,a) = \sqrt{\frac{2}{\pi a}} \frac{1}{\sqrt{1 - x/a}} \left[1 + \frac{1}{\left(1 - \frac{a}{W}\right)^{\frac{3}{2}}} \sum_{k,l} A_{kl} \left(\frac{a}{W}\right)^{\mu} \left(1 - \frac{x}{a}\right)^{k+1}\right] \tag{2.54}$$

and the coefficients of the matrix A_{kl} are given in Table 2.6. Equation (2.53) is solved for i intervals which is the number of strain measurements taken during the cut process. Prime [61] determined the stress distribution in a C(T) specimen by solving (2.53) with a Gaussian integration approach.

Table 2.6 Coefficients of A_{kl} used to determine the weight function for a C(T) specimen [63]

		l				
		0	**1**	**2**	**3**	**4**
k	**0**	2.673	-8.604	20.621	-14.635	0.477
	1	-3.557	24.9726	-53.398	50.707	-11.837
	2	1.230	-8.411	16.957	-12.157	-0.940
	3	-0.157	0.954	-1.284	-0.393	1.655

2.6.4 THE CONTOUR METHOD

The contour method is a destructive residual stress measurement technique used to determine stresses across a plane in a specimen. Whilst scattering techniques such as ND samples stresses at point locations, the contour method is unique as it measures a two dimensional field of a single stress component. In this method a specimen is sectioned using wire EDM through a straight plane. During cutting the residual stresses local to the new free surfaces are relieved which causes the surface to deform. The profile of the cut surfaces are measured and used to calculate the original residual stress field.

This technique is an extension of Bueckner's superposition principle [56] where stresses, strains and displacements on a body with different loading configurations may be summed if the material is linearly elastic [21, pp54-56]. Figure 2.14 shows the contour method concept. A body with residual stresses, σ_{yy}, where a tensile region in the centre of the specimen is balanced by compressive regions towards the outside is shown in (a). If the body is cut in half (b), the stresses normal to the cut plane are relieved and the cut surfaces deform. By forcing the deformed cut surface in a corresponding stress free body to become flat, stresses are generated near the cut surface (c). From the superposition principle the stress distributions of (b) summed with (c) must equal (a). Therefore (c) shows the residual stresses, σ_{yy}, in the original body through the cut plane [60, p110-112].

In practice, the deformation as shown in (b) is obtained experimentally and (c) is evaluated using FE simulations. In the simulation displacements are applied to nodal

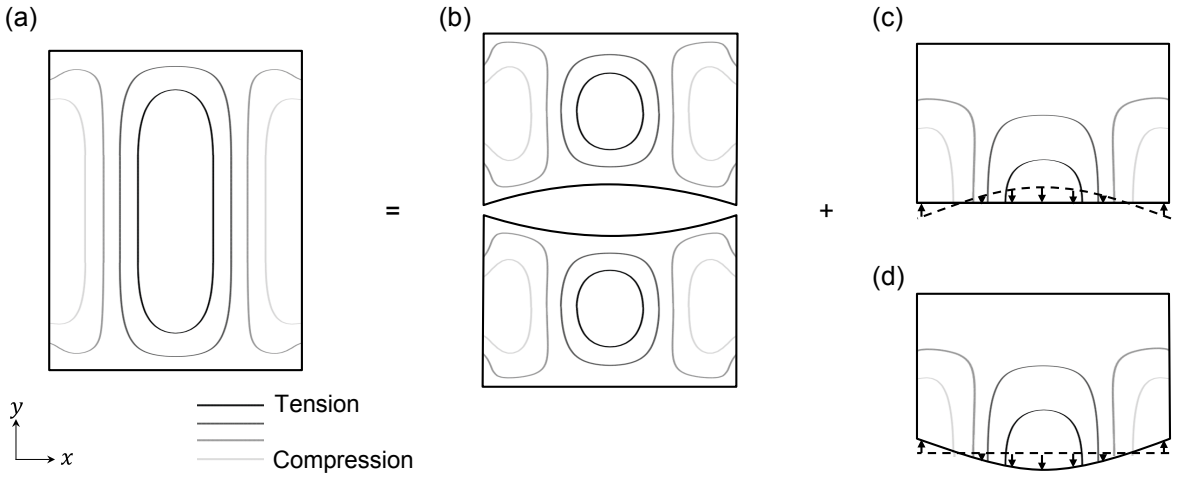


Figure 2.14 The contour method described by the superposition principle (a) body with residual stresses, σ_{yy} (b) deformed body after cutting and (c) loading on stress free deformed body to create flat cut surface

positions on the cut surface. To simplify the modelling process the displacements are applied to an initially flat surface as shown in Figure 2.14(d). It is assumed stress distributions in (c) and (d) are the same as the deformations are small and linear elasticity is assumed [64].

The superposition principle requires that the deformation of the specimen during cutting is elastic, therefore wire EDM is chosen for the cutting as this process does not impose large stresses on the specimen. Plasticity may arise when cutting into regions of residual stress, which is a possible source of error in the measurements [60, pp132-133].

The cut surfaces are assumed to be flat with respect to the uncut body. However if the EDM cut is not made in a straight line or the specimen deforms during the cut, this assumption is invalid. Deformation in the specimen during the cut is minimised by securely clamping both sides of the specimen. The effect of not cutting in a straight line is considered to be anti-symmetric, therefore averaging the deformations of both cut surfaces removes this error [60, pp112-115].

If the magnitudes of residual stress components exceed the material's yield strength, local plastic deformation around the cut tip may occur during cutting and may introduce errors in the measurement. Such errors are minimised by clamping the test specimen securely and symmetrically about the cut, to prevent deformation of the cut tip [65]. Recent studies have investigated an additional cutting error due to deformation of the cut tip [66]. During cutting it is assumed a constant width of material is removed by the EDM wire. However residual stresses cause the cut mouth to deform during cutting. The effect of this is considered to be small. Prime and Kastengren [66] describe a procedure to determine the displacements due to cut tip deformation by simulating the cutting process in FE. The displacement of the crack tip, which called the 'bulge error', is obtained from the simulation and used to correct the surface deformation measurements.

2.6.5 DIGITAL IMAGE CORRELATION

The DIC strain measurement technique can be used to determine the strains on the surface of a body during deformation. In this technique a sequence of images of the surface is recorded prior to and during deformation. The specimen's surface needs to be textured or have a random pattern applied, such as black and white speckles. Hence each region of the specimen's surface is associated to a light intensity level which displaces together with surface during deformation [67].

The images are analysed using DIC software, such as ARAMIS by GOM [68], which overlays a grid onto the surface to separate the surface area into facets. Each facet contains a random pattern that can be used to identify the same facet in other images of the specimen. The displacement of each facet relative to its corresponding position in the image of the undeformed specimen is computed and from this the strains are calculated [69]. The displacements are accurate to the distance associated with each pixel in the image [70]. A single camera positioned normal to the specimen's surface allows the in-plane displacements to be measured. Two cameras allow DIC to be performed in 3D where the out-of-plane displacement is also determined.

This technique has the advantage of being able to measure the deformation across the entire surface of a specimen. Whereas more conventional methods, such as strain gauges, extensometers and clip gauges, only measure displacements across a prescribed gauge length. The DIC technique is also contactless [71].

The accuracy of the DIC measurements is dependent on the size of the speckle pattern generated on the specimen. Based on the application, the dimensions of the region of interest will vary. If strain measurements over small areas are required, the speckle pattern must be very fine to enable small facets to be used during post-processing. However, the facet must also be sufficiently large such that it contains a distinctive pattern that enables that facet to be distinguished from others [70].

2.7 DISCUSSION

A review of methods to introduce residual stresses in fracture specimens has been presented in Section 2.4. These include pre-compression (in-plane and out-of-plane), welding and inducing long range residual stresses with a misfit in the test rig. CCG testing under the influence of residual stresses was carried out for the pre-compression specimens by various authors, where crack sizes from 0 to 2.1 mm were measured. However, the crack lengths observed were inconsistent with the magnitudes of the residual stress fields potentially because the crack growth rates were also influenced by the extent of plastic deformation [18]. As shown by tests on uniformly pre-compressed Type 316H stainless steel in Section 2.2.5, plasticity causes a reduction in the material's creep ductility and therefore faster crack growth rates occur. Where plasticity varies across the ligament of the C(T) specimen, it is difficult to distinguish between the effects of residual stresses and reduced creep ductility on crack growth.

The EB welded specimens shown in Section 2.4.4 have large weld residual stresses and therefore it was proposed that C(T) specimens were made with EB welds. Such a welding process was considered suitable for fabrication due to the autogenous nature of the weld and the narrow fusion zones produced. Furthermore, only a single weld pass was required which potentially limited the weld induced plastic zone in the specimen. The literature does not show the extent of plasticity caused by this welding process hence this needed further investigation, which is presented in Chapter 4. Ideally the pre-crack in the C(T) specimen would be located away from the region that underwent plastic deformation.

The three bar structure imposes long range residual stresses by a geometrical misfit between bars of different lengths. Similarly a wedge-loaded C(T) specimen design was proposed where residual stresses were induced by a geometrical misfit, which is presented in Chapter 5. This specimen is far simpler than the three bar test rig as the residual stresses are self-contained within the specimen, but only considers the low elastic follow up load condition which is similar to displacement controlled testing.

The CCG studies under secondary loads presented in Section 2.4.6 showed limited crack extensions in the C(T) specimens. Relaxation of the residual stresses occurred during testing at 550°C due to creep deformation. Therefore most of the creep damage and subsequent crack growth occurred early in the test where the residual stresses were large. However, for a crack to initiate and grow the material's creep ductility had to be sufficiently low. The specimen A1B4, tested by Nezhad, may have had a relatively high creep ductility and hence no crack growth was observed. Following the review of CCG tests under secondary loads, it was decided that the EB welded and wedge-loaded C(T) specimens, were to be made of ex-service Type 316H stainless steel which was uniformly pre-compressed to 8% plastic strain. This would reduce the material's creep ductility throughout the specimen to allow crack growth to occur during subsequent CCG tests. As the reduction in creep ductility would be uniform throughout the specimen, the effects of residual stress on crack growth could still be determined. The material properties for 8% pre-compressed Type 316H stainless steel were obtained by Mehmanparast et al. [18] and used in this study.

Methods to measure residual stress and strains that were used in this project are presented in Section 2.6. The ND method is non-destructive and therefore can be repeated at different manufacturing stages of the specimen and also before and after CCG testing, however slitting and the contour method are destructive procedures. All three techniques measure various stress components over different spatial domains: ND can measure all

stress components at point locations, the contour method can measure a single stress component across an entire plane and slitting determines a through thickness average of the stress and also K^S as a function of cut length. Where possible, multiple residual stress methods should be used for validation. The DIC strain measurement technique is a non-destructive method which is simple to implement however it can only take measurements at the surface of the specimen.

2.8 SUMMARY

A review of the fracture mechanics principles and deformation models which are relevant to CCG testing under secondary and combined loading conditions have been presented in this chapter. Methods of inducing residual stresses in C(T) specimens that have been published in literature were investigated. Following this two new specimen designs were proposed: the EB welded C(T) specimen and wedge-loaded C(T) specimen. The specimen designs and fabrication processes are detailed in the following chapters. The CCG studies under secondary loading conditions reviewed showed inconsistent crack growth rates between specimens which was considered to be due to variable creep ductilities between specimens. The EB welded and wedge-loaded C(T) specimens were to be made out of uniformly pre-compressed Type 316H stainless steel which has low creep ductility throughout the specimen and therefore increased the likelihood of crack growth to occur in subsequent CCG tests.

3 MEASUREMENT OF RESIDUAL STRESSES IN EB WELDED C(T) SPECIMENS

3.1 INTRODUCTION

A C(T) specimen design is presented in this chapter where EB welds are strategically located such that the weld induced residual stresses drive crack growth under creep conditions. Similar test specimens were manufactured by Davies et al. [42, 72] where EB welds were used to join extension arms onto ex-service MMA welds. Large tensile residual stresses were present near the EB welds which significantly affected the rate of crack initiation and growth in subsequent CCG tests. In the new specimen design, EB welds were made in parent material such that the tensile weld residual stresses provided the crack driving force in CCG tests.

Specimens were fabricated whilst instrumented with thermocouples to gather in-situ temperature measurements and were used to perform destructive and non-destructive residual stress measurements. This data supported the development and validation of numerical simulations of the welding process, to predict the residual stresses and plastic deformation in the C(T) specimens.

This chapter focuses on specimen manufacture and experimental measurements made to investigate the weld induced residual stresses. The numerical simulations of the fabrication processes are presented in Chapter 4. These simulations require a significant amount of input data, therefore these experimental measurements are presented in detail. The following section describes the process of residual stresses being induced near welds. The design of the EB welded C(T) specimen and manufacturing processes used for its fabrication are described in Section 3.3. Temperature measurements gathered during welding are presented in Section 3.4. Specimens were destructively examined to determine the sizes of the weld fusion boundaries and hardness measurements were made to assess the extent of work hardening, which are presented in Section 3.5. Following this, residual stress measurements are presented which were made using ND, slitting and the contour method. Near the weld, some differences in stress measurements between the three techniques were observed. Therefore the analysis shows the extent of errors that occurred to determine which of the measurements were most accurate.

3.2 GENERATION OF RESIDUAL STRESSES BY WELDING

EB welding is a joining process commonly used to manufacture components with high precision. In this process a beam of electrons is directed across two mating surfaces such that the kinetic energy of the electrons is transferred to the material causing it to melt and fuse together. EB welding can create welds which penetrate large depths whilst creating fusion zones which are substantially narrower than conventional welding techniques.

Residual stresses are induced near welds due to a misfit between the plastically deformed heat affected and fusion zones, and the parent material. During the welding process the weld metal and adjacent parent material heat up and cool down at different rates, depending on the distance from the weld pool. Thermal expansion and contraction of the metal due to the large temperature changes induces stresses in the HAZ and causes yielding. Once the weld pool has passed and the workpiece has cooled, the misfit between the plastically deformed region and the parent material is accommodated by strains in the material and therefore residual stresses remain [73].

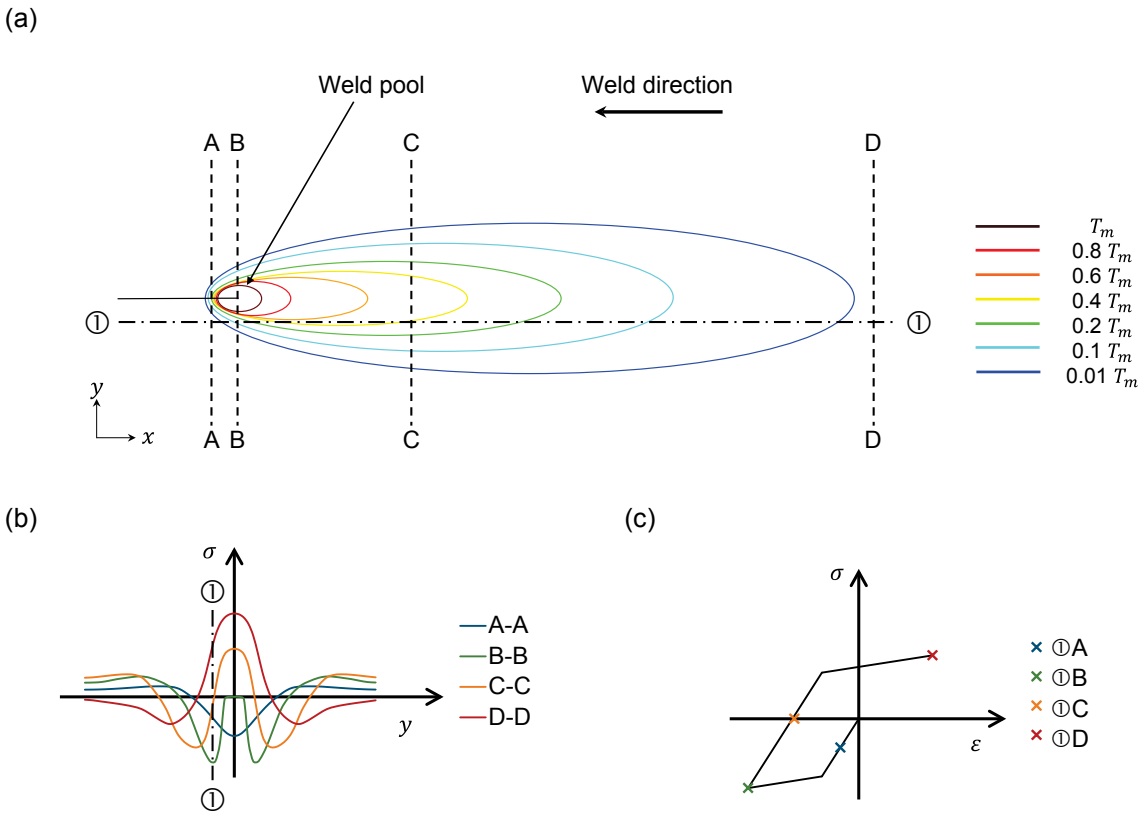


Figure 3.1 Schematic representation of (a) isotherms around a weld pool, (b) stresses across the weld pool at various stages of welding and (c) a typical stress-strain curve for the HAZ

The changes in temperature and development of stresses near a weld are shown in Figure 3.1. Figure 3.1(a) shows typical isotherms surrounding a weld pool relative to the materials melting temperature, T_m. Section A-A lies just ahead of the weld pool and experiences some heating. The weld arc is passing over section B-B causing the material to heat up further and melt to form a weld pool. The temperatures of the outer regions of sections A-A and B-B remain low. Along section C-C, where the weld arc has passed, the weld region cools whilst the temperature of the outer regions increase as heat is conducted away from weld. The temperatures eventually reach room temperature in section D-D which is far from the weld.

Typical stress distributions across the sections A-A to D-D are shown in Figure 3.1(b). Material near the weld pool is heated and experiences thermal expansion. However the surrounding material, which has a relatively low temperature, acts as a constraint to prevent this expansion and hence compressive stresses are generated, as shown in A-A in Figure 3.1(b). Tensile stresses exist away from the weld region in A-A to balance these compressive stresses. Line B-B in Figure 3.1(b) shows the stress distribution through the weld pool, underneath the weld torch the molten metal cannot support a load hence the stresses reduce to zero. The thermally expanding material around the weld is compressed further and at high temperature the material has a lower yield stress. Therefore the compressive stresses exceed the yield stress and local plastic deformation occurs [74].

Behind the weld, at section C-C, the material cools. Contraction of the fusion zone and HAZ during cooling is prevented by the adjacent material and due to this tensile stresses are induced. These stresses remain in the weld and HAZ as residual stresses at large times as shown by D-D in Figure 3.1(b), where the heat has been dissipated to the surrounding environment and the temperature reduces to ambient.

The evolution of stresses for material along line ① which is in the HAZ is shown in Figure 3.1(c), where the crosses indicated stresses at the stages considered in Figure 3.1(b). Near the weld, material undergoes yielding in compression followed by yielding in tension. Hence accurate predictions of residual stresses using numerical simulations requires the cyclic hardening behaviour to be described by the deformation model [75].

In some materials, such as ferritic steels, a solid-state phase transformation occurs during welding which influences the generation of residual stresses. In such cases the thermal dilatation during heating and cooling differs and has to be accounted for during

modelling for accurate stress predictions. However in austenitic steels the effect of phase changes is small and may be ignored [76].

3.3 SPECIMEN DESIGN AND MANUFACTURE

3.3.1 SPECIMEN DESIGN

A new specimen design is proposed where C(T) specimens contain EB welds such that the weld induced residual stresses drive crack growth in CCG tests. The specimen design is shown in Figure 3.2(a) where the weld is orientated in the centre of the specimen such that the stress component in the longitudinal direction to the weld is normal to the crack plane and therefore drives crack growth.

Specimens of the proposed design were manufactured with a width of W = 50 mm to ASTM 1457-13 [77] and with a thickness, B, of 25 mm. Key dimensions of the C(T) specimen are shown in Figure 3.2(b). The pre-crack was machined 3.0 mm beyond the centre of the weld creating an initial crack length, a_0, of 18.75 mm with a_0/W = 0.375. The location of the pre-crack was selected to ensure the tensile stresses ahead of the crack tip remained large whilst the pre-crack extended beyond the HAZ. The selection of the pre-crack length is discussed in Section 3.7.2.

To manufacture the C(T) specimens, EB welds were first made in C(T) blanks which had dimensions of 65.0 × 62.5 × 25.0 mm^3. During welding the C(T) blank was surrounded by sacrificial material to contain the start and ends of the weld, which were likely to contain defects, as shown in Figure 3.3. A backing block was also placed under the specimen to

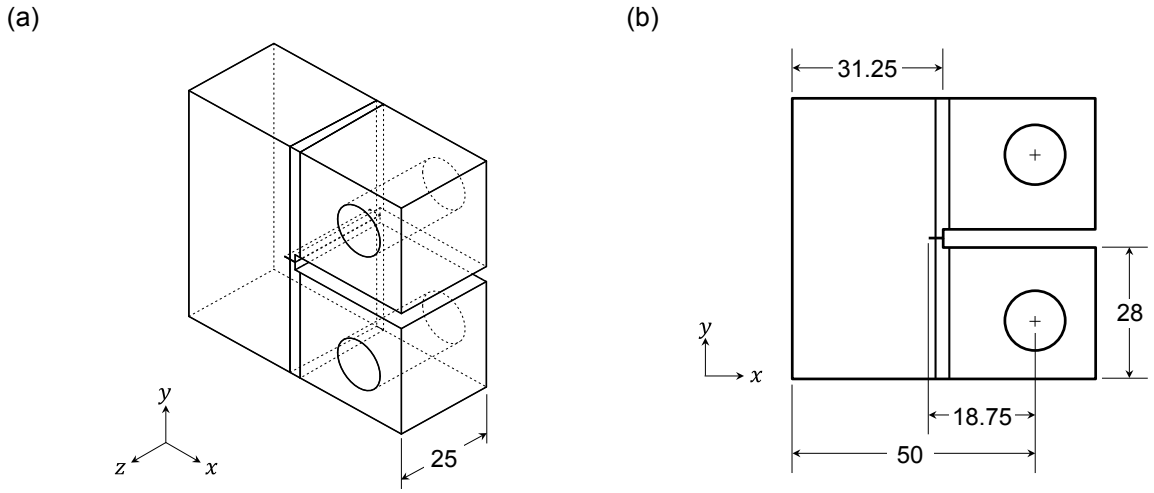


Figure 3.2 (a) Isometric view and (b) dimensions of the EB welded C(T) specimen

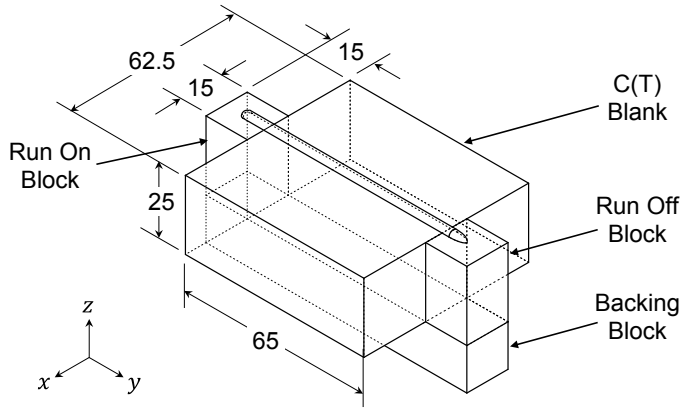


Figure 3.3 EB welded C(T) blank with sacrificial blocks

contain the weld root. In initial weld trial specimens [78], the backing block was not present and the EB penetrated through the thickness of the block. During welding, the weld pool flowed out of the bottom of the specimen and left an undercut at the weld cap. To prevent this, sacrificial material was placed underneath the C(T) blank when welding further specimens. The power of the EB was set such that the weld pool did not penetrate through the backing block. This prevented a deficiency of material at the top surface of the specimen and ensured a uniform and defect free weld cap. Following welding, the sacrificial blocks became fused to the C(T) blank which were removed using wire EDM.

A list of EB welded C(T) blanks are shown in Table 3.1. Two trial specimens, EBW1 and EBW2, were welded by The Welding Institute (TWI) which are detailed in [78]. The design was revised to reduce the size of the sacrificial blocks that contain the start and ends of the EB weld and additional sacrificial material was used to contain the weld root. Specimens EBW3 and EBW4 used the design shown in Figure 3.3 and were welded by Electron Beam Processes Ltd (EBP). These samples were used to develop and validate a numerical simulation of the welding process through destructive and non-destructive residual stress measurements and were sectioned to obtain weld macrographs. Three specimens, EBW5 to EBW7, were manufactured into EB welded C(T) specimens for CCG testing. Note,

Table 3.1 List of EB welded specimens

Specimen	Welder	Specimen Description	Material
EBW1	TWI	Tack weld and final pass	Type 316H As-received
EBW2	TWI	Tack weld and final pass	Type 316H As-received
EBW3	EBP	Single pass	Type 316H As-received
EBW4	EBP	Two passes	Type 316H As-received
EBW5	EBP	Single pass	Type 316H 8% Pre-Compressed
EBW6	EBP	Single pass	Type 316H 8% Pre-Compressed
EBW7	EBP	Single pass	Type 316H 8% Pre-Compressed

the width of specimens EBW3 and EBW4 were undersized to 60 mm, whereas the widths of EBW5 to EBW7 were 62.5 mm as shown in Figure 3.3. Two weld passes were made on specimen EBW4, with the second pass made directly over the first, to investigate whether cyclic hardening caused an increase in the residual stresses in the specimen.

3.3.2 SPECIMEN MANUFACTURE

The specimens were made from ex-service Type 316H austenitic stainless steel which was extracted from steam header plant components and supplied by EDF Energy Nuclear Generation Ltd. The first trial specimens, EBW1 and EBW2, were made using ex-service material identified as HYA 1D2/2 cast 55882 and extracted from the cylindrical section of the component. For further specimen development, material was extracted from the spherical dome section of the same steam header (HYA 1D2/2 cast 55882) and used for EBW3 and EBW4. The creep properties for material in the dome section are unknown and therefore test specimens are not usually extracted from such regions, however this material was considered suitable for specimen development. Specimens EBW1 to EBW4 were made from material in the as-received condition. Specimens EBW5 to EBW7 were made using ex-service Type 316H stainless steel which was pre-compressed to 8% plastic strain. These specimens were extracted from a cylindrical section of a steam header from an unidentified cast. Experimental testing by Mehmanparast et al. [18] has shown little variability is observed for Type 316H stainless steel in the pre-compressed condition from different casts and hence the material properties published in [18] and [79] were assumed.

EB welding was performed in a vacuum chamber under reduced pressure conditions to prevent electrons scattering with air molecules [80, pp26-27]. The welding parameters used are shown in Table 3.2. These parameters were determined by EBP after carrying out

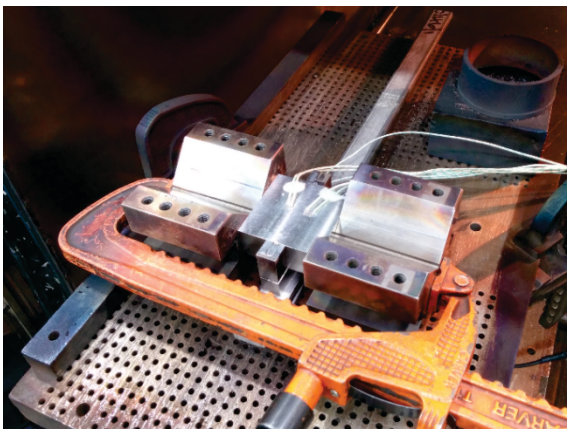


Figure 3.4 Clamping arrangement of specimens welded at Electron Beam Processes Ltd

trial welds on machining offcuts of ex-service Type 316H stainless steel. The beam current, weld speed and beam focal distance were optimised to ensure the weld penetrated through the thickness of the C(T) blank but not through the backing block, whilst minimising the weld width.

Prior to EB welding, the sacrificial blocks were attached to the C(T) blank using Tungsten Inert Gas (TIG) spot welds. The specimens were placed on a table inside the vacuum chamber and clamped as shown in Figure 3.4. The EB was positioned vertically over the sampled such that the EB was directed down onto the specimen.

Table 3.2 Beam parameters used during EB welding

	Voltage (kV)	**Current (mA)**	**Power (kW)**	**Weld Speed (mm/s)**
TWI	150	80	12.0	3.3
EBP	150	38	5.7	6.3

In-situ temperature measurements were made using eight type K thermocouples capable of measuring temperatures up to 1,250°C, the locations of which are shown in Figure 3.5. Temperatures were measured during the weld and as the sample cooled down to a uniform temperature. Large temperature gradients occurred across the specimens during welding, hence it was ensured temperature measurements were made at single points on the surface of the specimens. The tips of the thermocouple cables were melted to form beads which were spot welded onto the specimens to form point contacts between the surfaces and probes. The thermocouples were positioned close to and far from the welds to determine the temperature variations across the specimens. Measurements were made with a frequency of 10 Hz to ensure the peak temperatures were recorded.

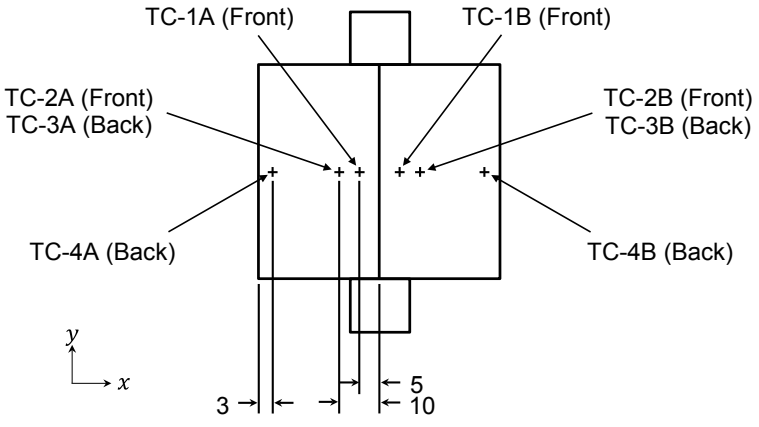


Figure 3.5 Location of thermocouples on EB weld specimens

3.4 TEMPERATURE MEASUREMENTS

The temperatures measured whilst welding specimens EBW3 to EBW7 are shown in Figure 3.6 for the first 150 s. The thermocouple responses are similar for EBW3, EBW5, EBW6 and EBW7 which all have a single weld pass. At large times the specimens had cooled to a uniform temperature. Temperature data for EBW4 is shown in Figure 3.6(b) for a longer time period of 600 s as two weld passes were made. Thermocouple TC-2B on specimen EBW6 became detached during welding and has not been included in the results.

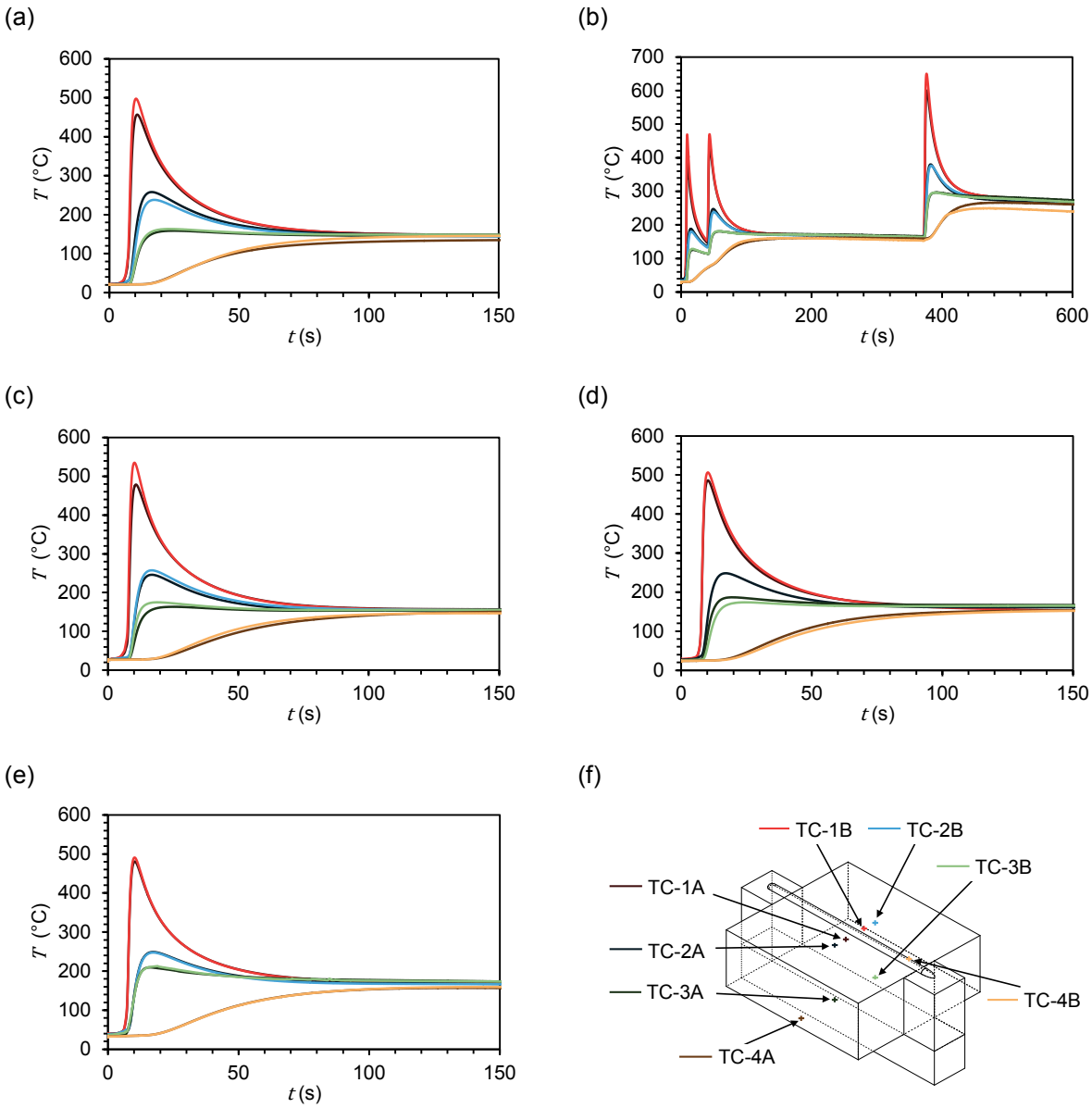


Figure 3.6 Temperatures measured during welding specimens (a) EBW3, (b) EBW4, (c) EBW5, (d) EBW6 and (e) EBW7, and (f) thermocouple colour legend

As expected, the thermocouples closest to the weld (TC-1A and TC-1B) recorded the highest temperatures, with a peak measured as the EB was close to the thermocouples. The far field thermocouples (TC-4A and TC-4B) did not show a peak temperature as the weld pool passed, instead these measurements gradually increased to reach their maximum value once the whole specimen had reached a uniform temperature.

Inspection of the thermocouple data whilst the specimen was at constant room temperature shows scatter of ± 0.1°C therefore the equipment used had very little noise which resulted in the smooth profiles observed in Figure 3.6. A high sampling rate was required to ensure the peak temperature for the thermocouples close to the weld was recorded. Inspection of the raw data showed the sampling rate of 10 Hz was sufficient to accurate capture the peak temperature to 0.1°C.

Specimen EBW4 had two weld passes and therefore the temperature data is shown for a longer period. During the first pass on EBW4, the EB experienced a power trip for approximately 30 s and as a result the first weld pass was made in two stages. For this second stage, the EB was moved back by a few millimetres to overlap the existing weld region. The beam position during the power trip was approximately 5 mm before the mid length of the specimen however this was estimated by eye from the operator as the exact location could not be determined. As the first pass was made in two stages, two temperature peaks are observed near the start of the thermocouple data. After the first weld pass was completed, the specimen was allowed to cool for approximately 5 min until it reached a uniform temperature. The second pass was then made directly over the first. As the initial temperature of the second pass was 163°C, the peak temperatures observed during the second pass are higher than those for the specimens with a single pass.

The peak temperatures recorded by all the thermocouples are compared in Table 3.3. In general the temperatures for specimens EBW3, EBW5, EBW6 and EBW7 are in good agreement. The mean of the peak temperatures at each measurement location are also shown in Table 3.3 for specimens with single and multiple weld passes. The error is calculated for specimens with a single weld pass as two standard deviations of the peak temperatures. The magnitudes of the error for thermocouple location TC-1A and TC-1B and location TC-3A and TC-3B are large. These were caused by inaccuracies in the placement of thermocouples. Table 3.4 shows the actual thermocouple locations measured on the specimens using digital callipers after welding. On average the thermocouples were mounted close to the nominal positions shown in Figure 3.5. However the errors shown in Table 3.4,

which are determined as two standard deviations of the thermocouple locations, are large relative to the nominal distance from the weld. EB welding induces large temperature gradients near the weld and therefore the peak temperatures were sensitive to the exact position of the thermocouples.

Table 3.3 Maximum temperature measured during EB welding

Thermocouple	T (°C)						
	EBW3	EBW4	EBW5	EBW6	EBW7	Mean 1 Pass	Mean 2 Passes
TC-1A	457	600	479	486	481	491 ± 46	625
TC-1B	497	650	535	506	491		
TC-2A	258	380	246	248	249	249 ± 14	378
TC-2B	238	376	257	–	248		
TC-3A	159	297	163	187	210	180 ± 42	296
TC-3B	163	296	175	174	213		
TC-4A	136	266	152	154	157	151 ± 15	258
TC-4B	146	249	147	153	160		

Table 3.4 Position of thermocouples measured after EB welding

Thermocouple	Distance from Weld, x (mm)					
	EBW3	EBW4	EBW5	EBW6	EBW7	Mean
TC-1A	5.1	5.0	5.3	4.6	4.8	4.8 ± 0.6
TC-1B	4.8	5.2	4.5	4.5	4.6	
TC-2A	10.0	10.0	10.4	9.8	9.6	9.9 ± 0.7
TC-2B	10.4	10.0	9.7	–	9.4	
TC-3A	10.3	10.4	10.5	9.6	9.7	10.1 ± 0.8
TC-3B	10.1	10.5	10.0	10.5	9.5	
TC-4A	3.0	3.2	2.1	3.8	2.6	2.9 ± 1.2
TC-4B	2.9	3.0	3.6	1.9	2.6	

It was considered that the variation of temperature data between specimens was largely due to errors caused by thermocouple probe placement. The heat input to all of the specimens with a single weld pass was considered as being consistent hence, the average temperature at each thermocouple location was used to develop the weld simulation presented in the following chapter. Specimens EBW5, EBW6 and EBW7 were the same size and made of the same material, therefore the residual stress induced in these specimens were assumed to be the same.

3.5 WELD IMAGES AND HARDNESS TESTING

Weld macrographs were produced from specimens EBW3 and EBW4 to determine the widths of the EB welds. Sectioning was performed using wire EDM. The cut surfaces were ground, polished and etched with Marble's Reagent to reveal the fusion zone.

Figure 3.7 shows the EB weld profiles of specimens EBW3 and EBW4 respectively. Average weld widths were measured as 1.1 mm and 1.3 mm for specimens EBW3 and EBW4 respectively. These were determined by measuring the weld widths at nine locations through the thickness of the specimen under a microscope. The weld width in specimen EBW4 was larger as two weld passes were made and the material reached a higher temperature, as shown in Figure 3.6.

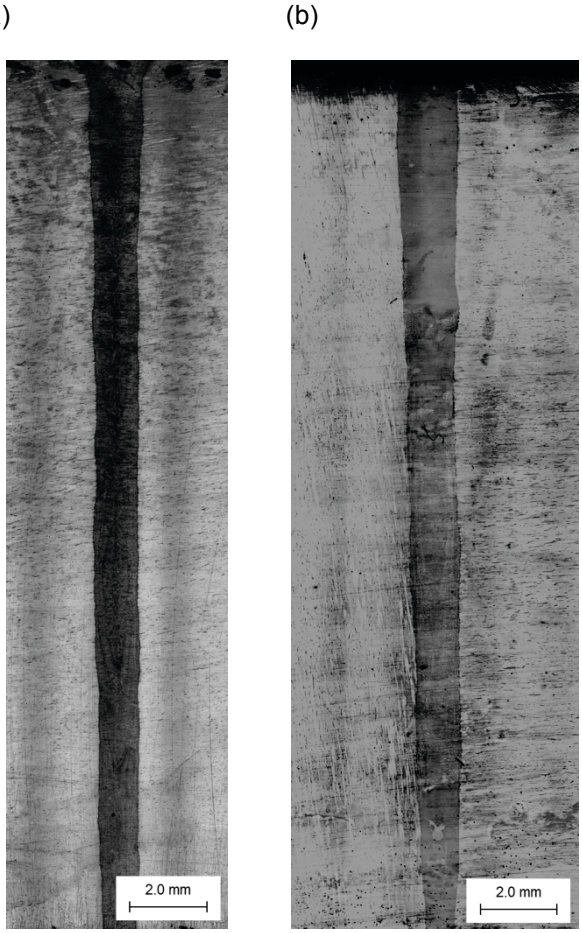


Figure 3.7 Weld micrograph of specimen (a) EBW3 and (b) EBW4

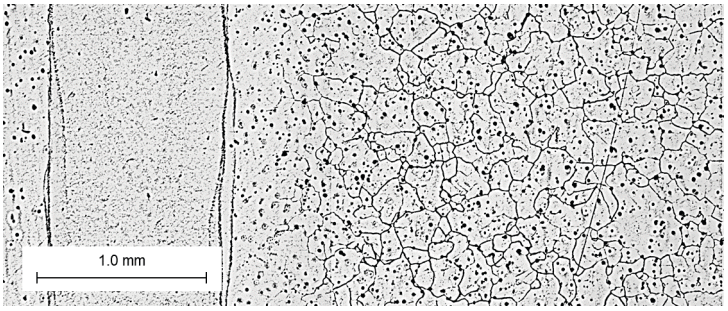


Figure 3.8 Weld micrograph of specimen EBW3

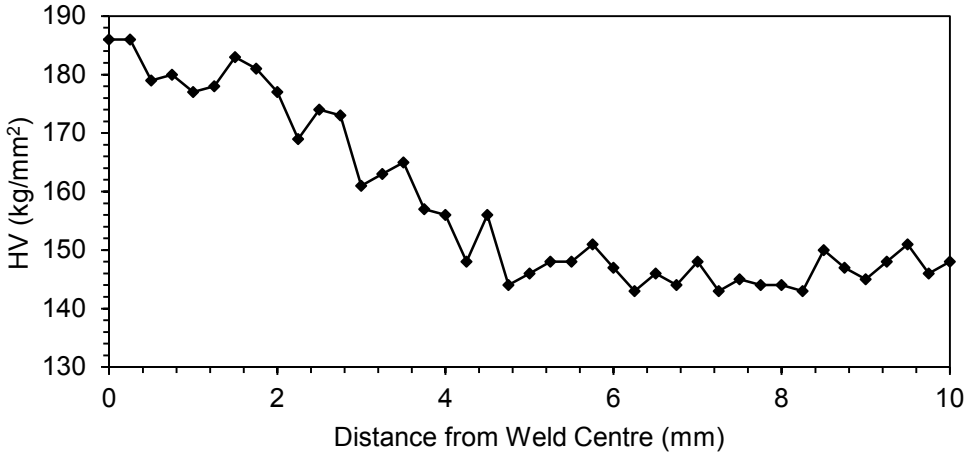


Figure 3.9 Profile of Vickers hardness values measured across EBW3

The microstructure in the weld, HAZ and parent material regions of specimen EBW3 are shown in Figure 3.8. This sample was polish and etched with Ferric Chloride to reveal the grain boundaries. This micrograph was obtained at mid-thickness of the specimen. The weld and HAZ both had widths of 1.0 mm, where the size of the HAZ was considered as the region adjacent to the weld with large grains. The grain diameter, d_g, of the parent material in EBW3 was determined to be 120 μm.

Vickers micro hardness tests were performed across the weld at mid-thickness of EBW3 to investigate the variation in strength. Indentations were carried out on the polished and etched surface from which the image in Figure 3.8 was obtained. Testing was performed with a load of 5 kgf with a hold time at maximum load of 20 s. Measurements were made at 0.25 mm intervals from the weld centre to 10 mm from the weld line. The hardness values are shown in Figure 3.9.

The peak hardness values (HV) of 186 kg/mm^2 were measured in the fusion zone. Hardness values reduced across the HAZ to reach a minimum of 144 kg/mm^2 and remain constant beyond 5 mm from the weld centre. Plastic deformation near the fusion zone caused the yield strength to increase and therefore the large hardness values were measured. The hardness test indicates the size of strain affected zone (SAZ) was 5 mm from the weld centre.

Toloczko et al. [81] present experimental data relating Vickers hardness values to tensile strengths of Type 316 stainless steel at room temperature, where the yield strength can is estimated by (3.1).

$$\sigma_y = 2.69\,\mathrm{HV} - 125 \tag{3.1}$$

where σ_y is in MPa and HV is in kg/mm^2. From (3.1), σ_y in the parent material and fusion zone of EBW3 are estimated as 264 MPa and 377 MPa respectively. In comparison, σ_y of Type 316H stainless steel parent material at room temperature is 264.6 MPa [32] which correlates well with the hardness measurements. Sakanashi et al. [82] performed Vickers hardness measurements across an ex-service Type 316H stainless steel multi-pass weld. The hardness value of the weldment was measured to be 220 kg/mm^2 which is larger than that measured in the fusion zone of EBW3. Hardness measurements were also made on ex-service Type 316H stainless steel parent material which had been pre-compressed to 8% plastic strain by Mehmanparast [83]. The hardness of the material was measured to be approximately 212 kg/mm^2 which is also greater than that measured in the EB weld.

3.6 RESIDUAL STRAINS AND STRESSES MEASURED BY NEUTRON DIFFRACTION

3.6.1 MEASUREMENT LOCATIONS

The ND measurement technique was used to measure strains in three orthogonal directions for specimens EBW3, EBW4 and EBW5. This non-destructive technique permitted measurements to be made in the as-welded samples and then throughout fabrication to determine how the weld residual stresses redistributed during each manufacturing stage. The measurements were made after welding, after the sacrificial blocks had been removed to manufacture the C(T) blanks and after the pre-crack had been inserted to form the C(T) specimens. Points were sampled along the lines shown in Figure 3.10. The measurement lines, AB, CD, and EF, are located at mid-thickness and at mid-height of the as-welded

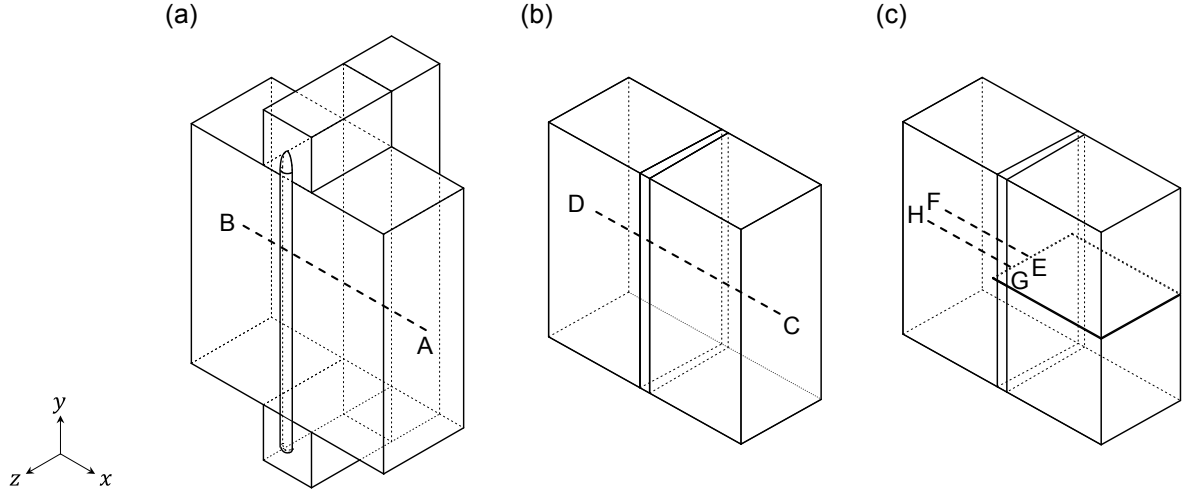


Figure 3.10 ND measurement lines on (a) EB welded specimen, (b) C(T) blank and (c) C(T) specimen

specimen, C(T) blank and C(T) specimen respectively. Line GH in the C(T) specimen is located at a distance which is quarter of the thickness of the specimen from the front face.

Measurements were made using three instruments: SALSA at the ILL, Grenoble [84], Stress-Spec at FRM II, Munich [85] and E3 at HZB, Berlin [86]. Strains were measured in the $\{311\}$ plane as the elastic response for this plane in austenitic stainless steels can be assumed to remain linear at large applied stresses [59, pp210-215]. Measurements using the instruments SALSA and Stress-Spec were made using gauge volumes of 2 × 2 × 2 mm^3. This size was considered a suitable compromise of a gauge volume which was large enough to sample a sufficient number of grains permitting reasonably low count times, whilst small enough to approximate the strain measurements to point locations. However the neutron source at HZB had less power than at ILL and FRM II and therefore the gauge volume used at E3 was set to 2 × 2 × 10 mm^3. This larger gauge volume ensured count times were kept reasonably low however strains were measured over a relatively larger region within the specimen and therefore reduced the accuracy of the measurements.

The material had relatively large grains and therefore all the specimens were oscillated to increase the number of grains sampled. The instrument SALSA oscillated the specimens by ± 2.4° in 0.8° steps whilst the instruments E3 and Stress-Spec continuously oscillated the specimens between ± 2.0°.

Near the weld plane and pre-crack region, measurements were made in 1.0 mm intervals, along the lines shown in Figure 3.10, as high strain gradients were expected. Further away points were measured at 2.0 mm intervals. The count times varied for each instrument depending on the neutron flux of the beam. Measurements made using the instruments Stress-Spec and SALSA used count times of approximately 30 min for the longitudinal elastic strain component, ε_{yy}^{e}, and 15 min for the transverse and normal elastic strain components, ε_{xx}^{e} and ε_{zz}^{e} respectively. Longer count times were used in the longitudinal direction as it was normal to the crack plane and was the direction of key interest. The neutron flux at HZB was lower relative to FRM II and ILL so the count times were increased to 60 min for each point.

Table 3.5 Instruments used to make ND measurements in EB welded C(T) specimens

Specimen	ND After Welding	ND on C(T) Blank	ND on C(T) Specimen
EBW3	SALSA, ILL	–	SALSA, ILL
EBW4	SALSA, ILL	SALSA, ILL & E3, HZB	–
EBW5	SALSA, ILL	SALSA, ILL	Stress-Spec, FRM II

3.6.2 MEASUREMENT OF THE REFERENCE SCATTERING ANGLE

Accurate residual strain measurements using ND require the reference lattice parameter, d_0, to be carefully determined, particularly across welds. Welding can change the microstructure and chemical composition of the material which can affect local values of d_0. Withers et al. [87] recommends making measurements in toothcomb specimens where an array of matchstick coupons is extracted across the weld. The macroscopic type I residual stresses are relieved by the cutting process, hence the measurements in these coupons are dependent on the chemical composition, microstructure and intergranular stresses. Microstructural changes across welds can cause a shift in the reference lattice spacing and can lead to incorrect residual strain measurements if not taken into account [88].

Toothcomb specimens were extracted from the EB weld specimens during the C(T) blank manufacturing stage. In early measurements where toothcombs were unavailable, as the samples had not been cut, reference scattering angles were determined in the parent material assumed to be stress free using the far field approach described by Withers et al. [87]. Measurements were made at the corner of each specimen in multiple orientations and the average angle was used as the reference scattering angle, $2\theta_0$. The variation of reference scattering angles across the weld specimen and validity of using a remote location in the specimen to measure, θ_0, was later investigated.

A toothcomb specimen that had teeth with cross sections of 1.8 × 3.0 mm^2, as shown in Figure 3.11(a), was tested using the instrument SALSA with a measurement gauge

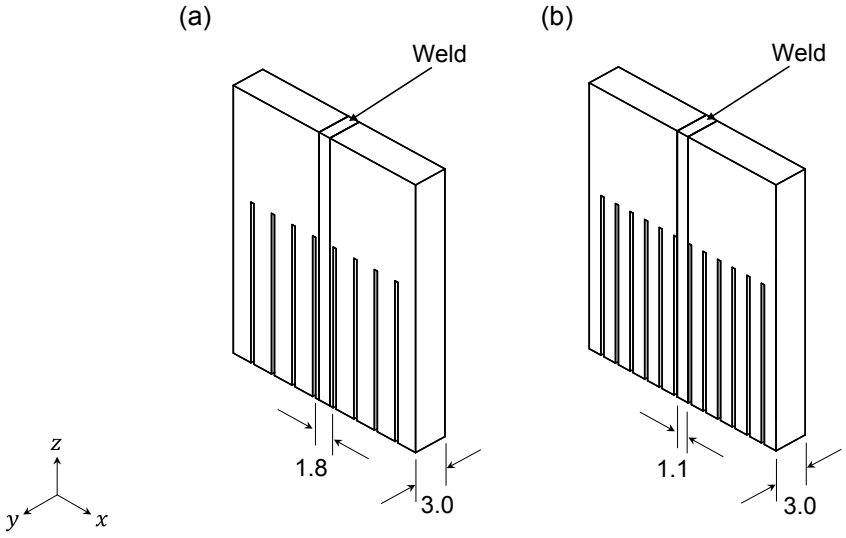


Figure 3.11 Geometry of toothcomb specimens used for reference measurements at the instrument (a) SALSA and (b) Stress-Spec

volume of 2 × 2 × 2 mm^3. Reference scattering angles, $2\theta_0$, were measured in the transverse, x, and longitudinal, y, directions and are shown in Figure 3.12(a). No clear trends were evident near the weld region. The variation of scattering angles across the toothcomb specimen may have been due to intergranular residual strains or due to the effect of a partially filled gauge volume [60, pp213-215]. A systematic variation of d_0 across the weld was not observed. The mean scattering angle measured across the toothcomb was 98.983 ± 0.031°, where the error was determined from two standard deviations of the data. The corners of the EB welded specimens were assumed to be stress free, as these locations were far from the welds and near free surfaces, and were used to make reference, $2\theta_0$, measurements. The scattering angle at the corner of the specimen EBW3 was measured to be 98.992 ± 0.004°, where the uncertainty was the error in fitting the Gaussian peak to the measured data. This corner measurement was within the scatter of the data obtained from the toothcomb specimen, shown in Figure 3.12(a).

The measurements across the toothcomb specimen with 1.8 × 3.0 mm^2 teeth did not show a trend through the weld. However the teeth were large relative to the widths of the weld and HAZ regions, which were 1.0 mm wide as observed in the weld micrographs in Figure 3.8. As the gauge volume was 2 × 2 × 2 mm^3, measurements were not made exclusively in each of these regions.

A smaller toothcomb specimen was cut with tooth area of 1.1 × 3.0 mm^2, as shown in Figure 3.11(b), and was measured with a gauge volume of 0.5 × 2 × 10 mm^3 using the instrument Stress-Spec at FRM II. The centre tooth contained the weld region only, whilst the adjacent teeth contained the HAZ regions. The reference scattering angles across the weld in the transverse, x, and longitudinal, y, directions are shown in Figure 3.12(b). The

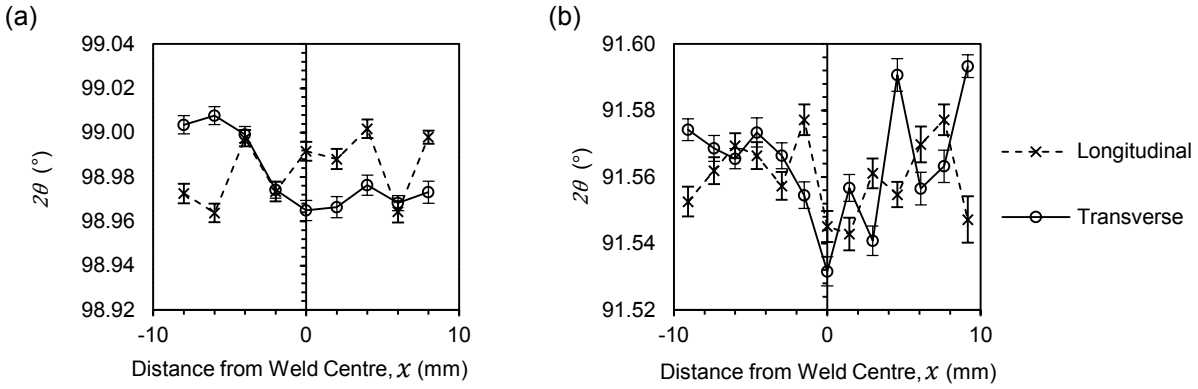


Figure 3.12 Scattering angles measured across toothcomb specimens using (a) 2 × 2 × 2 mm^3 and (b) 0.5 × 10 × 2 mm^3 gauge volumes

scattering angle in the transverse direction was marginally lower near the weld region however it was difficult to distinguish this trend from scatter in the data. The average scattering angle measured in this toothcomb was 91.562 ± 0.029°, where the error was determined as two standard deviations of the data. The scattering angles were different for the two toothcomb specimens as measurements were made at different instruments which had different beam wavelengths.

A systematic variation of lattice spacing across the EB weld was not observed in the toothcomb specimens. In general a change in lattice parameter can be caused by a change in composition of the material. During welding, the composition of the material surrounding the weld changes due to dissolution of second phase particles, which in turn increases the concentration of interstitial carbon atoms. Hutchings et al. [59, pp171-172] state that a change of 0.005 wt% carbon solute content in austenitic steels causes a change in lattice spacing that is equivalent to 600 $\mu\varepsilon$. EB welding produces narrow weld and HAZ regions and therefore any d_0 variations due to compositional changes were considered to only effect the measurements near the weld.

Type 316H stainless steel was found to have large grains and the variation in the lattice spacing measured in the toothcomb specimens near the weld could not be distinguished from scatter due to grain size effects. The uncertainties in the scattering angles from these toothcomb specimens, of 98.983 ± 0.031° and 91.562 ± 0.029°, were used to estimate an error in residual strain using (2.48). This was determined to be ± 200 $\mu\varepsilon$. For consistency reference measurements were obtained from the corner of each EB welded specimen in regions that were far from the weld and which were assumed to be stress free as they were close the free surfaces. To account for the scatter in d_0 across the weld, a reference strain error of ± 200 $\mu\varepsilon$ was conservatively assumed for all measurements.

3.6.3 RESIDUAL STRAINS

The residual elastic strain components measured for each of the EB welded specimens after welding, after manufacture into C(T) blanks and after manufacture into C(T) specimens are shown in Figure 3.13, Figure 3.14 and Figure 3.15 respectively. The measurement lines for each configuration are shown in Figure 3.10. The errors bars shown are the maximum of the error in fitting Gaussian peaks to the measured neutron scattering angles and the error in $2\theta_0$, determined in the previous sub-section (± 200 $\mu\varepsilon$).

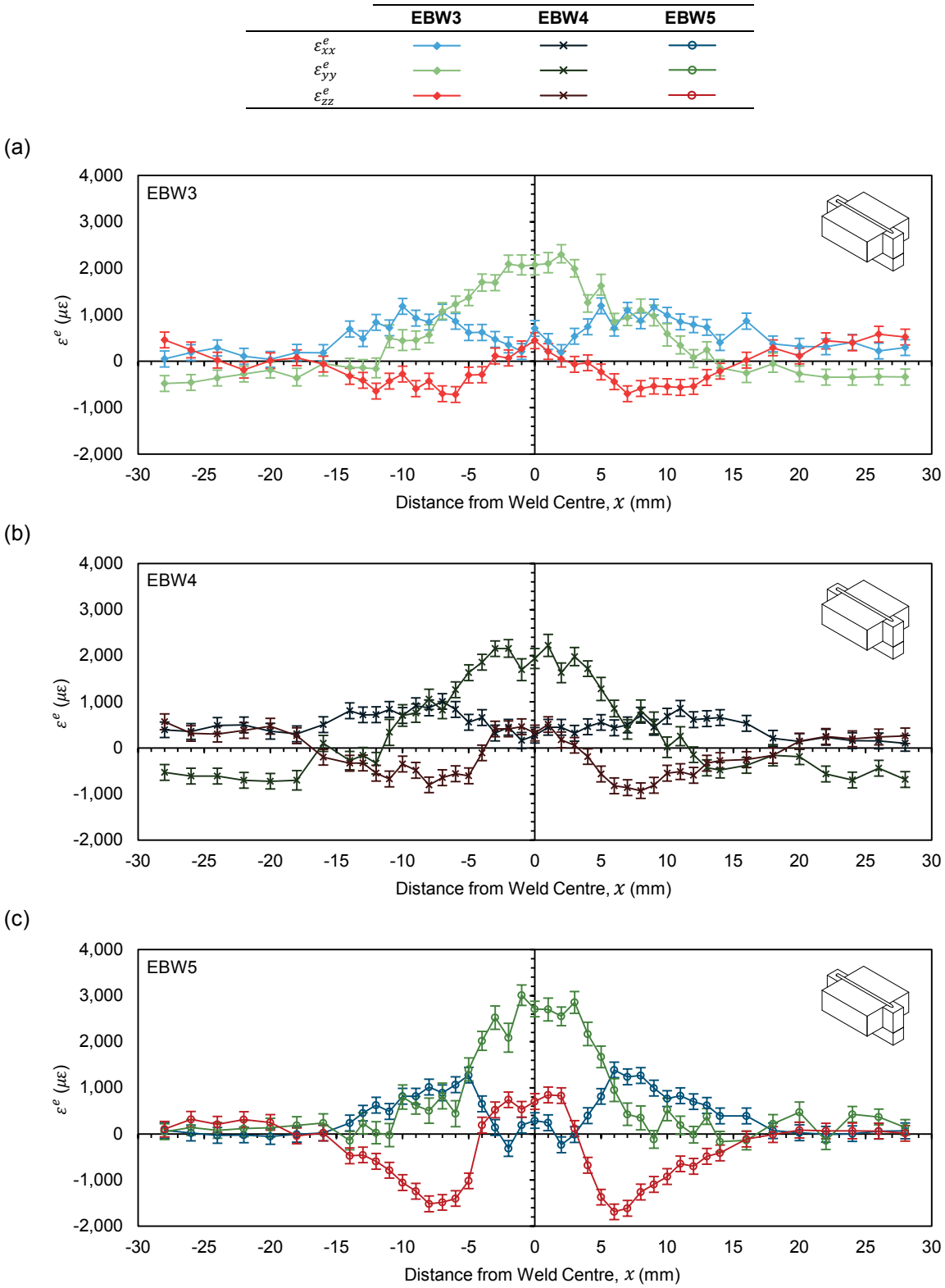


Figure 3.13 Residual strains measured using ND along line AB in specimens (a) EBW3, (b) EBW4 and (c) EBW5 after welding

The strain components, ε_{yy}^{e}, in EBW4 after machining into a C(T) blank were measured by two different instruments which enabled the performance of the two instruments to be compared. The strain profiles measured using the instruments SALSA and E3, at the ILL and HZB respectively, were in very good agreement as shown in Figure 3.14(a). The average peak fitting errors of measurements made using SALSA, Stress-Spec and E3 were ± 90 $\mu\varepsilon$, ± 80 $\mu\varepsilon$ and ± 200 $\mu\varepsilon$ respectively. E3 had relatively large peak fitting errors in comparison to the other instruments due to a low neutron flux of the incident beam. However the peak fitting errors were approximately the same size as the strain errors due to uncertainty in $2\theta_0$.

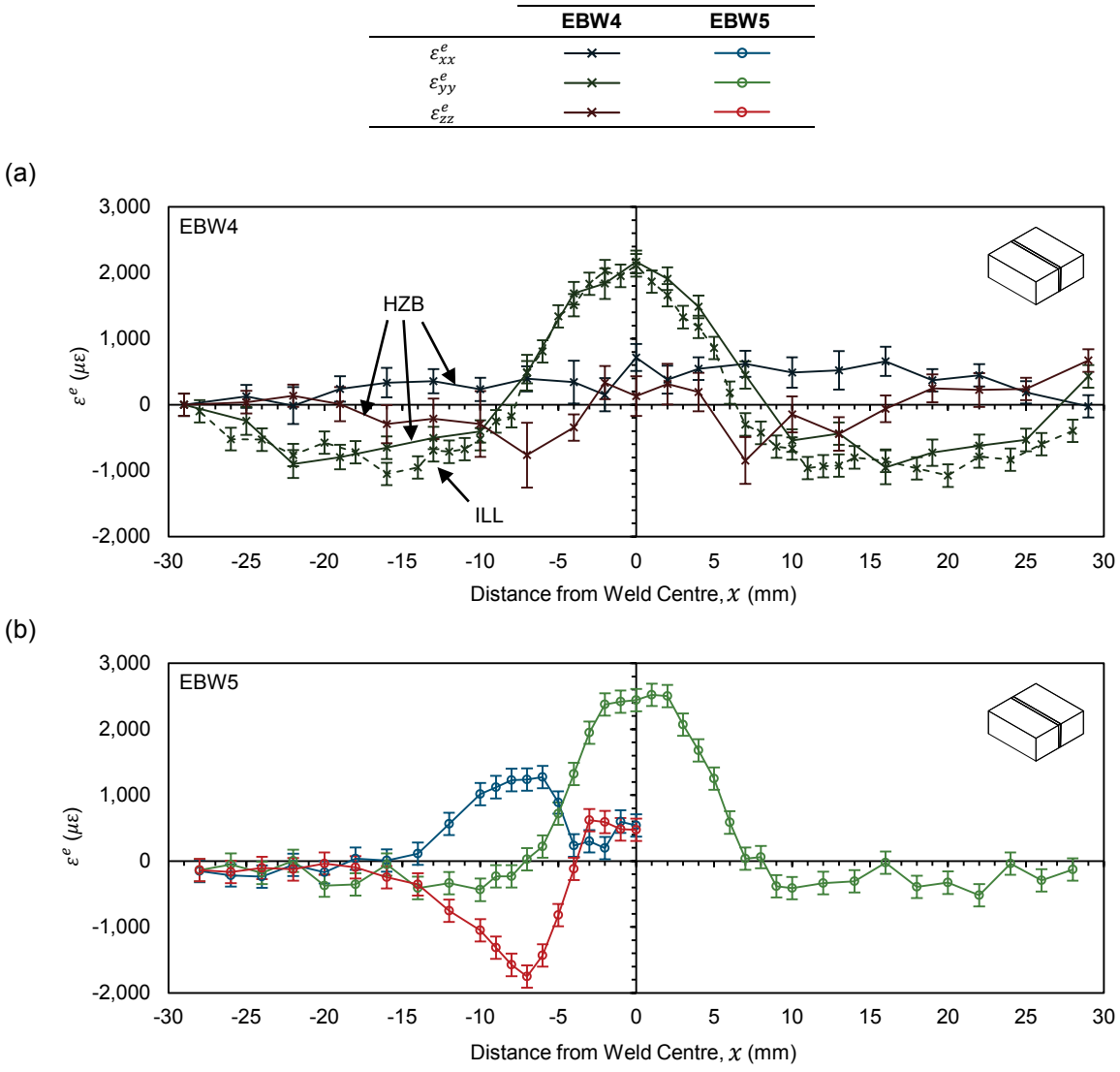


Figure 3.14 Residual strains measured using ND along line CD in specimens (a) EBW4 and (b) EBW5 after machining into a C(T) blank

The strain distributions for the as-welded and C(T) blank specimens were symmetric about the centre of the weld. Therefore averages of the strain components either side of the weld were used to determine residual stresses. In the C(T) blank machined from EBW5, the components ε^e_{xx} and ε^e_{zz} were measured on one half of the specimen only, as shown in Figure 3.14(b). The residual strains in the C(T) specimen are shown in Figure 3.15 for EBW3 and EBW5. The pre-crack extended 3.0 mm beyond the weld line and the first measurement point was made 1.0 mm away from the crack tip. The weld and HAZ regions were measured to be 1.0 mm wide using a weld micrograph, therefore all of the measurements in the C(T) specimens were in the parent material.

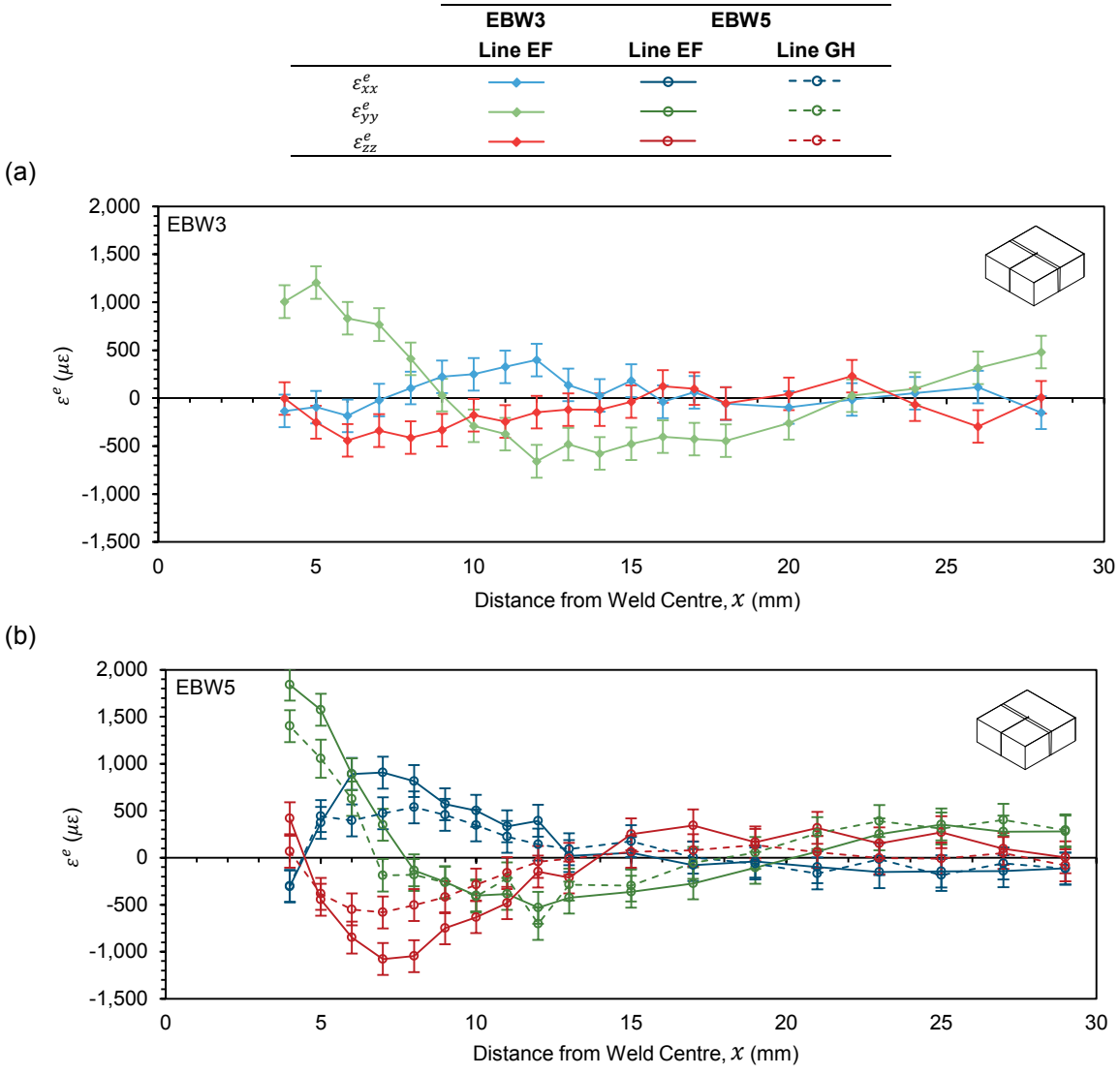


Figure 3.15 Residual strains measured using ND in specimens (a) EBW3 along line EF and (b) EBW5 along lines EF and GH, after machining into a C(T) specimen

3.6.4 RESIDUAL STRESSES

Residual stresses were determined form the strain measurements using (2.49), and constants for the Kröner model shown in Table 2.5. Figure 3.16 shows the residual stresses in EBW3, EBW4 and EBW5 after EB welding, along the measurement line shown in Figure 3.10(a). The error for each data point determined from the strain errors shown in Figure 3.13 was approximately ± 40 MPa, the error bars are not shown for clarity. Approaching the sides of the specimens, the transverse residual stresses, σ_{xx}, which were in the direction normal to the side faces reduced towards zero for all specimens as expected. This supported the use of far field scattering angles for reference, $2\theta_0$, measurements.

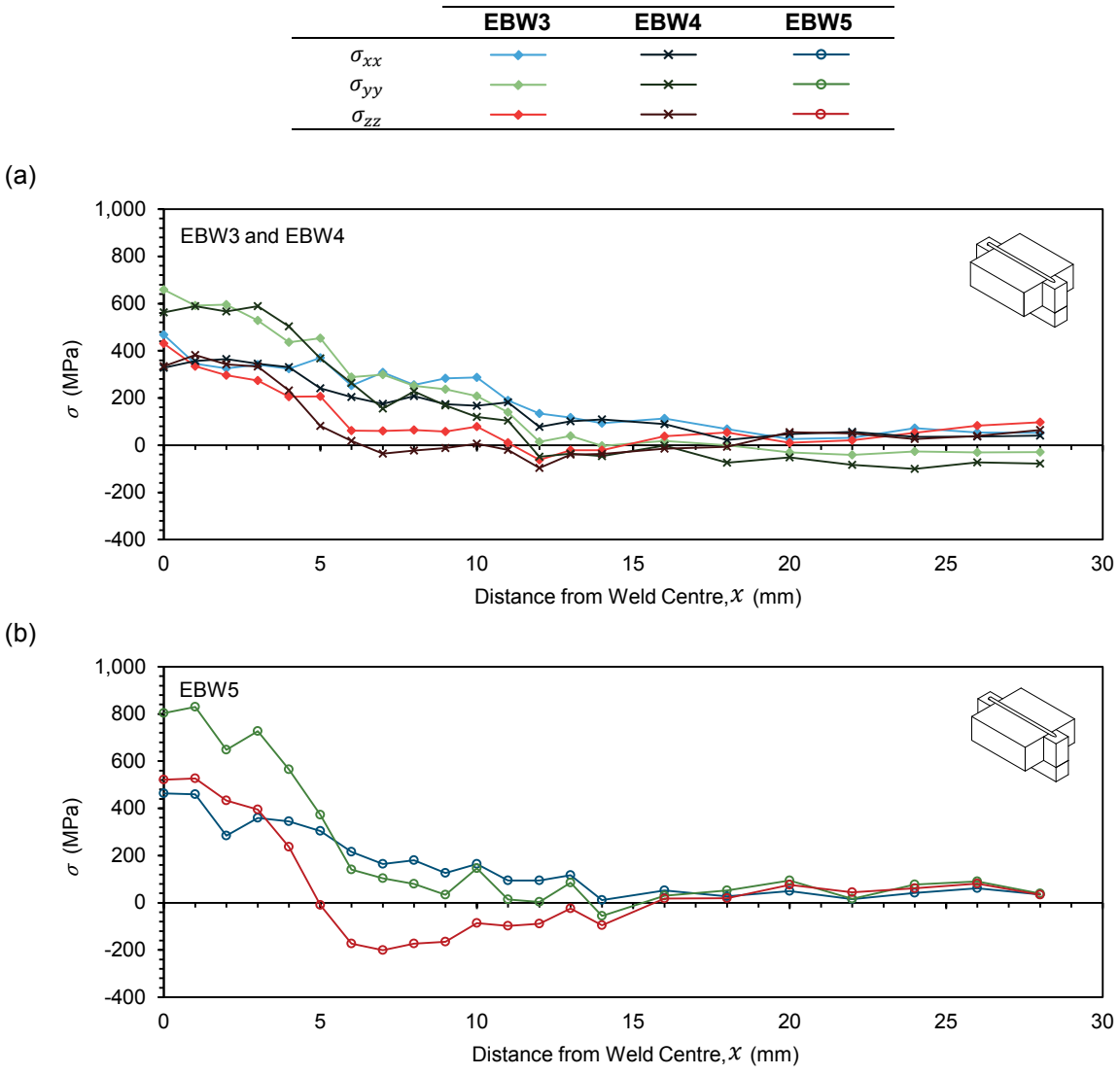


Figure 3.16 Residual stresses measured in as-welded specimens (a) EBW3 and EBW4, and (b) EBW5 along line AB

Tensile residual stresses of 660 MPa, 590 MPa and 830 MPa for EBW3, EBW4 and EBW5 respectively existed near the weld in the longitudinal direction. These stresses were far greater than σ_y, which were 264.6 MPa [32] and 256 MPa [83] for the as-received and pre-compressed material conditions respectively. Such large stress components existed as the stresses were highly triaxial and were consistent with the peak stress of 640 MPa measured by Traore et al. [89] in an EB welded austenitic stainless steel specimen. The longitudinal component, σ_{yy}, was normal to the plane of crack growth in the C(T) specimen and was of key interest as this component caused crack growth in subsequent CCG tests.

Specimen EBW5 was made from pre-compressed material, the longitudinal residual stresses increased by 170 MPa near the weld region in comparison to EBW3, as shown in Figure 3.16. The pre-compression process increased the proof strength of the material due to work hardening. Comparisons of the stress-strain properties of Type 316H stainless steel obtained from uniaxial tensile tests in as-received and uniformly pre-compressed conditions are shown in Section 4.5.2. When this material experiences high loads to induce stresses of around 500 MPa at room temperature, significantly less plastic strains are accumulated. Hence this material allows larger stress magnitudes to be induced without local plastic deformation in comparison to material in the as-received condition.

Specimen EBW3 had one weld pass and specimen EBW4 had two, the second pass was made directly over the first. The residual stresses measured in both specimens were similar, as shown in Figure 3.16(a). The difference between each of the stress components were less than the errors associated with the data points and the effect of multiple weld passes could not be identified from the measurements. The fusion zone from the first weld pass was completely melted upon the second pass hence the effect of the misfit between the weld region and parent material in specimens EBW3 and EBW4 were similar, as expected.

The redistribution of stresses for specimens EBW3, EBW4 and EBW5 following machining are shown in Figure 3.17, Figure 3.18 and Figure 3.19 respectively. The stresses after welding and after the sacrificial blocks were removed in EBW4 and EBW5 are shown in Figure 3.18 and Figure 3.19(a) respectively. Near the weld region little stress redistribution was observed by this machining process as the stress components matched closely in both configurations. However components σ_{xx} and σ_{yy} in EBW4, in the region 5 mm to 20 mm from the weld line, reduced by up to 200 MPa after machining into a C(T) blank. In EBW5, σ_{yy} reduced by approximately 100 MPa in this region.

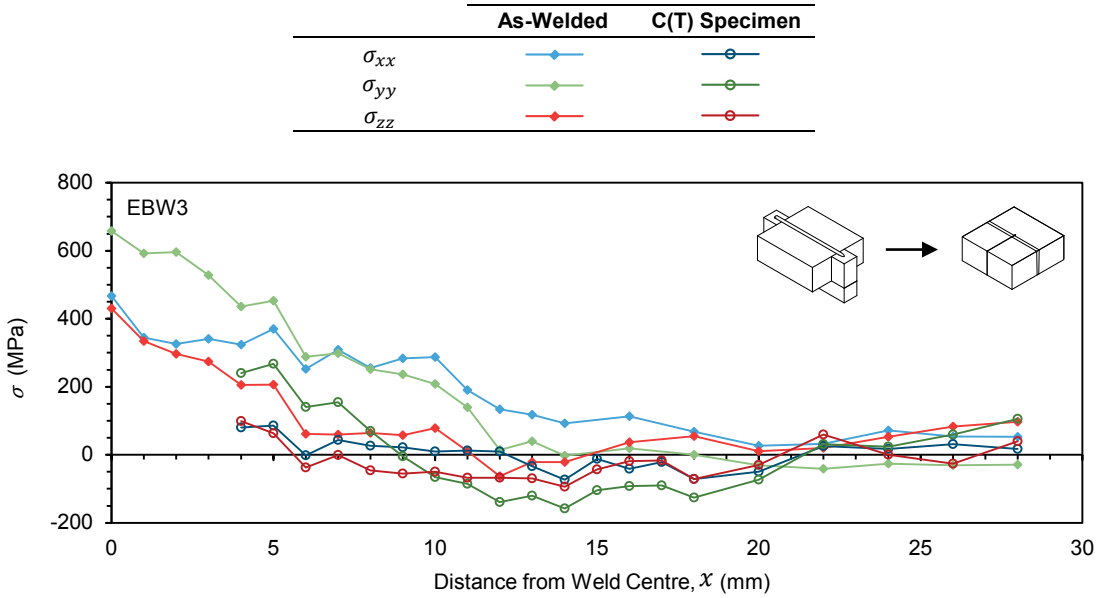


Figure 3.17 Redistribution of residual stresses in specimen EBW3 when machining C(T) specimen (line EF) from as-welded specimen (line AB)

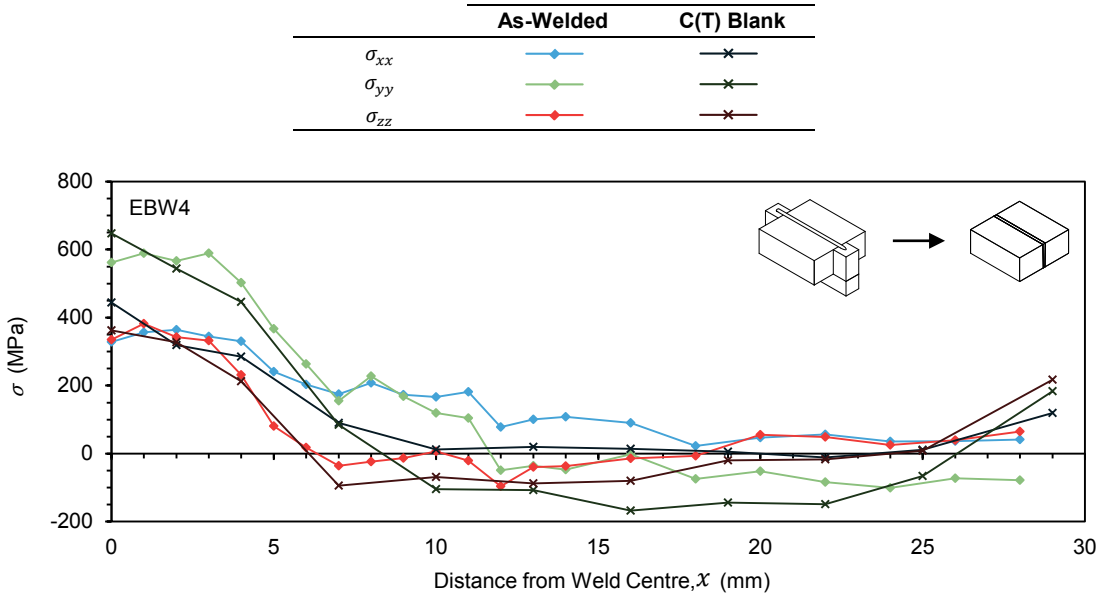


Figure 3.18 Redistribution of residual stresses in specimen EBW4 when machining C(T) blank (line CD) from as-welded specimen (line AB)

Pre-cracks were machined into the C(T) blank using wire EDM to manufacture the C(T) specimen. Figure 3.17 and Figure 3.19(b) show the magnitudes of all stress components reduced significantly during this cutting process for specimens EBW3 and EBW5 respectively.

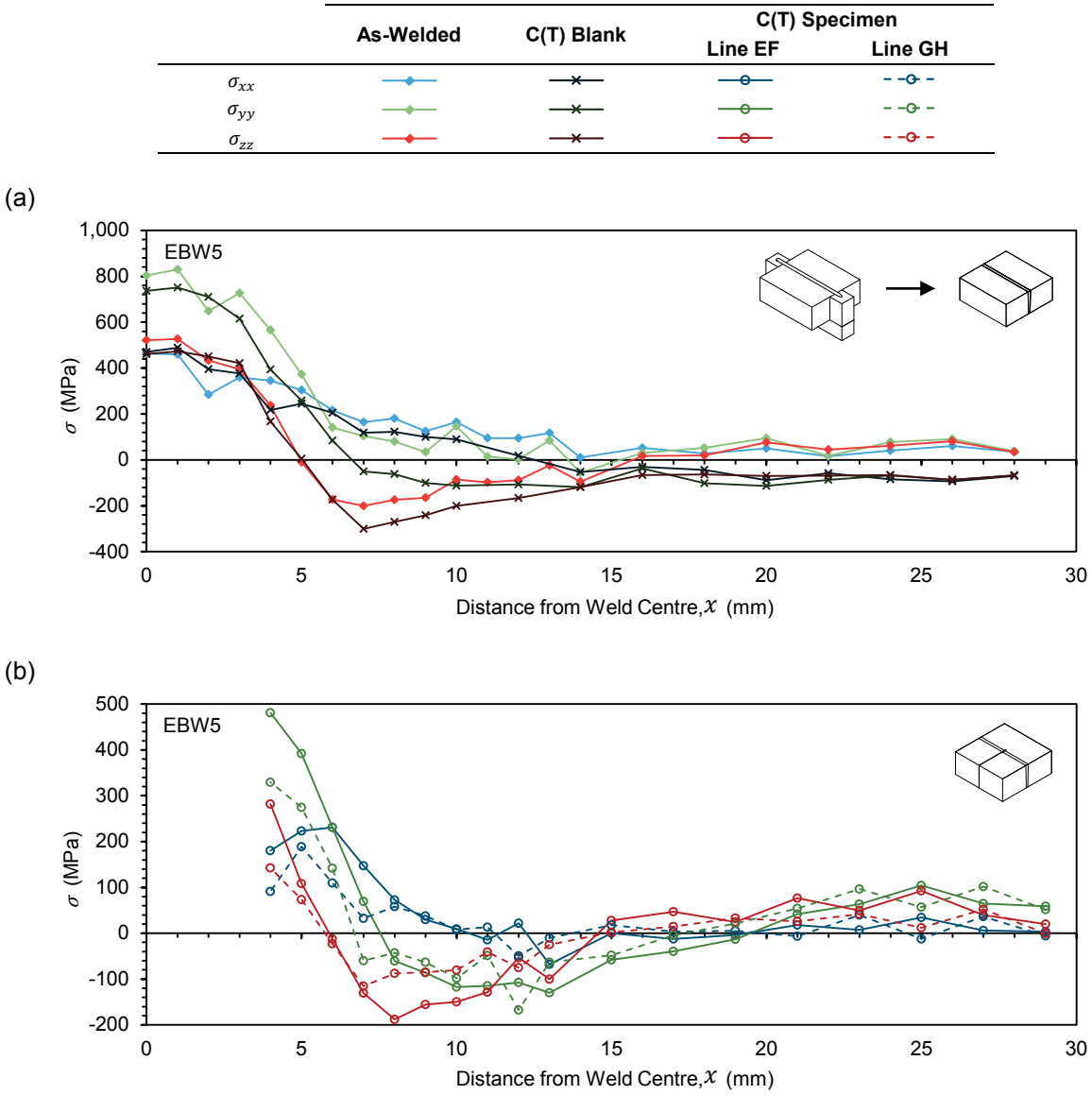


Figure 3.19 (a) Redistribution of residual stresses in specimen EBW5 when machining C(T) blank (line CD) from as-welded specimen (line AB) and (b) residual stresses in crack plane of C(T) specimen machined from EBW5

Weld residual stresses existed due to a misfit between a plastically deformed region and the surrounding elastic material. Insertion of the pre-crack beyond the weld region partially removed this misfit and therefore caused the reduction in residual stresses. The stress component, σ_{yy}, in EBW3 near the crack tip reduced from 530 MPa in the welded configuration to 270 MPa in the C(T) specimen. In specimen EBW5 the stresses reduced from 730 MPa to 480 MPa near the pre-crack at mid-thickness. The stresses in EBW5 were still large and hence provided a greater crack driving force in comparison to EBW3. Stresses at quarter thickness were measured for the C(T) specimen EBW5 and are shown in

Figure 3.19(b). The magnitude of the stress components are less at quarter thickness indicating a significant through thickness variation. Despite this, the longitudinal stresses near the weld, at quarter thickness, remained large at 330 MPa.

3.7 SIF AND RESIDUAL STRESS MEASURED BY THE SLITTING METHOD

3.7.1 CUTTING PROCEDURE

After welding specimen EBW4, the sacrificial blocks were removed to manufacture a C(T) blank which had dimensions of 60 × 60 × 25 mm^3. The slitting method was performed on this C(T) blank to determine the stress intensity factor as a function of crack length and to determine the stress component in the normal direction to this cutting plane. The cut plane is shown in Figure 3.20 which is the transverse – normal (x–z) plane to the weld. Therefore the longitudinal stress component as an average through the thickness of the specimen was determined.

Three strain gauges (type KFG-02-120-C1-11L5M3R) that had a gauge length of 0.2 mm were mounted on the back face of the specimen at mid-thickness and quarter thicknesses as shown in Figure 3.20. The gauges were encapsulated with the transparent silicon potting compound QSil 12 to ensure they remained waterproof whilst submerged in water during cutting.

Cutting was performed by wire EDM at the Open University, using a wire diameter of 0.25 mm whilst submerged in de-ionised water. Strain measurements were made at incremental cut distances of 0.3 mm. All measurements were made after the power to the EDM wire was stopped and the tank had been drained of water such that the specimen was in air. Only one side of the specimen was clamped allowing half of the component to deform during cutting. A bar was placed underneath the free side of the specimen to prevent it from

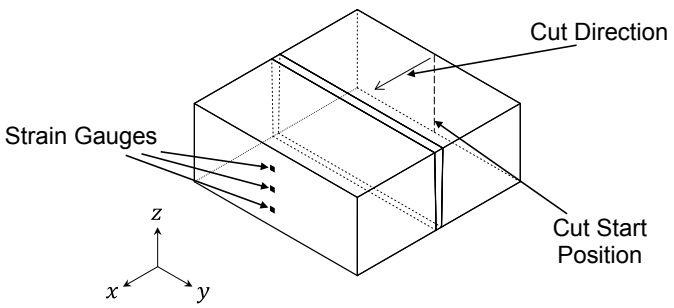


Figure 3.20 EBW4 C(T) blank showing strain gauge locations for slitting

falling following the cut. Figure 3.21 shows the specimen near the end of the cut where the cut direction is from right to left and the strain gauges are mounted on the left side of the specimen. The cut was visually inspected throughout to ensure mouth closure did not occur which would invalidate the slitting method.

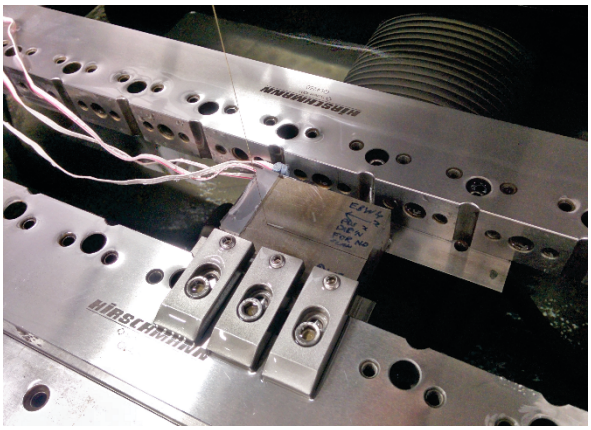


Figure 3.21 EBW4 C(T) blank during cutting for residual stress measurement by slitting

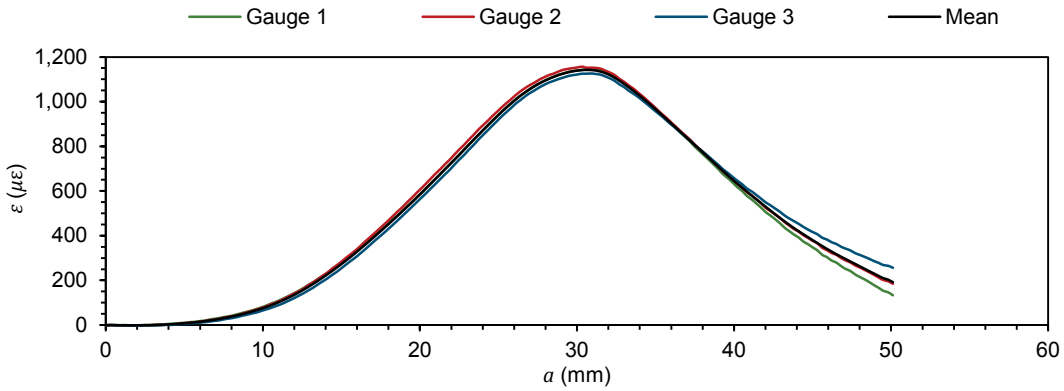


Figure 3.22 Back face strain measurements during slitting of C(T) blank from EBW4

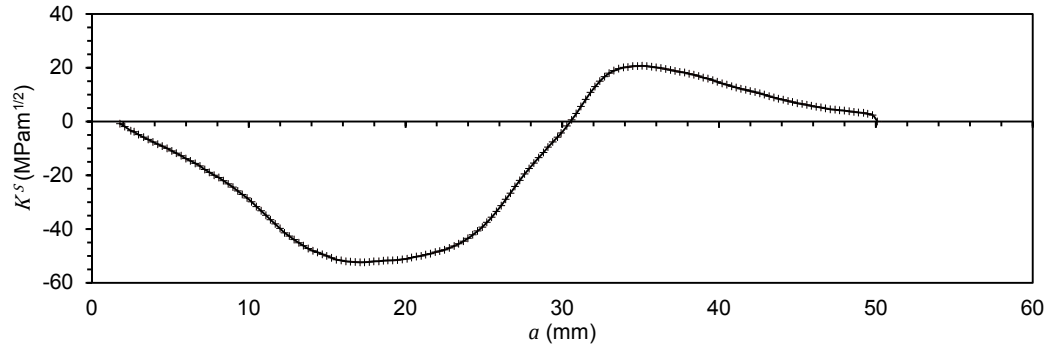


Figure 3.23 Stress intensity factor for EBW4 C(T) blank determined by slitting

3.7.2 STRESS INTENSITY FACTOR

The strains measured by the three strain gauges are shown in Figure 3.22, as a function of the cut length, a. Data is shown for the first 50 mm of the cut only as the encapsulant became detached from the specimen and the gauges were no longer sealed. The mean of the three strain gauges for each cut distance was used for the calculations. Noise in the measurements was removed using the incremental polynomial method in ASTM E1457-13 [77] where a second order polynomial was fitted to five successive data points. This polynomial was differentiated to determine $d\varepsilon/da$.

The stress intensity factor due to the secondary loads, K^s, was determined using (2.50) and is shown in Figure 3.23. The material properties E = 195.6 MPa and ν = 0.294 [32] were used and plane strain conditions were assumed in the calculation. The peak value of K^s was 20.7 MPam$^{1/2}$ which was obtained 5 mm beyond the weld centre. Negative values of K^s were obtained up until the weld which was located at a = 30 mm, hence the residual stresses imposed a compressive load on the cut tip for short cut lengths.

In the EB welded C(T) specimen design, a pre-crack length was selected as 3.0 mm beyond the centre of the weld using preliminary weld simulations modelling the residual stresses induced. The slitting experiment performed on specimen EBW4 showed K^s was greater than 18.0 MPam$^{1/2}$ in the region between 3 to 8 mm from weld centre with a peak of 20.7 MPam$^{1/2}$. Therefore the slitting measurements show the pre-crack length of 3.0 mm was suitable as K^s was initially large and the crack would grow into a region with high residual stresses.

3.7.3 RESIDUAL STRESS

The residual stress distribution in the direction normal to the cut face was calculated using (2.53), which was solved using a script written in the programming language, Python. The stresses are shown in Figure 3.24. This stress component corresponds to the longitudinal direction to the weld and was determined as an average through the thickness of the specimen. Tensile stresses were measured near the weld with the peak stress at a cut distance of 30.6 mm which corresponded well with the weld location. A comparison of these stresses to corresponding measurements made using ND and the contour method is presented in Section 3.9.

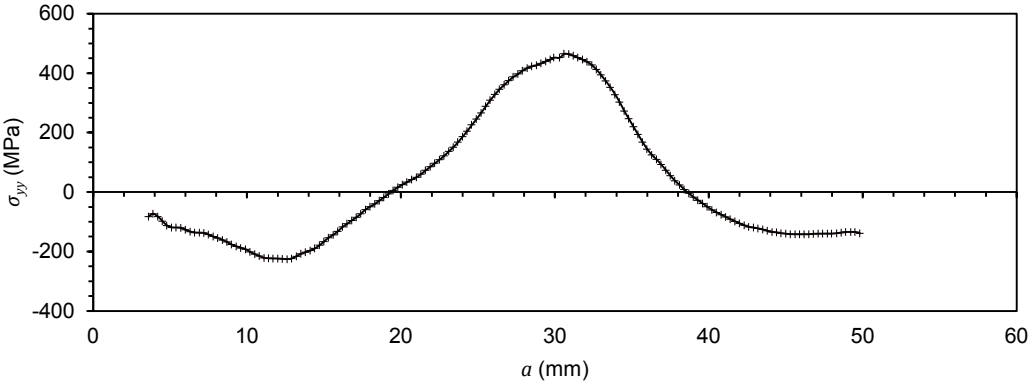


Figure 3.24 Longitudinal stress, σ_{yy}, for C(T) blank (EBW4) determined from the slitting method

3.8 RESIDUAL STRESSES MEASURED BY THE CONTOUR METHOD

3.8.1 CUTTING AND SURFACE MEASUREMENT

The contour method residual stress measurement technique was performed on the C(T) blank made from specimen EBW4. A cut was made normal to the weld direction and the deformations of the cut surfaces were measured. These displacements were applied to a FE model to determine the residual stresses in the longitudinal direction to the weld, as described in Section 2.6.4.

The cut surfaces were created when performing slitting, where the specimen was cut by wire EDM as shown in Figure 3.20. As both of these techniques were performed together, the cutting conditions were not ideal for the contour method. To perform slitting, only one side of the specimen was clamped allowing the specimen to deform such that the back face strains could be measured. However the contour method requires both sides of the specimen to be clamped to minimise plastic deformation of the cut surfaces [64]. Furthermore, to take strain measurements for the slitting method the cut was made incrementally, which could cause local cutting irregularities on the surface reducing the accuracy of the contour method. Although, this effect was minimised by using low power wire EDM settings [66].

The profiles of the deformed cut surfaces were measured by the Open University using a measurement procedure consistent with that reported in [89]. A Mitutoyo Crysta Plus 574 co-ordinate measuring machine (CMM) equipped with a 3 mm diameter Renishaw PH10M touch trigger probe was used which achieves a measurement accuracy of 4.9 μm. Measurements were made in a 0.5 × 0.5 mm^2 grid and the profiles of the perimeter of the cut parts were traced.

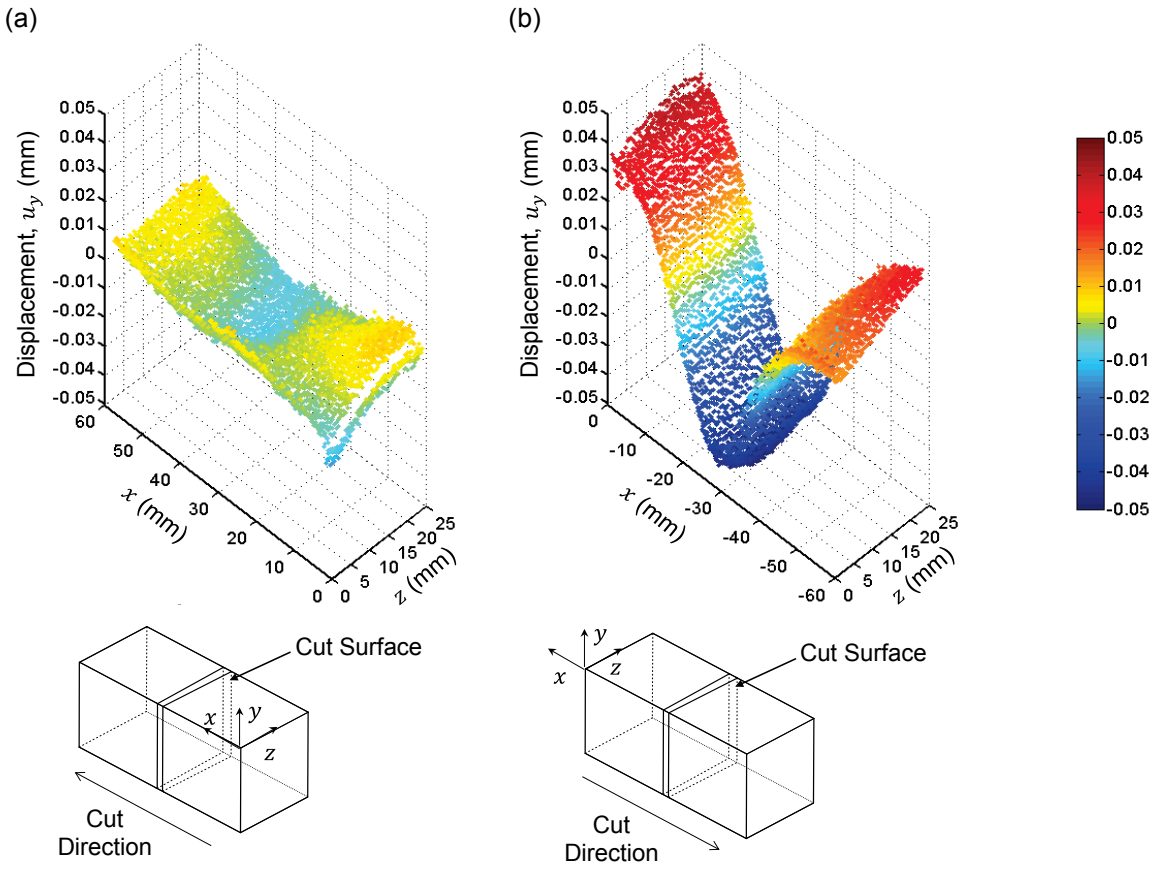


Figure 3.25 Deformation of cut faces of EBW4 C(T) blank for the contour method on (a) side A and (b) side B

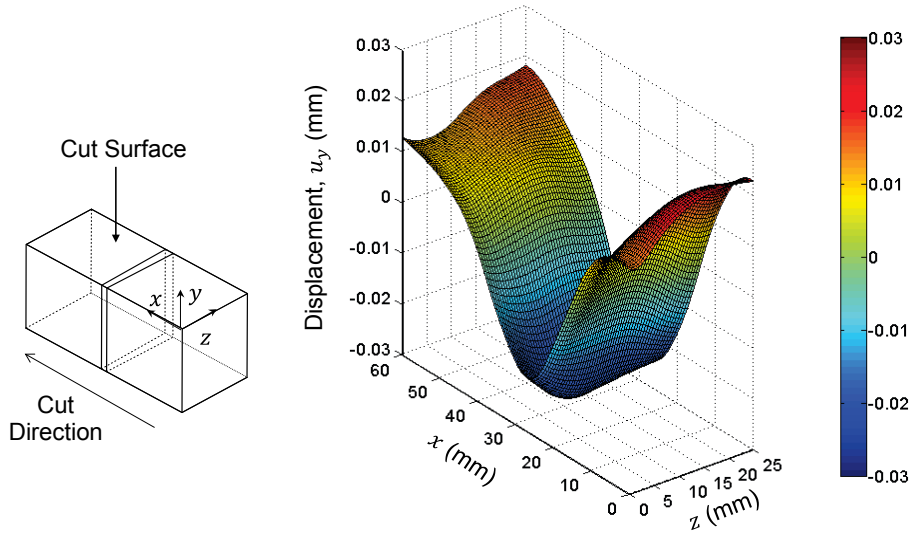


Figure 3.26 Averaged and smoothed displacements evaluated at nodal positions of the contour FE model for EBW4 C(T) blank

The raw data from surface measurements are shown in Figure 3.25. The deformation of the cut surfaces on side A and B were up to ± 0.01 mm and ± 0.05 mm respectively, hence the cut surfaces were non-symmetric. Side A was clamped to the EDM workbench whereas side B was free.

Similarly large differences between cut surfaces, where only one side of the specimen is clamped, are reported in other studies [66, 90, 91]. When a specimen mounted non-symmetrically is cut the specimen deforms during cutting. The contour method assumes a flat cut plane relative to the original shape of the specimen however this assumption becomes invalid. Prime and Kastengren [66] state the effect of uneven clamping is anti-symmetric and is removed after averaging the deformation on both sides of the specimen.

3.8.2 STRESS EVALUATION

The surface displacement measurements were analysed to remove erroneous data points, to determine the average deformation of the two cut surfaces and then to output displacements at nodal positions in the FE model used to calculate the stresses. The analysis procedure followed the recommendations by Prime and DeWald [60, pp117-119] and used MATLAB functions developed by Johnson [92]. After initial estimates of the residual stresses were obtained, further analyses were carried out to take into account local deformation of the cut tip to improve the accuracy of the residual stress predictions [66].

Outlier data points were visually identified and removed from the measurements in MATLAB. The data points close the top edge of the specimen where it appeared the entry of the EDM wire had removed additional material from the cut surface, as observed in Figure 3.25(a), were also removed. Data points on side B of the specimen were mirrored and aligned with side A using the perimeter measurements. The two data sets were averaged to remove anti-symmetric errors and the data was smoothed by fitting bivariate smoothing splines to the averaged data using MATLAB. Smoothing prevented noise in the data causing localised peaks in stresses in the subsequent FE analysis. In this method cubic polynomials were fitted to small regions of data. The extent of smoothing was defined using a parameter, called knot spacing, which defined the size of the area the polynomials were fitted to. A small knot spacing of 1 mm was selected to ensure the data was sufficiently smoothed to remove noise in the displacement data whilst ensuing the peak displacements near the weld were captured [92, 93]. The averaged and smoothed displacement profile is shown in Figure 3.26.

A three dimensional (3D) FE model of half of the C(T) blank was created using the FE software ABAQUS [49]. The perimeter profile of side A measured using the CMM was used to define the geometry of the model. The cut face was meshed with 1 × 1 × 1 mm^3 elements where the mesh was coarsened towards the back of the specimen. The model had 25,920 linear hexahedral elements (type C3D8) and 28,975 nodes. A linear elastic material model was used with Young's modulus, E, and Poisson's ratio, ν, of 195.6 GPa and 0.294 respectively [32]. The cubic polynomials in MATLAB were evaluated at nodal positions to determine the applied out-of-plane displacement of the cut face in the FE analysis. Additional boundary conditions were defined to prevent rigid body motion of the model.

The FE analysis was solved using the displacements shown in Figure 3.26 to determine an initial estimate of the residual stresses. A contour plot of the residual stress distribution is shown in Figure 3.27(a) and the stresses at mid-thickness are shown in Figure 3.28. The peak tensile stress had a magnitude of 423 MPa and was at mid-thickness of the specimen. However the peak region was positioned 1 mm away from the mid-width of the specimen which was where the weld was located.

The analysis was updated to take into account deformation of the cut tip during the EDM process using the procedure developed by Prime and Kastengren [66]. The initial estimate of the residual stresses were transferred to a full 3D model of the C(T) blank where the cutting process was simulated by incrementally removing elements, as shown in Figure 3.29. From this simulation the displacements associated with cut tip opening or closure were determined to apply a correction to the experimentally measured deformations.

In the cutting simulation the displacements, u_y, on two edges of the specimen were fixed to simulate the non-symmetric clamping arrangement shown in Figure 3.21. Further boundary conditions were defined to prevent rigid body motion. The deformation of the cut tip where the elements were removed to simulate a cut length of 8.0 mm is shown in Figure 3.29. The compressive stresses caused cut tip closure and the mouth had a width of 0.2978 mm. The initial distance between these nodes was 0.3000 mm which was the assumed cut width of the wire EDM. Therefore the FE study predicts an additional 0.0022 mm of material was removed from the specimen at this cut length. Due to symmetry, half of this displacement must be subtracted from the averaged CMM measured displacement data.

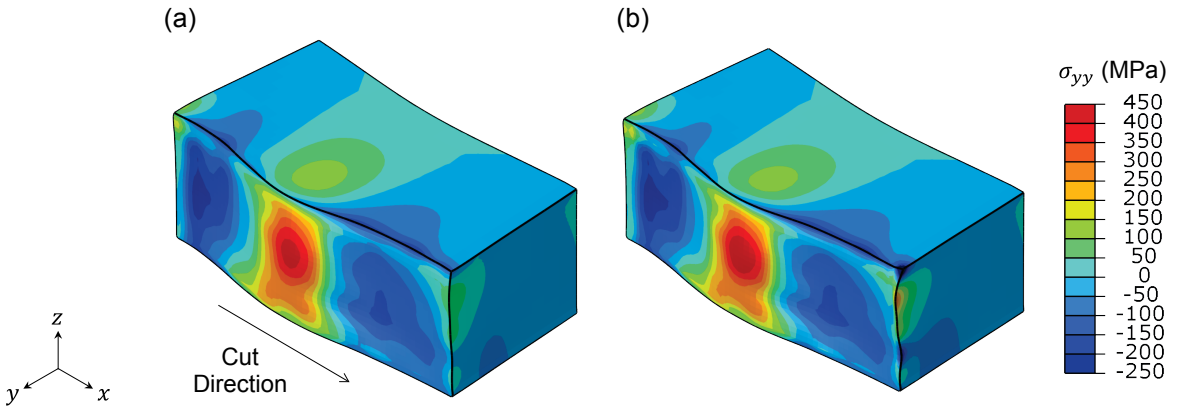


Figure 3.27 Longitudinal weld residual stresses, σ_{yy}, in EBW4 C(T) blank determined by the contour method (a) initial estimate (b) updated to take into account cut tip deformations

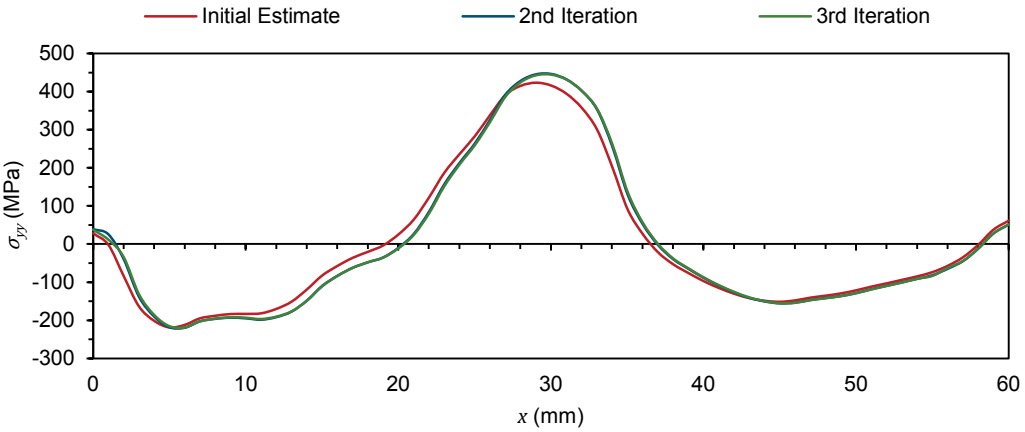


Figure 3.28 Longitudinal weld residual stresses, σ_{yy}, along mid-thickness of EBW4 C(T) blank determined by the contour method, cut direction from left to right

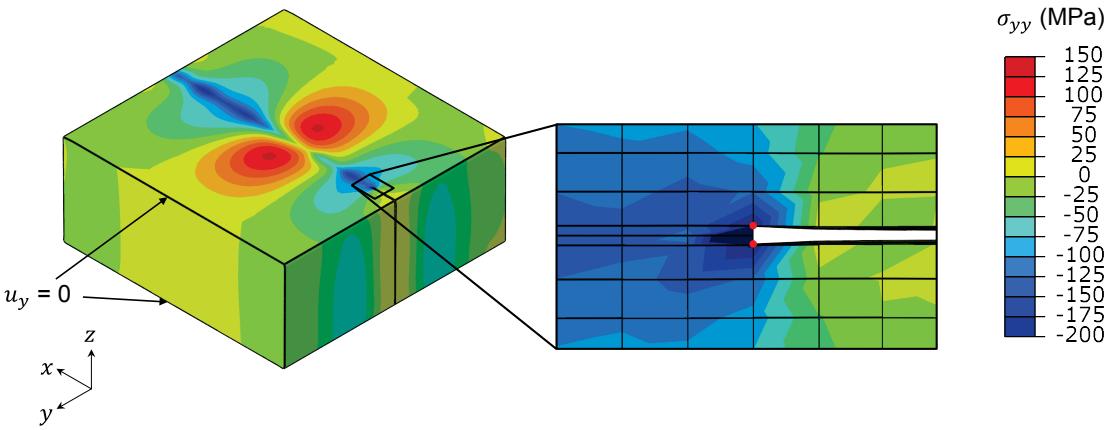


Figure 3.29 Simulating cutting of EBW4 C(T) blank to determine the deformation of the cut tip

The FE simulation determined cut tip displacements for each incremental cut length to define a displacement error for every node in the cut plane which are shown in Figure 3.30. The magnitudes of the displacements are up to 10% of the average displacements of the surface, which are shown in Figure 3.26. A positive cut tip displacement corresponds to mouth closure. The largest displacements of the cut tip were during the first half of the cut process where compressive residual stresses caused the mouth to close. At these locations the EDM wire would have removed additional material from the cut surfaces than what was assumed for a flat cut.

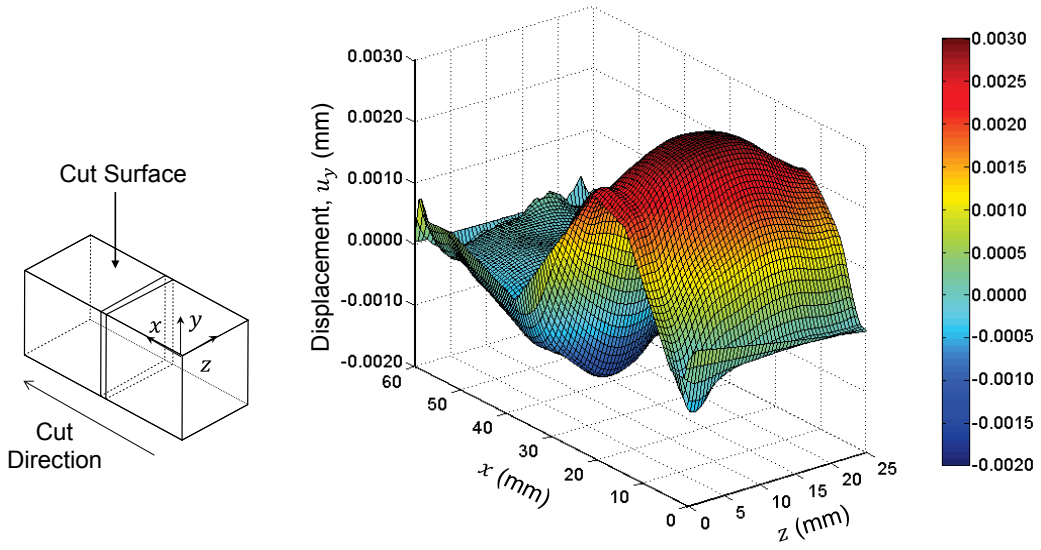


Figure 3.30 Displacement of cut tip at nodal positions of the contour FE model for EBW4 C(T) blank

The FE analysis to determine the residual stresses was repeated to include these errors. The cut tip displacements were subtracted from the averaged CMM measurements. The simulations to determine the cut tip displacements and residual stresses were iteratively repeated until the stress distributions converged. Figure 3.28 shows the second and third iterations, which show converges of the stress distributions. The peak tensile residual stress was 446 MPa and occurred at mid-width of the specimen. The inclusion of cut tip displacements caused the peak tensile stress to move towards the mid-width of the C(T) blank, which was the expected weld position, and also increased the magnitude of the tensile residual stress by 23 MPa.

The effective gauge size of the contour method is determined from the grid spacing of the CMM measurements, the FE element size and the knot spacing used for the spline fitting [65]. Surface displacements were made at 0.5 mm intervals whilst the FE element size and

knot spacing were 1.0 mm. These dimensions are of the order of the width of the EB weld. To increase the spatial resolution, the displacement measurements could be made using a smaller grid spacing and following this the FE model may be analysed with finer elements. This may improve the accuracy of the contour method measurements and should be investigated in future work.

3.9 COMPARISON OF EXPERIMENTAL RESIDUAL STRESS MEASUREMENTS

Longitudinal weld residual stresses in the C(T) blank, made from the weld specimen EBW4, were measured using ND, slitting and the contour method and are compared in Figure 3.31. Data for ND and the contour method in Figure 3.31(a) are for measurements made at point locations along line CD in Figure 3.10(b). However slitting determines stresses that are averages through the thickness of the specimen and therefore in Figure 3.31(b) the stresses from the contour method also averaged across the thickness of the C(T) blank.

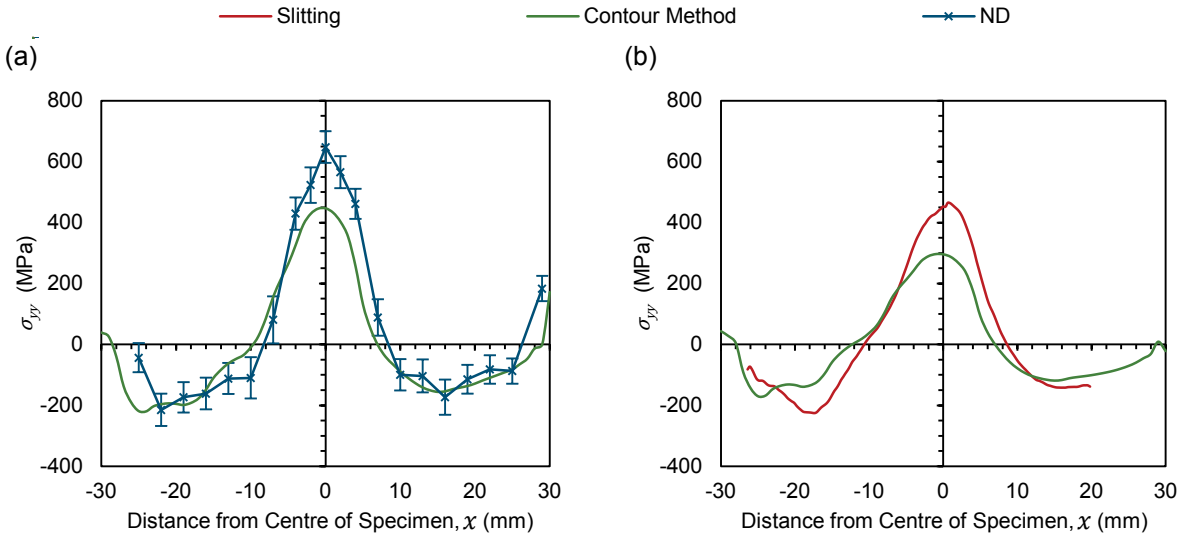


Figure 3.31 Comparison of longitudinal weld residual stresses in C(T) blank made from EBW4 using different measurement techniques (a) at mid-thickness and (b) averaged across thickness

The stress distributions show good agreement between the measurement methods. Peak tensile stresses were observed at the centre of the specimen width for all stress profiles which corresponded to the location of the EB weld. All the methods measured compressive stress of up to 200 MPa in the parent material. However the magnitudes of the peak tensile longitudinal stresses differed between the three measurement techniques.

The tensile stresses determined using ND were up to 200 MPa greater than those measured using slitting and the contour method. The peak tensile stress was measured as 650 MPa using ND. Errors in the ND measurements near the weld may have existed due to the use of a far field value of the reference scattering angle, $2\theta_o$. A variation in $2\theta_o$ was not clearly identified (Figure 3.12) and from these measurements an error of up to ± 40 MPa was determined from the scatter in reference strain measurements. This is shown by the error bars in Figure 3.31(a). In a study by Traore el al. [89] with an EB welded Esshete 1250 specimen, the reference strain variation between parent and EB weld metal was successfully determined. From the data published by Traore et al. it is estimated that the use of parent material reference strain measurements in the EB weld region could amount to overestimating the tensile stresses by 100 MPa.

The peak tensile stresses measured by slitting was 450 MPa. This is greater than the corresponding stress measurement using the contour method where the thickness averaged peak tensile stress was 300 MPa. It is likely plastic deformation occurred on the cut face of specimen EBW4 during sectioning due to the large stresses present. This would cause the elastic deformation assumption to be invalid and the surface profiles measured using CMM would not account for the total deformation of the specimen. It is considered that due to this the contour method measured stresses that were less than those in the specimen.

3.10 SUMMARY

EB welded C(T) specimens were designed and manufactured to be used to investigate CCG due to residual stresses. ND measurements were made at various stages of the fabrication process on three samples to determine the magnitude of residual stresses induced. Peak residual stresses of up to three times greater than the yield strength of the parent material were measured after welding. However, pre-cracking the specimens reduced this to approximately twice the yield stress.

Further residual stress measurements were made using slitting and the contour method which generally agree well with the ND measurements except for the region up to 2 mm from the weld centre. Possible sources of error have been identified in all three of the measurement techniques. In the ND measurements the variation in the reference strain measurements due to compositional and microstructural changes near the weld need to be taken into account. However, as EB welds were extremely narrow and due to the random variation in measurements caused by intergranular stresses, a change in reference strain

measurements across the weld was not observed. Microstructural examination of the weld shows that any error caused by this only effects measurements up to 2 mm from the centre of the weld due to the small fusion zone and HAZ. The slitting and contour methods assume elastic deformation during the associated cutting process however due to the large stresses present in the specimen plastic strains were induced at the cut tip. The contour method uses the deformed profile of these cut surfaces and due to this it was judged the measurements were lower than those in the specimen.

A number of EB weld specimen designs were manufactured. Specimen EBW4 was made with two EB weld passes to investigate whether the weld induced residual stresses increased due to cyclic hardening. However the residual stresses from one and two weld passes were indistinguishable from the ND measurements. Specimen EBW5 was made with 8% pre-compressed Type 316H stainless steel. The preconditioned material had increased yield strength which allowed greater residual stresses to be induced in the specimen, in comparison to specimens made from material in the as-received condition. This specimen would also have reduced creep ductility due to this pre-conditioning process and crack growth would be more likely in a CCG test. Hence two further test specimens, EBW6 and EBW7, were manufactured for CCG testing.

In-situ temperature measurements were consistent for all specimens with a single weld pass and therefore it was assumed that the residual stresses in EBW6 and EBW7, which were not measured, were the same as those in EBW5.

4 PREDICTION OF RESIDUAL STRESSES IN EB WELDED C(T) SPECIMENS

4.1 INTRODUCTION

Numerical simulations to predict the residual stresses induced in the EB welded C(T) specimens were developed using the FE software ABAQUS [94]. The models included simulations of the welding and cutting processes to determine the weld residual stresses induced and stress redistribution during manufacture.

The weld simulations were performed in two stages: the temperatures in the specimens were first predicted, and then the weld induced residual stresses were determined. An overview of weld modelling is provided in the following section where best practices are identified from literature. A heat source model is then detailed which is an input to the thermal simulation. The thermal and mechanical models are described in Section 4.4 and Section 4.5 respectively. Following this, comparisons of residual strain predictions with experimental measurements are presented to validate the mechanical simulation. The residual stresses which drive crack growth and determination of K^s are shown in Section 4.7.

This chapter focuses on weld simulations of the specimens manufactured at EBP which were used to perform CCG testing. A weld simulation of specimen EBW1 was developed and presented by Kapadia et al. [78] and Vlamis [95].

4.2 DESCRIPTION OF THE FE MODELS

Welding is a complex non-linear process and requires considerable effort to produce models to accurately predict weld induced residual stresses. Much work has been published in recent years to standardise the modelling approach. The EB weld simulations followed the modelling guidelines presented in Section III.15 of the R6 fracture assessment procedure [27] ensuring best practice was adopted. The weld models had similarities to specimens studied in recent round robin exercises of a single weld bead on a flat plate conducted by NeT Task Group 1 (TG1) [96], and of an edge welded beam, led by EDF Energy [32]. Both of these benchmark specimens were made of ex-service Type 316H austenitic stainless steel and had been welded with single weld passes, however these studies used MMA and TIG welding processes respectively. In these studies extensive temperature and residual stress measurements were made. Numerous contributors developed FE weld simulations that allowed the sensitivity of the residual stress predictions to modelling assumptions to be

investigated and recommendations for the modelling approaches to be made. The findings contributed to establishing best practice recommendations which are presented in the R6 procedure [27]. One of the recommendations is that the analyst is familiar with developing weld models. Therefore a simulation of the edge welded beam was initially created in this project. The results are presented by Aird et al. [6] where the solutions obtained are in excellent agreement with those determined by other analysts and experimental data. The findings from the weld bead on flat plate and edge welded beam round robins were used to form key modelling decisions for the EB welded specimens and are referred to throughout this chapter.

The EB weld process was modelled as a sequential thermo-mechanical problem where firstly a thermal FE analysis calculated the temperatures in the specimen during the weld. Subsequently, these temperature distributions were used as an input to a mechanical analysis where the deformation and stresses in the model were determined. The thermal and mechanical analyses were uncoupled as it was assumed the deformation of the workpiece during welding had little influence on heat transfer during the weld process.

The R6 procedure presents different approaches for modelling the heat input to the weld model, however those which provide the most accurate predictions are also the most complex and computationally expensive. To accurately predict the longitudinal component of the weld residual stresses a 3D model of the weld process was required. The longitudinal stresses were of key interest as this stress component was orientated normal to the crack plane in the C(T) specimens and therefore caused crack growth in subsequent CCG tests. The heat input to the thermal analysis was defined using a ‘moving heat source’ where the motion of the weld torch traversing across the specimen was modelled. Accurate weld models of conventional welding processes require the deposition of filler material into the weld to be modelled over multiple passes. However the EB welding process is relatively simple as filler metal is not used and therefore material deposition did not need to be considered. Furthermore as there were a low number of weld passes it was feasible to model the heat input from the EB use a moving heat source model in 3D. A large number of weld passes often require a two dimensional approximation to be made [97].

4.3 HEAT SOURCE MODEL

A heat source model calculates the heat flux at integration point locations in the thermal analysis which defines the extent of heating by the weld torch. The R6 weld modelling guidelines [27] recommends using modelling tools, such as the commercial software FEAT-WMT [98], to determine the heat source model as such tools are computationally efficient in calculating the weld parameters. However FEAT-WMT did not include a heat source model for EB welding and therefore an ABAQUS user subroutine was created to define the heat source. For simulations where the weld residual stresses in the longitudinal direction need to be determined accurately, the R6 weld modelling guidelines recommends the use of a 3D moving heat source model [27]. In this model the heat flux distribution around the EB was defined in 3D and this heat flux profile was traversed along the weld path.

Early heat source models for welds described the heat flux distribution on the surface of a work piece using Gaussian distributions. This was extended by Goldak et al. [99] to create a volumetric heat source called the double ellipsoid model where the flux distribution also varies along the depth of the weld as shown in Figure 4.1(a). This model improved the accuracy of temperature predictions in cases where most of the heat is transferred to the workpiece below the weld surface to create deeper penetrating welds. However the profile of the heat flux from the EB is more accurately defined by a conical distribution where the power density varies linearly along the depth of the weld as shown in Figure 4.1(b).

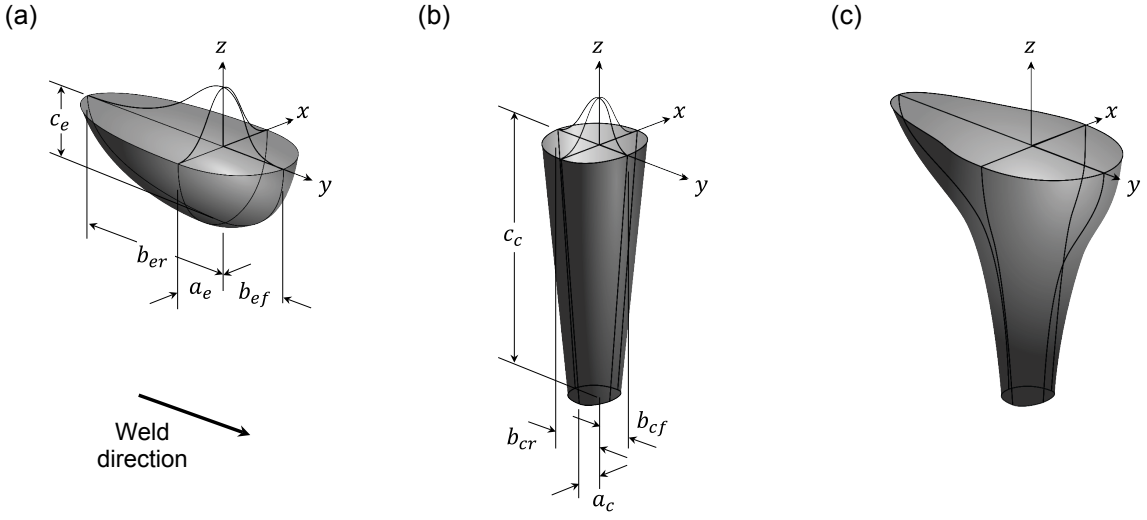


Figure 4.1 Heat flux distribution profiles in (a) double ellipsoidal, (b) conical and (c) combined heat source models, for a weld arc positioned along the z-axis moving in the y-direction

Lundbäck and Runnemalm [100] present a heat source model that combines the conical and double ellipsoid models which describe the through-thickness and near-surface heating effects of the EB respectively, shown in Figure 4.1(c). For a moving EB most of the heat is conducted behind the beam, therefore different Gaussian profiles are used to define the heat flux distribution ahead of and behind the EB. The equations defining the combined conical and double ellipsoid heat source model presented in [100] were modified for a moving heat source and are shown by (4.1) to (4.8). The constants in these equations representing the dimensions of the heat source are depicted in Figure 4.1.

The total heat flux, q, distribution is defined by:

$$q_{combi(x,y,z,t)} = \beta q_{e(x,y,z,t)} + (1-\beta) q_{c(x,y,z,t)} \tag{4.1}$$

where the constant β represents the heat flux contribution of the double ellipsoid model, q_e, relative to the conical ellipsoid model, q_c.

The heat flux of the double ellipsoid model, q_e, ahead of and behind the EB are defined by:

$$q_{e(x,y,z,t)} = \begin{cases} \dfrac{6\sqrt{3} f_{ef} Q}{a_e b_{ef} c_e \pi^{3/2}} e^{\left(-3\frac{x^2}{a_e^2}\right)} e^{\left(-3\frac{(y-vt)^2}{b_{ef}^2}\right)} e^{\left(-3\frac{z^2}{c_e^2}\right)}, & y - vt \geq 0 \\ \dfrac{6\sqrt{3} f_{er} Q}{a_e b_{er} c_e \pi^{3/2}} e^{\left(-3\frac{x^2}{a_e^2}\right)} e^{\left(-3\frac{(y-vt)^2}{b_{er}^2}\right)} e^{\left(-3\frac{z^2}{c_e^2}\right)}, & y - vt < 0 \end{cases} \tag{4.2}$$

where a_e, b_e, and c_e are the lengths that describe the size of the Gaussian distributions in the x, y and z directions respectively, with the subscripts f and r denoting the dimensions in front of and behind the weld respectively. The constants f_{ef} and f_{er} are defined by:

$$f_{ef} = \frac{2b_{ef}}{b_{ef} + b_{er}} \tag{4.3}$$

$$f_{ef} + f_{er} = 2 \tag{4.4}$$

The energy input rate, Q, is determined from the beam current, I, and voltage, V, by:

$$Q = \eta I V \tag{4.5}$$

where η is the efficiency of the heat from the EB transferred to the work piece. EB welding is considered to be a very efficient process when performed under vacuum conditions as few electrons from the beam are scattered before they penetrate the workpiece. The efficiency is generally estimated to be between 90 – 95% [80, p30].

The heat flux of the conical model, q_c, ahead of and behind the EB are defined by:

$$q_{c(x,y,z,t)} = \begin{cases} \dfrac{6f_{cf}Q}{a_c b_{cf} c_c \pi (1-d_c)} e^{\left(-3\frac{x^2}{a_c^2}\right)} e^{\left(-3\frac{(y-vt)^2}{b_{cf}^2}\right)} \left[1 - \dfrac{(1-d_c)|z|}{c_c}\right], & y - vt \geq 0 \\ \dfrac{3f_{cr}Q}{a_c b_{cr} c_c \pi (1-d_c)} e^{\left(-3\frac{x^2}{a_c^2}\right)} e^{\left(-3\frac{(y-vt)^2}{b_{cr}^2}\right)} \left[1 - \dfrac{(1-d_c)|z|}{c_c}\right], & y - vt < 0 \end{cases} \quad (4.6)$$

where a_c, b_c, and c_c are the lengths that describe the size of the distributions in the x, y and z directions respectively and d_c is a dimensionless parameter which defines the linear change of heat flux in the y direction. The constants f_{cf} and f_{cr} are defined by:

$$f_{cf} = \frac{2b_{cf}}{b_{cf} + b_{cr}} \quad (4.7)$$

$$f_{cf} + f_{cr} = 2 \quad (4.8)$$

A user-defined distributed heat flux was created in ABAQUS using the *DFLUX keyword and a FORTRAN coded subroutine. The subroutine solved (4.1) to (4.8) to determine the magnitude of heat flux at each integration point location during the thermal weld analysis. The parameters in the heat source model were determined iteratively by analysing the thermal model and comparing temperature predictions to experimental data measured with thermocouples during welding. The size of the weld was used as an initial estimate for the length parameters.

4.4 THERMAL ANALYSIS

4.4.1 MODEL DESCRIPTION

A 3D thermal model of the weld specimens was developed in ABAQUS which included the C(T) blank and the sacrificial material. Symmetry was assumed at the weld plane and therefore only half of the specimen was modelled as shown in Figure 4.2.

The model consisted of 162,290 3D quadratic heat transfer elements (ABAQUS type DC3D20) and 687,006 nodes. EB welds have a very high power density (up to 10^5 W/mm^2 [80, p4]) and therefore the temperature gradients near the weld are extremely large. Very small elements were required to describe the temperature profile of the material around the EB. Hence, the mesh was biased towards the weld such that the elements near the weld plane had dimensions of 0.5 × 0.5 × 0.5 mm^3. This ensured that there were four or five integration points across half of the weld width which satisfied the mesh criteria in R6 Section III.15 [27]. The distance between the start and stop positions was measured to be 78 ± 1 mm

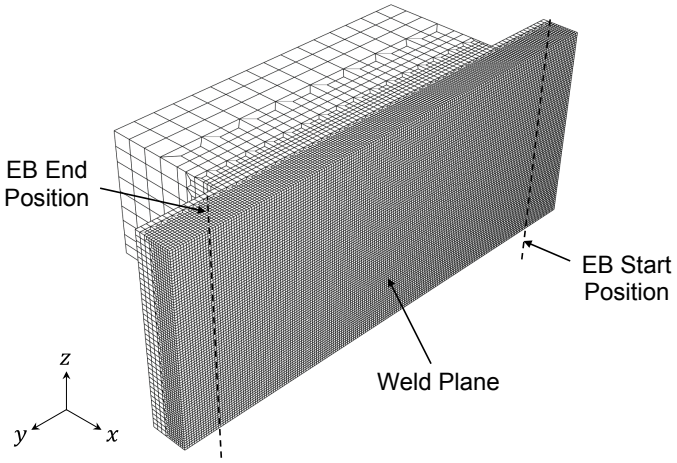


Figure 4.2 Thermal model of the EB weld specimen

in the welded samples and therefore the weld length was assumed to be 78 mm for all specimens. Specimen EBW3 and EBW4 had widths of 60.0 mm whilst EBW5 to EBW7 had widths of 62.5 mm. In the thermal simulation a width of 62.5 mm was assumed for all specimens.

The thermal analysis required the specific heat capacity, C_p, thermal conductivity, k, and density, ρ, to be defined for the material. These properties were published for Type 316H stainless steel for the edge welded beam round robin [6, 32] and are shown in Table 4.1. The thermal material properties were assumed to be independent of the material pre-conditioning treatment. Therefore EBW3 and EBW5 were simulated using one thermal model.

Welding was performed at reduced pressure in vacuum conditions. Hence, the dominant heat loss mechanism was assumed to be conduction to the work table and clamps, and through radiation from the free surfaces of the specimen. This was modelled simplistically by defining radiation on all surfaces except the weld plane. The emissivity was dependent on the surface finish of a component, the temperature and the wavelength of the radiation [101, pp118-132]. Some surfaces of the specimens had mill finishes whilst some were lightly oxidised after being cut by wire EDM. An emissivity of 0.6 was defined which have been experimentally found in steels that have a lightly oxidised surface [101, p128] and ambient temperature defined as 20°C.

The heat flux distribution from the EB was defined using the *DFLUX subroutine as described in Section 4.3. The constants which define the dimensions of the heat source model, as illustrated in Figure 4.1, are shown in Table 4.2.

Table 4.1 Thermo physical properties for Type 316H stainless steel [6, 32]

Temperature (°C)	Specific Heat Capacity (kJ/kg °C)	Conductivity (W/m °C)	Density (kg/m^3)
20	0.492	14.12	7,966 (Assumed temperature independent)
100	0.502	15.26	
200	0.514	16.69	
300	0.526	18.11	
400	0.538	19.54	
500	0.550	20.96	
600	0.562	22.38	
700	0.575	23.81	
800	0.587	25.23	
900	0.599	26.66	
1,000	0.611	28.08	
1,100	0.623	29.50	
1,200	0.635	30.93	
1,300	0.647	32.35	
1,400	0.659	33.78	

Table 4.2 Constants used in the heat source model

Constant	Value
a_e (mm)	1.0
b_{ef} (mm)	2.0
b_{er} (mm)	20.0
c_e (mm)	20.0
a_c (mm)	0.5
b_{cf} (mm)	0.5
b_{cr} (mm)	0.5
c_c (mm)	30.0
d_c	1.0
β	0.25
η	0.95

The heat source model was calibrated using thermocouple data, as opposed to using the weld macrograph, as this was considered as the most accurate approach in the NeT TG1 project [96]. The efficiency, η, was first found iteratively by matching the temperature response of the far field thermocouple location TC-4, as shown in Figure 3.5, to experimental measurements and was found to be 95%. This was consistent with typical values of 90 to 95% quoted in literature [80, p30]. The value of η determines the total thermal energy transferred to the specimen, the remaining constants affect the distribution of heat around the weld. The remaining constants, shown in were Table 4.2, which define the shape of the double ellipsoidal and conical heat source models were determined iteratively such that temperature predictions at thermocouple locations close to the weld matched experimental data.

The thermal analysis consisted of two heat transfer steps for specimens EBW3 and EBW5, and a further two steps for specimen EBW4 to model the second weld pass. The thermal simulation of the second weld pass in EBW4 was run as a restart analysis from the thermal model of EBW3 and EBW5.

Step 1: The weld pass was simulated by the heat source model moving along the weld line. The duration of the step was 20 s.

Step 2: The analysis continued to run for 1,000 s, for specimens EBW3 and EBW5, where the model cooled and the temperatures redistributed through the specimen. This step was only 360 s for specimen EBW4.

Step 3: The second weld pass for specimen EBW4 was simulated repeating the first weld pass. The duration of the step was also 20 s.

Step 4: The analysis for EBW4 continued to run for 1,000 s where the model cooled and the temperatures redistributed through the specimen.

The computational time required for the thermal analysis of the single weld pass was 84 h using eight cores. The analysis with two weld passes took 181 h with eight cores.

4.4.2 TIME INCREMENTATION

The FE code, ABAQUS, determines a solution for a heat transfer problem at discrete time increments. The time increment must not be larger than the time for the EB to travel the length of an element in the weld region otherwise the heat source model would skip past elements, the weld pool would not be continuous and insufficient heat would be transferred to the model. As the weld speed was 6.3 mm/s and the element length was 0.5 mm, the maximum time increment was defined as 0.08 s. ABAQUS recommends a minimum time increment, Δt_{min} , for heat transfer analyses of:

$$\Delta t_{min} > \frac{\rho c_p}{6k} \Delta l^2 \tag{4.9}$$

where Δl is the length of an element. Using material properties at 800°C in Table 4.1 and Δl = 0.5 mm, Δt_{min} is determined to be 0.037 s. If the time increment is smaller than this spurious oscillations can appear in the results and the analysis may fail to converge. This advice is also stated in clause III.15.4.7.4 of the R6 procedure [27].

The thermal analysis needed very small time increments (approaching 0.001 s) which did not satisfy this recommendation. In such cases the use of smaller elements is advised however due to large computational times it was unfeasible to use smaller elements. The temperature distribution through the weld specimen predicted by the thermal analysis is shown in Figure 4.3. The position of the EB is at mid-length of the specimen and is moving in the y direction. The dark red region represents molten material as Type 316H stainless steel's melting temperature, T_m, is 1,400°C. The contour profiles of temperature do not show any oscillations, as shown in Figure 4.3, and therefore the analysis does not appear to have been affected by this instability.

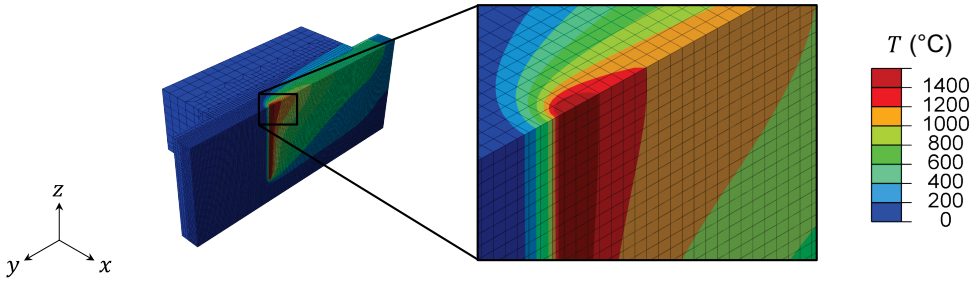


Figure 4.3 Temperature distribution in thermal analysis near weld pool

4.4.3 COMPARISON OF TEMPERATURE DATA

The constants used to define the heat source model were iteratively determined to ensure the temperatures predicted at the thermocouple locations matched the experimental data. The simulations were then validated by comparison of weld fusion boundaries predicted by the FE model to macrographs. The transient temperatures and fusion boundaries are presented in this sub-section.

FE predictions of the temperature history at the four thermocouple locations (identified in Figure 3.5) are compared to experimental measurements in Figure 4.4 and Table 4.3. For the single weld pass the experimental data was averaged between specimens, EBW3, EBW5, EBW6 and EBW7, and between thermocouples either side of the weld. The temperature predictions by the FE model were in excellent agreement with the experimental measurements for the single pass weld. The peak temperatures relative to the initial temperatures, $T_{peak} - T_0$, at the thermocouple locations predicted by the FE models were within 3% of the experimental measurements, as shown in Table 4.3. The weld specimen cooled to reach a uniform temperature at approximately 200 s in the analysis where the uniform temperature predicted by FE is within 4% of the experimental measurements.

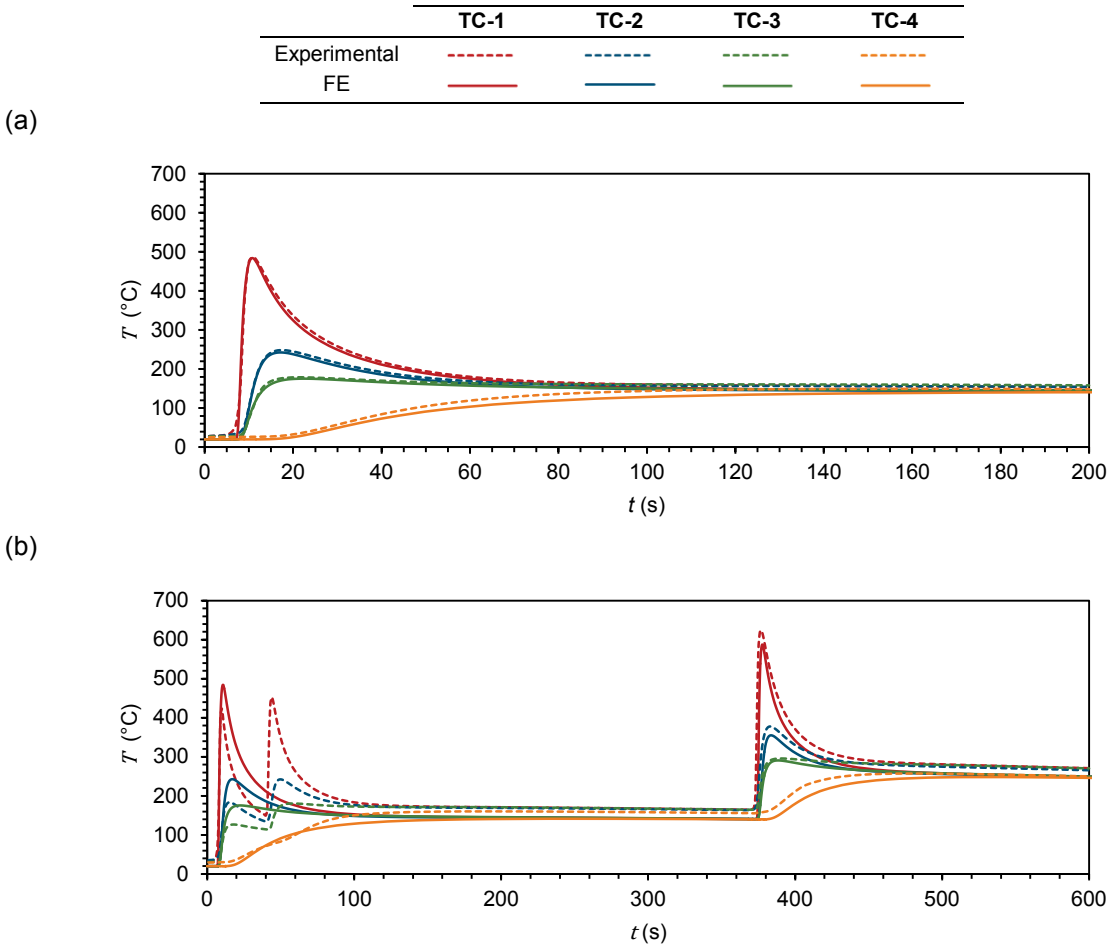


Figure 4.4 Comparison of FE temperature predictions at thermocouple locations with averaged experimental measurements for (a) a single pass weld and (b) a two pass weld

Studies were performed to investigate the sensitivity to the emissivity defined for radiation heat transfer. Little effect was observed on the temperatures as heat transfer in the analyses was dominated by conduction across the specimens. The rate of cooling increased as the specimens were taken out of the vacuum chamber and cooled in air. The specimens then continued to cool at uniform temperature, hence the residual stresses were assumed independent of the rate of cooling. Therefore, in the simulations the temperatures were linearly reduced to 20°C after uniform values across the samples were reached.

The temperatures predicted by the FE model of the two pass EB weld specimen are shown in Figure 4.4(b). The experimental measurements shown for comparison are an average of the thermocouple measurements made either side of the weld in specimen EBW4. The power trip that occurred to the EB whilst welding specimen EBW4 resulted in the two thermal peaks within the first 60 s of the experimental data. Due to this the temperature

measurements did not reach the magnitude predicted by the FE model or the experimental measurements for the single pass weld. When the EB was restarted a small overlap was made over previous weld to complete the pass. This overlap increased the total heat input into the specimen in comparison to the single pass weld and therefore the stabilised temperature after the first weld pass (168°C at 200 s) was greater than for the specimens with a single pass (154°C at 200 s). This overlap in the weld pass was not modelled in the FE simulation and therefore the temperatures before the second weld pass predicted by the simulation were less than those measured in EBW4.

Comparisons of the temperature increases during the second weld pass between the FE simulation and experimental measurements are shown in Table 4.4. For the second weld pass, the peak temperatures relative to the temperatures at 370 s, $T_{peak} - T(370)$, predicted by the FE model are generally in close agreement with the experimental data. At thermocouple location TC-3 the experimentally measured temperature increase was less than the FE prediction due to error in the placement of the probes, as shown in Table 3.4. The specimen was considered to have reached a uniform temperature at 600 s. The large error of 13.9% at TC-4 is due to one of the thermocouples measuring an unexpectedly lower temperature, shown by TC-4B in Figure 3.6(b). In general, the temperatures predicted by both thermal simulations are in close agreement to the experimentally measured data.

Table 4.3 FE temperature predictions and averaged experimental measurements for an EB weld specimen with a single pass weld

Thermo-couple	$T_{peak} - T(0)$			$T(200) - T(0)$		
	Exp. (°C)	FE (°C)	Error (%)	Exp. (°C)	FE (°C)	Error (%)
TC-1	458	464	1.2%	125	125	-0.3%
TC-2	221	223	1.1%	127	124	-2.0%
TC-3	151	155	2.5%	130	126	-3.2%
TC-4	124	121	-2.4%	123	121	-1.6%

Table 4.4 FE temperature predictions and averaged experimental measurements for the second weld pass of an EB weld specimen with a two pass weld

Thermo-couple	$T_{peak} - T(370)$			$T(600) - T(370)$		
	Exp. (°C)	FE (°C)	Error (%)	Exp. (°C)	FE (°C)	Error (%)
TC-1	459	446	-2.7%	106	108	2.5%
TC-2	214	214	0.2%	102	107	5.4%
TC-3	130	150	15.3%	105	108	2.8%
TC-4	101	108	6.8%	93	106	13.9%

4.4.4 COMPARISON OF WELD FUSION BOUNDARIES

The profiles of the weld fusion boundaries observed in the macrographs were compared with the size of the FE predicted fusion zone to validate the thermal model. The predicted fusion zones were defined as the material which exceeded the melting temperature, T_m, during the thermal analyses. A comparison of weld fusion boundaries for specimens EBW3 and EBW4 which has one and two weld passes respectively are shown in Figure 4.5.

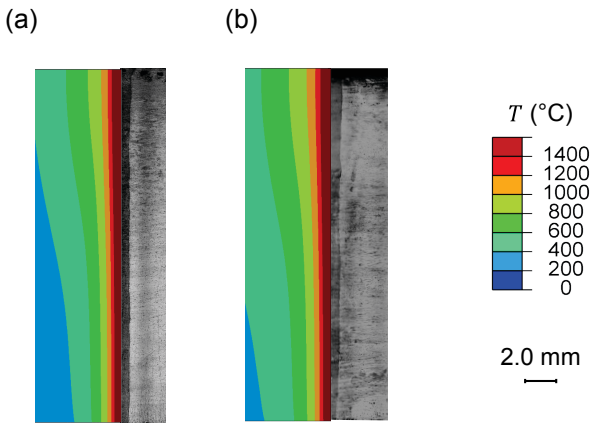


Figure 4.5 Comparison of weld fusion boundaries predicted by FE model with macrographs (a) EBW3 and (b) EBW4

The FE analyses predicted a tapered weld profile which was widest near the weld cap. The predicted widths of the weld in EBW3 at the top and bottom of the specimen were 1.3 mm and 0.9 mm respectively. Hence the predicted average weld width of 1.1 mm matched experimental measurements presented in Section 3.5. The predicted widths of EBW4 were 1.4 mm and 1.1 mm at the top and bottom surfaces respectively. Therefore the predicted average width of 1.25 mm also agreed with the 1.3 mm experimentally measured width.

4.5 MECHANICAL ANALYSIS

4.5.1 MODEL DESCRIPTION

Following the thermal analysis, the temperatures during welding were transferred to mechanical models of specimens EBW3, EBW4 and EBW5. The analyses determined the thermal expansion and contraction of different regions of the specimens during welding. This caused plastic deformation near the weld and the misfit of this plastic region within the specimen induced residual stresses. The manufacture of C(T) specimens from the welded

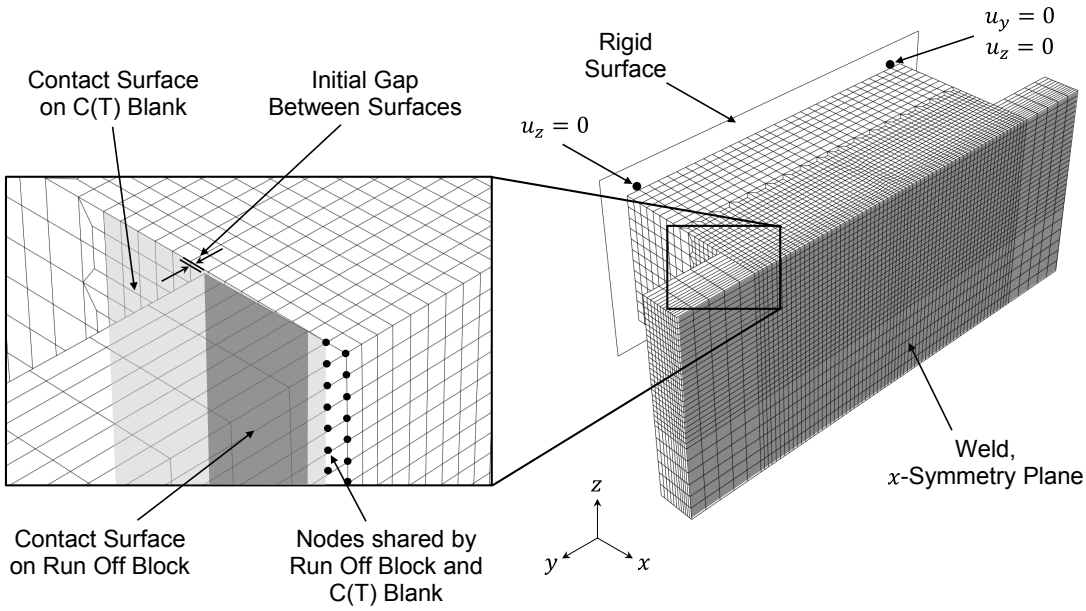


Figure 4.6 Mechanical model of the EB weld specimen

blocks were modelled by the removal of elements from the analysis and mapping the solution to a mesh of the C(T) specimen.

The FE model used in the mechanical weld simulation is shown in Figure 4.6. Models of specimen EBW3 and EBW4 had a width of 30 mm whereas the model of EBW5 had a width of 31.25 mm. These models consisted of 58,325 and 59,305 3D quadratic reduced integration hexahedral elements (ABAQUS type C3D20R) and 73,513 and 74,751 nodes respectively. The elements near the weld plane had dimensions of approximately 1.0 × 1.0 × 0.5 mm^3 with the smallest dimension in transverse, x, direction.

Rigid surfaces, which were fixed in position, restrained the specimens in the transverse, x, direction of the weld to model the clamps. Additional boundary conditions were applied to the specimens to prevent rigid body motion. The models were free to expand in the longitudinal and normal directions. The C(T) blanks and sacrificial blocks were assumed to be attached by the EB welds from the beginning of the analyses by defining common nodes between these parts as indicated in Figure 4.6. Elsewhere small gaps of 1 µm were modelled between the contacting surfaces and normal contact behaviour was defined which allowed these surfaces to move in and out of contact during the analyses. Sensitivity studies on modelling the gaps between these contacting surfaces were performed by Vlamis [95], which show the tack welds performed prior to welding did not need to be included in the models.

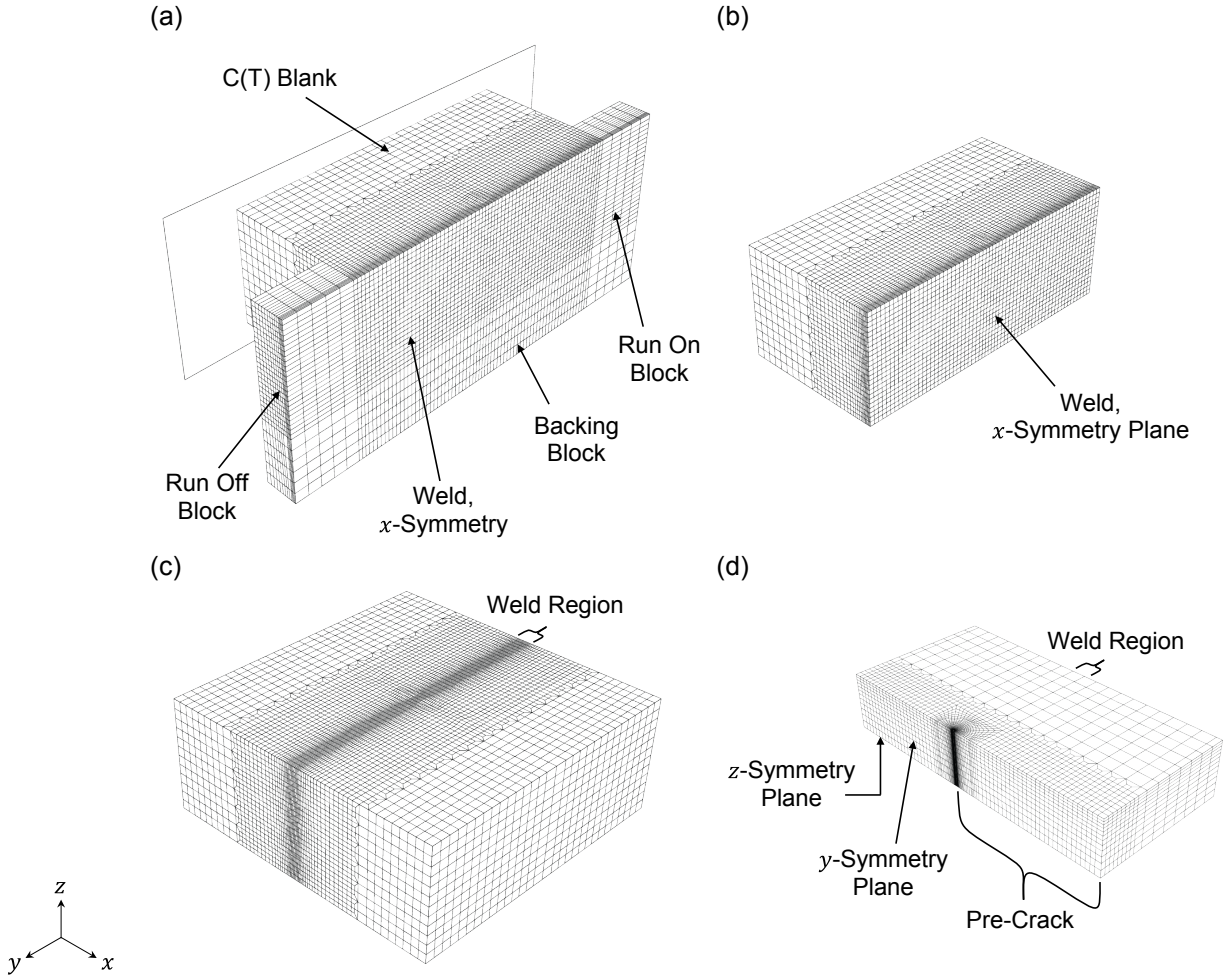


Figure 4.7 Mechanical models used to simulate fabrication of the EB welded C(T) specimen: (a) half model of EB welded specimen, (b) half model of C(T) blank, (c) full model of C(T) blank and (d) quarter model of C(T) specimen

Temperatures from the thermal simulation were transferred to the mechanical analyses which determined the deformation and stresses of the specimens during welding. After cooling to room temperature the clamps were removed from the analyses to remove any restraint on the specimens. The meshes in the mechanical simulations were course relative to the thermal simulations as these analyses were computationally expensive and less elements had to be used to ensure the analyses run times were reasonably low. Due to this, the nodal positions between the thermal and mechanical simulations did not coincide and ABAQUS interpolated the temperatures between the meshes.

Post weld machining was modelled in two stages. Elements were deleted from the analysis to remove the run on, run off and backing blocks to create the C(T) blank geometry. These regions were removed in the sequence of the cutting process however in a similar

model developed by Muránsky et al. [97] it was found that the cutting process did not induce plasticity and therefore was independent of the order of removal. The half model of the C(T) blank is shown in Figure 4.7(b).

The solution was then mirrored about the symmetry plane to create a full model of the C(T) blank (Figure 4.7(c)). This allowed the solution to be mapped to a new mesh of the C(T) specimen, as shown in Figure 4.7(d). Both the mirroring and mapping processes transferred the stresses and hardening history of the material. After each of these analysis steps, the stresses were allowed to redistribute to reach equilibrium.

The analyses were executed with the non-linear geometry option in ABAQUS turned on such that the problem was solved using large strain deformation theory. Furthermore the *CONTROLS, ANALYSIS=DISCONTINUOUS parameter was set to improve efficiency of the analysis which was discontinuous as different regions came in to and out of contact during the analysis [49]. The computational time required for the mechanical analysis of EBW5 was 95 h using eight cores. The analysis with two weld passes took 145 h with eight cores.

4.5.2 MATERIAL MODEL

Temperature dependant elastic material constants are shown in Table 4.5 [6], where α is the thermal expansion coefficient. Plasticity was defined using a mixed isotropic-kinematic hardening law as recommended in R6 Section III.15 [27]. During welding the HAZ experienced cyclic loading, as shown in Section 3.2, and therefore kinematic hardening was required to describe the reduction in σ_y due to the Bauschinger effect [5, p110]. Isotropic hardening described the increase in σ_y between each load cycle, this was important for modelling EBW4 which had multiple weld passes.

The stress-strain response was modelled using the Lemaitre and Chaboche formulation in ABAQUS [49]. Material constants for this hardening law have been found for numerous variants of Type 316 steels and have been published in literature [6, 96, 97, 102]. Cyclic uniaxial tensile tests at various temperatures were performed on ex-service Type 316H stainless steel (2D1/3 cast 69431) as part of the VORSAC European project [103]. This test data was used to determine the constants for the Lemaitre-Chaboche model in the NeT TG1 project for Type 316L stainless steel parent material [96]. Through sensitivity studies it was found that fitting the first half cycle of the model's stress-strain curve to monotonic tensile test data provided the most accurate stress predictions in weld simulations.

Table 4.5 Elastic properties for Type 316H stainless steel [6, 32]

T (°C)	E (GPa)	v	α (× 10^{-6} 1/°C)
20	195.6		14.56
100	191.2		15.39
200	1857		16.21
300	179.6		16.86
400	172.6		17.37
500	164.5		17.78
600	155.0	0.294	18.12
700	144.1	(Assumed temperature	18.43
800	131.4	independent)	18.72
900	116.8		18.99
1,000	100.0		19.27
1,100	80.0		19.53
1,200	57.0		19.79
1,300	30.0		20.02
1,400	2.0		20.21

Furthermore two pairs of C and γ constants were sufficient to accurately describe the non-linear kinematic hardening law [104]. This hardening model has been modified for other Type 316 stainless steels in similar weld modelling studies [6, 97, 102]. Using fitting guidelines developed by EDF Energy [105], the magnitude of the 1% proof stress in the first stress-strain loop predicted by the model is scaled to fit the 1% proof stress obtained from monotonic tensile tests for different Type 316 stainless steels.

Specimens EBW3 and EBW4 were made of Type 316H stainless steel in the as-received condition which was obtained from ex-service steam headers from cast 55882. This was the same cast of material used the edge welded beam study [6]. Therefore, the same constants were used for the Lemaitre-Chaboche model, which are shown in Table 2.1. The mechanical simulations in the edge welded beam study [6] show excellent residual stress predictions in comparison to the experimental measurements providing confidence the hardening model, for Type 316H stainless steel in the as-received condition, correctly predicts material behaviour.

For specimen EBW5, the hardening model was fitted using the fitting guidelines developed by EDF Energy [105]. The magnitude of the cyclic stress-strain curve defined by the Lemaitre-Chaboche model in [96] was scaled to match the 1% proof stress of the 8% pre-compressed Type 316H stainless steel, as determined from monotonic tensile tests in [79]. Therefore it was assumed the cyclic hardening behaviour of the 8% pre-compressed material was the same as the cyclic behaviour of material in the as-received condition. These constants are shown in Table 4.6.

Table 4.6 Constants for the Lemaitre-Chaboche formulation of the mixed hardening model for Type 316H stainless steel in the 8% pre-compressed condition

T (°C)	$\sigma\|_0$ (MPa)	C_{LC1} (MPa)	γ_1	C_{LC2} (MPa)	γ_2	Q_∞ (MPa)	b
20	270.2	156,435.0	1,410.85	6,134.0	47.19	8.8	6.9
275	235.1	100,631.0	1,410.85	5,568.0	47.19	36.7	6.9
550	208.6	64,341.0	1,410.85	5,227.0	47.19	51.1	6.9
750	165.9	56,232.0	1,410.85	4,108.0	47.19	0.0	6.9
900	170.9	49,588.0	1,410.85	292.1	47.19	0.0	6.9
1,000	82.2	0.0	1,410.85	0.0	47.19	0.0	6.9
1,100	50.9	0.0	1,410.85	0.0	47.19	0.0	6.9
1,400	5.5	0.0	1,410.85	0.0	47.19	0.0	6.9

Monotonic stress-strain data for Type 316H in the as-received and pre-compressed material conditions are shown in Figure 4.8 and were obtained from [32] and [18, 79] respectively. Data are shown at room temperature and at 550°C. Figure 4.8 also shows the stress-strain curves predicted by the Lemaitre-Chaboche hardening models for a strain range of ± 0.05 mm/mm which is a typical strain experienced by the HAZ during welding. The first loop of the models closely match the monotonic data.

During the weld process, as the material's temperature approached its melting point, recrystallisation occurred and any accumulated inelastic strain was relieved. In the mechanical simulation, a two stage annealing model was implemented where strain accumulation ceased at 800°C and prior work hardening was removed at 1,300°C. This approach was the same as that used in [6, 96, 97, 102]. This two stage approach stops abrupt changes in accumulated plasticity near the fusion zone in the simulation and results in more representative stress distributions [104]. The annealing model is implemented using a *UHARD subroutine coded in FORTRAN [106].

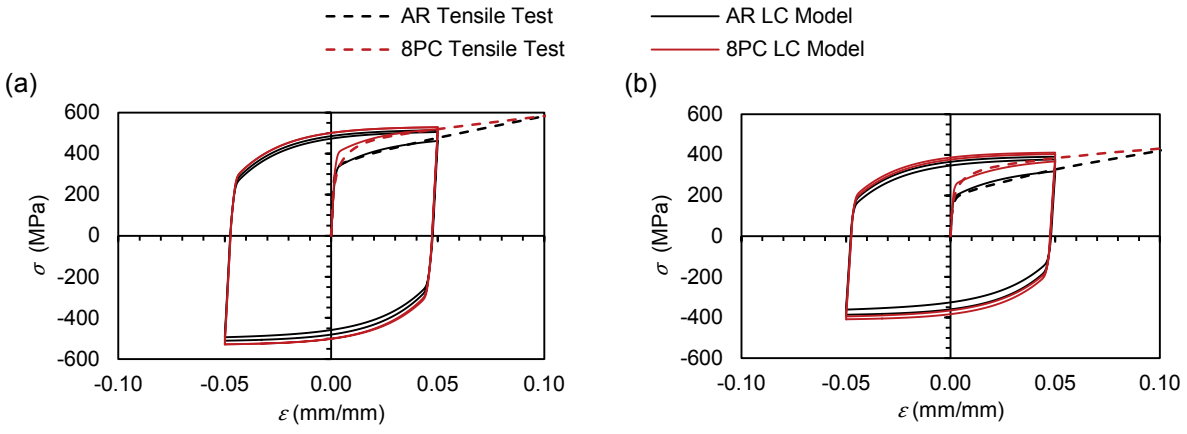


Figure 4.8 Lemaitre-Chaboche (LC) model fitted to monotonic uniaxial tensile test data for Type 316H in as-received (AR) and 8% pre-compressed (8PC) material conditions at (a) room temperature and (b) 550°C

4.5.3 COMPARISON OF FE WITH ND STRAIN MEASUREMENTS

Residual strains were measured in specimens EBW3, EBW4 and EBW5 using ND at various stages of manufacturing. The strains after EB welding and machining into C(T) blanks, along lines AB and CD identified in Figure 3.10, are compared to predictions from the FE simulations in Figure 4.9. Residual strains were used to validate the FE models instead of stresses as this removes the uncertainty associated with the elastic constants for the crystallographic planes [59, p204]. However this approach assumes the elastic response of the $\{311\}$ crystallographic plane is representative of that of the bulk material. The Young's modulus, E, of the bulk material is 195.6 GPa [32] whereas for the $\{311\}$ plane, E varies from 138.3 GPa to 225.5 GPa as shown in Table 2.5 based on various assumptions used to derive the constants. The Kröner model is considered to give the most accurate elastic constants (E = 183.5 GPa) [59, pp222-230]. Due to this, it is considered comparison of the residual strains in the $\{311\}$ plane measured by ND to those in the FE model, which uses bulk material properties, may introduce errors which could be ≈ 6% in this case.

Figure 4.9(a), (b) and (d) shows residual strains in the specimens after EB welding. Predictions of strain components ε_{xx}^{e} and ε_{zz}^{e} in the transverse and normal directions to the weld closely matched experimental measurements for all specimens. In the longitudinal, y, direction, the FE model accurately predicted the magnitude of the tensile strain, ε_{yy}^{e}, up to a distance of 6 mm from the weld centre. However at further distances from the weld the simulations predicted larger compressive strains in comparison to the ND measurements.

The residual strains measured in the C(T) blanks made from EBW4 and EBW5, i.e. after the sacrificial blocks were removed, are compared to FE predictions in Figure 4.9(c) and Figure 4.9(e). The FE predictions were generally in close agreement with the ND measurements. Once these blocks in EBW4 were machined away the compressive longitudinal strains experimentally measured increased in magnitude, as seen by comparison of Figure 4.9(b) and (c). Despite the longitudinal strains measured in the as-welded specimen not matching the FE predictions, once the sacrificial blocks were removed, the strains in the C(T) blank redistributed to become close to the FE predictions. Similarly the longitudinal compressive strains, ε_{yy}, in the EBW5 C(T) blank increased in magnitude from the as-welded specimen, shown in Figure 4.9(d) and (e). However the magnitudes of the compressive strains experimentally measured in the EBW5 C(T) blank remained less than those predicted by the corresponding FE analysis. Reasons for the difference in residual

strain between the FE model of the as-welded specimens and ND measurements are discussed in Section 4.6.

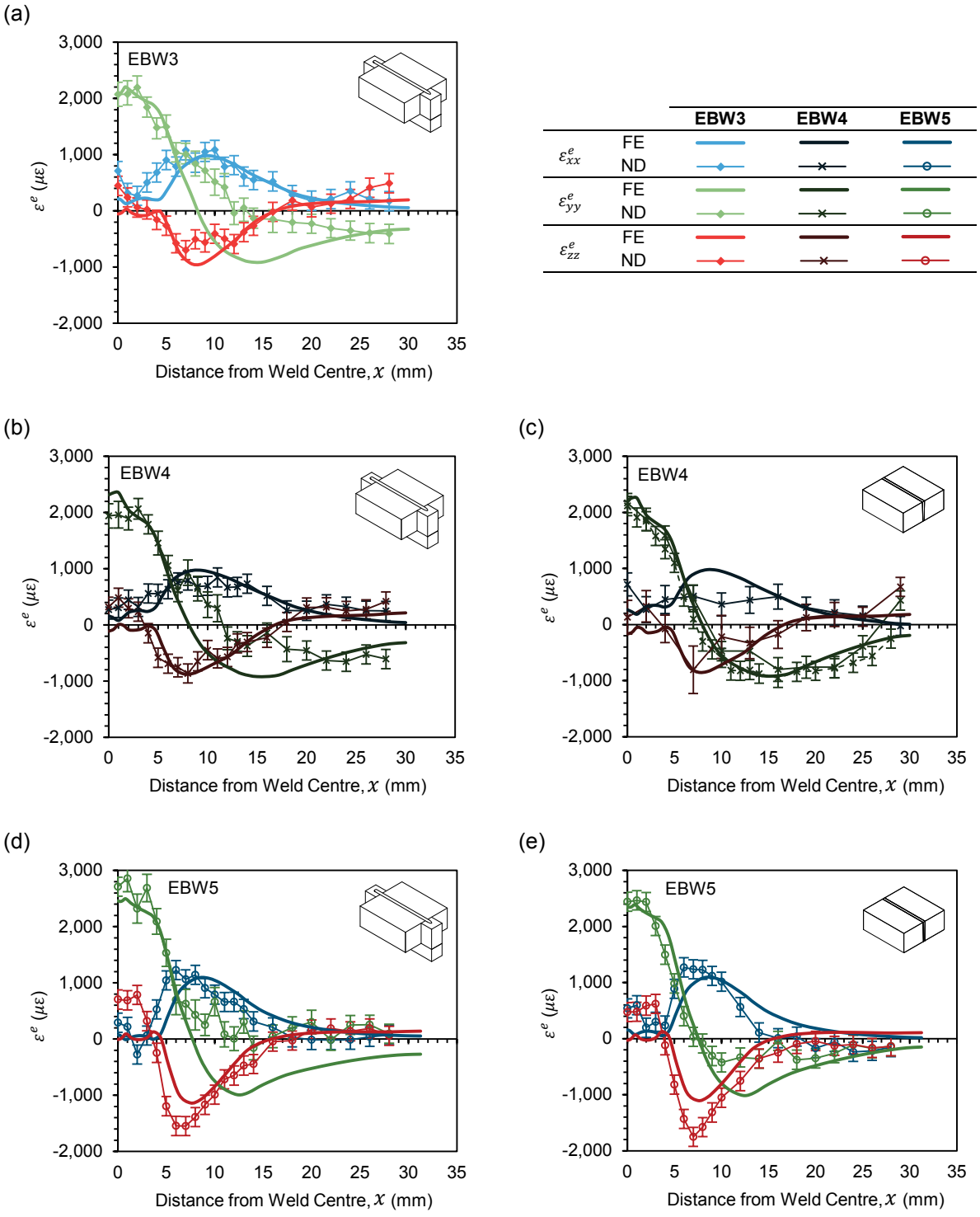


Figure 4.9 Comparison of residual strains predicted by FE analyses to ND measurements (a) EBW3 – as-welded, (b) EBW4 – as-welded, (c) EBW4 – C(T) blank, (d) EBW5 – as-weld and (e) EBW5 – C(T) blank

The strains measured following insertion of a pre-crack 3.0 mm beyond the centre of the weld in EBW3 and EBW5 are shown in Figure 4.10. In general, the FE predictions of residual strains closely matched ND measurements in specimen EBW3. Although, close to the pre-crack the experimentally determined strains were up to 600 $\mu\varepsilon$ less than the FE predictions. Large strain gradients existed near the crack tip caused by the stress concentration effect of the pre-crack, which are shown by the FE predictions. The strains measured by ND were dependent on where the randomly sampled grains within the gauge volume were located. The strains may have been measured in grains which had a relatively low stress magnitude in the gauge volume which would account for the difference in predicted and measured residual strains near the pre-crack. Furthermore with the ND technique, the closest measurement point to the pre-crack was 1.0 mm from the crack tip and therefore the peak strains at the crack tip could not be measured experimentally.

In specimen EBW5 the residual strains were measured along two measurement lines as shown in Figure 3.10(c). Line EF was located at mid-thickness of the specimen and line GH at quarter thickness which was on the side of the specimen closest to the weld cap. The longitudinal residual strains, ε_{yy}, predicted by FE were in good agreement with ND

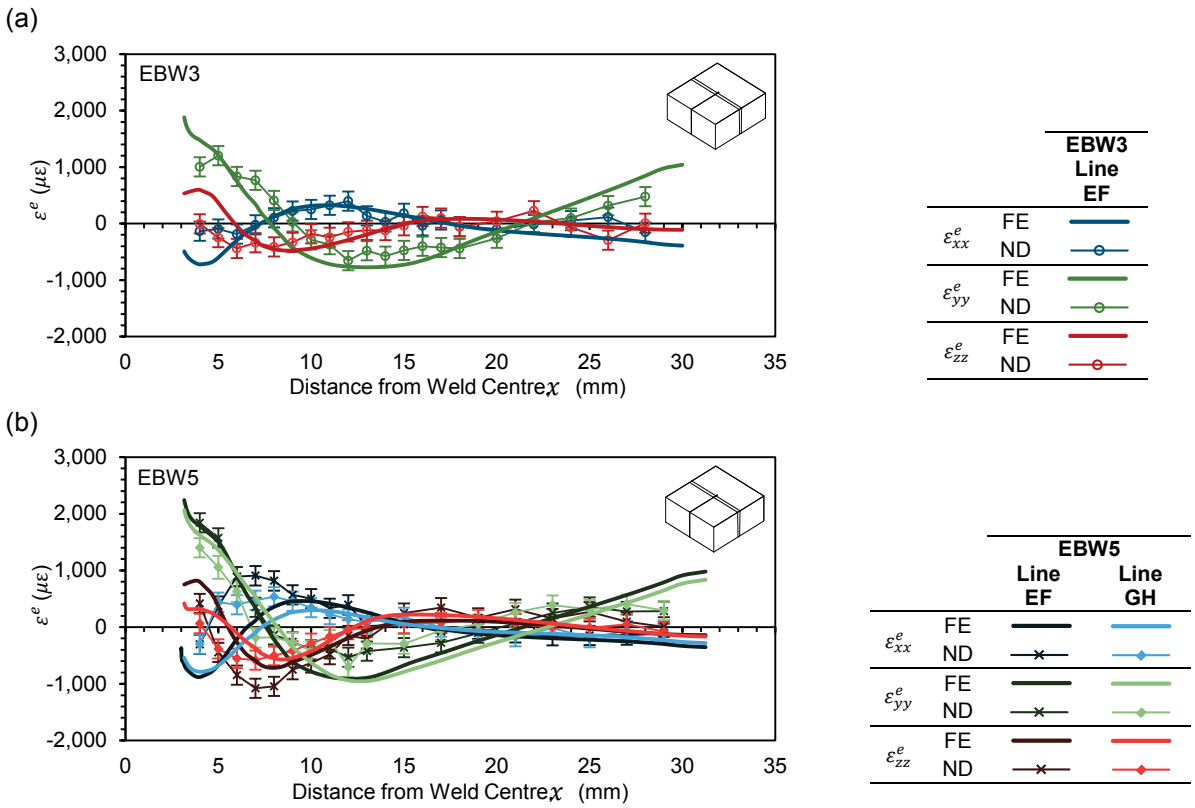


Figure 4.10 Comparison of residual strains predicted by FE analyses to ND measurements in C(T) specimens (a) EBW3 along line EF and (b) EBW5 along lines EF and GH

measurements especially near the pre-crack. Larger differences of up to 1,000 $\mu\varepsilon$ existed for the strain components in the transverse, ε_{xx}, and normal, ε_{zz}, direction to the weld up to 10 mm from the weld line.

4.5.4 COMPARISON OF LONGITUDINAL STRESSES WITH EXPERIMENTAL MEASUREMENTS

Three different residual stress measurement techniques were used to measure the longitudinal component of weld residual stresses in the C(T) blank machined from EBW4 as shown in Figure 3.31. These are compared to FE predictions in Figure 4.11, where the longitudinal stresses were extracted from a path at mid-thickness of the specimen in Figure 4.11(a) and were averaged through the thickness of component in Figure 4.11(b). The thickness averaged stresses permits comparison with the stresses determined from slitting.

The longitudinal stresses, σ_{yy}, predicted by the FE model were in very close agreement with the ND measurements whilst the through thickness averaged stresses closely matched those measured by slitting. However the tensile stresses near the weld measured by the contour method, at mid-thickness, were less than ND and FE predictions.

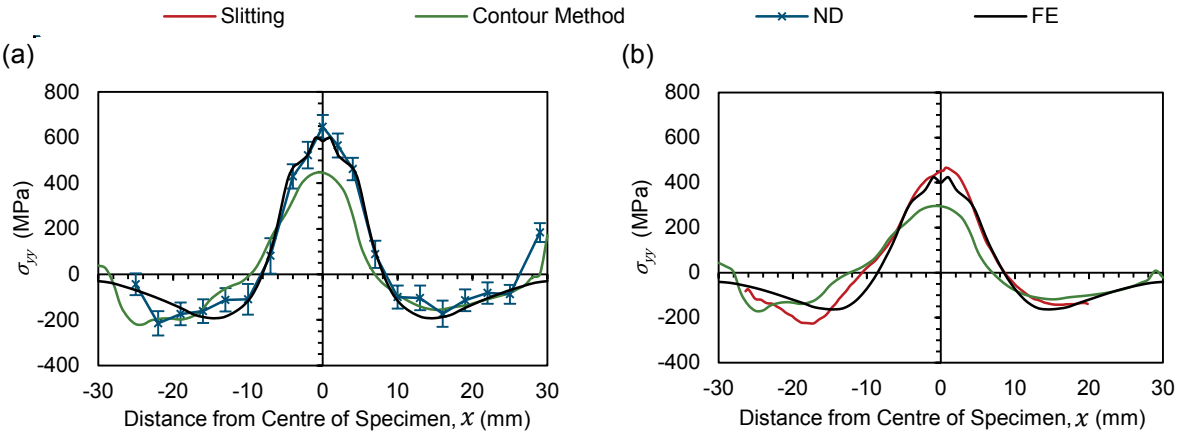


Figure 4.11 Comparison of longitudinal weld residual stress measurements in the C(T) blank made from EBW4 with FE predictions (a) at mid-thickness and (b) averaged across thickness

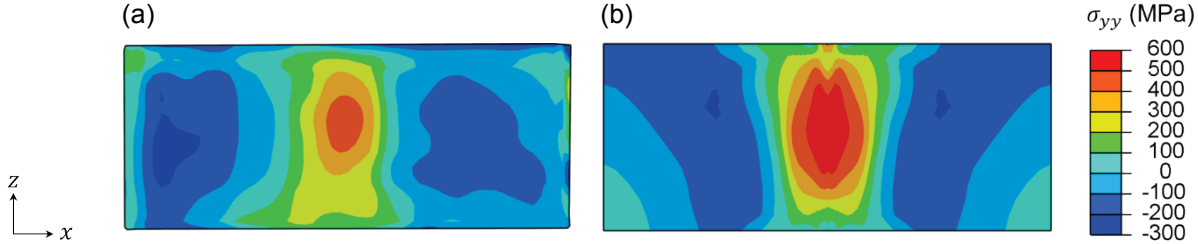


Figure 4.12 Contour plots of longitudinal weld residual stress, σ_{yy}, in C(T) blank made from EBW4 (a) measured by the contour method and (b) predicted by weld simulation

Differences in σ_{yy} were also observed between contour plots measured by the contour method and predicted by the FE weld simulation, as shown in Figure 4.12. Both showed a tensile region in the centre of the specimen near the weld which was surrounded by compressive stresses in the parent material. The contours showing the regions above 200 MPa were approximately the same size however the FE model predicted a small region of very high stress around the weld which was not measured using the contour method. Due to the large stresses near the weld and the non-ideal clamping arrangement, the deformation near the weld may not have been elastic causing errors in the contour method. At mid-thickness the FE predictions of compressive stress were in very good agreement with the contour method as also shown in Figure 4.11 and Figure 4.12. However near the edges of the specimen the compressive stresses measured by the contour method were less than the FE predictions, as shown in Figure 4.12. Errors can arise in contour measurements near the edges of a specimen due to local deformation during cutting [60, pp130-131].

4.6 DISCUSSION

The thermal simulations of the weld process were validated by comparison of temperature predictions with in-situ thermocouple measurements and fusion boundary profiles which were in excellent agreement. The efficiency of the welding process was predicted to be 95% which closely matched efficiencies published in literature. This provided confidence of the accuracy of the thermal simulations.

Mechanical models in weld simulations are sensitive to the material model used to describe the hardening behaviour of the material. Similar weld modelling studies have shown that the mixed isotropic-kinematic hardening model provides the most accurate residual stress solutions for Type 316H stainless steels. The Lemaitre-Chaboche formulation of this hardening model was developed for Type 316L stainless steel as part of the NeT TG1 bead on plate project [96] and was modified for use with Type 316H stainless steel in the as-received and pre-compressed material conditions.

The residual stresses predicted by the mechanical models were compared to residual stress measurements made by ND, slitting and the contour method. In general the residual stresses predicted by the FE models of EBW3 and EBW4, which were made with material in the as-received condition, closely matched the experimental data. However the compressive strains in the as-welded configuration predicted by the model were larger than those measured by ND. It is considered that the constraint on the welded specimen by the

sacrificial blocks was not captured in the simulation, as once these blocks were removed to create the model of the C(T) blank the residual strain predictions closely matched the experimental data.

The effect of constraint on the welded specimen was investigated further with sensitivity studies by Vlamis [95]. The sacrificial blocks were tack welded at point locations prior to EB welding to hold the assembly in place. The constraint from these tack welds was modelled in detail by Vlamis however the residual stresses were found to be insensitive to the presence of these tack welds. In the mechanical model it was assumed that the sacrificial blocks were attached to the C(T) blank throughout the analysis by sharing common nodes. It is considered that this assumption provided an additional constraint that caused the difference in stresses between the FE predictions and ND measurements for the as-welded specimens. As the effect of this additional constraint was not present in the final C(T) specimen configuration, the interaction between the sacrificial blocks and the C(T) blank during welding was not considered further in this study.

A mechanical model of the weld specimen EBW5 was developed using material properties for Type 316H pre-compressed to 8% plastic strain. Comparisons of residual strain predictions with ND measurements have generally shown good agreement. The magnitude of the strains increased in comparison to the specimens made from material in the as-received condition. This result was expected as the pre-compressed material had increased yield strength due to work hardening. However, in some regions of the specimen there were differences between the FE models and ND measurements. Up to 10 mm from the weld, the transverse, ε_{xx}^{e}, and normal, ε_{zz}^{e}, strain components measured using ND in the C(T) specimen were up to 1,000 $\mu\varepsilon$ greater in magnitude in comparison to the FE predictions. This was consistent with comparisons of ε_{xx}^{e} and ε_{zz}^{e} in the C(T) blank over this region. Despite this, the longitudinal strains, ε_{yy}, predicted by the FE models were in very good agreement with ND measurements near the weld. The material data used to fit the Lemaitre-Chaboche hardening model was based on uniaxial tensile test data obtained in the direction of pre-compression. However the pre-compression process was anisotropic and therefore the material behaviour in the directions normal to pre-compression appeared to be different, which caused errors in the predictions of ε_{xx} and ε_{zz}. Overall the strain predictions in specimen EBW5 were considered to be sufficiently accurate to enable the models to be used for the subsequent crack growth simulations.

4.7 CRACK DRIVING FORCE DUE TO SECONDARY LOADS

4.7.1 REDISTRIBUTED STRESSES AT 550°C

CCG testing of the EB welded C(T) specimens was performed at 550°C. As the specimens were heated the material's yield strength decreased and as a result stress redistribution occurred. The experimental residual stress measurements were all performed at room temperature therefore the validated FE simulations were used to determine the stresses in the specimen at 550°C, which are presented in this section. The residual stress field in the EB welded C(T) specimens existed due to a misfit between the plastically deformed weld region and the parent material which remained elastic. Modifying the C(T) specimens to include pin holes and side grooves would cause the residual stresses to redistribute. The extent of stress redistribution due to these machining processes was investigated using the FE simulations.

The model of specimen EBW5 was used for this investigation which was made of Type 316H stainless steel in the pre-compressed material condition. The FE meshes used to model a quarter of the C(T) specimens with and without side grooves are shown in Figure 4.13. Both models had two planes of symmetry which were located at mid-thickness of the specimen and through the crack plane. Each side groove had a depth of 2.5 mm such that the net thickness of the specimen was reduced by 20% and the acuity of the side grooves were 60°. A focused mesh was used in the pre-crack region where the element

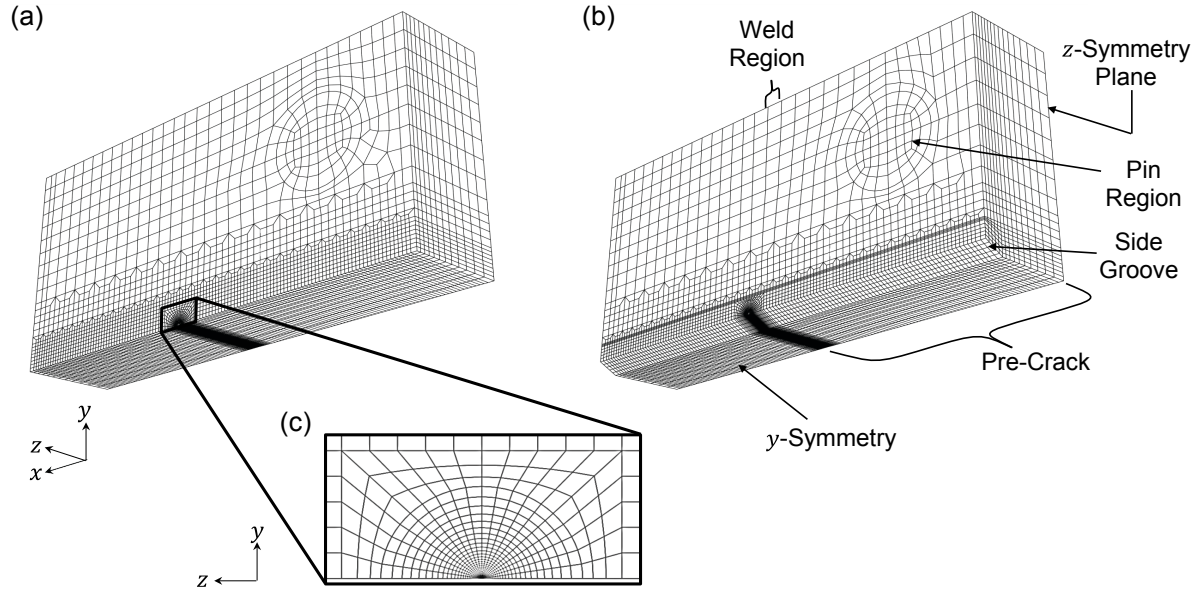


Figure 4.13 Mesh of EB welded C(T) specimen (a) without side groove, (b) with side groove and (c) focused mesh at crack tip

length was 5 μm at the crack tip. This mesh enabled contour integrals to be evaluated to determine K^s using the methods presented in Section 2.5. The contour integrals were evaluated over 35 contours up to 1.8 mm from the crack tip. The crack tip was meshed using 20 noded hexahedral elements which had collapsed sides such that the nodes along one side of the element were at the same location in the beginning of the analysis. As the crack mouth opened the nodes moved apart to model crack tip blunting.

Initially the y-symmetry boundary conditions were defined along the ligament of the specimens and on the crack faces to model C(T) blanks. The stresses and hardening history of the material from the weld simulation of specimen EBW5 were mapped to the models of the C(T) specimens and the stresses were allowed to redistribute to reach equilibrium. The pre-cracks were then inserted by removing the y-symmetry boundary conditions on the crack faces at room temperature and successively the elements in the pin hole were also removed. After each machining process was modelled, the temperature was increased to 550°C to allow the stress distributions at the beginning of a CCG test to be assessed.

Contour plots of the stress components in the crack plane and also at mid-thickness of the specimen are shown from Figure 4.14 to Figure 4.17 for various configurations of the C(T) specimen. The stresses are shown after the specimen was heated to 550°C where the stresses reduced in magnitude in comparison to those at room temperature. The stress components along line CD in the C(T) blank and line EF in the C(T) specimen, as defined in Figure 3.10, are shown in Figure 4.18 for the various configurations of the C(T) specimen.

Comparison of the stress components in the pre-cracked C(T) specimen (Figure 4.15) with the C(T) blank (Figure 4.14) show significant stress redistribution occurred during insertion of the pre-crack. In the crack plane the component σ_{xx} relaxed by up to 160 MPa throughout the ligament whereas there was very little change in σ_{zz}. In the component σ_{yy} stress redistribution was limited to the back face of the specimen and the region near the pre-crack where σ_{yy} reduced by up to 100 MPa.

The FE model predicted that the stress redistribution that occurred during machining of the pin holes was local to the holes and that the stresses along the crack plane were unaffected, as shown by comparison of Figure 4.15 and Figure 4.16. Machining of side-grooves into the specimens caused stress redistribution near the sides of the specimen however the stresses near mid-thickness remained unchanged as shown by comparison of Figure 4.16 and Figure 4.17, and in Figure 4.18.

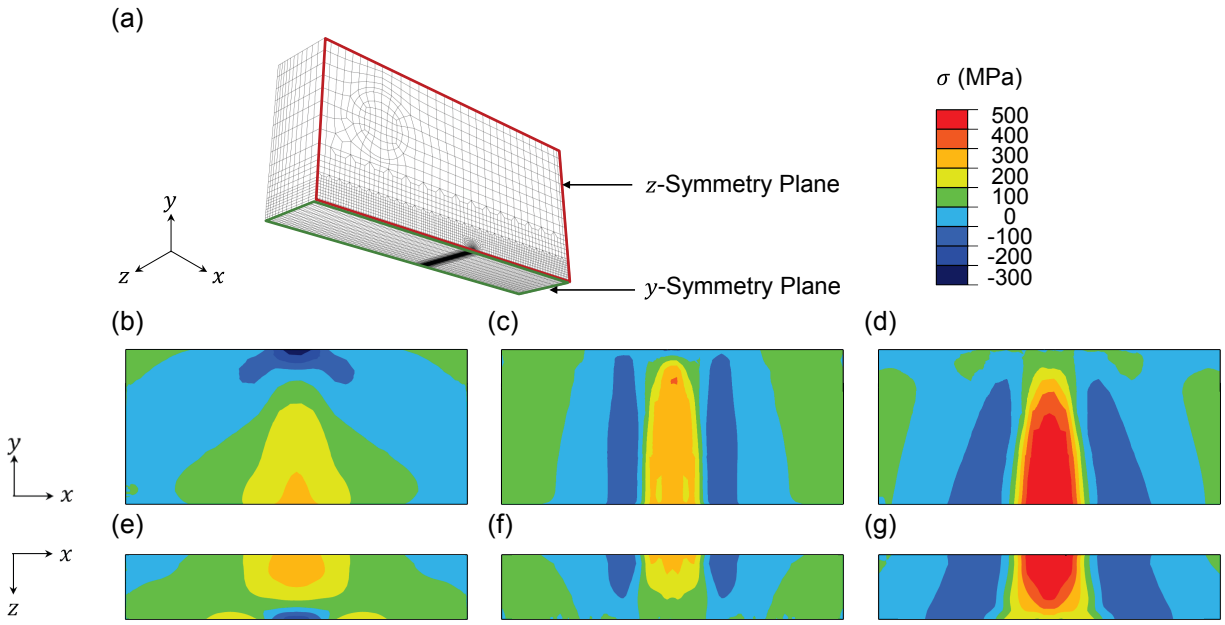


Figure 4.14 Stress components in EB welded C(T) blank at 550°C (a) FE model, (b) σ_{xx}, (c) σ_{yy} and (d) σ_{zz} on the z-symmetry plane, and (e) σ_{xx}, (f) σ_{yy} and (g) σ_{zz} on the y-symmetry plane

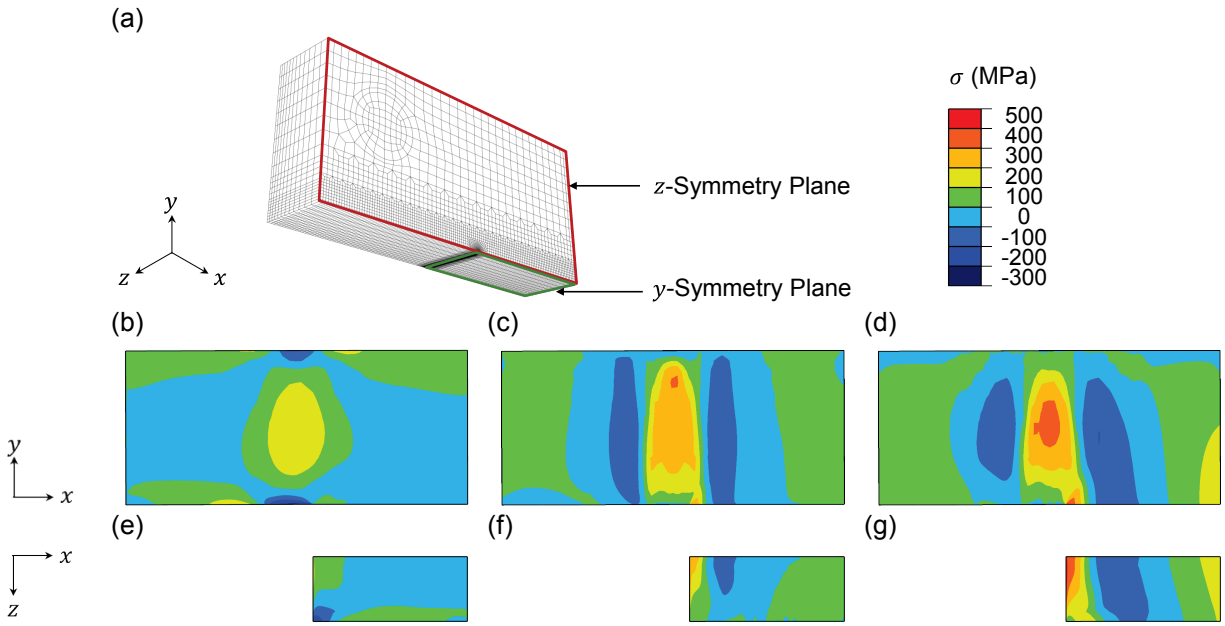


Figure 4.15 Stress components in EB welded C(T) specimen with pre-crack only at 550°C (a) FE model, (b) σ_{xx}, (c) σ_{yy} and (d) σ_{zz} on the z-symmetry plane, and (e) σ_{xx}, (f) σ_{yy} and (g) σ_{zz} on the y-symmetry plane

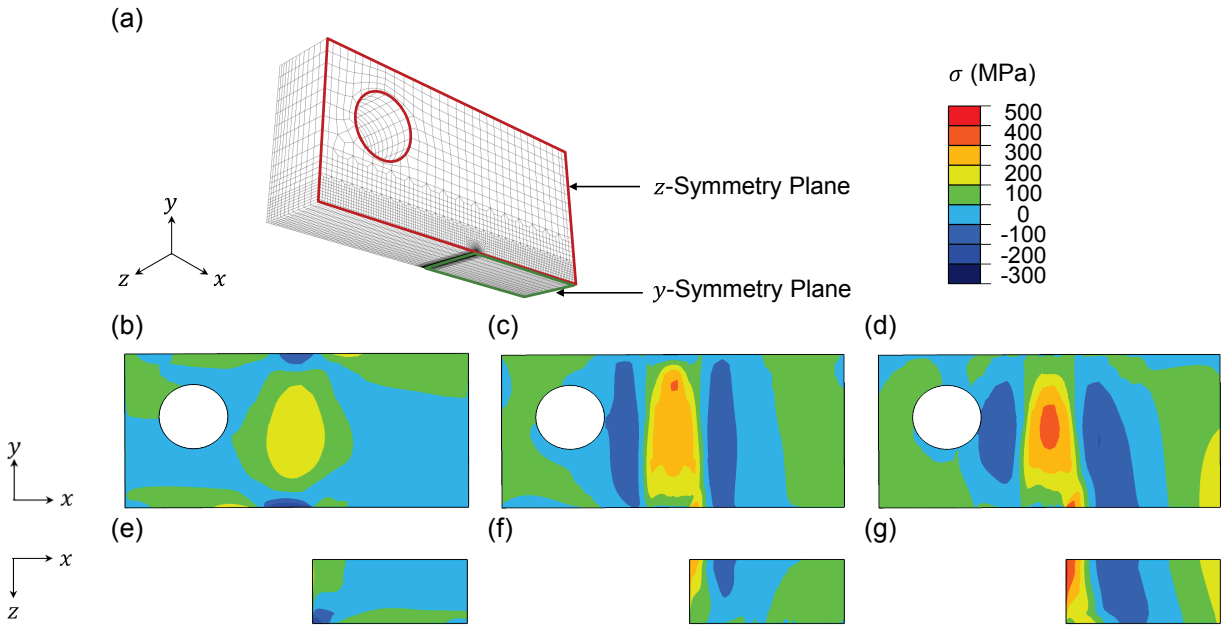


Figure 4.16 Stress components in EB welded C(T) specimen with pre-crack and pin holes at 550°C (a) FE model, (b) σ_{xx}, (c) σ_{yy} and (d) σ_{zz} on the z-symmetry plane, and (e) σ_{xx}, (f) σ_{yy} and (g) σ_{zz} on the y-symmetry plane

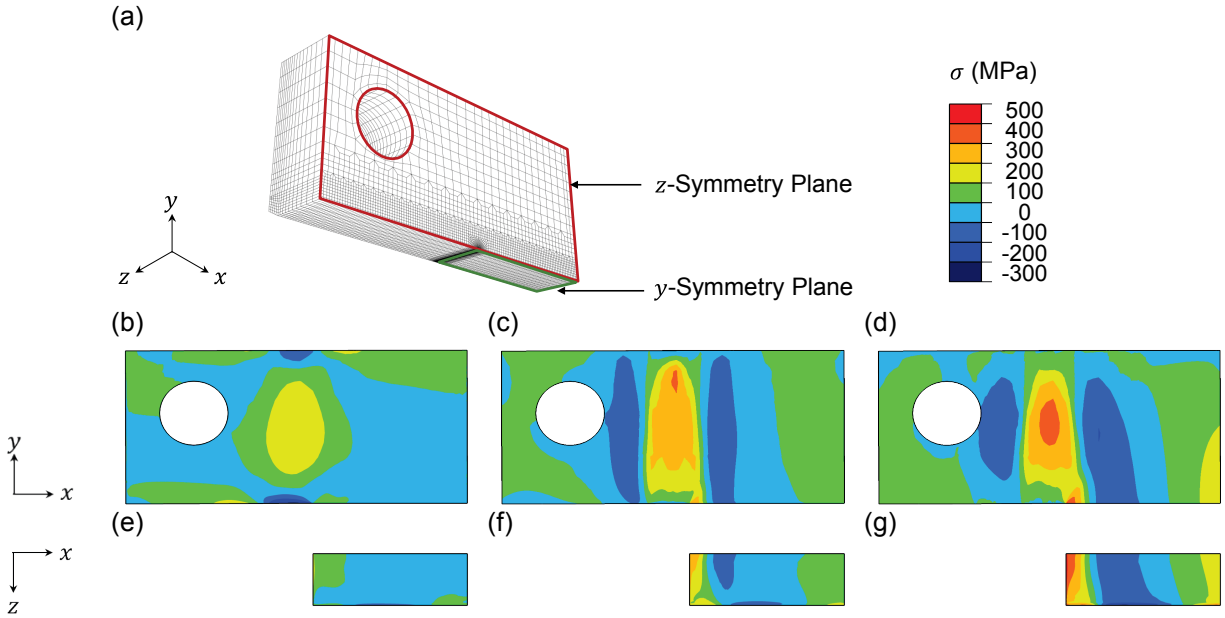


Figure 4.17 Stress components in EB welded C(T) specimen with pre-crack, pin holes and side grooves at 550°C (a) FE model, (b) σ_{xx}, (c) σ_{yy} and (d) σ_{zz} on the z-symmetry plane, and (e) σ_{xx}, (f) σ_{yy} and (g) σ_{zz} on the y-symmetry plane

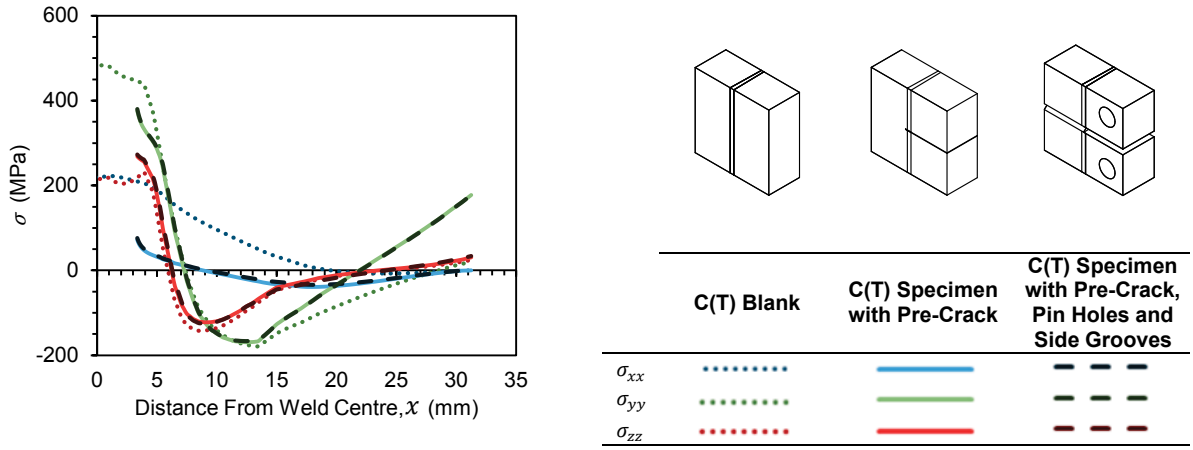


Figure 4.18 Stress components along line CD for the C(T) blank and line EF for the C(T) specimen at 550°C

The equivalent plastic strains ε^{pl} in the C(T) blank and the C(T) specimen from the FE model of EBW5, at mid-thickness of the crack plane, are shown in Figure 4.19. Large plastic strains were induced near the weld in the C(T) blank. The pre-crack extended across this plastic zone such that strains of up to 3% existed in the C(T) specimen.

Of all the machining operations considered, insertion of the pre-crack caused the most significant stress redistribution. The residual stresses in the C(T) blank were present due to the misfit of the plastically deformed region near the weld with the surrounding parent material. The pre-crack was cut to 3.0 mm beyond the centre of the weld which extended across the plastic zone, as shown in Figure 4.19. This reduced the influence of the misfit and relieved the residual stresses. Machining the pin holes and the side grooves did not affect the plastically deformed region in the specimen, hence the misfit and the residual stresses ahead of the pre-crack remained mostly unchanged.

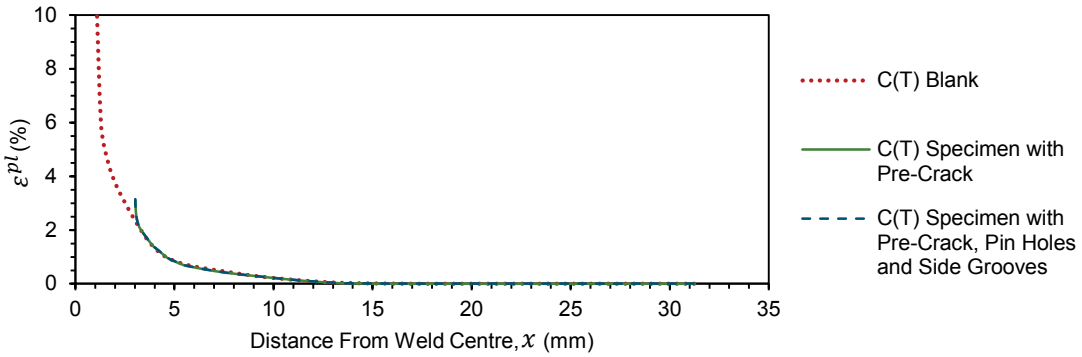


Figure 4.19 Equivalent plastic strain ε^{pl} along line CD for the C(T) blank and line EF for the C(T) specimen EBW5

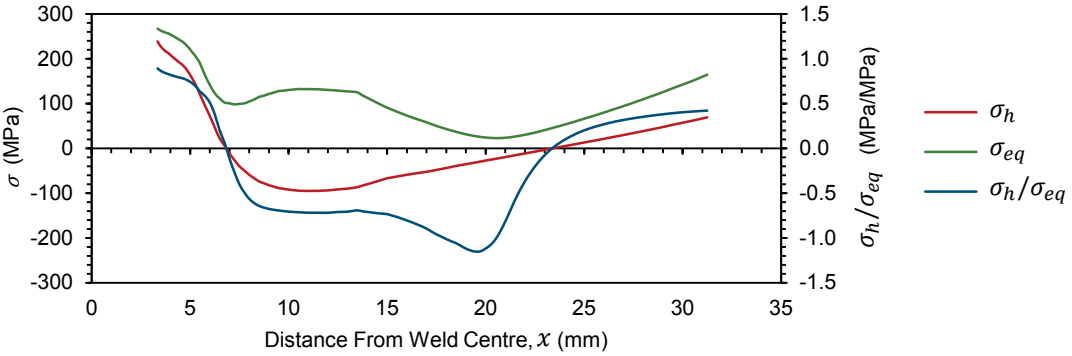


Figure 4.20 Hydrostatic stress, σ_h, equivalent stress, σ_{eq}, and triaxiality, σ_h/σ_{eq}, along line EF in C(T) specimen EBW5 at 550°C

CCG tests were performed under secondary loads on EBW5 which had a pre-crack only. Two tests were performed under combined loading conditions using EBW6 and EBW7 which had pin holes to allow application of a primary load. None of the specimens tested had side grooves. The hydrostatic stress, σ_h, equivalent stress, σ_{eq}, and triaxiality, σ_h/σ_{eq}, along line EF in EBW5, after heating to 550°C, are shown in Figure 4.20. The stresses were triaxial at the crack tip where σ_h/σ_{eq} = 0.9, which allowed stress components greater than σ_y to exist in the region as shown in Figure 4.19.

4.7.2 STRESS INTENSITY FACTOR

The crack driving forces from the residual stresses were quantified by the stress intensity factor, K^s, and was determined for EBW3 and EBW5 after heating to 550°C. The J-integral and superposition approaches were used to determine the variation of K^s through the thickness of these specimens. Both approaches are detailed in Section 2.5 and Appendix A shows a simple test model of an edge cracked plate to validate the implementation of these approaches in ABAQUS.

The J-integral solutions were evaluated using the quarter models of the C(T) specimen with focused meshes. The stresses and hardening history of the material from the weld simulation were transferred to the model of the C(T) specimen where symmetry boundary conditions were defined on two faces to model the C(T) blank, as shown in Figure 4.14(a). The y-symmetry boundary conditions on the crack face were removed to model insertion of the pre-crack, as shown in Figure 4.15(a). The y-symmetry boundary conditions were removed simultaneously on all crack face nodes, as recommended by Lei et al. [45]. This prevented plastic deformation at the crack face which would have reduced the accuracy of

the J contour integral analyses. For the evaluation of the J-integral to include the effects of the residual stress field using (2.44), the C(T) blank was defined as the initial state.

The J-integrals were evaluated at 25 node planes through the thickness of the model to allow the through thickness variation of J to be determined. The J-integrals for the contour domains through three of these planes for EBW5 are shown in Figure 4.21(b). The value of J tended towards constant values far from the crack tip and therefore path independence was achieved. Effective stress intensity factors, K_J^s, were determined from path independent values of J, using (2.45), and are shown through the thickness of the specimen in Figure 4.21(c). These were determined assuming plane strain conditions through the central region of the specimen and plane stress for the region up to 3.0 mm from the side face. At mid-thickness K_J^s = 22.2 MPam$^{1/2}$ whilst close to the side face K_J^s = 0.0 MPam$^{1/2}$ which was caused by compressive stresses on the crack face near the side wall. An average of K_J^s through the thickness of EBW5 was determined as 14.5 MPam$^{1/2}$.

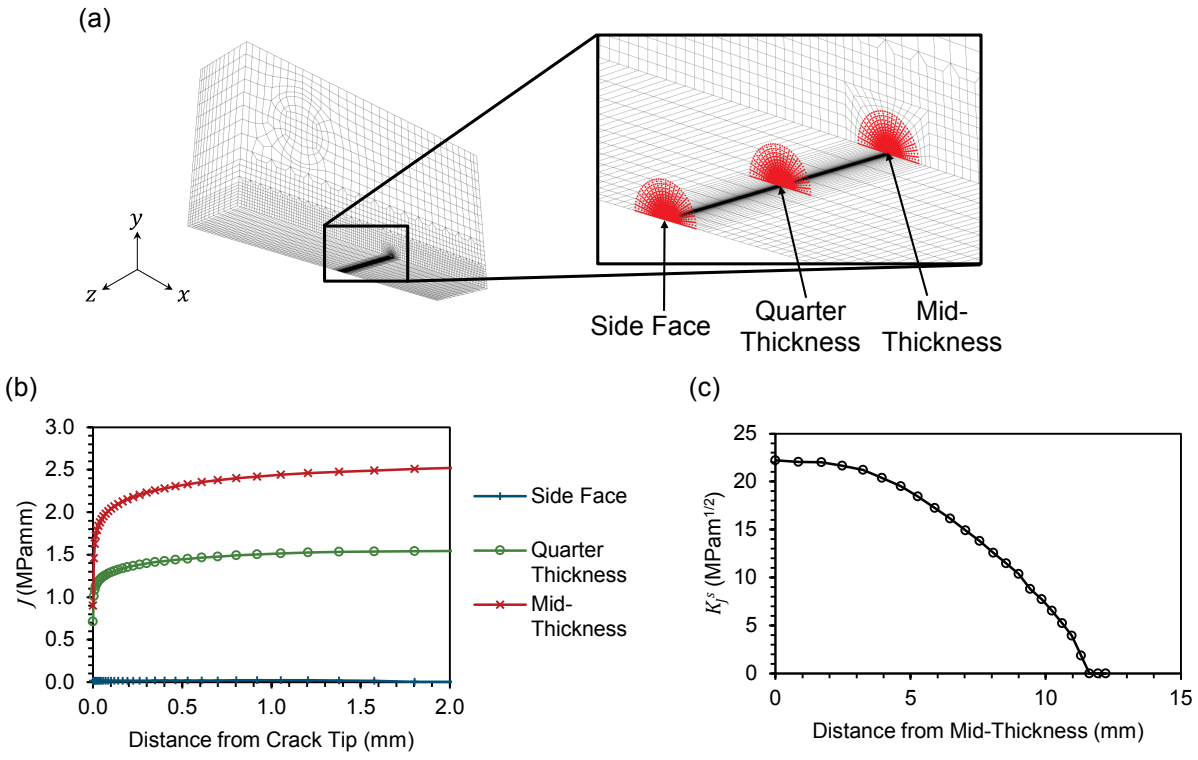


Figure 4.21 (a) Node regions for three contour integrals in C(T) specimen EBW5, (b) J-integral determined for the three node planes and (c) converged values of K_J^s across the thickness of the specimen

Using the superposition approach to determine K^s, the stresses, σ_{yy}, along the mid-plane of the EBW5 C(T) blank, modelled with elastic-plastic material properties and at 550°C, were applied to the crack face of another FE model of the C(T) specimen. The stresses at the surface integration points from the elastic-plastic model for EBW5 are shown in Figure 4.22. These stresses were used to define a distributed pressure load, on the crack face of a linear elastic model of the C(T) specimen at high temperature, using the DLOAD subroutine. ABAQUS was then used to compute K. The mesh was identical to that used for the J-integral analysis.

The values of K^s evaluated at three node planes, at mid-thickness, quarter thickness and the side face, are shown in Figure 4.23(a). Path independence was achieved at the second contour domain. The path independent values of K^s are shown across the thickness of the specimen in Figure 4.23(b). At mid-thickness K^s = 21.7 MPam$^{1/2}$ and decreased as the side face was approached. The average K through the thickness of EBW5 was 14.6 MPam$^{1/2}$.

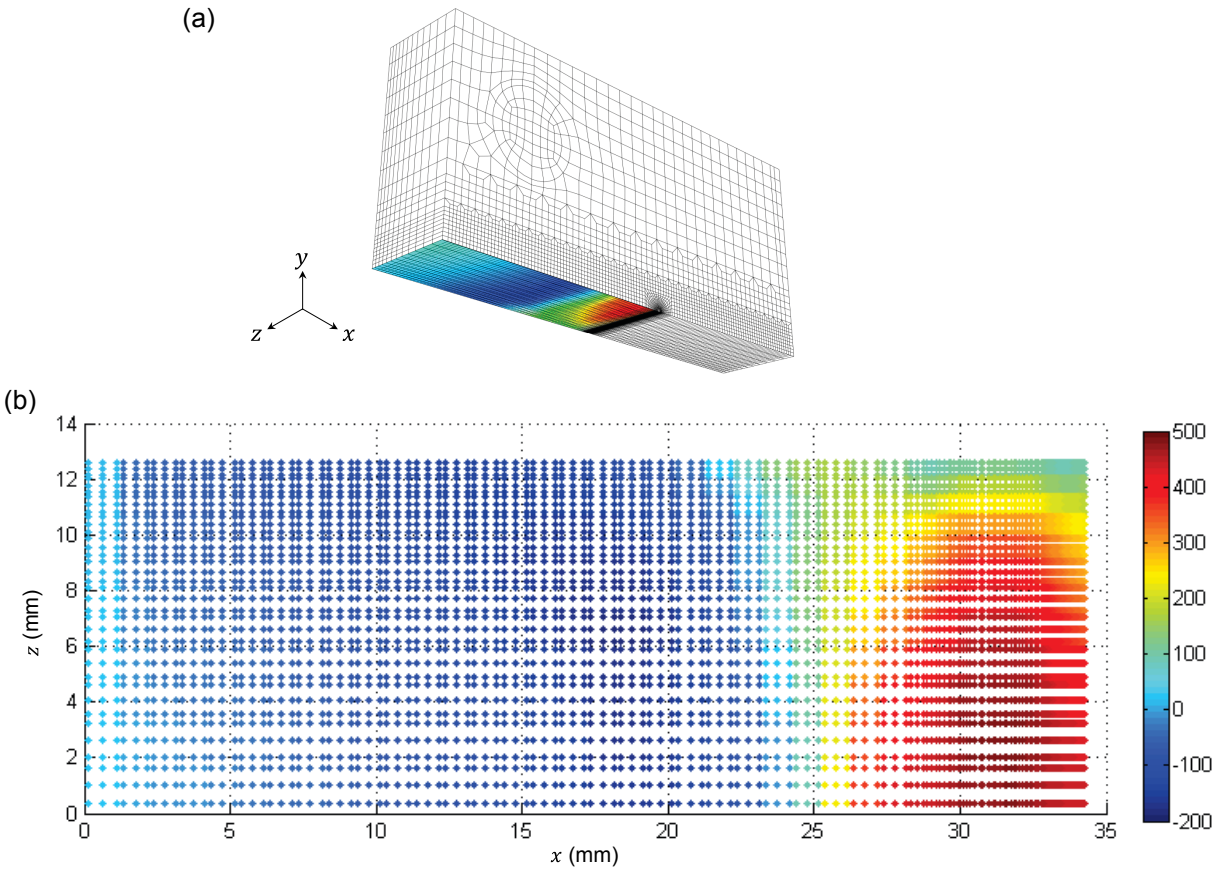


Figure 4.22 (a) The crack face region of the C(T) specimen EBW5 (b) the distributed pressure, in MPa, at the integration points on the crack face

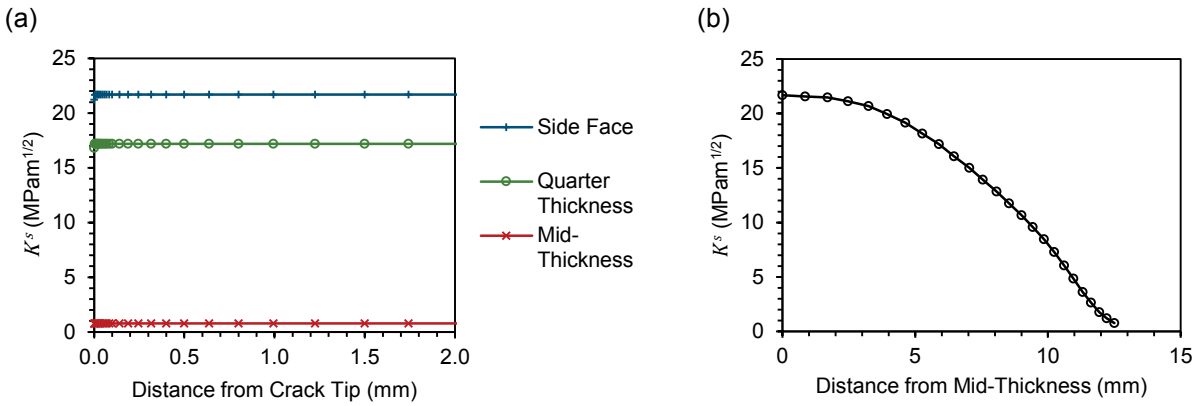


Figure 4.23 (a) K^s in C(T) specimen EBW5 through three node planes determined using the superposition method (b) K^s across the thickness of C(T) specimen EBW5

Comparisons of K^s determined from the two approaches for EBW5 are shown in Figure 4.24. The J-integral and the superposition methods predicted values of K^s at mid-thickness of 22.2 MPam$^{1/2}$ and 21.7 MPam$^{1/2}$ respectively which were in excellent agreement to each other. Both methods showed K^s reduced towards 0 MPam$^{1/2}$ at the side face of the specimen where the residual stress component σ_{yy} was close to zero.

The distribution of K_J^s through the thickness of the side-grooved C(T) specimen with pin holes was also determined using the J-integral approach for comparison with the plane sided specimen, which is shown in Figure 4.25. The value of K_J^s remained unchanged near mid-thickness of the specimen. Therefore there was no benefit to side-grooving EB welded C(T) specimens that were tested due to secondary loads only.

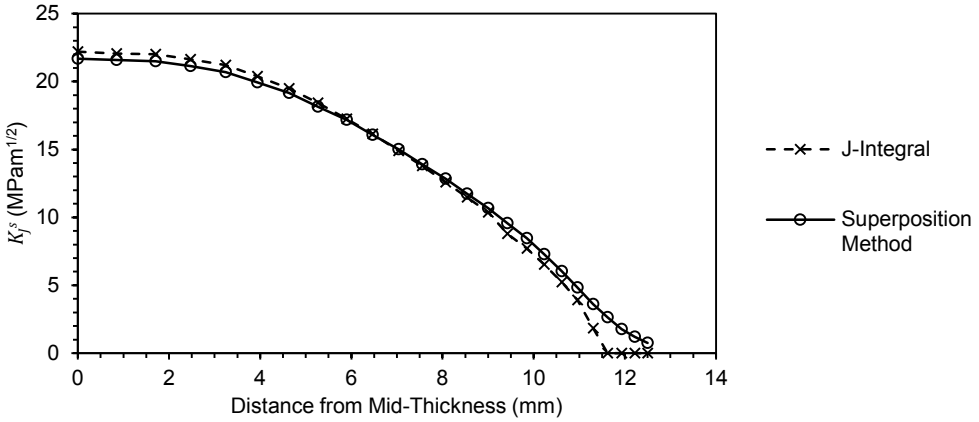


Figure 4.24 Comparison of stress intensity factors, K_J^s, determined by two different approaches for C(T) specimen EBW5 at 550°C

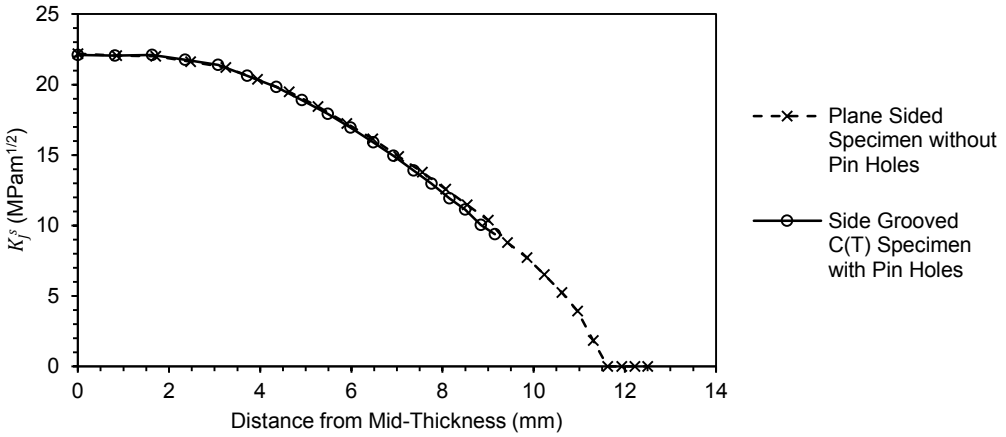


Figure 4.25 Comparison of stress intensity factors, K_J^S, determined for two EB welded C(T) specimen configurations at 550°C

The stress intensity factor K_J^S was determined for C(T) specimen EBW3 using the J-integral approach and is shown in Figure 4.26. As the residual stresses in EBW3 were less than EBW5, K_J^S was also smaller. In EBW3, at mid-thickness K_J^S = 16.0 MPam$^{1/2}$ whilst the average through the thickness of the specimen was determined as 9.3 MPam$^{1/2}$.

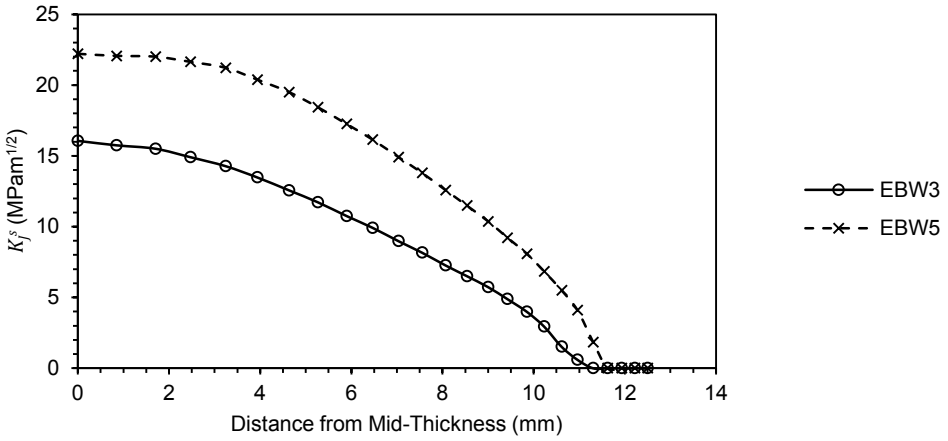


Figure 4.26 Comparison of stress intensity factors, K_J^S, determined for C(T) specimens EBW3 and EBW5 at 550°C

4.8 SUMMARY

Simulations of the generation of residual stresses in the welded blocks were developed using the recently published weld modelling guidelines in the R6 fracture assessment procedure [27]. Although the guidelines were not written specifically for EB welding, the advice was mostly relevant for this application. In some respects the model was simpler than conventional welding processes such as MMA welds as few weld passes were

performed and no filler metal was used. However the heat flux from the EB had high intensity and as a result great demands were placed on mesh dimensions to accurately model the heat input.

The residual stress and strain measurements for the EB weld specimens made from material in the as-received condition were in excellent agreement with FE predictions to validate the models. Residual strain predictions for the specimens made of the preconditioned material were in good agreement for the longitudinal direction however the models underestimated the strain components in the normal and transverse directions. It was considered that this could be due to anisotropic behaviour in the pre-compressed material which was not accounted for in the material model. The residual stress predictions show the weld modelling guidelines presented in the R6 procedure allow accurate and reliable weld simulations to be developed.

FE models of the machining processes to manufacture the C(T) specimens showed significant stress redistribution occurred during insertion of the pre-crack. The pre-crack cut through the weld which reduced the effect of the misfit between the plastically deformed weld region and the elastic parent material. In other machining processes, such as machining pin holes or side grooves in the specimen, the plastically deformed region of the specimen was unchanged and therefore these processes did not affect the residual stresses in the crack plane.

Stress intensity factors due to secondary loading were calculated using the J-integral solution modified to account for residual stresses in ABAQUS and the superposition approach. The crack driving force was determined after heating the specimen to 550°C which caused stress redistribution to occur. Both methods are in excellent agreement with each other and predict peak K_J^S = 22.2 MPam$^{1/2}$ for EBW5.

5 RESIDUAL STRESSES IN WEDGE-LOADED C(T) SPECIMENS

5.1 INTRODUCTION

Secondary loading conditions were simulated in a laboratory environment using constant-displacement fracture tests where the crack mouth of a C(T) specimen was held open at a fixed displacement. ASTM E1221-12a [107] describes a testing procedure where a wedge is inserted into the side of a C(T) specimen to determine the crack-arrest fracture toughness. A similar design was proposed for creep crack growth (CCG) testing where an oversized wedge was inserted into the mouth of a modified C(T) specimen, which had a tapered profile to match that of the wedge. Residual stresses were induced due to the geometrical misfit between the wedge and the modified C(T) specimen, with tensile residual stresses ahead of the crack tip. These specimens were then placed in a furnace, without any applied loads, to perform CCG tests where the residual stresses caused crack growth. A similar specimen design is used to measure crack arrest toughness as detailed by Anderson [21, pp330-334], however in this study the wedge-loaded C(T) specimen design was uniquely used for CCG testing.

The loading condition of the wedge-loaded C(T) specimen was similar to that of specimens in a displacement controlled test. As the applied load in the wedge-loaded C(T) specimen was self-contained, the design had the advantage that the specimen was simple to test under creep conditions in comparison to displacement controlled tests, which typically require a servo-controlled testing machine to control the mouth opening displacement of C(T) specimen. However in the wedge-loaded C(T) specimen, the load applied to the C(T) specimen by the wedge was unknown. This had to be determined from supporting FE simulations. In the wedge-loaded design, it was assumed the mouth of the C(T) specimen was held open at a fixed displacement, however there may have been elastic follow up in the wedge. To minimise this, the wedge was made of the creep resistant material, Nimonic 115.

A FE simulation of the wedge insertion process was created to predict the residual stresses and plastic deformation in the specimens. These models were developed using experimental data gathered during wedge insertion to measure the deformation of the specimens. Non-destructive residual strain measurements, using ND, were made after wedge insertion to validate these FE models. In this chapter the specimen design, numerical simulation of the wedge insertion process and supporting experimental data are detailed. The residual stresses predicted from validated numerical simulations are also presented.

5.2 SPECIMEN DESIGN AND MANUFACTURE

5.2.1 SPECIMEN DESIGN

The geometry of the wedge-loaded C(T) specimen is shown in Figure 5.1. The dimensions were based on standard C(T) specimens sized to ASTM 1457-13 [77] with a width, W, of 50 mm and a thickness, B, of 25 mm. The mouth of the C(T) specimen was shaped to match the profile of the wedge creating a large contact area. Friction held the wedge in place upon wedge insertion. The pre-cracks in the modified C(T) specimens were machined using wire EDM, with a wire diameter of 0.25 mm to achieve a crack tip radius of 0.15 mm. These specimens had an initial crack length, a_0/W, of 0.45 when measuring the crack length from the load line in a standard C(T) specimen in ASTM 1457-13 [77].

Three specimens, WC(T)3, WC(T)4 and WC(T)5, sized to W = 50 mm were made of ex-service Type 316H stainless steel in the 8% pre-compressed material condition. The pre-compression direction was normal to the crack plane. The wedge was made of Nimonic 115 [108] which is a creep resistant nickel based alloy. These three specimens had different wedge insertion depths, Δ_d, to vary the magnitudes of residual stresses induced. All the specimens were plane sided, i.e. without side grooves.

A list of the specimens fabricated is shown in Table 5.1. Initially two trial specimens were fabricated to prove the design concept and to support the development of the numerical simulation of wedge insertion. These trial specimens, WC(T)1 and WC(T)2, were made of ex-service Type 316H stainless steel extracted from parent and HAZ regions respectively of a steam header. The development of the trial specimens are detailed in [109]. Preliminary

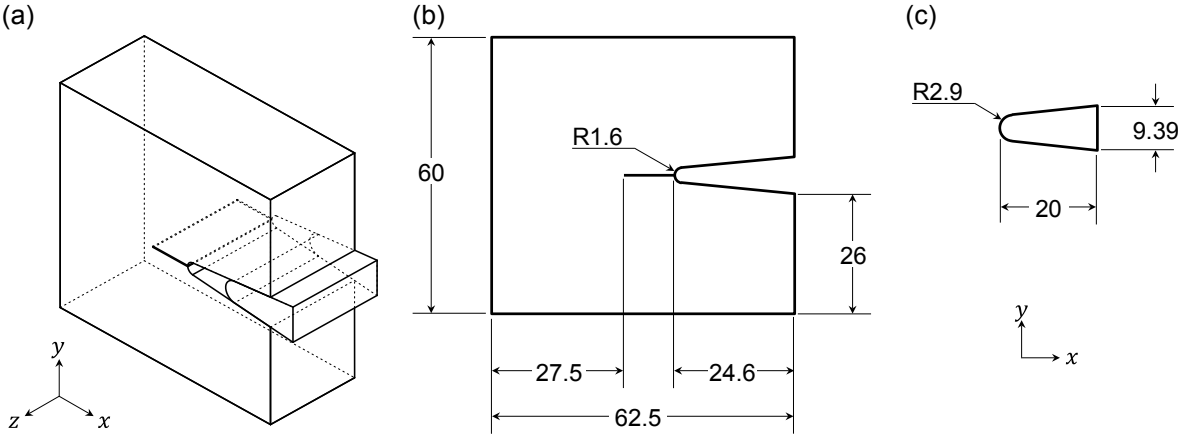


Figure 5.1 Wedge-loaded C(T) specimen (a) isometric view, (b) dimensions of the modified C(T) specimen and (c) dimensions of the wedge

CCG tests were conducted on these two specimens however no crack growth was observed. Specimens WC(T)3 to WC(T)5 were then made with a thickness of 25 mm to achieve plane strain conditions at mid-thickness and using material in the pre-compressed condition which had reduced creep ductility. This chapter focuses on FE models and experimental data supporting specimens WC(T)3 to WC(T)5.

Table 5.1 List of wedge-loaded C(T) specimens fabricated

Specimen	C(T) Specimen Material	Wedge Material	Dimensions		Δ_{MOD-CG} (mm)
			W (mm)	B (mm)	
WC(T)1	Type 316H Parent	Inconel	40	10	0.15
WC(T)2	Type 316H HAZ	Inconel	40	10	0.15
WC(T)3	Type 316H 8% Pre-Compressed	Nimonic 115	50	25	0.23
WC(T)4	Type 316H 8% Pre-Compressed	Nimonic 115	50	25	0.45
WC(T)5	Type 316H 8% Pre-Compressed	Nimonic 115	50	25	0.29

5.2.2 SPECIMEN FABRICATION

The specimens were fabricated from the pre-compressed blocks using wire EDM allowing the profiles of the mouths and wedges to be accurately machined. An Instron testing machine fitted with compression platens was then used to carefully insert the wedges into the modified C(T) specimens, as shown in Figure 5.2. Aluminium plates, with a thickness of 1 mm, were placed between the platens and the specimen to prevent damage to the surface of the platens. The insertion of the wedge was performed under displacement control using a displacement rate of 0.4 mm/min.

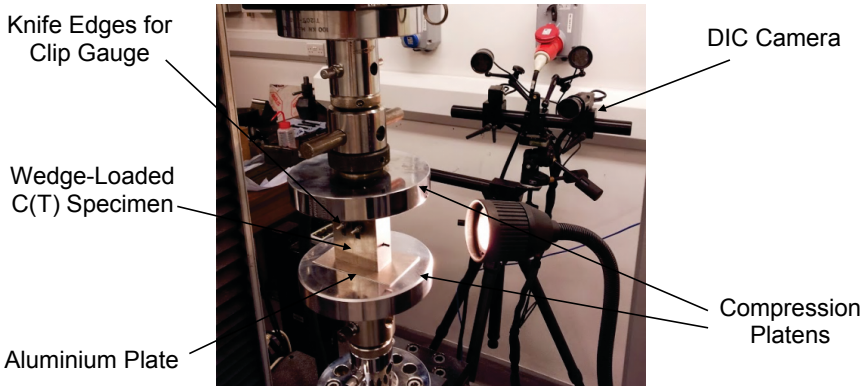


Figure 5.2 Wedge-loaded C(T) specimen in during wedge insertion using an Instron testing machine

A clip gauge was used to measure the mouth opening displacement, Δ_{MOD-CG}, between the knife edges shown in Figure 5.2. Threaded studs were spot welded to the side faces of the specimens. Knife edges were attached to the studs using nuts and washers ensuring the edges were free to rotate and remain parallel as the mouth of the C(T) specimen opened. End of test conditions were set to when the clip gauge measured specified Δ_{MOD-CG}, which are shown in Table 5.1.

The DIC strain measurement technique, in two dimensions, was used to determine displacements and in-plane strains on the surface of the wedge-loaded C(T) specimens during wedge insertion. A black and white speckle pattern was sprayed onto the side face of the specimens, opposite of the face which had the clip gauge mounted. A camera, shown in Figure 5.2, recorded images of the specimens during wedge insertion. The commercial software ARAMIS [68] was used to compute the displacements and strain fields of small regions, or facets, on the surface [69]. The DIC measurements were used to measure the mouth opening displacement, $\Delta_{MOD-DIC}$, and in-plane strain components which were used to develop and validate the numerical simulation.

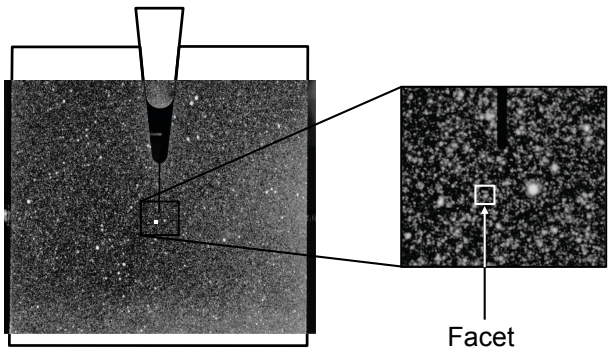


Figure 5.3 Speckle pattern on wedge-loaded C(T) specimen, WC(T)5, showing a typical facet used in the DIC measurement technique

5.3 EXPERIMENTAL MEASUREMENTS

5.3.1 MOUTH OPENING DISPLACEMENT

The mouth opening displacements measured by a clip gauge, Δ_{MOD-CG}, against wedge displacements, Δ_d, for specimens WC(T)3, WC(T)4 and WC(T)5 are shown in Figure 5.4. At short times Δ_d increased whilst Δ_{MOD-CG} remained unchanged. This was due to machine displacement and local deformation of the contacting surfaces [109]. Hence, from Δ_d it was difficult to determine the end of test condition for wedge insertion. Instead wedge insertion was stopped when Δ_{MOD-CG} reached the displacements shown in Table 5.1.

The mouth opening displacement was also determined using the DIC technique, $\Delta_{MOD-DIC}$, by using the software ARAMIS to measure the distance between two points either side of the crack mouth during wedge insertion. The locations of these measurement points and $\Delta_{MOD-DIC}$ against Δ_d are shown in Figure 5.5. The displacements were measured at the locations shown in Figure 5.5(b), which were different to the clip gauge locations shown in Figure 5.4(b) and therefore $\Delta_{MOD-DIC}$ was less than Δ_{MOD-CG}. Both $\Delta_{MOD-DIC}$ and Δ_{MOD-CG} were used to develop the numerical simulations presented in Section 5.4.

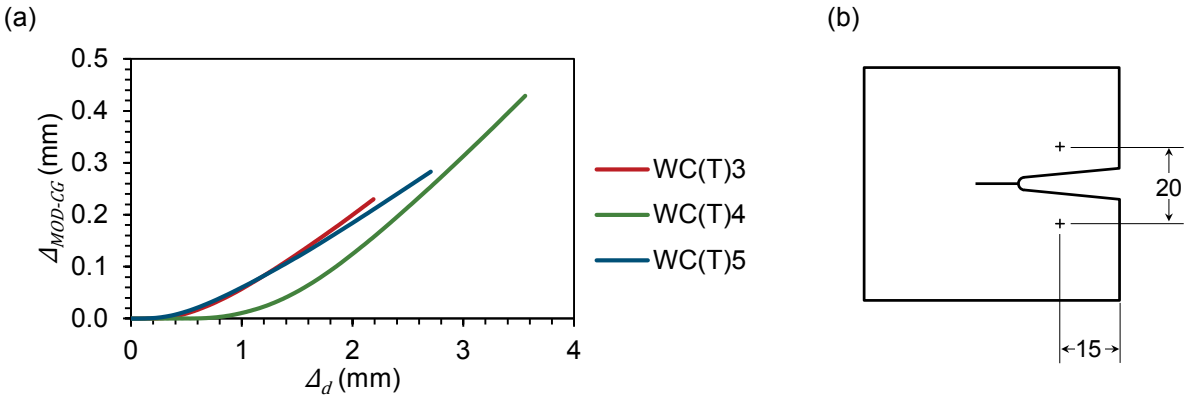


Figure 5.4 (a) Mouth opening displacement in wedge-loaded C(T) specimens measured by clip gauge (b) Clip gauge attachment points

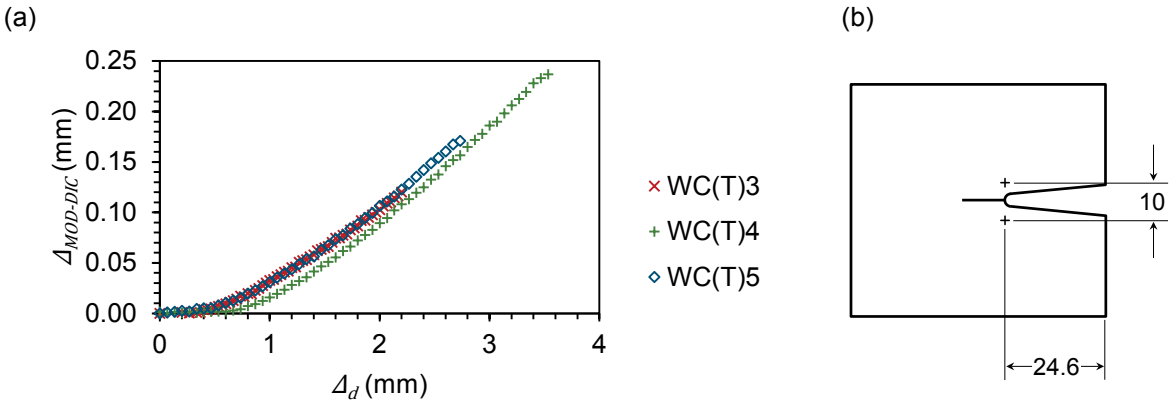


Figure 5.5 (a) Mouth opening displacement in wedge-loaded C(T) specimens measured by DIC (b) Initial position of facets used to measure mouth opening displacement with DIC

5.3.2 SURFACE STRAIN MEASUREMENTS

ARAMIS was used to compute the in-plane strains on the surface of the wedge-loaded C(T) specimens from the captured images. This software overlaid a grid of facets onto the image, each containing a cluster of speckles as shown in Figure 5.3. Strain components

were determined for each of these facets. The accuracy of the solution improved as the facet size increased and more speckles were contained within this region. However the facet also had to be sufficiently small to accurately quantify the large strain gradients that were present. A facet size of 0.68 × 0.68 mm^2 was selected as a suitable compromise between accuracy and capturing the large strain gradients near the pre-crack. The in-plane strain components, measured using DIC, for each of the wedge-loaded C(T) specimens are presented in Figure 5.10 and Figure 5.11 in Section 5.4.2 where the results are compared to FE predictions.

5.3.3 RESIDUAL STRAIN AND STRESS MEASUREMENTS

Residual strain measurements were made using ND after wedge insertion. Specimens WC(T)3 and WC(T)4 were tested using the instrument SALSA at the ILL, Grenoble and WC(T)5 was tested using the instrument Stress-Spec at FRM II, Munich. All measurements were made using a 2 × 2 × 2 mm^3 gauge volume. The material had a relatively large grain size, hence the gauge volume was rotated to increase number of grains sampled. Specimens WC(T)3 and WC(T)4, which were measured using SALSA, were rotated by ± 2.4° in 0.8° steps and specimen WC(T)5, measured by Stress-Spec, was continuously oscillated between ± 2.0°.

The measurements were made along the ligament of the wedge-loaded C(T) specimens at mid-thickness which is the plane along which the crack was expected to grow in subsequent CCG tests. This measurement line is labelled as line AB in Figure 5.6. There were up to 17 measurement locations per sample. Measurements were made along the ligament at 1 mm intervals close to the pre-crack and at 2 mm intervals further away. Count times of up to 30 min were used for each measurement point.

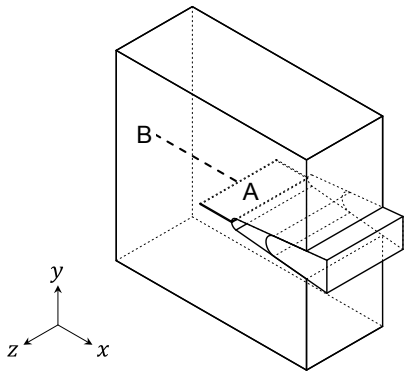


Figure 5.6 Measurement line AB in wedge-loaded C(T) specimens sampled during ND tests

The elastic strain response of the $\{311\}$ lattice plane was measured in these tests. Reference, d_0, measurements were made on material extracted from the mouth of the C(T) specimen and also on the corner of each specimen which were considered to have low stresses. As the material had been pre-compressed, measurements were made in multiple directions to test for variations in d_0 measurements however significant differences were not observed.

The residual strain components along the ligament of the wedge-loaded C(T) specimen at mid-thickness, designated line AB, are shown in Figure 5.7. These strains were determined from the measured neutron scattering angles using (2.48). The shapes of the strain distributions along line AB were similar for all specimens. Generally the specimens with larger Δ_{MOD} had increasing magnitudes of residual strains, however the strain components in specimen WC(T)4 were only slightly greater than WC(T)5.

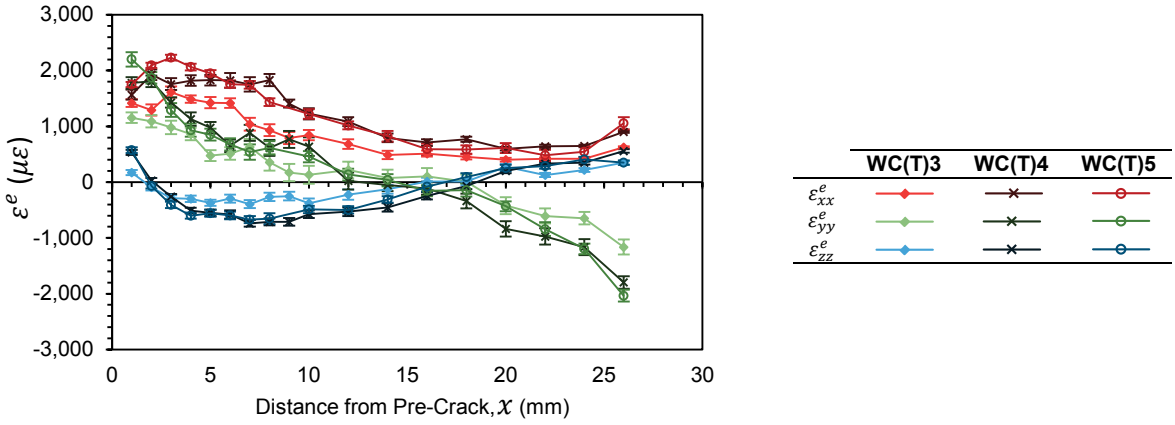


Figure 5.7 Residual strain components measured by ND in the wedge-loaded C(T) specimens

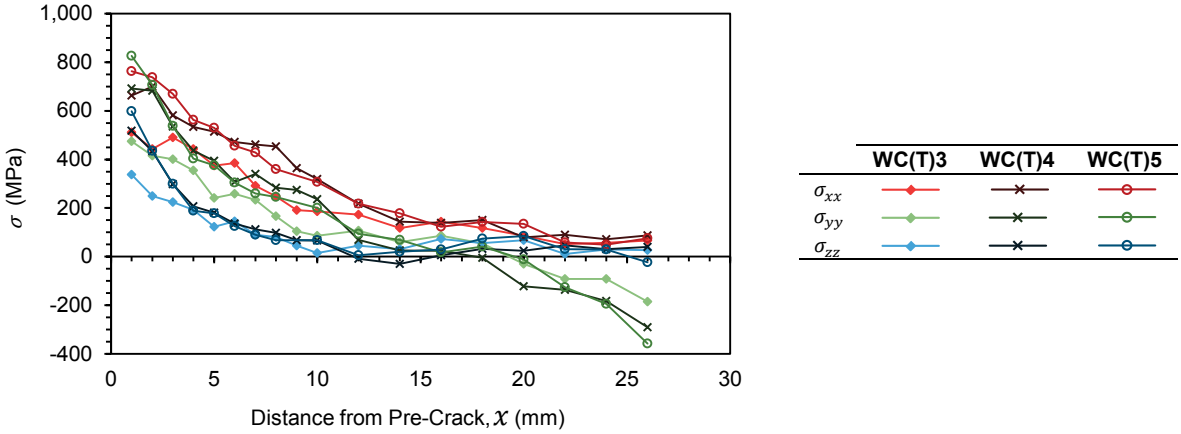


Figure 5.8 Residual stress components determined from ND measurements in the wedge-loaded C(T) specimens

The errors bars show uncertainty from fitting Gaussian distributions to the neutron scattering angles, which are up to ± 200 $\mu\varepsilon$. The fitting error was low relative to the variation in strain across the sample and therefore the count times were judged to have been sufficient. There were some large variations between successive data points such as the ε_{yy}^{e} component in WC(T)4 between 5 to 10 mm from the pre-crack. This scatter was due to the random location of the sampled grains within the measurement gauge volume.

The residual stresses were determined from the ND measurements using (2.49) and elastic constants defined by the Kröner model which are shown in Figure 5.8. The error for each stress measurement, from the uncertainty in fitting Gaussian distributions to the neutron scattering angles, were up to ± 30 MPa and are not shown in Figure 5.8 for clarity. All three stress components were tensile near the crack tip. The components normal to crack growth, σ_{yy}, were compressive towards the back face of the specimens, whilst components σ_{xx} and σ_{zz} tended towards zero. The stresses were largest at the closest measurement point to the pre-crack where the component σ_{yy} was 480 MPa, 700 MPa and 830 MPa for WC(T)3, WC(T)4 and WC(T)5 respectively. The tensile stresses near the crack tip in WC(T)5 were expected to be less than those in WC(T)4. This error was likely to have been due to scatter inherent in the ND technique caused by the random location of the sampled grains within the measurement gauge volume.

5.4 NUMERICAL ANALYSIS

5.4.1 MODEL DESCRIPTION

The wedge insertion process was simulated using the FE software, ABAQUS [49], to predict the residual stresses and plastic deformation from wedge insertion. A 3D model of a quarter of the geometry was developed which assumed two symmetry planes, as shown in Figure 5.9. Simulations of the trial specimens, presented in [109], showed a 3D analysis was required to obtain the correct deformation in the through thickness, z, direction.

The compression platens fitted to the Instron testing machine were modelled as analytically rigid surfaces. The bottom surface was held fixed whilst the top surface was displaced in the x-direction to model the movement of the compression platen. Three models were analysed, where the displacements, Δ_d, were selected to obtain Δ_{MOD-CG} and $\Delta_{MOD-DIC}$ measured experimentally in specimens WC(T)3 to WC(T)5. The rigid surface was then moved away from the wedge such that friction held the wedge in the mouth of the specimen. Some elastic unloading occurred as the surface was moved out of contact with the wedge. There was some uncertainty of the initial position of the wedge as the wedges were placed in the mouths of the C(T) specimens by hand. However by comparing of the experimental mouth opening displacements to the FE model, the analysis was insensitive to the initial wedge position.

A coefficient of friction, μ, of 0.78 was used to define the contact condition between the wedge and the modified C(T) specimen [110]. Sensitivity studies on the trial specimen showed the deformation of the specimen was insensitive to the coefficient of friction for $\mu \leq 0.8$ [109]. Frictionless contact was assumed between the analytical rigid surfaces and the wedge-loaded C(T) specimen.

The model consisted of 35,990 hexahedral quadratic elements (ABAQUS type C3D20R) and 146,025 nodes, which were analysed using reduced integration. A focused mesh was used with small elements of length 5 μm located near the crack tip. The model had 12 elements through the thickness of the specimen. Small elements were biased towards the side face of the specimen where large stress gradients were expected as plane stress conditions were approached.

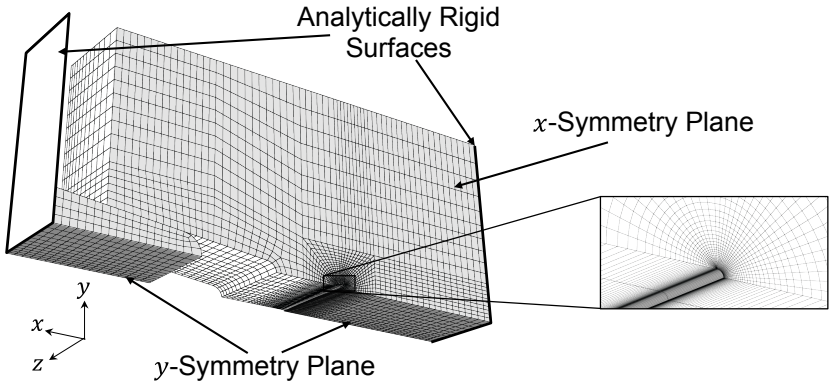


Figure 5.9 FE model of wedge-loaded C(T) specimen

The modified C(T) specimen was made of ex-service Type 316H stainless steel uniformly pre-compressed to 8% plastic strain. The material properties were specified using stress and plastic strain data from uniaxial tensile tests [18], where isotropic hardening behaviour was assumed. A study performed on the trial specimen showed the deformation was not sensitive to the hardening model as the material does not experience reverse loading [109]. The wedge was made of Nimonic 115 which is a creep resistant nickel based alloy. Nimonic 115 has a Young's modulus, E, a yield strength, σ_y, and an ultimate tensile strength, σ_{UTS}, of 216 GPa, 875 MPa and 1,275 MPa respectively at room temperature. At 550°C, these constants are 185 GPa, 775 MPa and 1,125 MPa respectively [108].

The simulation was used to determine the residual stresses which caused crack growth during high temperature testing of the wedge-loaded C(T) specimens. As the specimens were heated, stress redistribution occured due to the thermal expansion of the wedge relative to the modified C(T) specimen and due to the reduction in tensile strength at high temperature. Heating from 20°C to 550°C was simulated in the FE analyses. The thermal expansion coefficient, α, for Nimonic 115 is 13.65 × 10^{-6} mm/mm°C when heating from 20°C to 550°C [108] and for Type 316H stainless steel is shown in Table 4.5 for a range of temperatures.

5.4.2 VALIDATION OF THE FE PREDICTIONS

MOUTH OPENING DISPLACEMENTS

In the FE analyses the wedges were displaced into the mouths of the C(T) specimens until the mouth opening displacements, Δ_{MOD-CG} and $\Delta_{MOD-DIC}$, match those measured experimentally. The wedges were displaced by 1.40 mm, 1.83 mm and 2.53 mm for specimens WC(T)3, WC(T)4 and WC(T)5 respectively. Table 5.2 shows a comparison of the displacements measured by the clip gauge, Δ_{MOD-CG}, and the DIC technique, $\Delta_{MOD-DIC}$, to corresponding displacements at node locations in the FE model. The FE model predicts the mouth opening displacements to 0.01 mm of the experimental measurements.

Table 5.2 Comparison of Δ_{MOD} predicted by FE analyses to experimental data

Specimen	Δ_{MOD-CG} (mm)			$\Delta_{MOD-DIC}$ (mm)		
	Clip Gauge	FE	Error	DIC	FE	Error
WC(T)3	0.23	0.22	-4%	0.12	0.13	4%
WC(T)4	0.43	0.41	-4%	0.24	0.24	3%
WC(T)5	0.28	0.29	3%	0.17	0.17	0.2%

DIC MEASURED RESIDUAL STRAINS

Contour plots of the strain components ε_{xx} and ε_{yy} on the side face of the specimens are shown in Figure 5.10 and Figure 5.11 and respectively. The top half of the figures show FE predictions and the bottom half show the corresponding DIC measurements.

The magnitudes of strain components surrounding the pre-crack increased from specimens WC(T)3 to WC(T)5 and to WC(T)4, which had increasing wedge insertion depths, for both FE predictions and DIC measurements. There was generally good agreement between the shapes and sizes of the contours from the FE analyses and DIC measurements. The size of the ε_{yy} contour regions near the pre-crack measured by DIC clearly grew for each specimen with increasing wedge insertion depths, which was also predicted by the FE models.

The FE predictions of surface strains are in close agreement with the DIC strain measurements. The small facet size used in the DIC analyses allowed strains to be

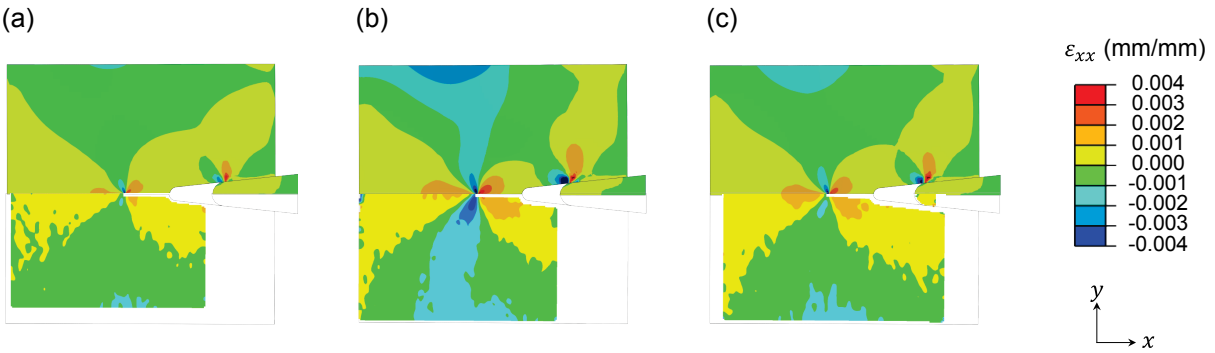


Figure 5.10 FE predictions of strain component ε_{xx} on the side face of specimens (a) WC(T)3, (b) WC(T)4 and (c) WC(T)5 compared to DIC measurements

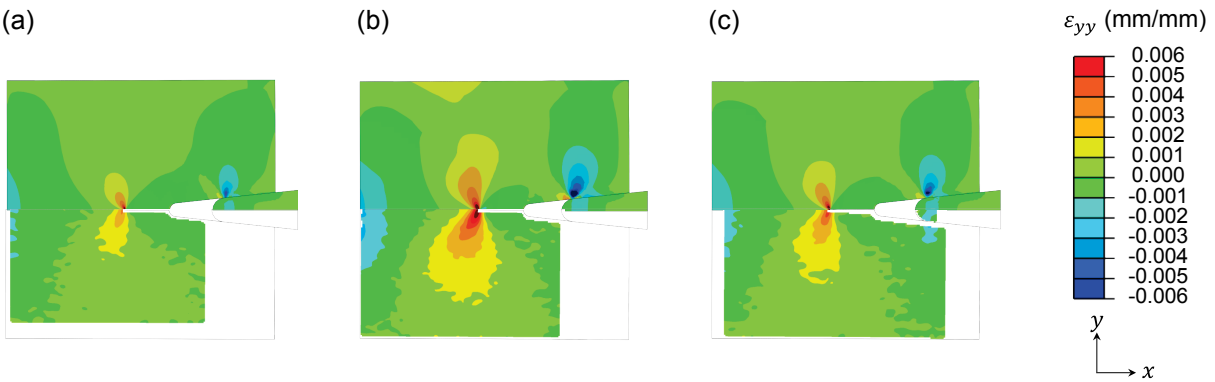


Figure 5.11 FE predictions of strain component ε_{yy} on the side face of specimens (a) WC(T)3, (b) WC(T)4 and (c) WC(T)5 compared to DIC measurements

measured at short distances from the pre-crack and enabled the large strain gradients to be quantified. However the technique was limited to making surface measurements only where larger stresses were expected at mid-thickness.

MID-THICKNESS STRAINS MEASURED BY ND

The elastic strain components after wedge insertion predicted by the FE analyses, along line AB, as shown in Figure 5.6, are compared to the ND measurements in Figure 5.12. The strain distributions predicted by the FE models were similar to the experimental data. However the FE models predicted large variations in strains up to 2 mm ahead of the pre-crack which were not observed in the ND measurements. The length of the measurement gauge volume was approximately 3 mm (i.e. the diagonal of the 2 × 2 mm^2 cross section) which was too large to measure these large strain gradients.

The largest difference between the FE predictions and the ND measurements were for the elastic strain component ε_{xx}^{e} measured up to 10 mm from the pre-crack. The strains predicted by the FE simulation were up to 900 $\mu\varepsilon$ less than the ND measurements. Conversely in the trial specimen the FE predictions were up to 500 $\mu\varepsilon$ greater than ND measurements [109]. Thickness was a key difference between the trial specimen and specimens WC(T)3 to WC(T)5, which were 10 mm and 25 mm thick respectively. The effect of constraint on the residual strain distributions was investigated by considering plane stress and plane strain conditions in [109]. However this did not account for the observed differences between the experimental data and FE predictions. In the EB welded C(T) specimens, differences in the experimentally measured strains and FE predictions were also observed in this direction. It was considered that this could be due to anisotropy of the pre-compressed material.

Overall the deformation of the wedge-loaded C(T) specimens predicted by the FE models matched well with the experimentally measured data to validate the numerical simulations. The mouth opening displacements predicted by the FE analyses closely matched the measurements made using the clip gauge and DIC. The strain components measured using DIC and ND were mostly in close agreement with FE predictions. Whilst some small differences were observed between these experimentally measured strains near the pre-crack with FE predictions, the strain distributions were in sufficient agreement to consider the numerical simulation correctly predicted the deformation of the specimens.

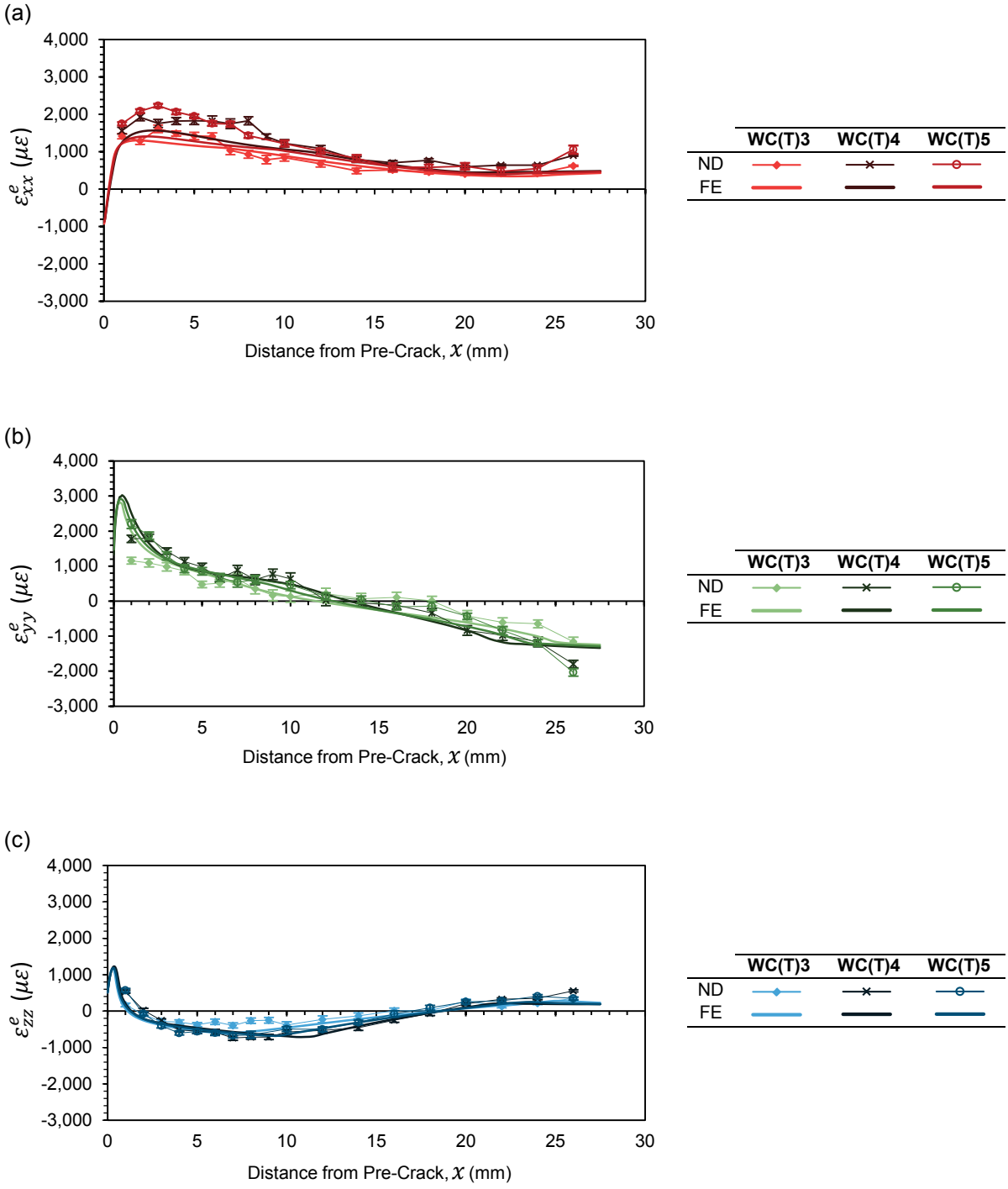


Figure 5.12 Comparison of residual strains in the wedge-loaded C(T) specimen predicted by FE simulation to ND measurements (a) ε^e_{xx}, (b) ε^e_{yy} and (c) ε^e_{zz}

5.5 CRACK DRIVING FORCE DUE TO SECONDARY LOADS

5.5.1 REDISTRIBUTED STRESSES AT 550°C

For CCG testing the specimens were heated to 550°C. The temperature dependent material properties and relative thermal expansion coefficients of the wedges and modified C(T) specimens caused stress redistribution to occur at high temperature. The validated FE models were used to predict the stresses in these specimens prior to CCG testing. Contour plots of the stress components at 550°C in the crack plane of the wedge-loaded C(T) specimens are shown in Figure 5.13. The stress components along the ligament of the specimens at mid-thickness, which is identified as line AB in Figure 5.6, are shown in Figure 5.14(a) to (c). The hydrostatic stress, σ_h, equivalent stress, σ_{eq}, stress triaxiality and equivalent plastic strain, ε^{pl}, are also shown in Figure 5.14(d) to (g).

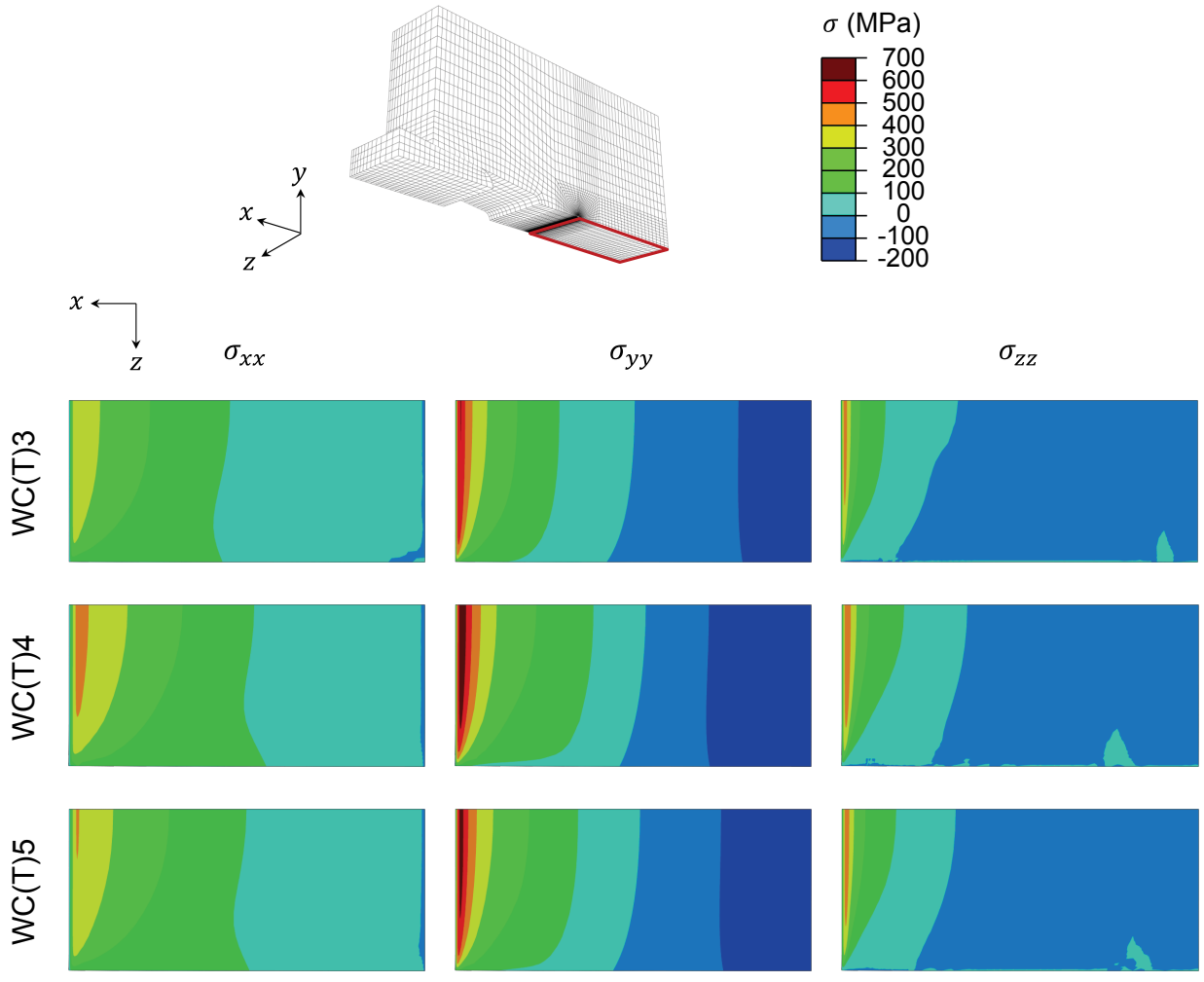


Figure 5.13 Stress components on the crack plane of the wedge-loaded C(T) specimens at 550°C

Tensile stresses were predicted near the notch for all three stress components. Due to the high triaxiality in the region yielding was inhibited and stresses remained which were far in excess of the materials yield strength (177 MPa at 550°C [18]). Of the three stress components, σ_{yy} was the largest with magnitudes of 602 MPa, 657 MPa and 629 MPa for specimens WC(T)3, WC(T)4 and WC(T)5 respectively, where the specimen with the largest Δ_{MOD} had the largest crack tip tensile stresses. The peak stresses occurred at approximately 0.5 mm ahead of the pre-crack for all three specimens. The tensile stresses were focused at the root of the pre-crack during wedge insertion but as the rigid surface modelling the compression platen was removed from the analysis some elastic stress redistribution occurred where stresses near the blunt notch reduced.

The tensile σ_{yy} stresses at the crack tip were balanced by compressive stresses at the back face of the specimen which was large enough to cause some yielding as shown in Figure 5.14(g). The magnitudes of all three stress components reduced towards the side faces of the specimen where plane stress conditions were approached.

Very little plasticity occurred ahead of the pre-crack in these specimens in comparison to the EB welded C(T) specimen and pre-compressed C(T) specimens reviewed in Section 4.7.1 and Section 2.4.6 respectively. The size of the plastic zones (where ε^{pl} < 0.2%) were predicted to be 0.56 mm, 1.20 mm and 0.73 mm for specimens WC(T)3, WC(T)4 and WC(T)5 respectively. Further FE simulations with larger wedge insertion depths were analysed to show with increasing wedge insertion depths, the plastic zone would grow whilst the magnitude of the crack tip tensile stresses would only increase by a relatively small amount. It was considered that the wedge insertion depths chosen for this study produced crack tip plasticity which was sufficiently low such that CCG due to the relaxation of residual stresses could be investigated without the influence of plasticity.

Time dependent plastic strains can accumulate in Type 316 stainless steels at room temperature due to a phenomenon known as cold creep [111]. However the R6 procedure [27] states that such strains are only significant at loads close to the plastic collapse load. The FE models show there is little plasticity in the specimen and therefore cold creep was not considered in this study.

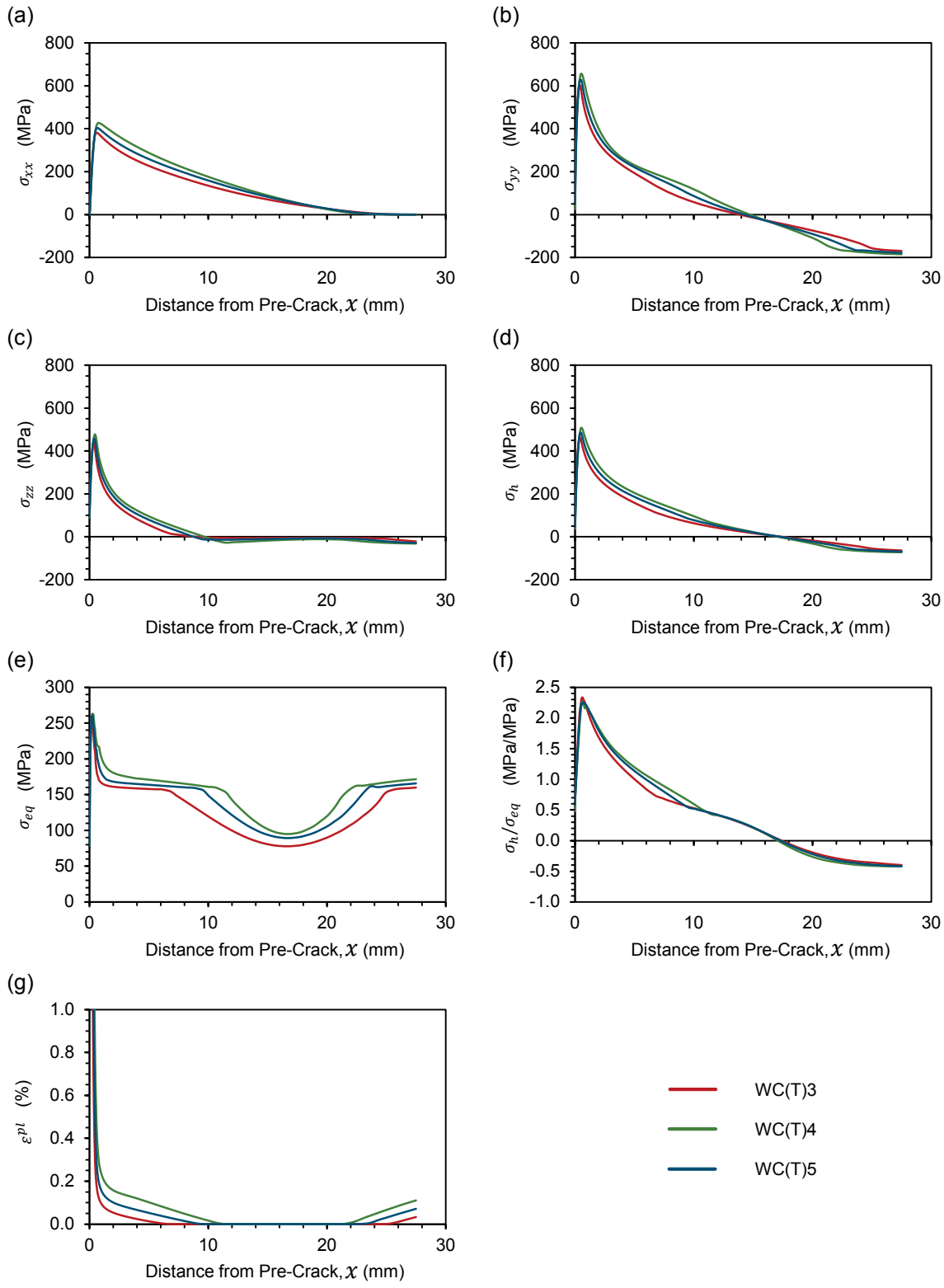


Figure 5.14 FE predictions of stress and plasticity along the ligament of the wedge C(T) specimens at 550°C (a) σ_{xx}, (b) σ_{yy}, (c) σ_{zz}, (d) σ_h, (e) σ_{eq}, (f) σ_h/σ_{eq} and (g) ε_{pl}

5.5.2 STRESS INTENSITY FACTOR

The stress intensity factors, K^s, were determined using FE models of the wedge-loaded C(T) specimens. Following insertion of the wedges by the compression platen, shown in Figure 5.2, some elastic unloading occurred as the platen was moved away from the specimens. Therefore the load applied by the wedge onto the modified C(T) specimen did not increase monotonically and the J-integral determined by (2.26) could not be used. Furthermore the modified expression to include the effect of residual stresses (2.44) was also not applicable as the strain field without the pre-crack could not be obtained. In this specimen design the pre-crack was present before the residual stresses were induced and therefore the stress and strains in the uncracked body were unknown.

To determine K^s an equivalent elastic model was used where loads were applied to the modified C(T) specimen that were representative of the contact forces between the wedge and the C(T) specimen. This followed the concept of the superposition approach, shown in Section 2.5.3, however the loads were not applied at the crack face.

The contact stresses exerted by the wedge onto the modified C(T) specimen in WC(T)5 at 550°C are shown in Figure 5.15. These stresses act in the direction normal to the crack plane. Contact was made over a small region which could be approximated to a line contact near the front of the wedge. This is consistent with the strain distributions shown in Figure 5.10 and Figure 5.11 where deformation was concentrated towards the front of the wedge. The direct and shear force components due to the contact were extracted from the FE analyses at the node locations. These were applied as concentrated forces on an identical elastic model of the modified C(T) specimen at 550°C where K^s was determined.

A focused mesh was used near the crack tip to allow K^s to be determined by ABAQUS at node planes across the thickness of the specimen. The mesh was biased towards the side face where there were large changes in K^s as plane stress conditions were approached. Figure 5.16(b) shows the K^s solutions at the three node planes shown in Figure 5.16(a) for WC(T)5. The solutions converged to a constant value 0.25 mm from the crack tip.

The converged K^s solutions across the thickness of WC(T)3, WC(T)4 and WC(T)5 are shown in Figure 5.16(c). The peak values of K^s are at mid-thickness and remain large across the middle of the specimen. The average and peak values of K^s for WC(T)3, WC(T)4 and WC(T)5 are shown in Table 5.3. Large crack driving forces were generated in these

specimens with K^s of up to 43.6 MPam$^{1/2}$. In comparison, CCG tests on C(T) specimens made of 8% pre-compressed Type 316H stainless steel under primary loads have been tested with an initial K of 25 to 35 MPam$^{1/2}$ [18].

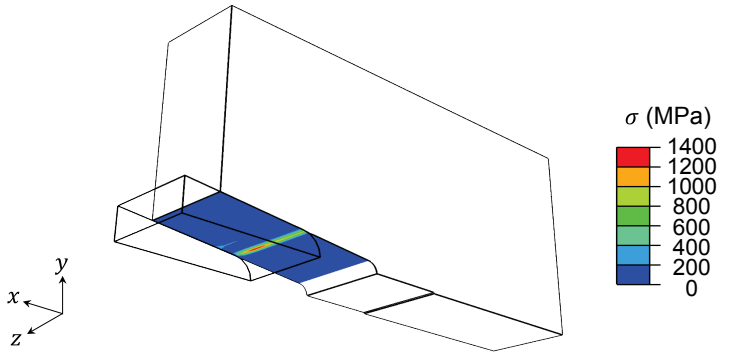


Figure 5.15 Contact stresses between wedge and modified C(T) specimen at 550°C in WC(T)5

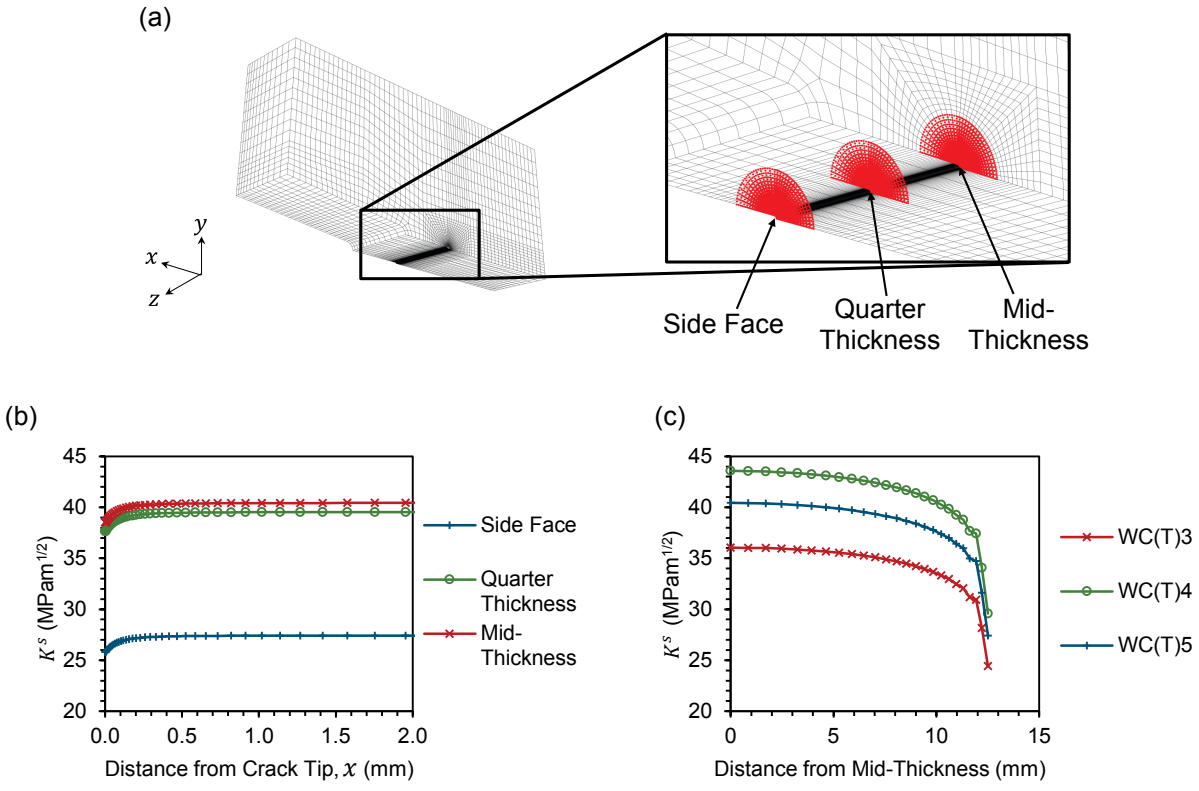


Figure 5.16 (a) Node regions for three contour integrals in the wedge-loaded C(T) specimen, (b) K^s through three node planes in WC(T)5 and (c) K^s across the thickness of the wedge-loaded C(T) specimens

Table 5.3 Peak and average K^s for wedge-loaded C(T) specimens at 550°C

Specimen	K^s (MPam$^{1/2}$)	
	Peak	Average
WC(T)3	36.0	34.5
WC(T)4	43.6	41.8
WC(T)5	40.4	38.9

5.6 SUMMARY

Residual stresses were generated in C(T) specimens by controlled insertion of Nimonic 115 wedges into the mouths of the specimens which were made of Type 316H stainless steel in the pre-compressed material condition. This induced large tensile stresses ahead of the pre-crack which would drive crack growth in CCG tests. The large stresses existed due to high triaxiality which inhibited plastic deformation. Tensile stresses of up 830 MPa were measured using the ND measurement technique. FE models of the insertion process were developed and validated using these residual strain measurements. The models were used to predict the extent of stress redistribution after heating to 550°C which was caused by temperature dependent material properties and stresses generated due to the relative thermal expansion of the wedges and the modified C(T) specimens.

Stress intensity factors due to the secondary loads, K^s, were determined using FE models based on the superposition approach. Peak values of K^s were found to be 36.0 MPam$^{1/2}$, 43.6 MPam$^{1/2}$ and 40.4 MPam$^{1/2}$ for specimens WC(T)3, WC(T)4 and WC(T)5 respectively indicating the crack driving forces in the specimens were initially very large. The FE modelling also showed plastic deformation induced from wedge insertion was limited to very small distances from the crack tip. This allowed the effect of secondary loads on CCG to be investigated without the influence of plasticity.

6 CCG TESTING OF SPECIMENS WITH RESIDUAL STRESSES

6.1 INTRODUCTION

Creep crack growth studies were conducted with the EB welded and wedge-loaded C(T) specimens to determine the influence of the residual stresses on crack growth. Two EB welded C(T) specimens and three wedge-loaded C(T) specimens were placed in a furnace and heated to a nominal temperature of 550°C for up to 1,320 h without any applied loads. These tests allowed crack growth under secondary loading conditions to be investigated. Two further EB welded C(T) specimens were tested with applied loads to conduct CCG tests under combined loading conditions. This chapter presents the experimental procedure and measurements obtained during the CCG tests. Upon completion of the tests, the specimens were destructively examined to determine the shape and size of the cracks which are also presented.

6.2 TEST SPECIMENS

The test specimens used for CCG testing with the test duration, t_f, and the test temperature, T, are shown in Table 6.1. All but one of the specimens were manufactured from Type 316H stainless steel in the pre-compressed material condition. Specimen EBW3 was made from material in the as-received condition to investigate whether a crack would initiate in a material with high creep ductility. The EB weld induced residual stresses were greater in the specimens made from the pre-compressed material and therefore caused larger crack driving forces as shown by K^s in Table 6.1. Specimens EBW6 and EBW7 additionally had small applied loads of 5.0 MPam$^{1/2}$ and 10.0 MPam$^{1/2}$ respectively. The values of K^s shown are those determined in Chapter 4 and Chapter 5 and hence were determined at 550°C. The temperatures were not constant for some specimens as shown in Table 6.1, due to difficulties incurred during testing. These are detailed in Section 6.4. In this

Table 6.1 List of specimens with residual stresses used to conduct CCG testing

Specimen	t_T (h)	T (°C)	K^p (MPam$^{1/2}$)	K^s (MPam$^{1/2}$)
WC(T)3	329	540-550	0.0	36.0
WC(T)4	329	510-570	0.0	43.6
WC(T)5	885	550	0.0	40.4
EBW3	1,320	550	0.0	16.0
EBW5	1,340	550	0.0	22.2
EBW6	1,300	550	5.0	22.2
EBW7	1,320	550	10.0	22.2

study specimens were tested under secondary or combined loading conditions only, Mehmanparast et al. [18, 19] performed CCG tests on Type 316H stainless steel pre-compressed to 8% plastic strain under primary load conditions. The tests performed by Mehmanparast et al. show a variation of crack growth rates between specimens which can be attributed to material scatter. Specimens were made from ex-service material which had different operational histories and also differences in microstructures were observed across the steam header components. A similar variation of crack growth rates is expected in the specimens shown in Table 6.1.

6.3 TEST PROCEDURE

The test procedure was based on the guidance in ASTM 1457-13 [77] and as reported by McLennon and Allport [112] where the testing methodology used at EDF Energy are described. Both of these documents are focused on testing under primary load conditions. Some aspects of the test method used in this study differed from those in the guidance documents due to the presence of residual stresses, which are reported in this section.

Pre-cracks were inserted in all specimens using wire EDM. Specimens WC(T)3, WC(T)4, WC(T)5, EBW3 and EBW5 were machined using a wire diameter of 0.25 mm to achieve a pre-crack width of 0.30 mm. Specimens EBW6 and EBW7 were pre-cracked using a wire diameter of 0.10 mm to achieve a crack width of 0.15 mm. The difference in pre-crack widths in the EB welded C(T) specimens could affect the initial crack growth rates in CCG testing. The widths of the pre-cracks in the wedge-loaded C(T) specimens increased after wedge insertion, the crack mouth opened to a width of 0.375 ± 0.025 mm[†].

The specimens were instrumented with three type K thermocouples located across the thickness of the specimen to ensure the temperature field was uniform. The specimens were tested in three zone electric resistance furnaces. In tests under primary load conditions, ASTM 1457-13 recommends specimens, which are 25 mm thick, are slowly heated to and maintained at the test temperature for at least 1 h before any loads are applied. However in specimens with residual stresses, stress relaxation occurred as soon as the specimens were heated into the creep regime and therefore the heat up time was minimised. This was accomplished by placing a dummy sample into the furnace and determining the settings required on the furnace to quickly heat the specimen whilst ensuring the furnace heated to 550°C without any temperature overshoot. The temperature of the furnace then remained

[†] Measurements made using feeler gauges which are accurate to increments of 0.05 mm

stable at 550 ± 1°C to confirm it was operating correctly. Using these settings the furnace was able to heat up the test specimens to approximately 545°C in 1.5 h and fine adjustments were made over another hour to reach 550°C.

The direct current potential drop (DCPD) technique was used to measure the extent of crack growth during the test. The current input leads were located on the top and bottom surfaces of the C(T) specimens and voltages were measured using potential drop (PD) output leads spot welded to either side of the crack on opposing faces of the specimen as recommended by McLennon and Allport [112]. By attaching the output leads close to the pre-crack (2 mm above and below the crack plane) the measurements were very sensitive to crack growth [113]. The measured voltages, V, were smoothed to remove noise by fitting a curve as a function of time, t, as recommended by McLennon and Allport. The curve was in the form:

$$\frac{V}{V_f} = c_{PD}\left[1 - e^{d_{PD}\left(\frac{t}{t_f}\right)^{r_{PD}}}\right] + g_{PD}\left(\frac{t}{t_f}\right) \tag{6.1}$$

where V_f is the final voltage, t_f is the final time and, c_{PD}, d_{PD}, g_{PD} and r_{PD} are fitted constants. Upon completion of the test, the final crack size was determined by breaking open the sample and using nine measurement points to determine the crack area in accordance with ASTM 1457-13. The voltage measurements were linearly interpolated with the initial and final crack dimensions to determine crack extension as a function of time.

Capacitance gauges were mounted into the mouths of C(T) specimens such that the gap between the parallel mouth faces were measured. This device could not be used with the wedge-loaded C(T) specimens due to the presence of the wedge. The capacitance gauge was available for use with the combined loading tests performed with the EB welded C(T) specimens (EBW6 and EBW7), and was used to measure mouth opening displacements, Δ_{MOD}. The device, supplied by EDF Energy, was designed to measure Δ_{MOD} at the load line [112]. The device was calibrated using an Instron tensile testing machine fitted with compression platens where a platen was displaced at fixed increments relative to the capacitance gauge and the measured voltages noted. The voltages varied linearly with the displacement and could measure displacement of up to 6 mm.

The method of placing the specimens in the furnace varied between the specimens tested. The combined loaded test specimens, EBW6 and EBW7, were held in shackles using

loading pins consistent with testing standard C(T) specimens under primary loads. However the remaining specimens could not be held with loading pins to allow deformation during relaxation and redistribution of the residual stresses. The specimens were either rested on a platform or suspended inside the furnace. The first thermal soaking tests were performed on the wedge-loaded C(T) specimens which were suspended in parallel inside a furnace. However difficulties in maintaining a constant temperature were encountered. Subsequently the EB welded C(T) specimens were rested inside the mouth of a loading shackle. Further details of this problem are presented in the following section.

6.4 RESULTS

6.4.1 THERMOCOUPLE, DCPD AND CAPACITANCE GAUGE MEASUREMENTS

Temperature and DCPD measurements recorded from CCG testing of the wedge-loaded C(T) specimens are shown in Figure 6.1 and Figure 6.2. Data are shown for the central thermocouple only for clarity as the variation of temperatures measured by all the thermocouples were within 1°C.

Specimens WC(T)3 and WC(T)4 were only tested for a short duration of 329 h. Both of these specimens were suspended in parallel inside the furnace using the current input strips for the DCPD technique. The specimens were initially at a temperature 550°C however within 2 h of the test the temperature of WC(T)4 began to rise whilst WC(T)3 reduced to 540°C. At 30 h the temperature of WC(T)4 peaked at 610°C and then suddenly reduced by 100°C. The stud weld holding the brass strip had failed and the specimen had fallen to the bottom of the

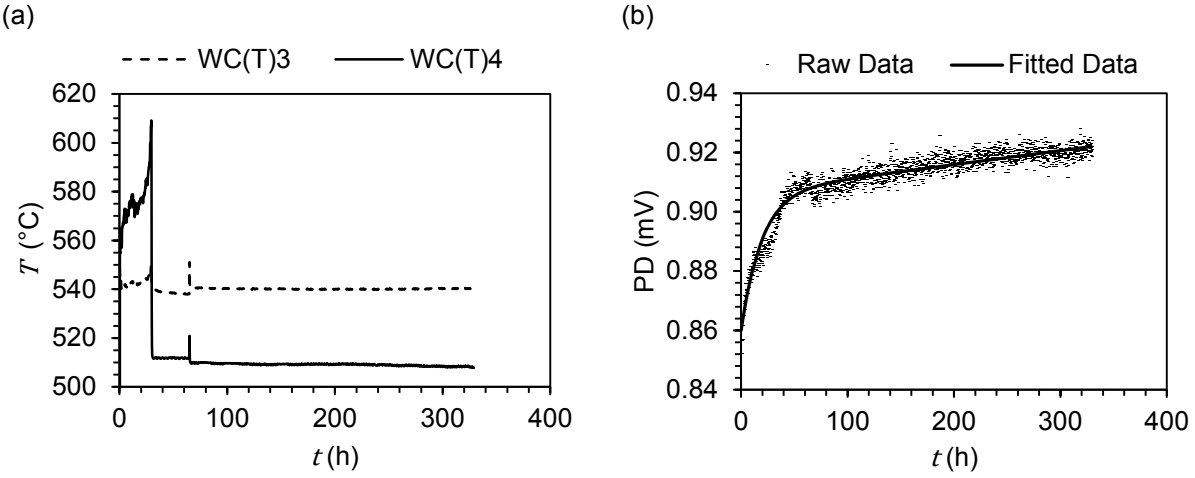


Figure 6.1 (a) Temperature measurements for specimen WC(T)3 and WC(T)4 (b) DCPD voltage measurements for specimen WC(T)3

furnace. The test continued for a further 300 h where WC(T)3 and WC(T)4 remained at 540°C and 510°C respectively.

Figure 6.1(b) shows the voltage measurements made using the DCPD technique for WC(T)3. The measurements show a large increase up to 60 h into the test and then subsequently a gentle rise for the remaining test duration indicating crack growth at a steady rate. No measurements were obtained for WC(T)4 due to the failure of the input lead and noise in the PD measurements at short durations caused by the unstable temperatures.

Specimen WC(T)5 was subsequently tested and held in a wire cradle inside the furnace to prevent the failure that occurred on WC(T)4. The input current for the DCPD technique was also reduced to 20 A whereas 30 A was used for specimens WC(T)3 and WC(T)4 to reduce the effect of resistive heating. It was considered that this may have had an

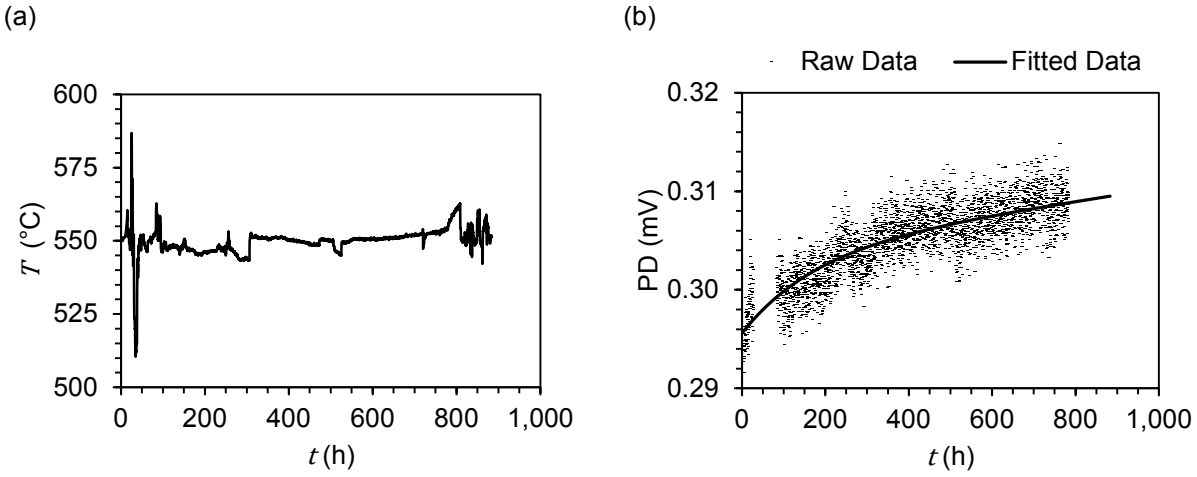


Figure 6.2 (a) Temperature measurements and (b) DCPD voltage measurements for specimen WC(T)5

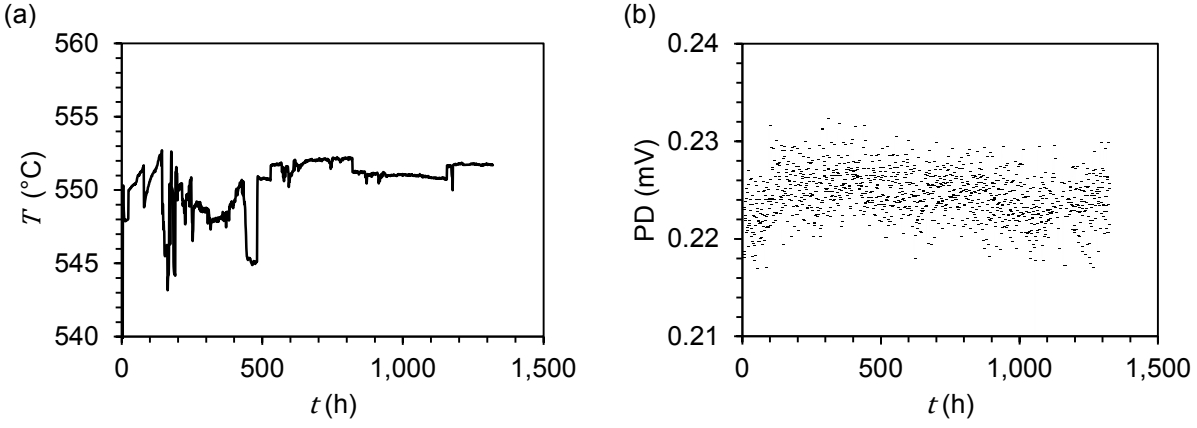


Figure 6.3 (a) Temperature, (b) DCPD voltage for specimen EBW3

effect on the temperature stability in the previous test. However, large temperature variations were again observed during testing of WC(T)5 between 10 and 100 h and after 780 h, as shown in Figure 6.2(a). There was significant noise in the DCPD measurements during these periods and hence these data points were removed from Figure 6.2(b). The remaining results indicate an increasing crack growth rate at the beginning of the test which became steady after 400 h.

Following this test, the cause of the temperature fluctuations was investigated by heating a test sample without residual stresses suspended in the furnace. It was found that fluctuations occurred when the DCPD input current was greater than 30 A. The heat induced by the electric resistance of the sample caused the temperature rise and at high currents the temperature fluctuated erratically, similar to that observed in the wedge-loaded C(T) specimens. When the sample was rested on a loading shackle, which is normally used with a pin to hold a standard C(T) specimen, heat induced by the DCPD current was conducted

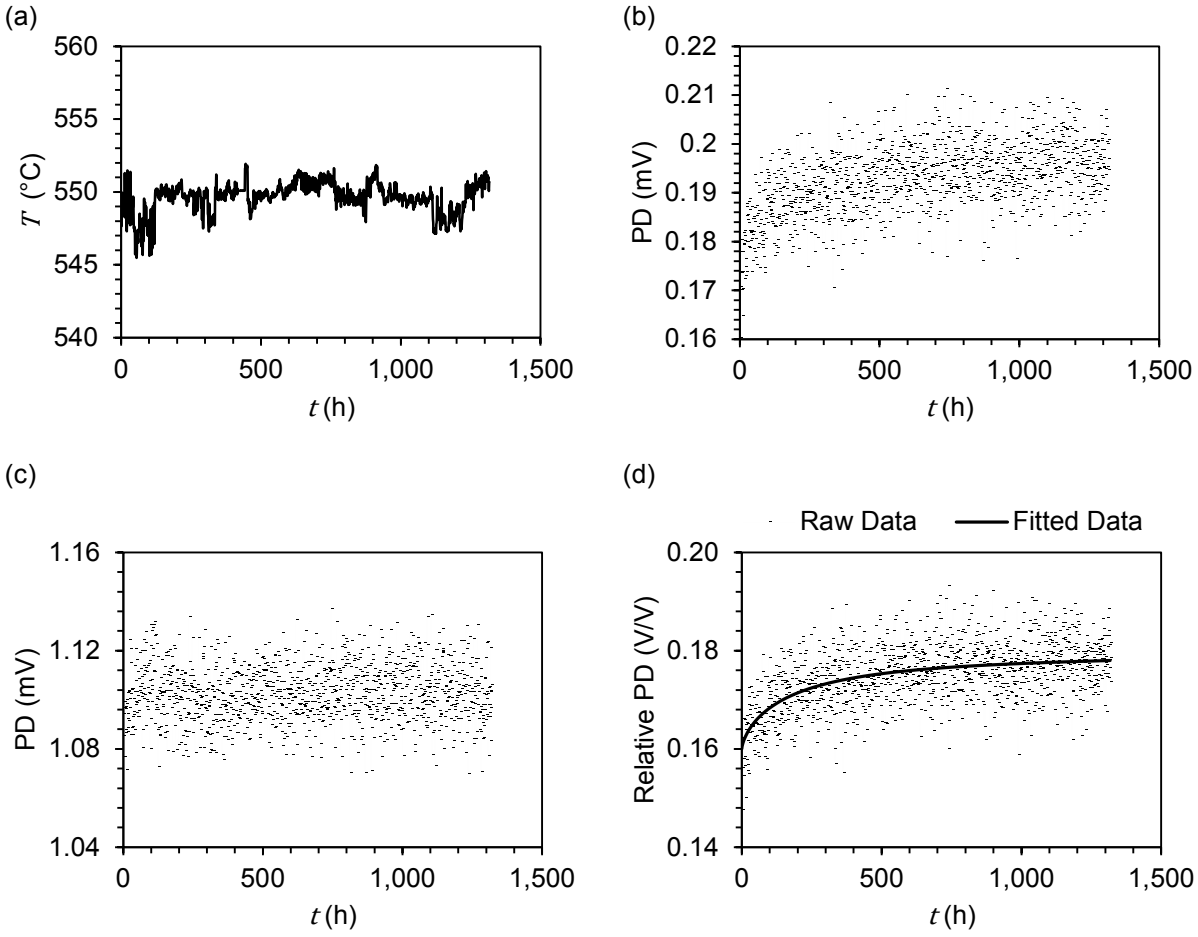


Figure 6.4 (a) Temperature, (b) DCPD voltage, (c) DCPD reference voltage and (d) relative DCPD voltage measurements for specimen EBW5

away to the test rig and due to this, large temperature fluctuations did not occur. Subsequent testing of the EB welded C(T) specimens were performed by resting the specimen on the shackle.

The temperature and DCPD voltage measurements for specimens EBW3 and EBW5 are shown in Figure 6.3 and Figure 6.4 respectively. Temperature fluctuations persisted in these specimens however were less severe than for the wedge-loaded C(T) specimens. The PD voltages measured in specimen EBW3 were relatively constant for the duration of the test suggesting no crack growth. In specimen EBW5 the PD voltage increased during the first 500 h of the test only. In specimen EBW5 reference voltage measurements were taken across the back face of the sample which was far from the pre-crack. Here the voltage increase due to temperature changes in the material was measured, which could be used to

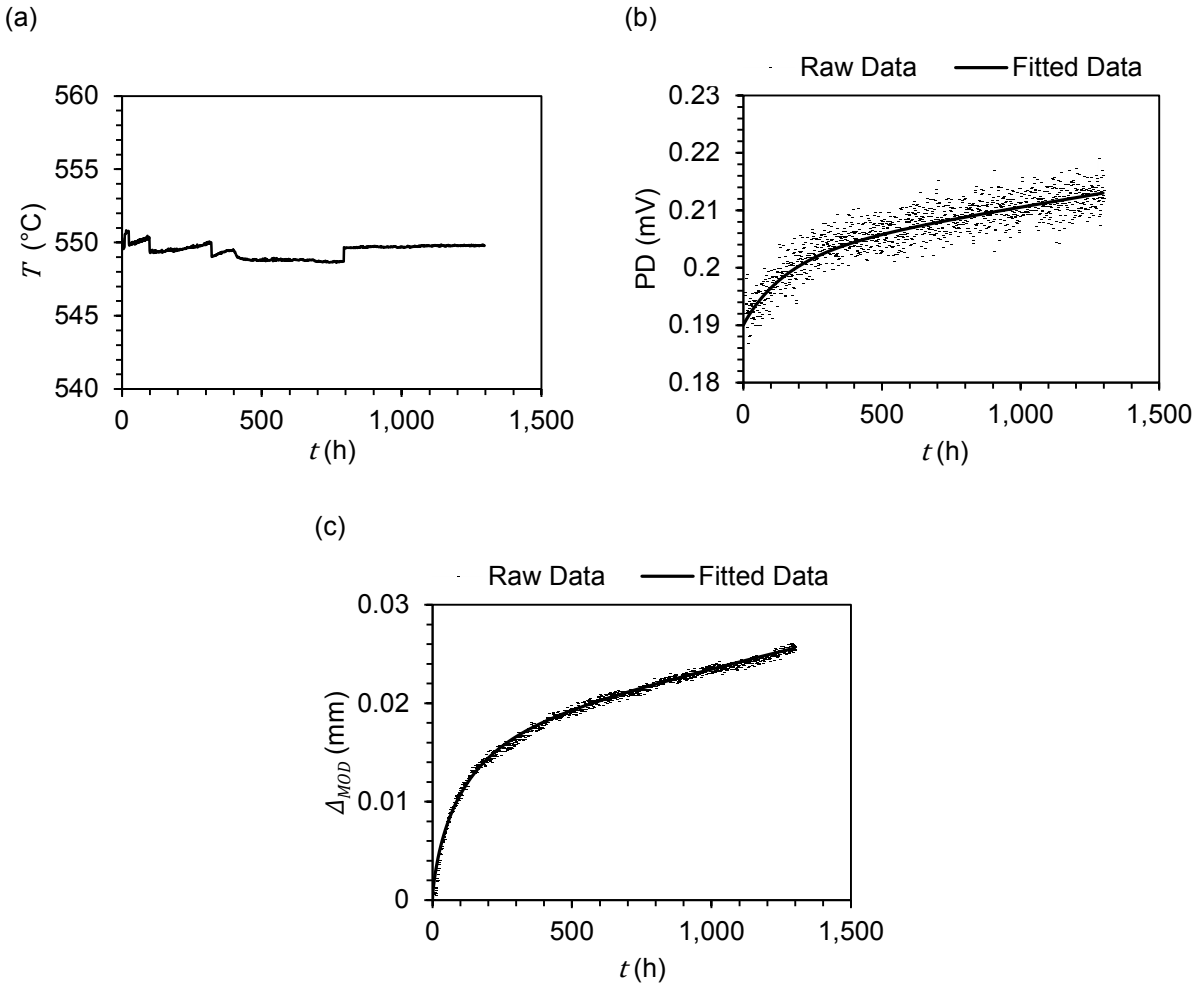


Figure 6.5 (a) Temperature, (b) DCPD voltage and (c) mouth opening displacement measurements for specimen EBW6

normalise the PD measurements for this sample. However the change in reference PD voltage during the test was indistinguishable from the noise in the voltage measurements.

In-situ measurements made in specimens EBW6 and EBW7 which were tested under combined loading conditions are shown in Figure 6.5 and Figure 6.6 respectively. In addition to temperature and PD measurements, load line displacements were also measured using capacitance gauges. The temperature measurements for both specimens were stable during the test, here the local heating effect from the DCPD technique was not encountered. The PD and capacitance gauges show large amounts of deformation and cracking respectively in the early stages of the test. At longer times the deformation and crack growth rates are observed to be constantly increasing.

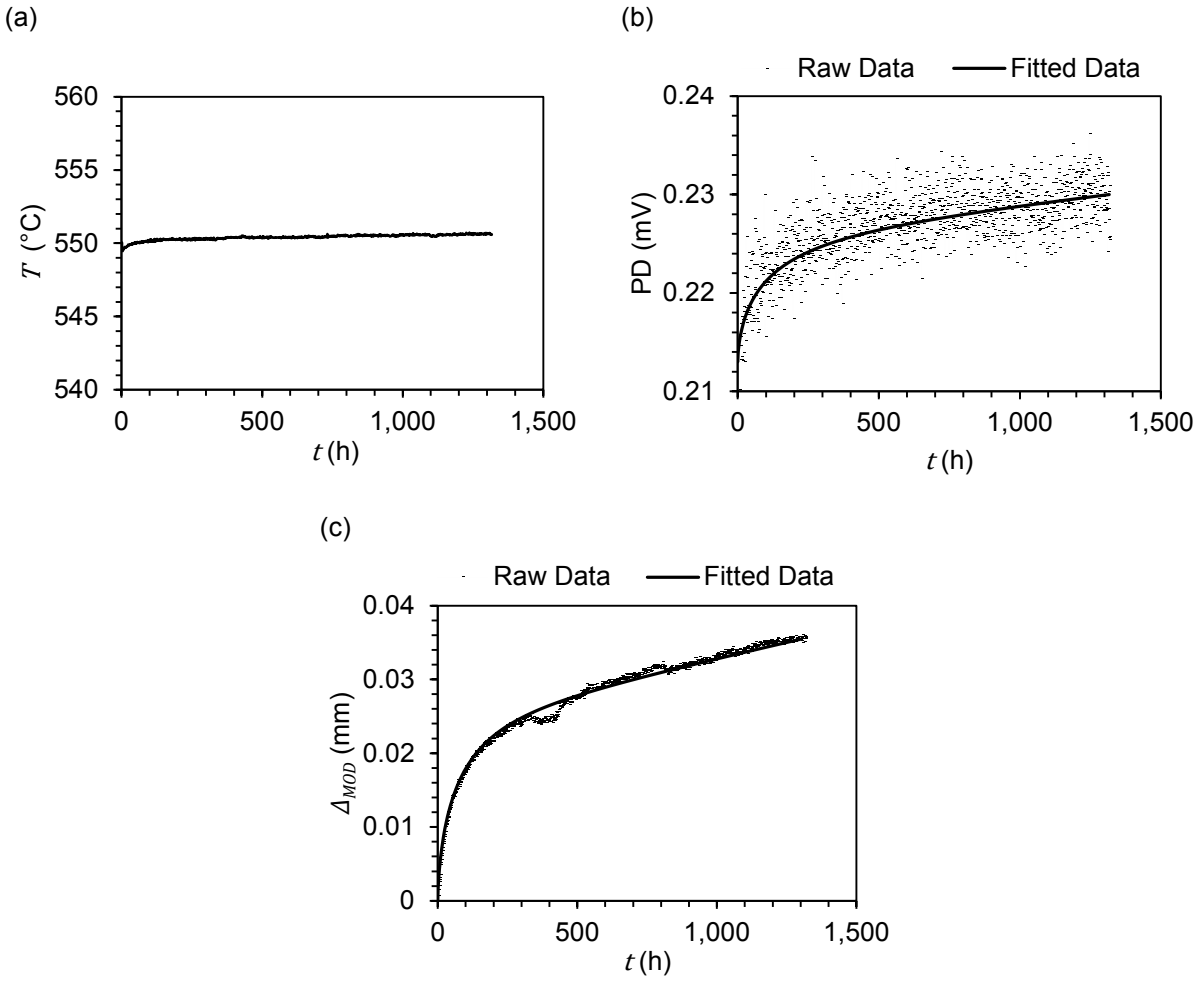


Figure 6.6 (a) Temperature, (b) DCPD voltage and (c) relative DCPD voltage measurements for specimen EBW7

6.4.2 METALLOGRAPHY

The specimens were broken open following CCG testing to assess the extent of crack growth. Using wire EDM a 5 mm slice from mid-thickness of the specimens were extracted to create micrographs of the crack. The slice was ground, polished and etched using Ferric Chloride to reveal the microstructure surrounding the crack. The outer 10 mm regions of the specimens were broken open to assess the shape of the crack fronts. The specimens were frozen in liquid nitrogen and fractured open using an Instron tensile testing machine. Creep crack growth was identified by dark regions on the fracture surface which discoloured due to oxidation at high temperature. In specimen WC(T)3 only a 5 mm wide slice, near mid-thickness, was fractured open.

The micrographs of the cracks were obtained from planes A and C as shown in Figure 6.7 for the wedge-loaded and EB welded C(T) specimens respectively. Similarly the fracture surface regions were extracted from planes B and D, which are shown from Figure 6.8 to Figure 6.14 for all the C(T) specimens tested. These images were used to determine the final crack lengths. A straight fronted crack was assumed in the central region of the specimens where material was extracted to obtain the micrographs. The maximum and average crack extensions, Δa_{max} and Δa_{avg} respectively, are shown in Table 6.2. Of the wedge-loaded C(T) specimens, WC(T)5 had the largest crack depth. All the wedge-loaded C(T) specimens had bowed crack fronts with little or no crack growth on the side faces. Discontinuous cracking was observed near the crack tip as shown in the micrographs. The crack lengths, Δa_{max}, were measured from the deepest cracks observed in the micrographs. These crack lengths were in close agreement with those measured near the mid-thickness region in the fracture surface images.

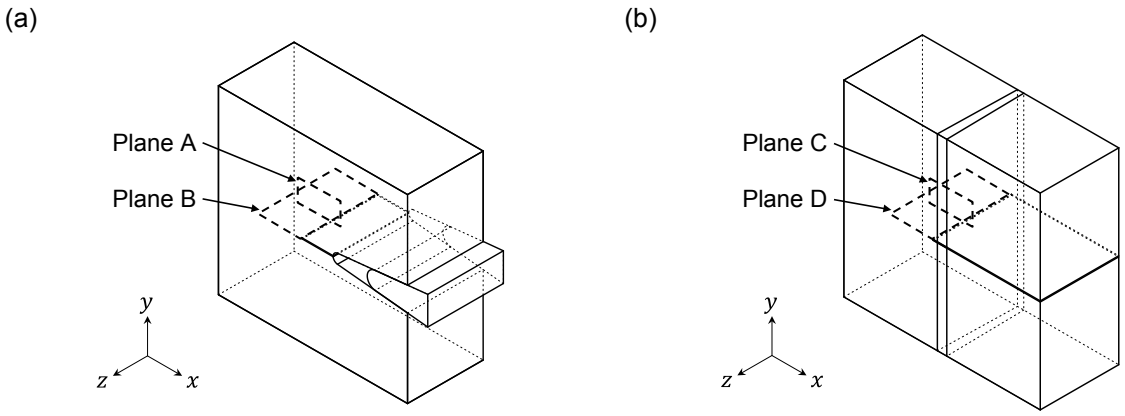


Figure 6.7 Location of planes used to image crack micrographs and fracture surfaces in (a) wedge-loaded C(T) specimens and (b) EB welded C(T) specimens

(a) (b)

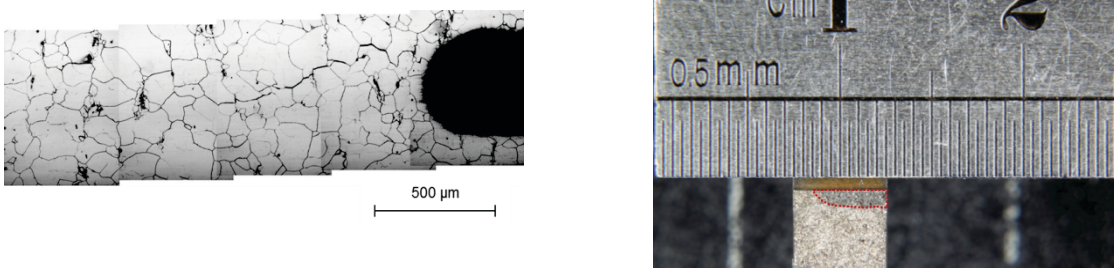


Figure 6.8 (a) Crack micrograph and (b) fracture surface of specimen WC(T)3

(a) (b)

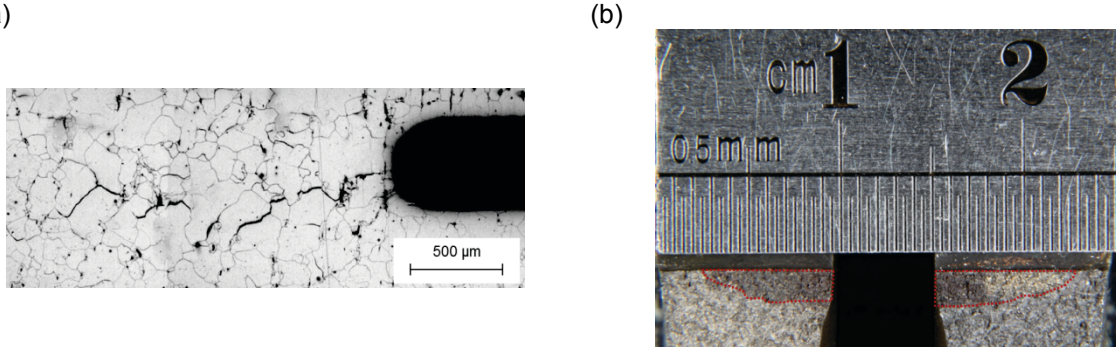
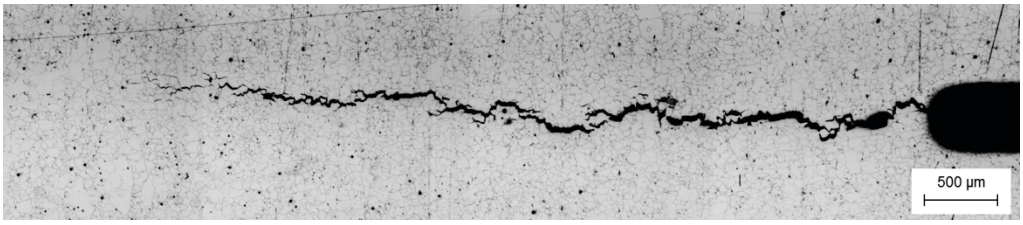


Figure 6.9 (a) Crack micrograph and (b) fracture surface of specimen WC(T)4

(a)



(b)

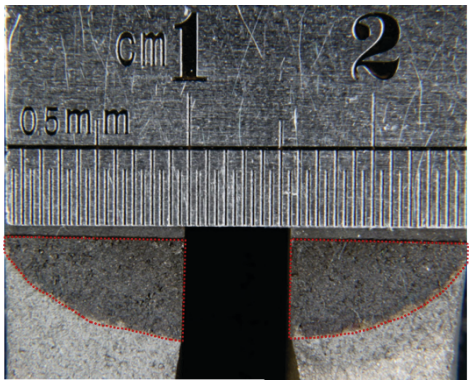


Figure 6.10 (a) Crack micrograph and (b) fracture surface of specimen WC(T)5

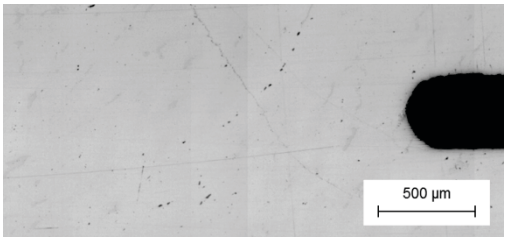
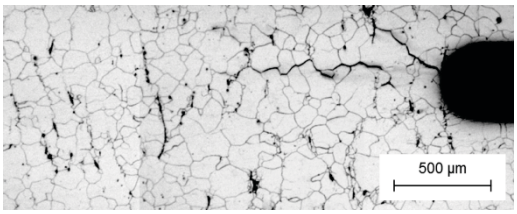


Figure 6.11 Crack micrograph of specimen EBW3

(a)



(b)

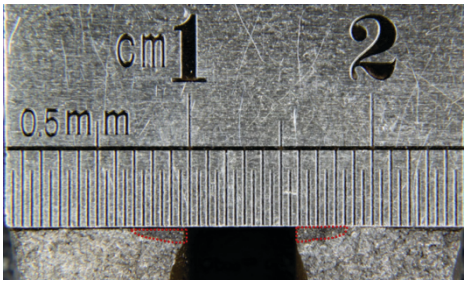
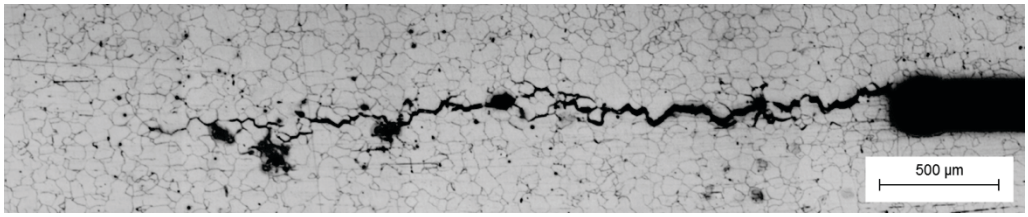


Figure 6.12 (a) Crack micrograph and (b) fracture surface of specimen EBW5

(a)



(b)

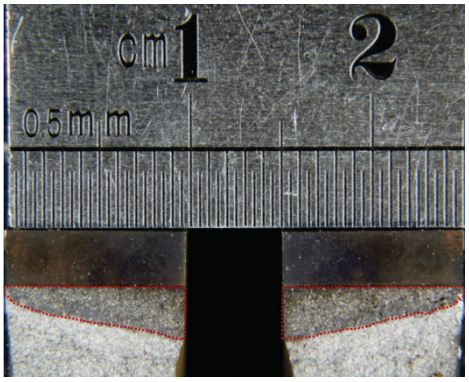
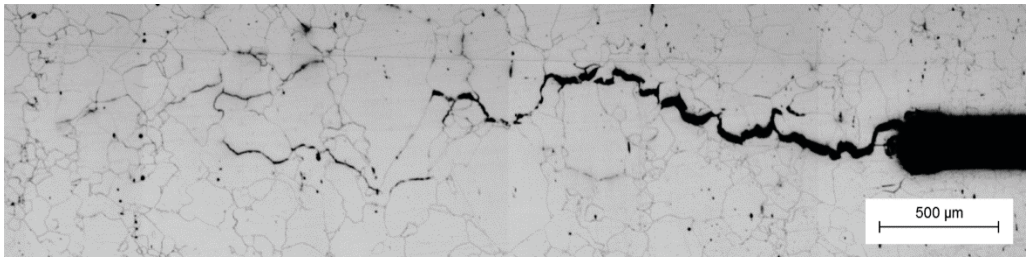


Figure 6.13 (a) Crack micrograph and (b) fracture surface of specimen EBW6

(a)



(b)

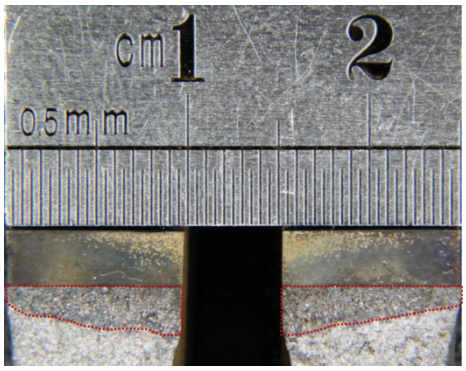


Figure 6.14 (a) Crack micrograph and (b) fracture surface of specimen EBW7

Specimen EBW3, which was made of Type 316H stainless steel in the as-received material condition, had no crack growth. Whereas EBW5, which was made of 8% pre-compressed Type 316H stainless steel, had crack growth of up to 1.2 mm. No crack growth was observed on the sides of EBW5 with cracking limited to the mid-thickness region. In EBW6 and EBW7, which were tested under combined loading, crack extensions of up to 3.3 mm were observed which was greater than EBW5, which had no primary load. Both EBW6 and EBW7 showed similar amounts of cracking.

Crack growth in all specimens was intergranular. In specimen WC(T)3, WC(T)4 and EBW5 the micrographs show the crack is discontinuous, indicating that microcracks had formed on grain boundaries which eventually linked to form a macrocrack. Average grain sizes were also determined from the micrographs and are shown in Table 6.2. The grain

Table 6.2 Maximum crack length, average crack length and grain diameter in C(T) specimens

Specimen	Δa_{max} (mm)	Δa_{avg} (mm)	d_g (µm)
WC(T)3	0.9	0.3	90
WC(T)4	1.8	1.2	110
WC(T)5	5.4	4.1	60
EBW3	0.0	0.0	120
EBW5	1.2	0.4	90
EBW6	3.1	2.0	80
EBW7	3.3	2.1	120

diameters, d_g, varied significantly between specimens where diameters of between 60 μm to 120 μm were observed.

Estimated crack lengths during the CCG tests were determined by interpolating the DCPD voltages with crack length measurements and are shown in Figure 6.15 and Figure 6.16 for the wedge-loaded and EB welded C(T) specimens respectively.

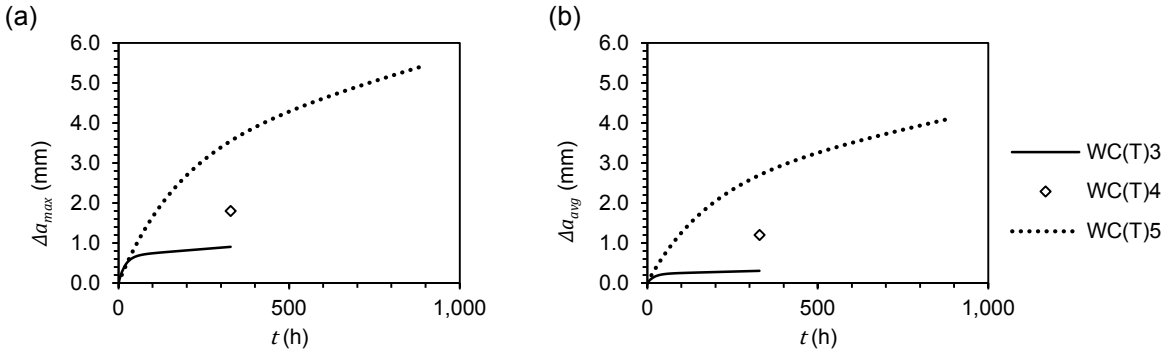


Figure 6.15 (a) Maximum and (b) average crack length during CCG testing of wedge-loaded C(T) specimens determined using PD data

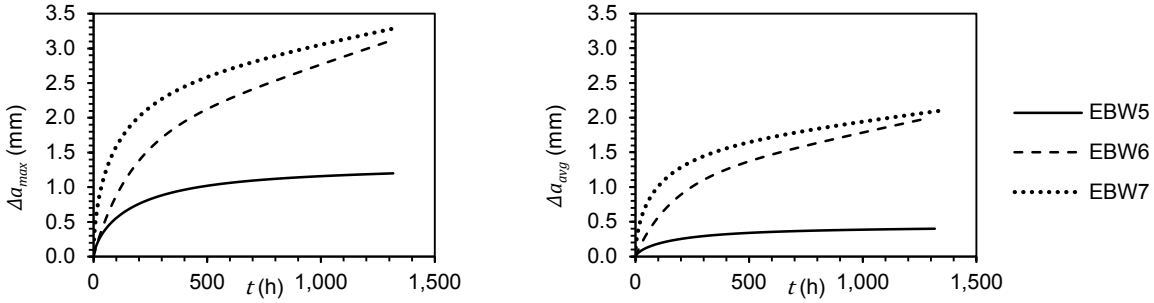


Figure 6.16 (a) Maximum and (b) average crack length during CCG testing of EB welded C(T) specimens determined using PD data

6.5 DISCUSSION

The experimental results presented in this chapter show large crack extensions occurred in the C(T) specimens due to the influence of residual stresses. This enabled crack growth estimates under secondary and combined loading conditions to be made, which are presented in the following chapter. Five specimens were tested under secondary loading conditions, which each had different initial crack driving forces. Crack growth was observed in all but one of these specimens when thermally soaked at 550°C. Two further tests were conducted under combined loading conditions, using the EB welded C(T) specimen design, which showed larger crack lengths for increasing applied loads.

Some variations in the crack growth rates were observed in the wedge-loaded C(T) specimens. The crack grew quicker in WC(T)5 in comparison to WC(T)4, as shown in Figure 6.15, whereas K^S was greater in WC(T)4. The slow crack growth rate observed in WC(T)4 occurred due to the low test temperature of 510°C that was applied for most of the test duration and also due to the differences in microstructure between specimens. All of the wedge-loaded C(T) specimens were extracted from the same ex-service steam header. However, WC(T)5 was obtained from a different region of the component which had a relatively fine microstructure, as shown in Table 6.2. Similarly, some variation in crack growth rates were observed in the tests performed under combined loading conditions. Specimen EBW6 had almost as much crack growth as EBW7, in which the primary load was twice as large. Table 6.2 shows the grain size of EBW6 was smaller than EBW7.

The variation in crack lengths between specimens appeared to be linked to the different microstructures observed in the crack region. Under certain creep mechanisms such as diffusional creep, strain rates increase for materials with a fine grain size [114, pp53-60]. In small grains, vacancies need to diffuse shorter distances to nucleate on grain boundaries and contributes to reducing the creep resistance of the material. The specimens with smaller grains were observed to have relatively large crack extensions. The variation in crack lengths are consistent with the scatter in CCG rates observed in primary loaded C(T) specimens made of Type 316H stainless steel [18].

All DCPD measurements showed large increases in voltage in the initial stages of the CCG tests. This may have been caused by large strains accumulated in the primary creep regime rather than crack growth [77]. Dogan et al. [115] recommend that this initial increase is removed from the dataset. However, as the residual stresses relaxed during the tests, the crack growth rate also reduced. The change in PD measurement due to creep deformation and crack growth could not be distinguished. From the PD data, it is unclear when crack initiation occurred, further work is needed to investigate this.

In Section 2.4, other specimens used to perform CCG tests under secondary loads on Type 316H stainless steel at 550°C were reviewed. The residual stress component normal to the crack plane in the EB welded and wedge-loaded C(T) specimens are compared to those in pre-compressed and side-punched C(T) specimens in Figure 6.17(a). The data are from FE analyses of each specimen and were determined at mid-thickness and at room temperature. All specimens had large tensile residual stresses at the crack tip. The tensile stresses in the wedge-loaded C(T) specimens acted over a much longer length scale relative

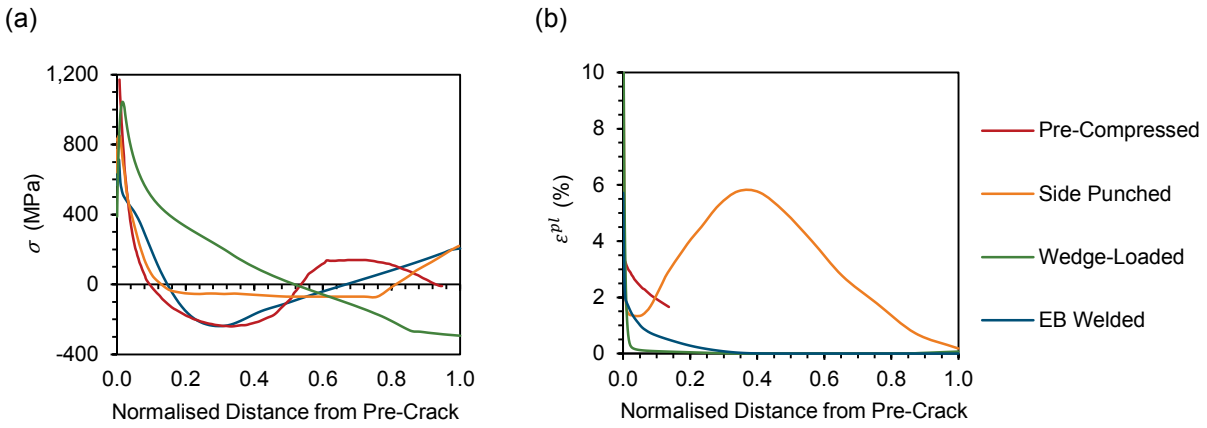


Figure 6.17 Comparison of (a) stress normal to crack plane and (b) ε^{pl} for C(T) specimens under secondary loading conditions (data from [33] and [38])

to the other specimens. Figure 6.17(b) shows all specimens had large plastic strains near the crack tip due to the stress concentration effect of the pre-crack. However, ε^{pl} reduced rapidly from the crack tip in the wedge-loaded C(T) specimens, whereas the pre-compressed C(T) specimen had the largest plastic strains around the pre-crack. The wedge-loaded C(T) specimen is an ideal design to perform CCG tests under secondary loading conditions, due to the large magnitude of tensile stresses, which act over a relatively long length scale, and furthermore due to the limited plasticity across the ligament of the specimen. This allows the effects of residual stresses on CCG to be separated from the influence of plasticity, which was a key objective in this study.

CCG tests were performed in pre-compressed C(T) specimens made of ex-service Type 316H stainless steel by Turski et al. [3, 33] where cracks of up to 2.1 mm were formed. Initially K^s was determined to be 37.6 MPam$^{1/2}$ at the mid-thickness of specimen CT1 which was comparable to WC(T)3. The test duration was considerably longer at 4,500 h. Using the DCPD measurements presented by Turski [33], Webster et al. [116] estimated the crack extensions during the test. At 300 h, approximately 1.1 mm of crack growth was estimated in specimen CT1. This was similar to that in observed in WC(T)3 and therefore the results appear consistent between these two studies.

Some CCG tests under secondary loading conditions conducted by Hossain et al. [38] and Nezhad [31] on side punched and pre-compressed C(T) specimens respectively showed very small crack extensions. The residual stresses relaxed before significant crack growth occurred. The EB welded C(T) specimen, EBW3, was tested using material in the as-received condition and also had no crack growth. In comparison, the specimens fabricated

from material that had been uniformly pre-compressed and which were tested under secondary loading conditions had large crack extensions. This demonstrated the benefit of using uniformly pre-compressed material where the creep ductility of the material was reduced to increase the likelihood for crack growth to occur due to residual stresses alone. As the pre-compression process caused plastic strains that were uniform across the specimen, the creep ductility was also assumed to be uniformly reduced across the specimens. Therefore the rate of crack growth was assumed to be independent of plasticity.

At mid-thickness, specimens EBW6 and EBW7 had an initial total K of 27.2 MPam$^{1/2}$ and 32.2 MPam$^{1/2}$ respectively. These are comparable to the CCG tests performed on 8% pre-compressed Type 316H stainless steel by Mehmanparast et al. [18] under primary loading conditions, which had an initial K between 25 MPam$^{1/2}$ and 35 MPam$^{1/2}$. The duration of these tests were from 194 h to 1,303 h where the tests were stopped prior to final fracture. The crack lengths measured by Mehmanparast et al. were much longer than those in EBW6 and EBW7. In the tests under primary load conditions, the crack driving force increased with crack extension. This caused the crack growth rate to accelerate at large times. In comparison, in loading conditions dominated by residual stresses, the crack driving force reduces at large times due to stress relaxation and hence the crack growth rate decreases.

Davies et al. [117] performed CCG tests on C(T) specimens extracted from ex-service MMA weldments made of Type 316H stainless steel, where the cracks were positioned in the HAZ region as shown in Section 2.4.4. The specimens were fabricated using EB welding to attach the loading arms of the C(T) specimen where the EB weld was also located approximately 3 mm away from the pre-crack. Tensile stresses of approximately 350 MPa were measured ahead of the pre-crack by ND diffraction which is comparable with that measured in EBW5. Hence the initial K^s in these specimens are also assumed to be similar to the EB welded C(T) specimens tested in this study. Primary loads with K^p of 28 MPam$^{1/2}$ and above were used by Davies et al. to test these HAZ specimens, which were far greater than those applied to EBW6 and EBW7. Due to the high combined load, large crack growth rates were measured where failure occurred in all but one of the tests within 933 h. The residual stresses from the EB welds had a significant effect on crack initiation and growth rates during testing of the HAZ specimens. Therefore the location of EB welds, when used as a joining technique to fabricate C(T) specimens, must be carefully considered to prevent the residual stresses from adversely effecting subsequent CCG tests.

6.6 SUMMARY

CCG studies were conducted under secondary and combined loading conditions where significant cracking was observed in all specimens made of Type 316H stainless steel in the pre-compressed material condition. The wedge-loaded C(T) specimen, which had little variation of plasticity ahead of the crack tip, was found to be an ideal specimen design to investigate the effect of CCG due to the relaxation of residual stresses. Pre-conditioning the material during specimen fabrication was shown to be necessary to allow CCG under secondary conditions to be investigated. Some of the crack lengths appear to be inconsistent between specimens, however this was attributed to the variation of creep ductilities between specimens which is commonly observed in CCG testing of this material.

The extent of creep crack growth observed was consistent with similar tests performed under primary, secondary and combined loading conditions. Comparison to primary loaded specimens which initially have similar crack driving forces highlight the effect of stress relaxation which causes crack growth rates to reduce at large times.

7 ASSESSMENT OF STRESS RELAXATION AND CRACK GROWTH

7.1 INTRODUCTION

Relaxation of residual stresses occurs in components when operating at high temperatures, within the materials creep regime. Misfits between different components or regions of material (e.g. between the SAZ and parent material near welds) cause elastic strains to exist within the component. During operation at high temperature creep strains accumulate to reduce the magnitude of these elastic strains. Hence the effect of the misfit is reduced and the residual stresses relax.

This chapter presents a study of stress relaxation in C(T) specimens under secondary loading conditions. The creep deformation models detailed in Section 2.2.3 were first used to predict stress relaxation in uniaxial constant-displacement tests on Type 316H stainless steel to assess the accuracy of the creep deformation models in a simple load case. Following this, the creep models were used to predict relaxation of residual stresses in the C(T) specimens during CCG tests. Comparisons of these stress predictions with ND residual stress measurements made after CCG testing are presented.

As the C(T) specimens were thermally soaked, the accumulation of creep strains caused creep damage at the grain boundaries, which in turn resulted in intergranular cracking. Estimates of crack lengths in the C(T) specimens tested under secondary and combined loading were made using analytical approaches based on the $C(t)$ parameter, as defined in the recently updated R5 procedure [2]. Comparisons of the crack length predictions with the experimental measurements presented in Chapter 6 were used to assess the R5 approach. Crack length estimates were also made by numerical modelling using the creep damage concepts detailed in Section 2.2.4. In this chapter a comparison of these crack length predictions with the experimentally measured crack lengths are presented.

7.2 RELAXATION OF RESIDUAL STRESSES

7.2.1 ESTIMATION OF STRESS RELAXATION

The stress relaxation rate in an uncracked body under displacement controlled loading may be determined analytically. In such a test the total strain, ε, on the specimen can be fixed and therefore the total strain rate, $\dot{\varepsilon}$, is zero.

The stress relaxation rate, $\dot{\sigma}$, under secondary loading and elastic creep conditions may be determined by:

$$\dot{\varepsilon} = \dot{\varepsilon}^e + \dot{\varepsilon}^c = 0$$
$$\frac{\dot{\sigma}}{E} = -\dot{\varepsilon}^c \tag{7.1}$$

The extent of stress relaxation may be determined analytically by integration of (7.1) between the limits of $\sigma(0) = \sigma_0$ and $\sigma(t) = \sigma$. For $\dot{\varepsilon}_c(\sigma, t)$ defined by the Norton creep law (2.6) and the primary regime of the RCC-MR model with time hardening (2.18), stress relaxation is determined by (7.2) and (7.3) respectively.

$$\sigma = [\sigma^{1-n} + CE\,(n-1)t]^{1/1-n} \tag{7.2}$$

$$\sigma = [\sigma^{1-n_1} + C_1E\,(n_1-1)t^{C_2}]^{1/1-n_1} \tag{7.3}$$

where the constants are defined in Section 2.2.3. At large times the second terms in (7.2) and (7.3) dominate and the equations show the relaxed stresses become independent of the initial stress.

Alternatively where an analytical solution for (7.1) cannot be obtained, e.g. for the RCC-MR creep model with strain hardening (2.19), σ must be evaluated numerically. In such cases (7.1) may be solved using explicit numerical integration such as the Runge-Kutta method [118, pp64-70] or using FE analyses.

7.2.2 STRESS RELAXATION IN UNIAXIAL SPECIMENS

Douglas et al. [13] investigated stress relaxation in ex-service Type 316H stainless steel using uniaxial creep tests conducted at constant-displacement. Ten tests were performed at temperatures ranging from 500°C to 600°C, with initial stresses from 125 MPa to 230 MPa and test durations of up to 14,367 h. Three test specimens, R0394, FLZ002 and R0395, were conducted at 550°C with initial stresses, σ_0, of 125 MPa, 190 MPa and 230 MPa respectively. The results of these three tests are shown in Figure 7.1, where the data was obtained from [13].

Stress relaxation occurred in all three test specimens with the stresses reducing towards the same magnitude at large times. However, the stress relaxation rates were observed to be inconsistent between the specimens. The stress magnitude for specimen FLZ002 (σ_0 = 190 MPa) was expected to remain below specimen R0395 (σ_0 = 230 MPa) for

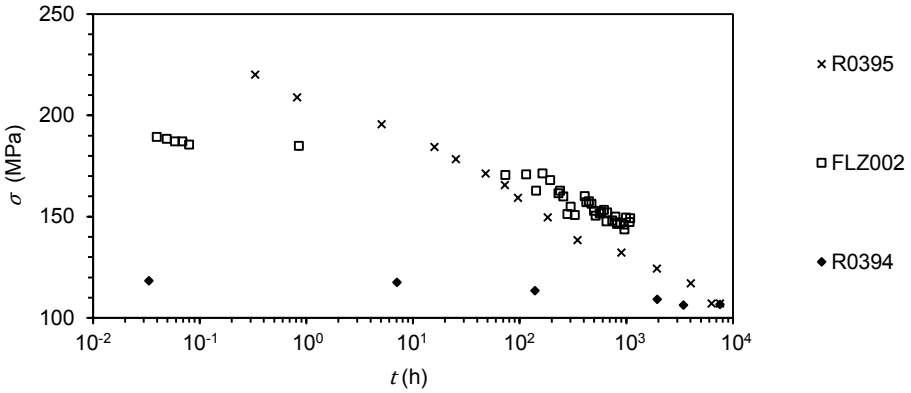


Figure 7.1 Stress relaxation measured from constant-displacement creep tests of Type 316H stainless steel at 550°C (data from [13])

the duration of the test however this was not observed in the experimental data. After 100 h of testing the stress in R0395 had unexpectedly relaxed to below FLZ002. In specimen R0394 which had an initial stress of 125 MPa only a small amount of stress relaxation was observed.

The inconsistency in stress relaxation rates may have been due to the variation in material properties between test samples or due to different testing approaches. The tests were performed on material of the same cast (69431) however FLZ002 was obtained from a different steam header component to R0394 and R0395 and therefore experienced different thermal loads during service. Specimen FLZ002 was held at constant-displacement using a servo-controlled testing machine whereas the load was reduced manually in tests R0394 and R0395. In general all the tests presented in [13] which were performed using the servo-controlled testing machines showed less stress relaxation than the manually unloaded machines [119].

Stress relaxation predictions were made for the uniaxial constant-displacement creep tests using a single element plane stress FE simulation. Predictions were made using the RCC-MR creep law using time hardening, (2.18), and strain hardening assumptions, (2.19), the Norton creep law with average creep strain rate, (2.7), and using the exponential creep laws fitted by Douglas et al. [13], (2.12), and Chen et al. [11], (2.13). The models were defined using the CREEP user-subroutine in ABAQUS [49]. The stress predictions were compared to the experimental measurements, as shown in Figure 7.2. The time axes are shown using logarithmic and linear scales to highlight the short term and long term predictions. The comparison enabled the accuracy of each deformation model at predicting

stress relaxation to be determined. This comparison also allowed the user-subroutines that defined creep deformations in the FE model to be validated.

The RCC-MR strain hardening model provided the best estimate for test specimen R0395 (σ_0 = 230 MPa) whilst the average creep model and exponential creep model fitted by Chen et al. gave the closest predictions for specimen FLZ002 (σ_0 = 190 MPa). The average creep model and exponential creep model fitted by Chen et al. provided reasonable predictions for specimen R0394 (σ_0 = 125 MPa), however this test specimen showed comparatively less stress relaxation.

Creep deformation maps for Type 316 stainless steel [120, p65] show that at low stresses the creep mechanism is diffusion creep instead of power-law creep, which has lower creep strain rates. The creep deformation laws were determined for creep in the power-law creep region, e.g. Chen et al. fitted the model to uniaxial tests between 230 MPa and 300 MPa. Therefore these creep models could not accurately predict creep deformation at low stresses.

Overall, none of the models provided stress relaxation predictions which closely agreed with all three experimental tests. However, this was partially due to the inconsistent stress relaxation rates in the test data. The exponential creep models use an internal stress term which was empirically fitted to the test data shown in Figure 7.1 by Douglas et al. and Chen et al. to improve stress relaxation predictions. It is recommended further uniaxial constant-displacement tests are conducted to improve the accuracy of this fit.

To understand stress relaxation behaviour Chen et al. performed further studies to understand the presence of internal stresses in Type 316H stainless steel [121]. The internal stresses are caused by type II residual stresses i.e. the misfit between different grains within a polycrystalline structure. This study also introduces an internal resistance term which defines the material microstructure's tendency to impede dislocation motion and recommends this effect should also be included in creep constitutive models. A new creep model for Type 316H stainless steel is currently under development as part of the High Temperature Behaviour of Austenitic Stainless Steels (HTBASS) programme which should provide improved stress relaxation predictions [122].

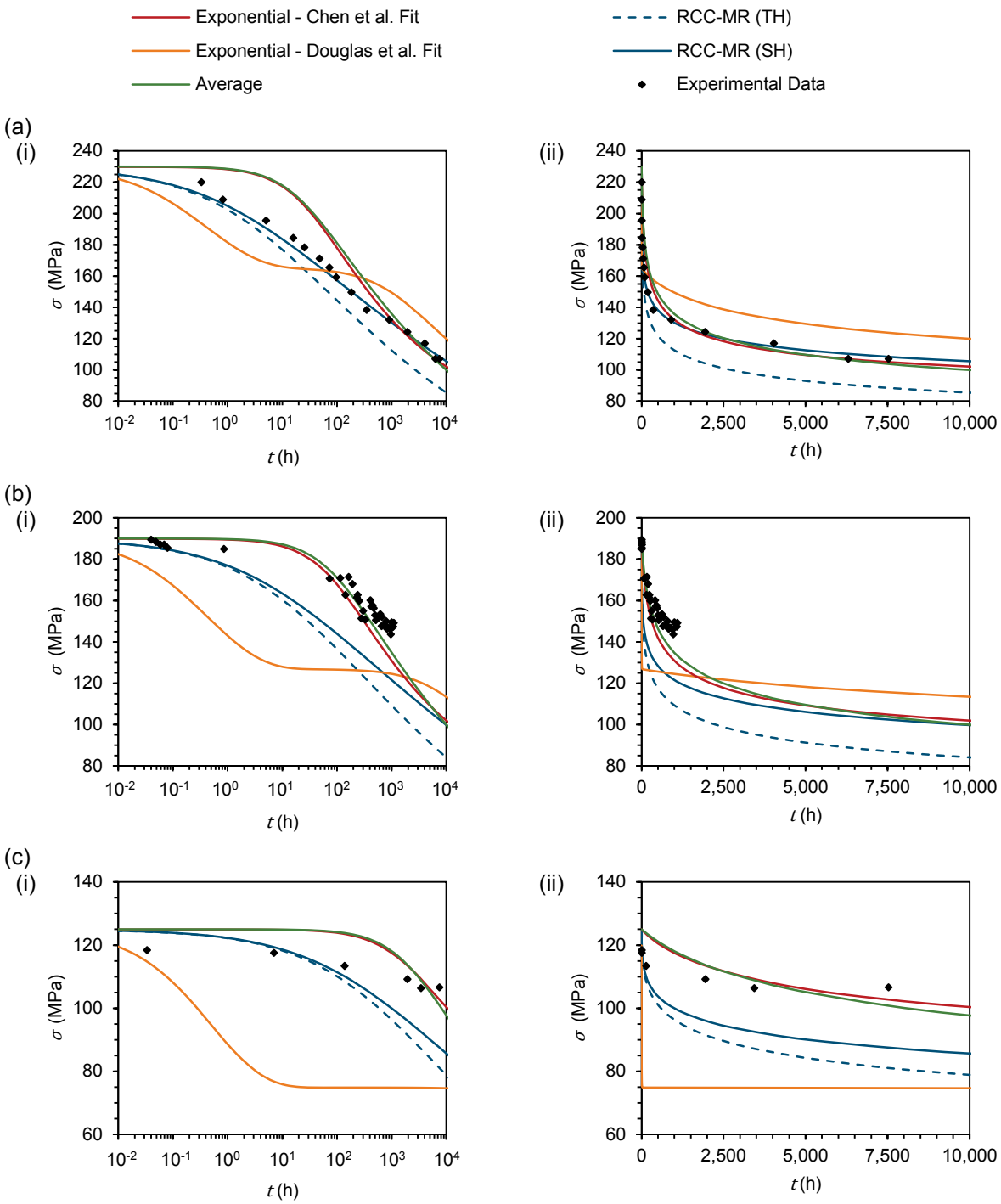


Figure 7.2 Comparison of stress relaxation predicted by creep deformation laws with uniaxial constant-displacement creep tests at 550°C: (a) σ_0 = 230 MPa (R0395), (b) σ_0 = 190 MPa (FLZ002) and (c) σ_0 = 125 MPa (R0394); (i) log-linear plot and (ii) linear-linear plot.

7.2.3 STRESS RELAXATION IN C(T) SPECIMENS

Stress relaxation in specimens WC(T)3, WC(T)5 and EBW5 were predicted using the creep deformation models shown in Section 2.2.3 and the FE models developed in Chapter 4 and Chapter 5. Creep was modelled for 329 h, 885 h and 1,340 h for specimens WC(T)3, WC(T)5 and EBW5 respectively. No crack growth was modelled in these simulations. Cooling of the specimens to 20°C was also modelled to determine the residual stresses at room temperature for comparison with ND measurements.

The residual stresses were measured in the specimens at mid-thickness along the ligament of the specimens by ND after CCG testing. Specimen WC(T)3 was measured using the instrument Stress-Spec at FRM II and WC(T)5 and EBW5 were measured using instrument E3 at HZB. The measurement procedures were consistent with those made during fabrication of the C(T) specimens as presented in Section 3.6 and Section 5.3.3, where gauge volumes of 2 × 2 × 2 mm^3 and 2 × 2 × 10 mm^3 were used for Stress-Spec and E3 respectively. For each specimen, the stress component normal to the plane of crack growth is compared with FE predictions using the various creep deformation models in Figure 7.3.

In general all creep models under-estimated the extent of stress relaxation in specimens WC(T)3 and EBW5. In specimen WC(T)3, the exponential creep law defined by Douglas et al. predicted the largest reduction in stress magnitude which was consistent with that for the short term predictions in the uniaxial constant-displacement tests. However the stresses still remained greater than the ND measurements. In specimen EBW5, all creep models predicted similar magnitudes of stress relaxation. At a distance 2 mm from the pre-crack the reduction in stress was measured experimentally as 300 MPa whereas the FE models predicted a smaller reduction of up to 150 MPa.

The FE models do not take into account redistribution due to crack extension. The effect of redistribution can be seen in the ND measurements in Figure 7.3(b) for specimen WC(T)5, where Δa = 5.4 mm. Despite stress relaxation occurring, stress redistribution due to cracking caused the stresses to have the same magnitude in the uncracked ligament after CCG testing.

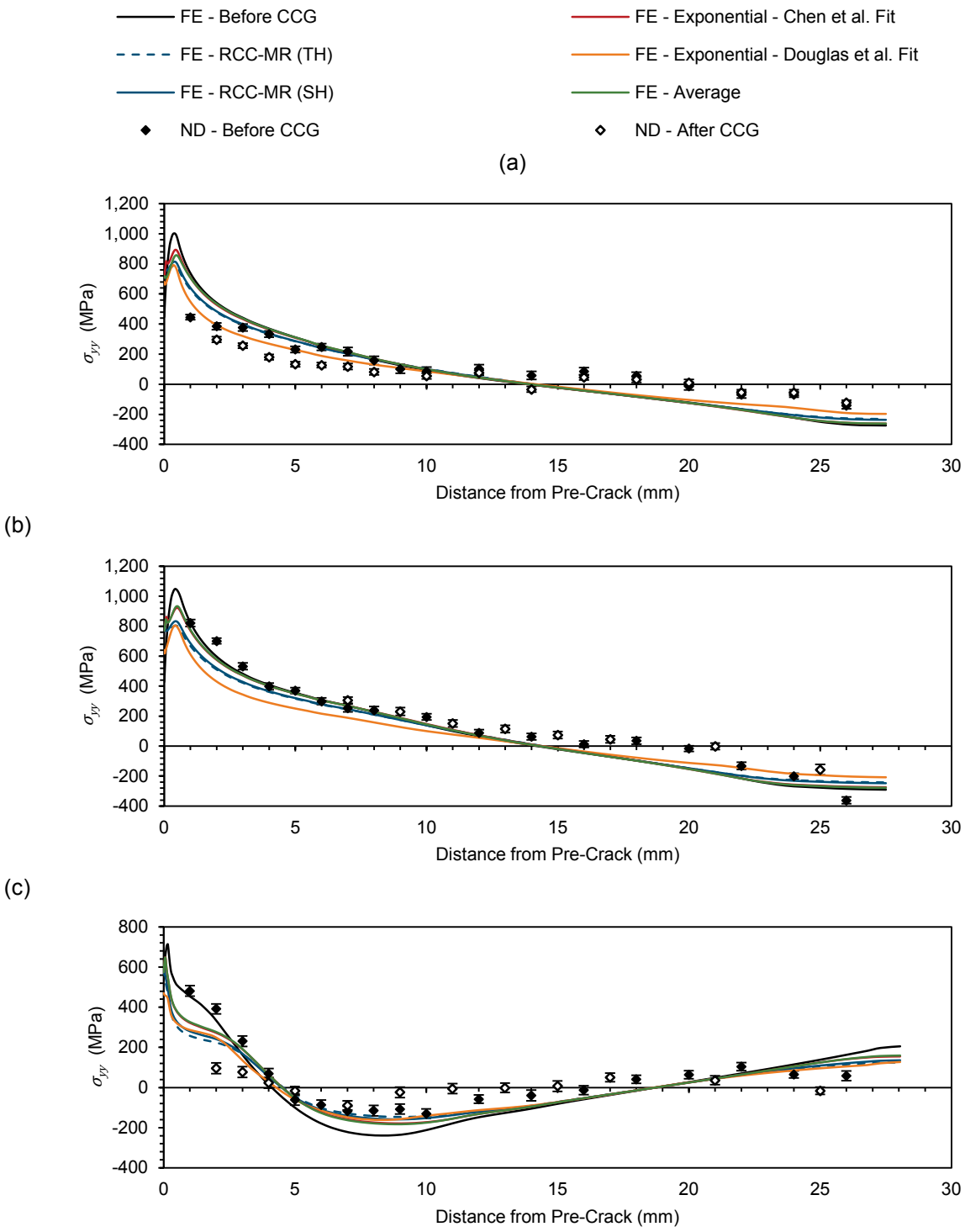


Figure 7.3 Comparison of residual stress measurements in secondary loaded C(T) specimens before and after thermal soaking with FE predictions using various creep deformation models (a) WC(T)3, (b) WC(T)4 and (c) EBW5

7.2.4 ASSESSMENT OF CREEP DEFORMATION MODELS IN PREDICTING STRESS RELAXATION

All the creep deformation models predict similar amounts of stress relaxation for the C(T) specimens. However the extent of stress relaxation predicted in specimens WC(T)3 and EBW5, which had small crack extensions, was less than that measured by ND. The estimates of stress relaxation under uniaxial conditions, shown in Figure 7.2, were in closer agreement with the experimental measurements in comparison to the C(T) specimens which were tested under multiaxial conditions.

To validate the large reduction in stresses experimentally measured in the C(T) specimens, comparisons were made with a study by Chen et al. [123] where the extent of stress relaxation in quenched cylinders made of Type 316H stainless steel was investigated. The cylinders had a highly triaxial stress state and initial stress components of ≈ 300 MPa. These stresses relaxed to less than 100 MPa after exposure to 550°C for 1,800 h. This is consistent with the extent of stress relaxation experimentally measured for specimen EBW5.

The study of stress relaxation of secondary loads shows that under multiaxial conditions the creep deformation models under-predict the extent of stress relaxation in comparison with experimental measurements. The creep deformation models determine creep strains using the equivalent stress, σ_{eq}. The residual stresses in the C(T) specimens were highly triaxial as shown by Figure 4.20 and Figure 5.14, therefore σ_{eq} were low. Hence, the creep deformation models predicted small creep strains. Further work is needed to investigate stress relaxation under multiaxial stress conditions. To achieve this, the wedge-loaded C(T) specimens could be fabricated with blunt notches instead of pre-cracks such that crack growth during creep conditions is inhibited. This would allow stress relaxation to be investigated without the influence of crack growth.

7.3 CRACK GROWTH PREDICTIONS USING $C(t)$ DURING STRESS RELAXATION

7.3.1 THE $C(t)$-INTEGRAL

The stress and deformation fields around a crack tip experiencing steady state creep may be defined using the fracture mechanics parameter C^*. During the primary creep regime and where the creep process zone is growing away from the crack tip, transient conditions are said to exist and the stress and deformation fields around the crack tip is described by $C(t)$ as presented in Section 2.3.3. The parameter $C(t)$ is defined by (2.33) and can be evaluated using FE simulations [49]. Analytical solutions of $C(t)$ may be estimated by

interpolation between short term and long term stress distributions during creep, which are defined by J and C^* respectively [7, pp111-117].

The parameter $C(t)$ was determined using both analytical and numerical approaches for the CCG specimens tested in this study and are compared in this section. The parameters $C(t)$ and C^* are correlated with the rate of creep crack growth, $\dot{a}$, and were used to produce crack extension predictions in the wedge-loaded and EB welded C(T) test specimens which are compared to experimental measurements.

7.3.2 EVALUATING THE $C(t)$-INTEGRAL USING FE ANALYSES

The crack driving force due to the secondary and combined loading conditions were obtained by computing $C(t)$ contour integrals from numerical simulations of stress relaxation. These were used to validate the $C(t)$ estimates determined using the R5 procedure [2].The general definition of the contour integral to evaluate $C(t)$ is (2.33). This expression is analogous to the J-integral shown in (2.26) where the strain and displacement terms are replaced by strain rate and displacement rate terms respectively. In Section 2.5.2 the J-integral was expressed as an area integral to enable the evaluation over a region of elements in a FE analysis. Similarly the $C(t)$-integral is evaluated using FE analyses in two dimensions using [124]:

$$C(t) = \lim_{A \to 0} \int_A \left[\sigma_{ij} \frac{\partial \dot{u}_j}{\partial x_1} - \dot{W}_{SED} \delta_{1i} \right] \frac{\partial q_1}{\partial x_i} dA \tag{7.4}$$

where $\dot{u}_j$ is the displacement rate vector, $\dot{W}_{SED}$ is the strain energy rate density as defined by (2.32) and the remaining terms are as defined in Section 2.3.2.

The J contour integral is path independent when monotonic and proportional loading are assumed. During creep, stresses relax and redistribute around the crack tip which causes the initially high stresses to reduce. Therefore, the load is no longer monotonic and a path independent expression of $C(t)$ cannot be obtained. To determine $C(t)$, (7.4) is integrated in the limit of a small region around the crack tip.

Where user-subroutines are used with ABAQUS to define the creep deformation model, $\dot{W}_{SED}$ must be calculated within the subroutine. For a power-law deformation model such as the RCC-MR model the strain energy rate density is determined as [125]:

$$\dot{W}_{SED} = \frac{n}{n+1} \sigma \dot{\varepsilon}_c \tag{7.5}$$

7.3.3 $C(t)$ DEFINITION IN THE R5 PROCEDURE

Estimates of the transient creep parameter $C(t)$ are presented in the R5 procedure [2] using the reference stress approach. The reference stress is a measure of proximity to plastic collapse and for primary loading is defined by:

$$\sigma_{ref}^{p} = \frac{P}{P_{LC}}\,\sigma_y \tag{7.6}$$

where P is the applied load and P_{LC} is the limit load which is the load that causes plastic collapse of the structure.

Appendix A2 of R5 Volume 4/5 presents a calculation procedure for $C(t)$ under steady creep loading which is applicable for primary loading only. Appendix A3 presents a solution for combined loading, which includes the effect of relaxation of residual stresses. In the R5 procedure, the stress relaxation rate under combined loading conditions is defined as:

$$\dot{\sigma}_{ref} = -\frac{E}{Z}\left(\dot{\varepsilon}_c(\sigma_{ref}) - \dot{\varepsilon}_c(\sigma_{ref}^{p})\right) \tag{7.7}$$

where $\dot{\varepsilon}_c$ is the creep strain rate determined at the total reference stress, σ_{ref}, or the primary reference stress, σ_{ref}^{p}. This is similar to (7.1) however the creep strain rate due to the primary load is subtracted from the total creep strain rate to account for combined loading. The effect of elastic follow up is also included in (7.7), by the parameter Z.

For small amounts of crack growth, $C(t)$ is determined by:

$$\frac{C(t)}{C^*} = \left(\frac{\sigma_{ref}}{\sigma_{ref}^{p}}\right)^{n+1}\left[\frac{\left(\varepsilon_{ref}/\varepsilon_{ref}^{0}\right)^{n+1}}{\phi(t)\left[\left(\varepsilon_{ref}/\varepsilon_{ref}^{0}\right)^{n+1} - 1\right] + \left(1 - \sigma_{ref}^{0}/E\varepsilon_{ref}^{0}\right)}\right] \tag{7.8}$$

where ε_{ref} is the total reference strain, ε_{ref}^{0} is the initial reference strain and n is the creep exponent. The strain ε_{ref} includes elastic, plastic and creep deformations. The parameter C^* is included in the expression as a normalising parameter and is defined by:

$$C^* = \sigma_{ref}^{p}\varepsilon_{ref}^{p}R' \tag{7.9}$$

where ε_{ref}^{p} is the reference strain due to primary loads only and R' is a characteristic length defined by:

$$R' = \left(\frac{K_p}{\sigma_{ref}^{p}}\right)^{2} \tag{7.10}$$

Under secondary loading conditions only Lei [126] proposed (7.8) is normalised by C_0^* which is the steady state value of C^* that would exist if the initial residual stress was induced by a primary load that does not relax:

$$C_0^* = \sigma_{ref}^0 \varepsilon_{ref}^0 R' \tag{7.11}$$

Therefore:

$$\frac{C(t)}{C_0^*} = \left(\frac{\sigma_{ref}}{\sigma_{ref}^0}\right)^{n+1} \left[\frac{\left(\varepsilon_{ref}/\varepsilon_{ref}^0\right)^{n+1}}{\phi(t)[\left(\varepsilon_{ref}/\varepsilon_{ref}^0\right)^{n+1} - 1] + \left(1 - \sigma_{ref}^0/E\varepsilon_{ref}^0\right)}\right] \tag{7.12}$$

which may be used for both secondary and combined loading conditions. The normalisation approach does not change the estimate of $C(t)$.

In (7.8) and (7.12) the parameter ϕ is a function of Z which may be time dependent and has the value $1 \leq \phi(t) \leq Z/(Z-1)$. R5 Volume 4/5 Appendix A3 (Section A3.4.3.3) recommends a conservative estimate of $\phi(t)$ = 1.0 may be taken when Z is unknown.

Under elastic-creep conditions (7.12) reduces to:

$$\frac{C(t)}{C_0^*} = \left(\frac{\sigma_{ref}}{\sigma_{ref}^0}\right)^{n+1} \left[\frac{\left(E\varepsilon_{ref}/\sigma_{ref}^0\right)^{n+1}}{\phi(t)\left(E\varepsilon_{ref}/\sigma_{ref}^0\right)^{n+1} - 1}\right] \tag{7.13}$$

For combined loading the reference stress in R5 Volume 4/5 Appendix A3 (Section A3.4.1.1) Method 1 may be determined from the primary and secondary stress intensity factors, K^p and K^s, which follows the R6 [27] method to determine J.

$$\sigma_{ref}^0 \varepsilon_{ref}^0 = \frac{\left(\sigma_{ref}^p\right)^2}{E} \frac{(1 + V\,K^s/K^p)^2}{f^2(L_r)} \tag{7.14}$$

where the parameter V defines the interaction between the primary and secondary stress and $f(L_r)$ is the failure assessment curve which are defined in R6. In R6 Section II.6.2 the Option 2 failure assessment diagram (FAD) is given by:

$$f(L_r) = \left(\frac{\varepsilon_{ref}E}{\sigma_{ref}} + \frac{0.5\,{L_r}^2}{\varepsilon_{ref}E/\sigma_{ref}}\right)^{-\frac{1}{2}} \tag{7.15}$$

where the ratio L_r defines the proximity to plastic collapse and is determined by:

$$L_r = \frac{P}{P_{LC}} = \frac{\sigma_{ref}^p}{\sigma_y} \tag{7.16}$$

For a C(T) specimen P_{LC} is given in R6 Section IV.1.9.1 as:

$$P_{LC} = \left(\frac{2}{\sqrt{3}}\right)\sigma_y WB\left[\sqrt{2.702 + 4.599\left(\frac{a}{W}\right)^2} - 1 - 1.702\left(\frac{a}{W}\right)\right] \tag{7.17}$$

for plane strain conditions with the von Mises yield criterion. The constant W is the distance from the back face of the specimen to the load line and B is the thickness.

Lei [126] expresses (7.14) as:

$$\sigma^0_{ref}\varepsilon^0_{ref} = \frac{\left(\sigma^p_{ref} + \xi\, K^s_J/\sqrt{R'}\right)^2}{Ef^2(L_r)} \tag{7.18}$$

which is more convenient to solve for secondary loading conditions and uses the effective stress intensity factor for secondary loads, K^s_J, which is determined from the J-integral. For secondary loads only, K^s is equal to K^s_J in accordance with R6 Section 11.6.4.2. The parameter ξ is a constant determined from V and is tabulated in R6 Table II.6.3. For secondary loads only L_r = 0 and due to this, ξ = 1 and $f(L_r)$ = 1.

The parameter R' is defined by (7.10). As both K^p and σ^p_{ref} are a function of the applied load, P, the parameter R' may still be determined for secondary loading where P = 0. However, this approach assumes the stress distribution defined by K^p and σ^p_{ref} are representative of that produced by the residual stresses.

For elastic-creep conditions (7.18) reduces to:

$$\sigma^0_{ref} = \sigma^p_{ref} + \frac{K^s}{\sqrt{R'}} \tag{7.19}$$

The reference strain is defined in R5 Volume 4/5 Appendix A3 as:

$$\varepsilon_{ref} = \varepsilon^0_{ref} - \frac{\sigma^0_{ref} - \sigma_{ref}}{E} + \varepsilon^c_{ref} \tag{7.20}$$

where ε^0_{ref} is the initial reference strain and ε^c_{ref} is the reference creep strain. The first term, ε^0_{ref}, includes elastic and plastic strains, and the second term defines the reduction in elastic strain during stress relaxation. In this definition the plastic contribution of the initial reference strain remains throughout stress relaxation. Estimates of ε^0_{ref} may be made using a materials stress-strain curve or a constitutive model such as the Ramberg-Osgood model shown by (2.1).

7.3.4 $C(t)$ ESTIMATION USING REFERENCE STRESSES

INITIAL REFERENCE STRESS

The initial reference stresses, σ_{ref}^{0}, in the EB welded and wedge-loaded C(T) specimens were estimated using (7.18) and (7.19) which are applicable for secondary or combined loading conditions. These equations determine σ_{ref}^{0} assuming elastic-plastic and elastic material behaviour respectively. The stress-strain behaviour determined from the uniaxial tensile test at 550°C, shown in Figure 4.8, was used to solve (7.18) and to define $f(L_r)$, (7.15). The stress intensity factors due to secondary load, K^s, at mid-thickness of the specimens, evaluated in Chapter 4 and Chapter 5, were used to determine σ_{ref}^{0} which are shown in Table 7.1.

Estimates of σ_{ref}^{0} for the specimens under secondary loads only determined for elastic-plastic and elastic materials were the same. When $f(L_r)$ is defined using the R6 Option 2 FAD and $L_r = 0$, (7.18) reduces to (7.19). For specimens EBW6 and EBW7 which were tested under combined loading conditions σ_{ref}^{0} estimates using (7.18) and (7.19) were very similar as the applied loads were small.

RELAXATION OF THE REFERENCE STRESS

Relaxation of the reference stress determined by (7.7) was evaluated numerically using the Runge-Kutta approach [118, pp64-70] and using the Norton creep law assuming an average creep strain rate as shown in Section 2.2.3. An elastic follow up factor of Z = 3.0 was estimated for all specimens. Stress relaxation estimations for the wedge-loaded and EB welded C(T) specimens are shown in Figure 7.4 and Figure 7.5 respectively where time is shown on log-scales. The reference stress remains constant for the first 100 h and then relaxes for larger times.

Table 7.1 Reference stress estimates for C(T) specimens with secondary and combined loads

Specimen	K^s (MPam$^{1/2}$)	K^p (MPam$^{1/2}$)	σ_{ref}^{p} (MPa)	L_r	R' (mm)	ξ	σ_{ref}^{0} (MPa) Eq. (7.18)	σ_{ref}^{0} (MPa) Eq. (7.19)
EBW5	22.2	0.0	0.0	0.00	94.1	1.000	71.7	71.7
EBW6	22.2	5.0	16.3	0.06	94.1	1.009	88.6	88.0
EBW7	22.2	10.0	32.6	0.13	94.1	1.018	105.6	104.3
WC(T)3	36.0	0.0	0.0	0.00	94.2	1.000	117.3	117.3
WC(T)4	43.6	0.0	0.0	0.00	96.0	1.000	140.7	140.7
WC(T)5	40.4	0.0	0.0	0.00	95.1	1.000	131.0	131.0

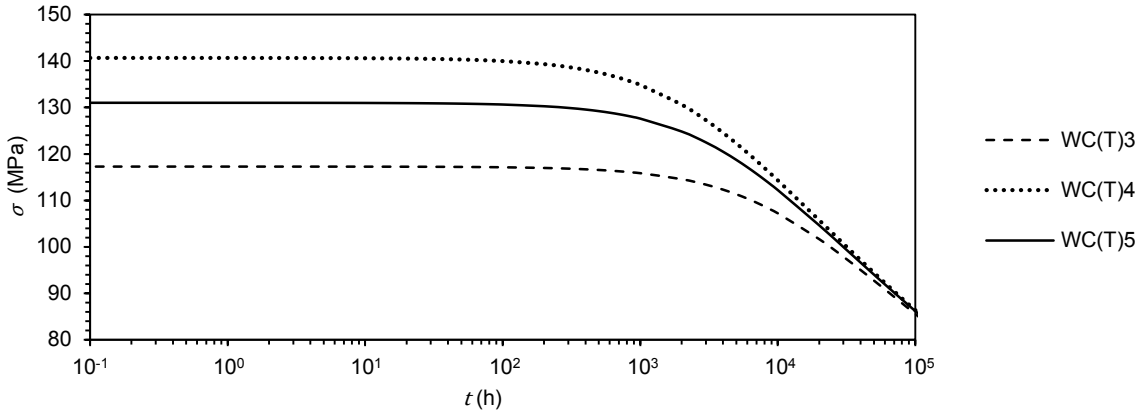


Figure 7.4 Relaxation of reference stress in wedge-loaded C(T) specimens

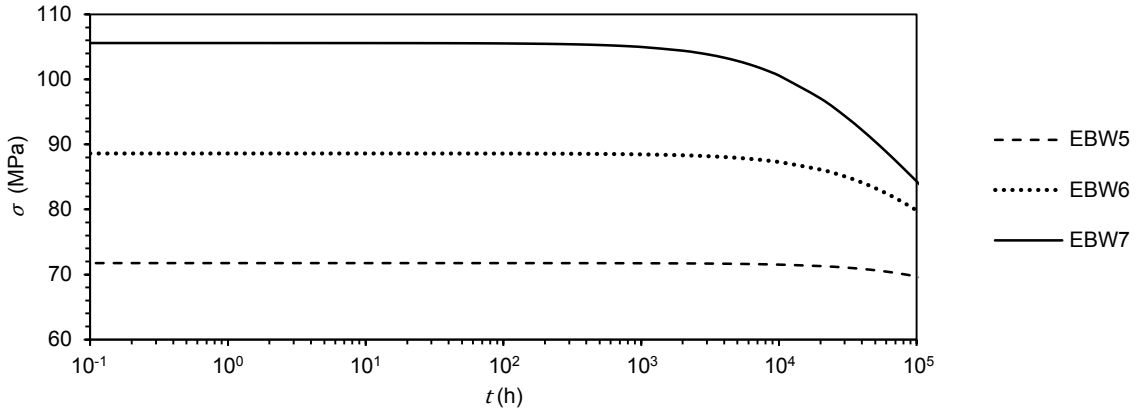


Figure 7.5 Relaxation of reference stress in EB welded C(T) specimens

For tests under secondary loading, stress relaxation will continue for large times until the residual stresses relax completely. Under combined loading conditions the stresses will reduce until the reference stress due to the primary load, σ_{ref}^{p}, is reached. In Figure 7.6 stress relaxation is shown on log-log scales up to large times for specimens EBW6 and EBW7 to show the stresses relaxing to σ_{ref}^{p}. During intermediate times the reference stress is independent of σ_{ref}^{0} and σ_{ref}^{p} as shown in Figure 7.6.

The time to reach steady-state creep conditions, where the stresses are characterised by the parameter C^*, is estimated by the redistribution time, t_{red}. This is defined as the time for the elastic strains to be converted to creep strains. For a material where an average creep strain rate is assumed:

$$t_{red} = \frac{\sigma_{ref}^{p}/E}{C(\sigma_{ref}^{p})^{n}} \tag{7.21}$$

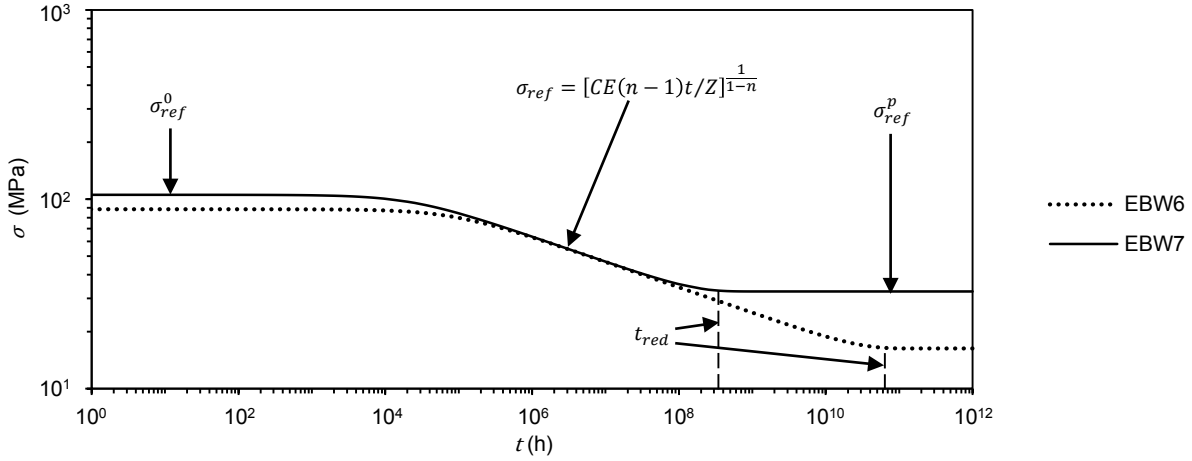


Figure 7.6 Stress relaxation in specimen EBW6 determined using reference stress approach

Redistribution times for the primary load are shown in Table 7.2 for specimens EBW6 and EBW7. The time t_{red} is approximately the time taken for σ_{ref} to relax to σ_{ref}^p, as shown in Figure 7.6.

Table 7.2 Redistribution time, t_{red}, for C(T) specimens tested under combined loads

Specimen	t_{red} (h)
EBW6	6.35×10^{10}
EBW7	3.63×10^{8}

$C(t)$ ESTIMATES

The parameter $C(t)$ was estimated for the wedge-loaded and EB welded C(T) specimens using the definitions in the R5 procedure, as shown in (7.12) and (7.13) which assume elastic-plastic-creep and elastic- creep behaviour respectively.

The elastic follow up factor, Z, was required to determine the rate of stress relaxation as defined by (7.7). For a displacement controlled condition $Z \rightarrow 1$ whilst $Z \rightarrow \infty$ under load control. The wedge-loaded C(T) specimens resembled a displacement controlled test where the wedge held the mouth of the C(T) specimen open during the CCG test. However the wedge experienced compression upon insertion. As creep strains accumulated in the C(T) specimen at 550°C, partial elastic unloading of the wedge occurred. An estimate of Z = 3.0 was used for the C(T) specimens and sensitivity studies were performed using specimen WC(T)5 to determine the sensitivity of $C(t)$ estimations to Z. The parameter $\phi(t)$ in (7.12) is also a function of Z, a conservative estimate was taken as 1.0 as recommended in R5

Volume 4/5 Appendix A3 (Section A3.4.3.3) with a further sensitivity analysis performed to investigate the effect of $\phi(t)$ on $C(t)$.

The parameter C_0^* was used as a normalising parameter to determine $C(t)$ and is the steady state value of C^* that would exist if the initial residual stress was induced by a primary load which does not relax. Table 7.3 shows estimates of C_0^* for the wedge-loaded and EB welded C(T) specimens.

Table 7.3 C_0^* determined for the C(T) specimens

Specimen	C_0^* (MPam/h)
EBW5	3.40×10^{-9}
EBW6	2.50×10^{-8}
EBW7	1.31×10^{-7}
WC(T)3	3.54×10^{-7}
WC(T)4	2.02×10^{-6}
WC(T)5	1.02×10^{-6}

Estimates of $C(t)$ for the wedge-loaded and EB welded C(T) specimens are shown in Figure 7.7 and Figure 7.8 respectively on log-log axes. The parameter $C(t)$ was determined for elastic-creep and elastic-plastic-creep conditions using (7.13) and (7.12) respectively. Plasticity reduced the magnitude of $C(t)$ at short times. Approaching the limit, $t \to 0$, $C(t)$ under elastic-plastic-creep conditions is determined by:

$$\frac{C(t)}{C_0^*} = \frac{1}{1 - \sigma_{ref}^0 / E\varepsilon_{ref}^0} \tag{7.22}$$

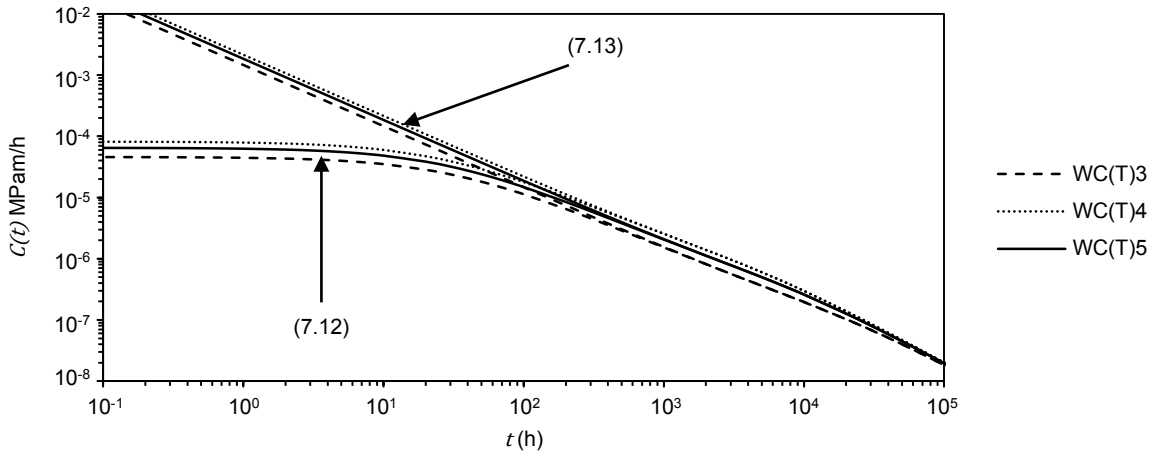


Figure 7.7 $C(t)$ estimation in wedge-loaded C(T) specimens using reference stress approaches

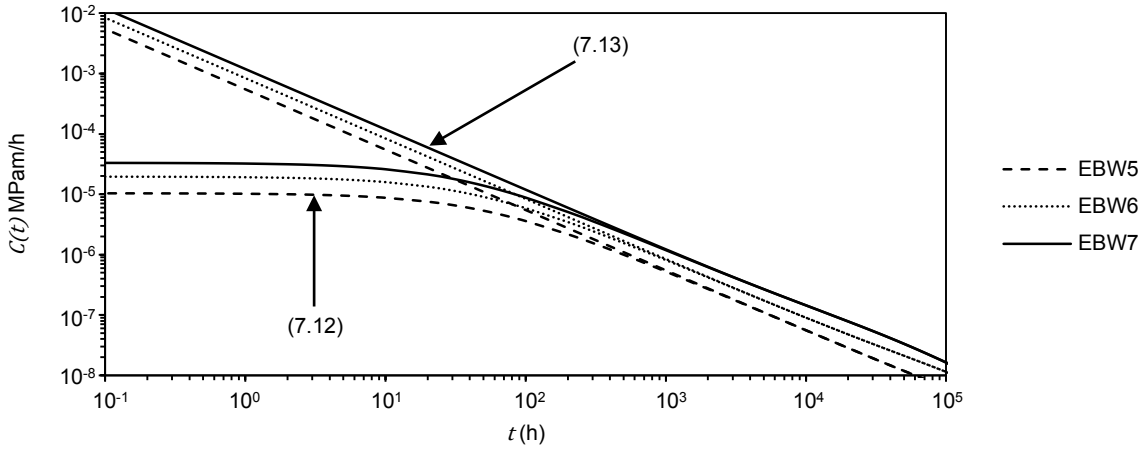


Figure 7.8 $C(t)$ estimation in EB welded C(T) specimens using reference stress approaches

At short times the $C(t)$ estimates for the various specimens differed due to σ_{ref}^{0}. At large times the reference stresses in the wedge-loaded C(T) specimens relaxed to become equal, as shown in Figure 7.4, hence $C(t)$ was also approximately equal. The time to reach C^* conditions in the specimens under combined loading were determined as t_{red} in Table 7.2. These times were much larger than those presented in Figure 7.8 therefore decreasing values of $C(t)$ were estimated for the time scale considered. The values of $C(t)$ were used to determined crack growth predictions which are presented in Section 7.3.6.

The following sub sections present sensitivity studies of $C(t)$ determined using the R5 procedure to various input parameters and also comparisons with $C(t)$ determined using FE analyses for validation.

SENSITIVITY STUDIES

The sensitivity of $C(t)$ to the elastic-plastic material model, Z and $\phi(t)$ were investigated. True stress vs. plastic strain from a uniaxial constant-load tensile test on ex-service Type 316H stainless steel, which was pre-compressed to 8% plastic strain, is shown in Figure 7.9. Comparisons were made with the Ramberg-Osgood model where the material constants were fitted to the entire tensile curve and where the model was fitted up to ε^{pl} = 10% only. Constants for the two fits are shown in Table 7.4, the constants fitted up to

Table 7.4 Constants for different fits of the Ramberg-Osgood model to 8% pre-compressed Type 316H stainless steel (for σ in MPa and ε in mm/mm)

Ramberg-Osgood Fit	A	N
To Failure	5.11×10^{-15}	5.00
To ε^{pl} = 10%	2.56×10^{-21}	7.45

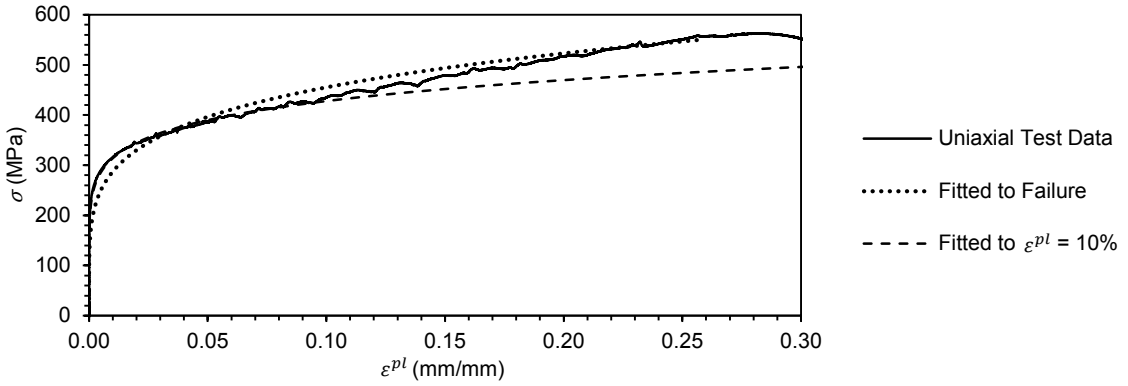


Figure 7.9 True stress vs. plastic strain from uniaxial tensile test of 8% pre-compressed Type 316H stainless steel at 550°C compared to Ramberg-Osgood models (data from [18])

failure were determined by Mehmanparast et al. [18]. Each of these fits are compared to the tensile test data in Figure 7.9.

Figure 7.9 shows at low stresses the model fitted to the whole tensile test over-estimates the plastic strains. For specimen WC(T)5 which has an initial reference stress of σ_{ref}^{0} = 131.0 MPa, the plastic strain, ε^{pl}, for the Ramberg-Osgood model fitted to failure and ε^{pl} = 10% were determined to be 0.02% and 0.001% respectively. Estimates of $C(t)$ for each of these deformation models and the limiting case of ε^{pl} = 0%, for specimen WC(T)5, are shown in Figure 7.10. The $C(t)$ estimates at short times are very sensitive to ε^{pl} and therefore the plasticity model assumed. As σ_{ref}^{0} were low for all C(T) specimens tested in this study, the Ramberg-Osgood model fitted up to ε^{pl} = 10% was considered to give the most accurate predictions. This model was used to determine the $C(t)$ estimates, which assumed elastic-plastic-creep deformation, shown in Figure 7.7 and Figure 7.8.

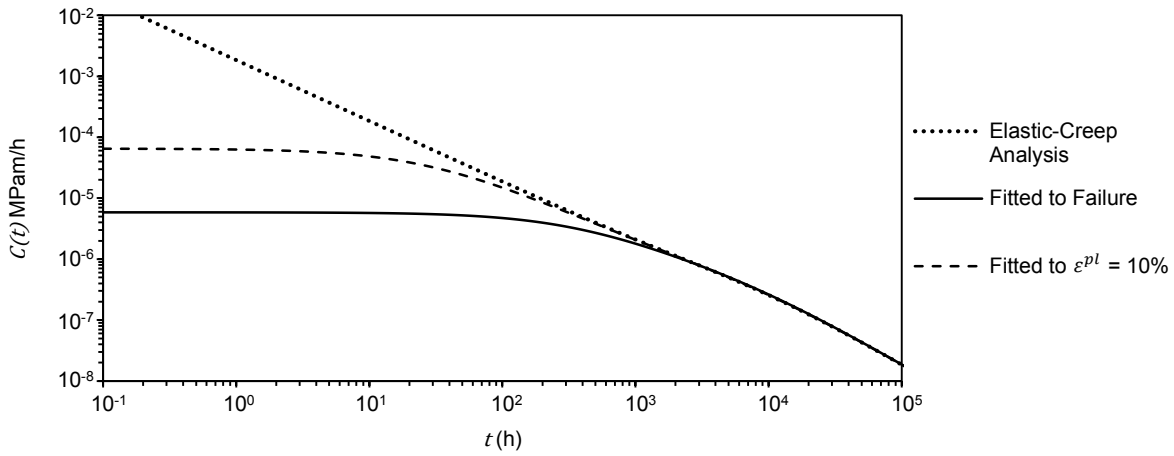


Figure 7.10 Sensitivity of $C(t)$ estimation in WC(T)5 to plastic strain

An elastic follow up factor of Z = 3.0 was assumed for the $C(t)$ assessments. For specimen WC(T)5 this estimate was compared to Z = 1.5 and 5.0 and is shown in Figure 7.11, the parameter $\phi(t)$ was equal to 1.0 for all of these estimates. At small times the elastic-plastic-creep estimate of $C(t)$ was found to be insensitive to Z. At long times $C(t)$ increased with Z and in the limit $Z \to \infty$, $C(t)$ approaches C_0^* at large times. At short times $C(t)$ estimated assuming elastic-creep increased as Z decreased.

The parameter $\phi(t)$ is defined as $Z/(Z-1)$ in the R5 procedure however a conservative estimate of 1.0 is recommended if Z is unknown. For Z = 3.0, $\phi(t)$ was determined to be 1.5 and was compared to a value of 1.0, as shown in Figure 7.12. For an elastic-plastic-creep material, $C(t)$ at short times was insensitive to $\phi(t)$, whereas at large times $C(t)$ reduced as $\phi(t)$ increased.

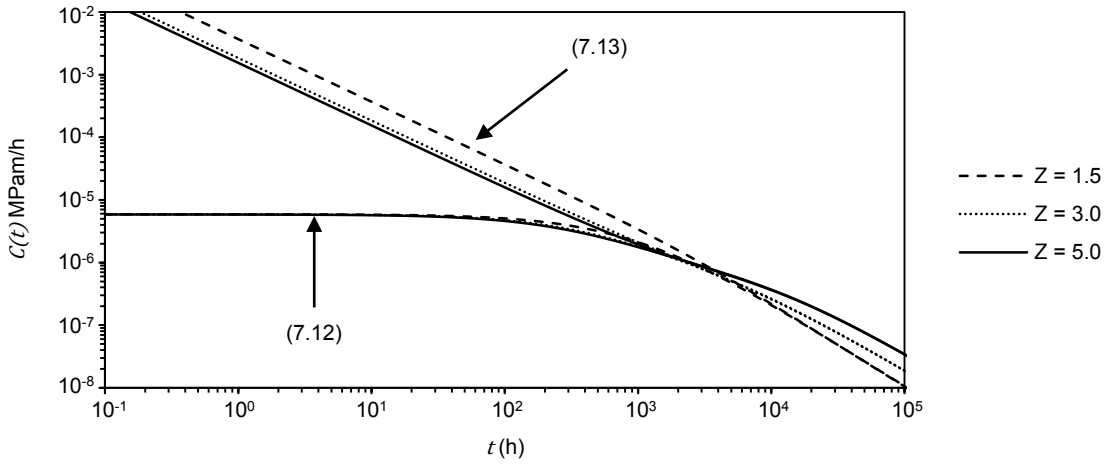


Figure 7.11 Sensitivity of $C(t)$ estimation in WC(T)5 to elastic follow up factor, Z

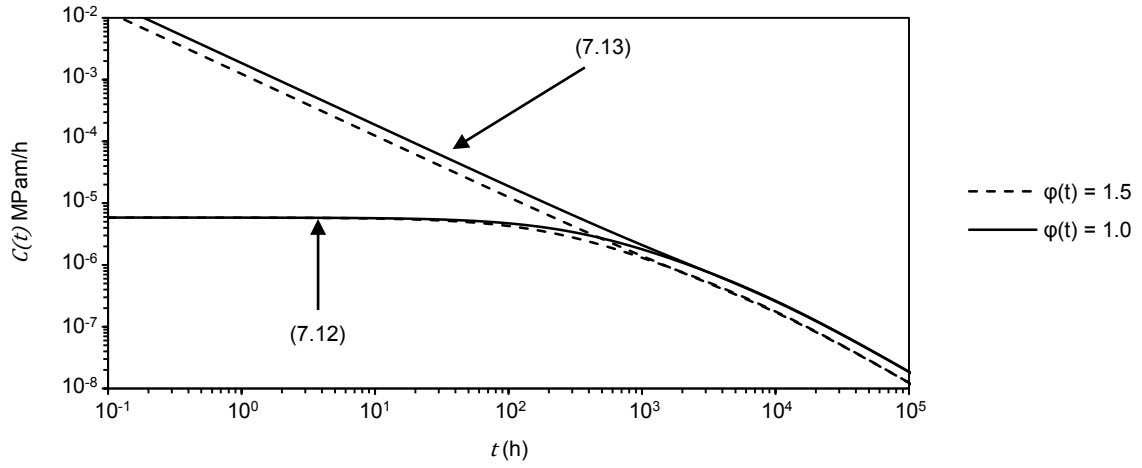


Figure 7.12 Sensitivity of $C(t)$ estimation in WC(T)5 to the parameter $\phi(t)$

In general $C(t)$ was found to be very sensitive to the plastic strain assumed in the specimens. CCG predictions were made assuming elastic-creep deformation and also elastic-plastic-creep deformation, which are presented in Section 7.3.6. The $C(t)$ predictions presented in Figure 7.7 and Figure 7.8 which assumed Z = 3.0 and $\phi(t)$ = 1.0 were considered to be suitable estimates as $C(t)$ was not very sensitive to these parameters.

7.3.5 COMPARISON OF $C(t)$ DETERMINED USING FE AND THE R5 PROCEDURE

The parameter $C(t)$ was determined for the C(T) specimens using FE analyses to enable comparisons to be made with $C(t)$ determined using the R5 procedure. The analytical definitions of $C(t)$, which are presented in Section 7.3.3, were expected to provide conservative estimates of the crack driving force.

Stress relaxation during creep was modelled in FE using the Norton creep law assuming an average creep strain rate (2.7) for direct comparison with the elastic-plastic-creep $C(t)$ estimate made using the R5 procedure. Additionally, creep was modelled using the RCC-MR law (2.8) with time hardening to investigate the effect of including the primary creep regime in the deformation model. These stress relaxation models were consistent with those presented in Section 7.2.3, however creep deformation was modelled for 10^5 h.

The FE meshes were identical to those used to evaluate the J-integral in Section 4.7 and Section 0. Due to the path dependence of $C(t)$, it is recommened by Moran and Shih [124] that the contour integral is evaluated close to the crack tip. For specimen WC(T)5, $C(t)$ evaluated by FE analysis using the Norton creep law which assumed an average creep strain rate, is shown in Figure 7.13(a). The parameter $C(t)$ is shown for contour domains of increasing distance from the crack tip. All values were determined at the mid-thickness plane of the specimen. Figure 7.13(a) shows the largest values of $C(t)$ were not at the contour domains closest to the crack tip, where the peak value was approximately 0.5 mm from the crack tip. This coincided with the position of the peak stresses ahead of the crack tip as shown in Figure 7.13(b) and Figure 7.13(c). Therefore where residual stresses are present, the contour domain used to evaluate $C(t)$ must be large enough to include the peak residual stresses ahead of the crack tip. To characterise the crack driving force due to the residual stresses, the contour domain 0.25 mm from the pre-crack was used to evaluate $C(t)$ which was close to maximum $C(t)$ as shown by Figure 7.13(a).

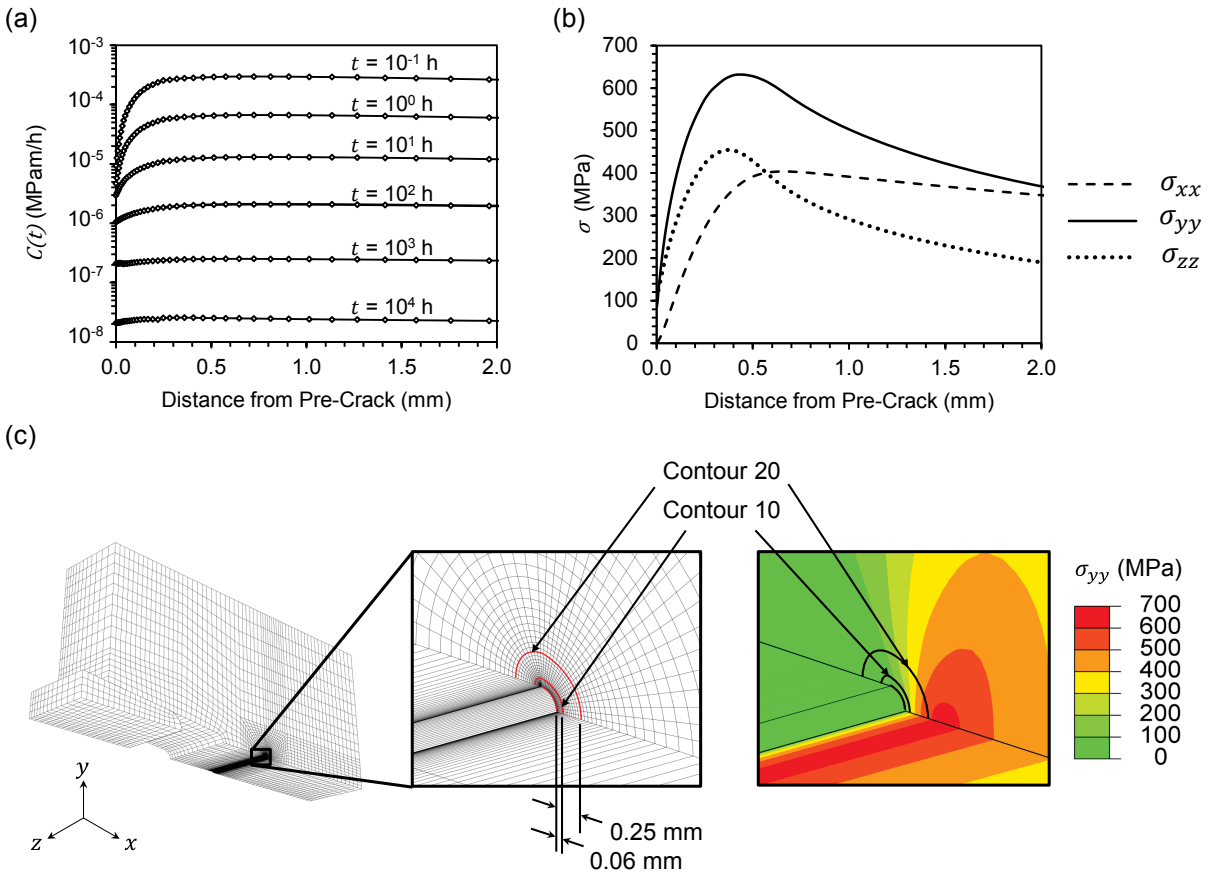


Figure 7.13 $C(t)$ determined from a FE model of WC(T)5 where the creep deformation model assumes an average creep strain rate

Estimates of $C(t)$ determined using FE simulations of specimens WC(T)5 and EBW5 were compared to the predictions using the R5 procedure and are shown in Figure 7.14 and Figure 7.15 respectively. Both used elastic-plastic tensile properties and a creep deformation model that assumed an average creep strain rate. For WC(T)5, the R5 procedure which uses a reference stress approach produced conservative estimates of $C(t)$ in comparison to the FE analysis.

For specimen EBW5 $C(t)$ determined using the R5 procedure, assuming a creep model with average creep strain rate, was slightly non-conservative relative to the corresponding FE model at short times. However beyond 40 h, the R5 procedure was conservative. The value of $C(t)$ at short times was found to be sensitive to the extent of crack tip plasticity as shown Section 7.3.4. In the FE model of EBW5 the tensile properties were defined using a mixed isotropic-kinematic hardening model that was optimised to obtain accurate residual stress predictions from the weld simulation. It is considered that this

material model was less accurate at defining crack tip plastic strains in comparison to tabulated true stress vs. plastic strain data, which was used for WC(T)5, and caused the large $C(t)$ predictions by FE analysis at short times.

The FE model was also used to predict $C(t)$ using the RCC-MR creep deformation model which includes primary and secondary creep regimes, and are also shown in Figure 7.14 and Figure 7.15. At short times this model predicted large values of $C(t)$ for specimens WC(T)5 and EBW5. The parameter $C(t)$ is a product of stress and strain rate. The creep strain rates during primary creep were greater than the average creep strain rate and hence resulted in larger $C(t)$ predictions. However the relatively large creep strain rate during primary creep also caused stress relaxation to occur quickly, as observed in Figure 7.2. Due to the low stresses in the material, $C(t)$ reduced to below the predictions

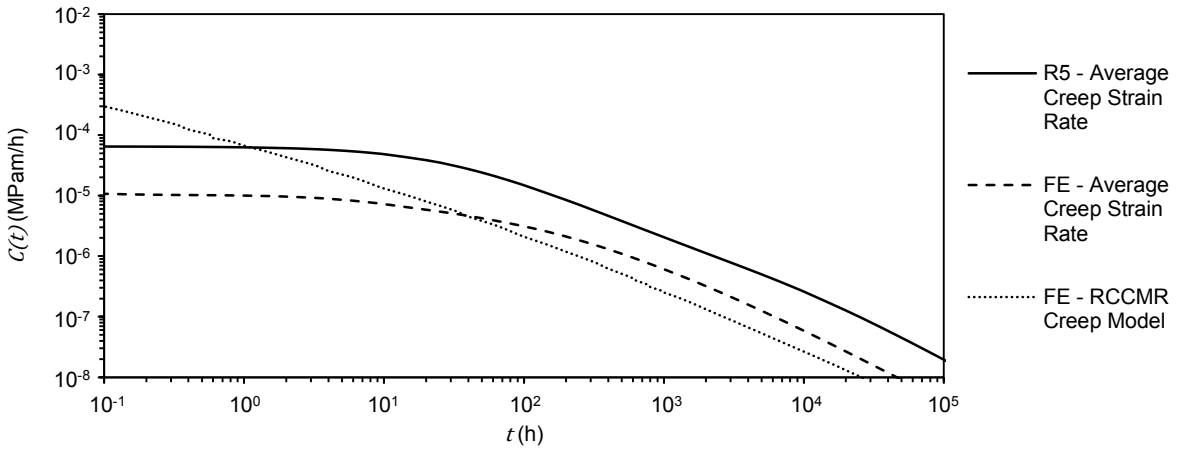


Figure 7.14 Comparison of $C(t)$ estimation in WC(T)5 using R5 to FE analyses

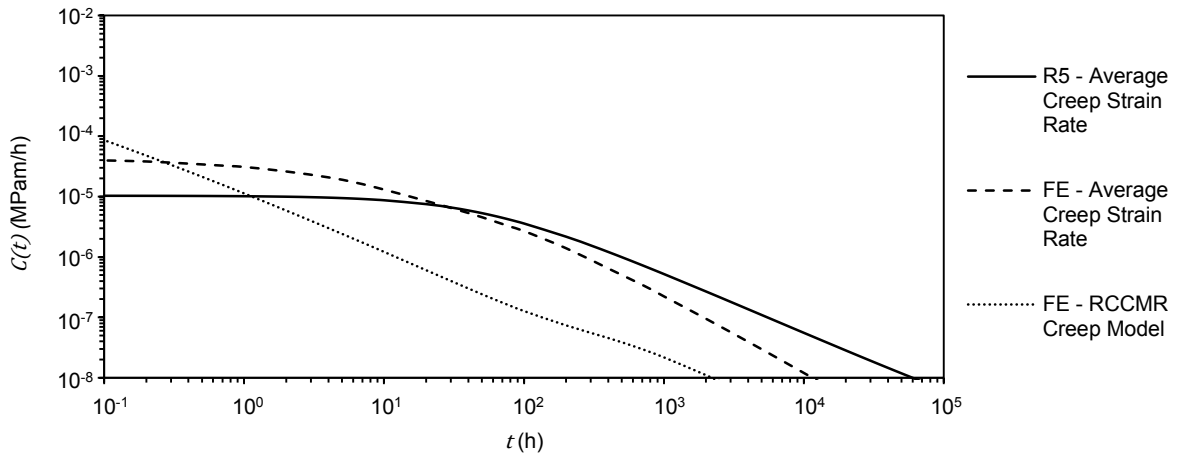


Figure 7.15 Comparison of $C(t)$ estimation in EBW5 using R5 to FE analyses

using the average creep strain rate. Therefore, $C(t)$ predictions using the R5 procedure assuming a creep model with average creep strain rate are judged to be conservative.

7.3.6 ESTIMATES OF CCG USING THE R5 PROCEDURE

The crack growth rate, $\dot{a}$, was predicted using the estimates of $C(t)$ and the crack growth law given in R5 Volume 4/5 Section 10.7.1.2:

$$\dot{a} = D\left(C(t)\right)^{\phi} \tag{7.23}$$

where D and ϕ are material constants that can be determined empirically from experimental data. CCG tests on 8% pre-compressed Type 316H stainless steel under primary load conditions at 550°C were conducted by Mehmanparast et al. [18]. The constants shown in Table 7.5 were determined from the test data. Due to large scatter in the CCG data, a multiplicative factor for the constant D was determined by Mehmanparast et al. to determine the upper bound and lower bound fits.

Table 7.5 Creep crack growth rate properties for 8% pre-compressed Type 316H stainless steel at 550°C (for $\dot{a}$ in mm/h and $C(t)$ in MPam/h)

D	ϕ	UB/LB Factor
94	0.91	3.01

Estimates of crack growth in the C(T) specimens were made using (7.23) with $C(t)$ estimates shown in Figure 7.7 and Figure 7.8. Crack growth predictions were made for $C(t)$ determined using elastic-creep and elastic-plastic-creep deformation assumptions which are shown in Figure 7.16 and Figure 7.17 for the wedge-loaded and EB welded C(T) specimens respectively. These estimates were made using the mean, upper and lower bound creep crack growth properties shown in Table 7.5.

Conservative crack extensions were predicted using $C(t)$ estimates assuming elastic-creep deformation and mean crack growth properties for WC(T)3 and WC(T)4, as shown in Figure 7.16(a)(i) and Figure 7.16(b)(i). However Figure 7.16(c)(i) shows the crack growth predicted in WC(T)5 assuming elastic-creep deformation and mean CCG properties was less than the experimental measurement. The CCG predictions made using the upper bound CCG properties with elastic-creep deformation were all conservative. However these predictions were five times greater than experimental measurements for WC(T)3 and WC(T)4 and therefore were overly conservative. In general a large $C(t)$ was predicted at

short times when elastic-creep deformation was assumed and following this, crack growth rates predicted by (7.23) were initially significantly larger than experimental measurements.

The crack extensions predicted assuming elastic-plastic-creep deformation were less than that assuming elastic-creep deformations due to lower values of $C(t)$ at short times. The crack growth predictions assuming elastic-plastic-creep deformations and mean CCG properties were in close agreement with the experimental measurements in WC(T)3 and WC(T)4 as shown in Figure 7.16(a)(ii) and Figure 7.16(b)(ii). For specimen WC(T)5, the crack length measurements were close to the upper bound elastic-plastic-creep predictions. Specimen WC(T)5 had small grains in comparison to WC(T)3 and WC(T)4, as shown in

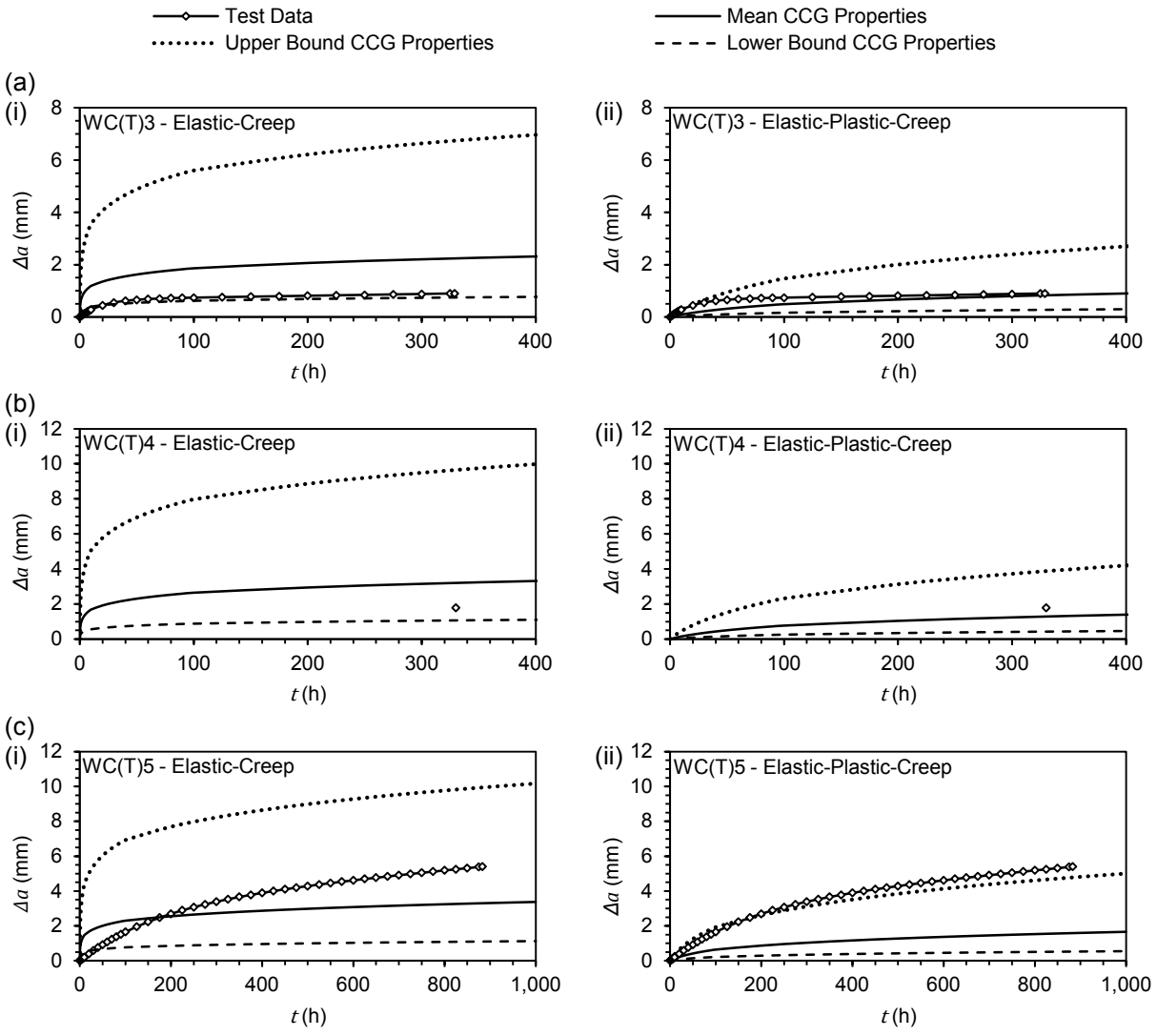


Figure 7.16 Comparison of crack growth predictions from $C(t)$ with experimentally measured crack length in wedge-loaded C(T) specimens: (a) WC(T)3 (b) WC(T)4 and (c) WC(T)5 for (i) elastic-creep and (ii) elastic-plastic-creep deformations

Chapter 6. It was considered that this difference in microstructure contributed to a faster crack growth rate and hence the upper bound crack growth properties provided more accurate predictions. In general the upper and lower bound predictions show a large spread in crack lengths which is typical of the material tested. Large differences in creep ductilities have been observed based on the cast and service history of the material [9, 16].

The crack growth predictions in the EB welded C(T) specimens followed a similar trend to the wedge-loaded C(T) specimens. Crack growth predictions assuming elastic-creep deformation were conservative which predicted very fast crack growth rates at short times, as shown in Figure 7.17. Experimentally measured crack growth was most accurately

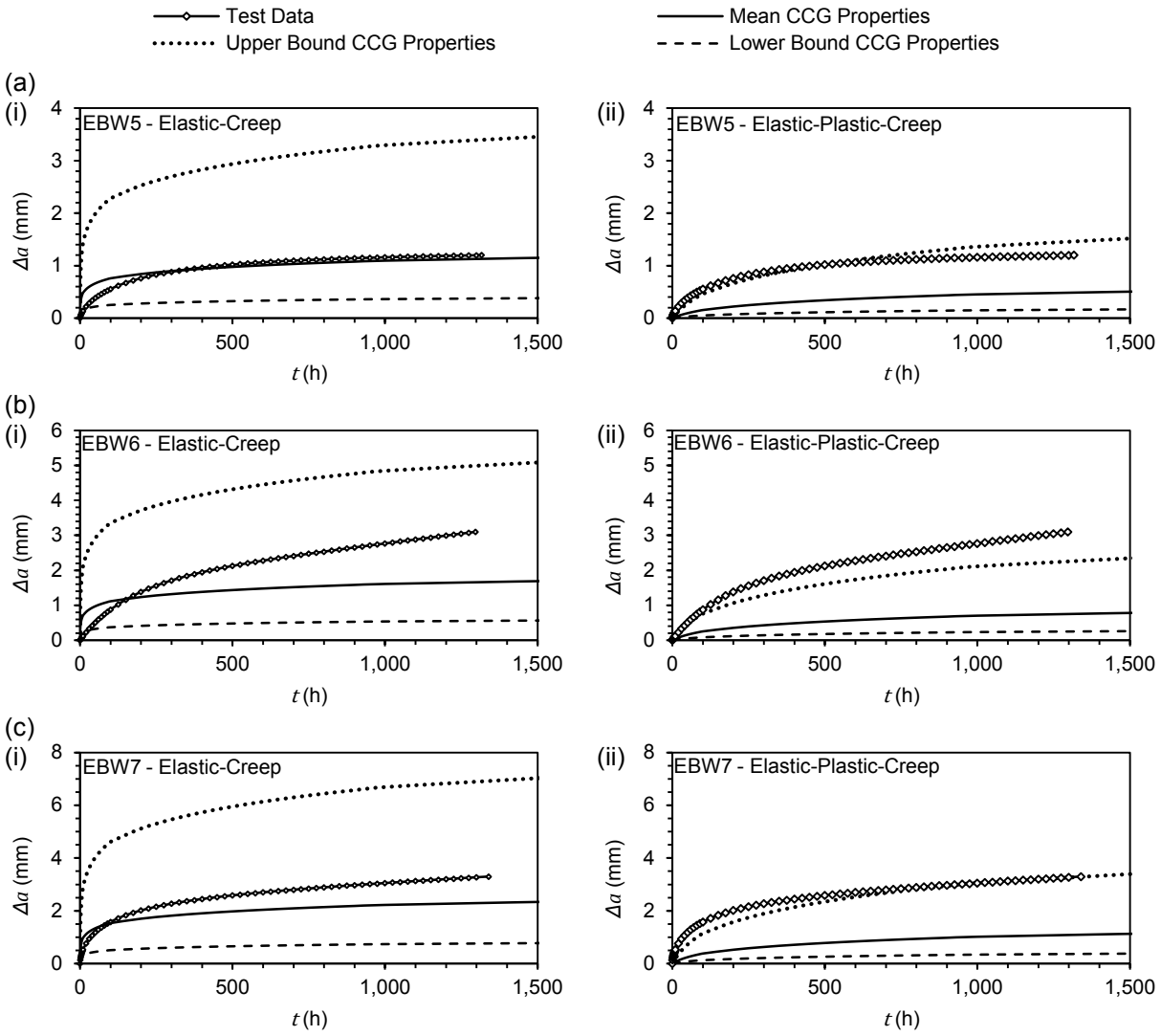


Figure 7.17 Comparison of crack growth predictions from $C(t)$ with experimentally measured crack length in EB welded C(T) specimens: (a) EBW5 (b) EBW6 and (c) EBW7 for (i) elastic-creep and (ii) elastic-plastic-creep deformations

predicted by estimates assuming elastic-plastic-creep deformation. However, the experimental measurements were greater than predictions made using the mean crack growth properties and close to the upper bound estimates. In these specimens, up to 3% weld induced plastic strains existed ahead of the crack tip, as shown in Figure 4.19. Plasticity reduced the creep ductility of the material and hence this contributed to the increased crack growth rates measured in comparison to the predictions made using the mean CCG properties of material in the 8% pre-compressed condition.

7.4 CCG PREDICTIONS USING DAMAGE MODELLING IN FE SIMULATIONS

7.4.1 FINITE ELEMENT MODEL

The numerical simulations of the C(T) specimens during CCG testing were developed incorporating creep damage models, where the extent of damage was defined as the ratio of the accumulated creep strain to the material's creep ductility, ε_f, using (2.20). Under multiaxial conditions the creep ductility, ε_f^*, was determined using the empirical model (2.22) recommended in R5 Volume 2/3 Appendix A1 (Section A1.11.1.2) [2].

The mesh of the FE models used to conduct the CCG analyses for the wedge-loaded and EB welded C(T) specimens are shown in Figure 7.18. A three dimensional quarter model was used which was consistent with that used to determine $C(t)$, however a fine and regular

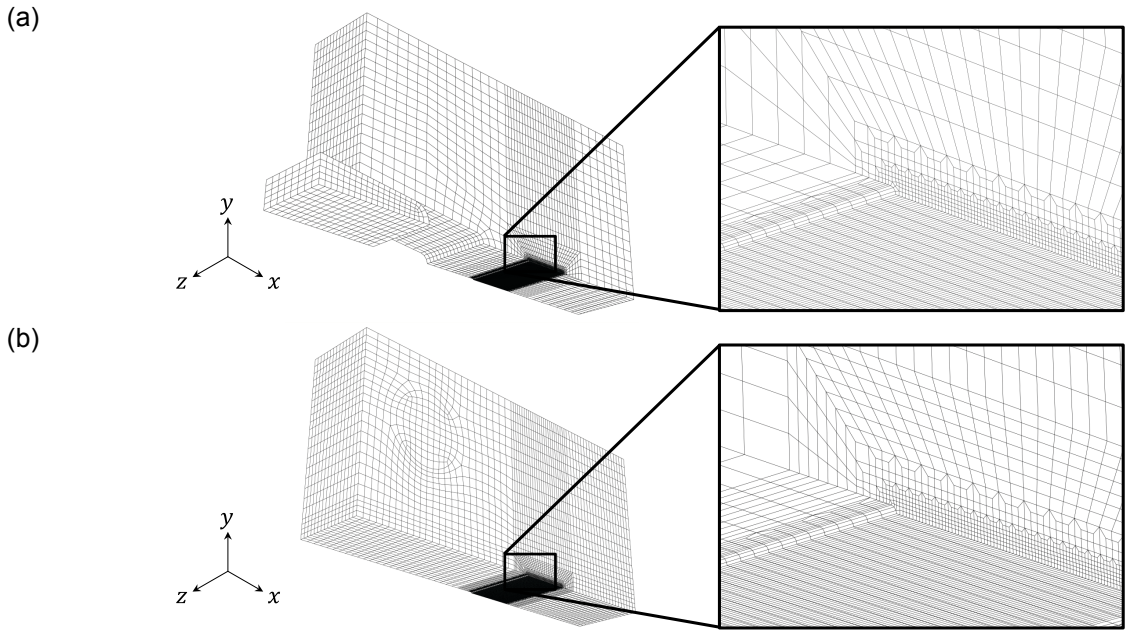


Figure 7.18 Finite element mesh for CCG analyses of (a) wedge-loaded and (b) EB welded C(T) specimens

mesh was used around the crack tip region where elements had a cross sectional area of 100 × 100 (μm)^2. The sensitivity of crack growth rates to mesh size was investigated and are presented in Section 7.4.3. The fine mesh region extended 8 mm from the crack tip allowing crack growth up to this length to be simulated. All models were run using the RCC-MR creep model assuming time hardening behaviour.

The damage model was implemented using the USDFLD user-subroutine in ABAQUS, where the extent of damage was calculated at each integration point for the elements along the ligament of the C(T) specimens. Once the damage parameter, D_c, reached unity, the material was considered to have failed and indicated crack initiation. To model the crack front propagating through the specimen during the test, damaged elements were effectively removed from the analysis by modifying the material properties to remove their load carrying capacity. This was achieved by reducing the yield stress of the material to 1 MPa for the damaged elements [127, 128].

The multiaxial creep ductility was determined using the void growth model proposed by Spindler [15] which is presented in the R5 procedure [2]. The constants p and q in (2.22) were defined as 0.15 and 1.25 respectively for Type 316 stainless steel as recommended in the R5 procedure. The multiaxial creep ductility predicted by Spindler's model is sensitive to stress triaxiality, σ_h/σ_{eq}, as shown in Figure 7.19. In this void growth model the ductility is also a function of the principal stress, σ_1, hence creep ductilities for three magnitudes of principal stress are shown. The value of the constant p, for Type 316 stainless steel, is small and therefore the failure ductility is insensitive to σ_1. Figure 7.19 also shows the ratio of multiaxial to uniaxial creep ductilities predicted using Cocks and Ashby's void growth model, as shown in (2.21), where the creep strain exponent, n, is 8.2. Both models predict a similar

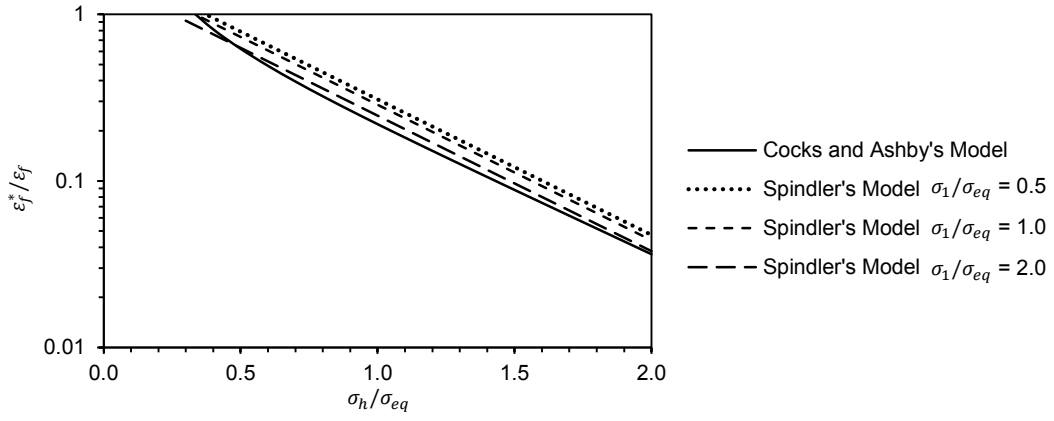


Figure 7.19 Comparison of multiaxial creep ductilities predicted by various void growth models

relationship between ε_f^* and σ_h/σ_{eq} where Cocks and Ashby's model is conservative unless σ_1/σ_{eq} is large. Spindler's model was used to define the multiaxial creep ductilities in the FE analyses of the C(T) specimens as recommended in the R5 procedure. Crack growth predictions were compared to that made using Cocks and Ashby's model in a sensitivity analysis which is presented in Section 7.4.3.

The mean uniaxial creep ductility, ε_f, of ex-service Type 316H stainless steel in the 8% pre-compressed condition at 550°C was determined by Mehmanparast et al. [18] as 2.1%. Minimum and maximum values of ε_f were measured as 1.2% and 3.4% respectively which were used to determine upper and lower bound estimates for crack lengths in the wedge-loaded C(T) specimens. Similarly, maximum and mean values of ε_f for the EB welded C(T) specimens were considered as 3.4% and 2.1%. The minimum creep ductility of HAZ in Type 316H weldments is 0.9% [129] and was used to determine the upper bound crack length in the EB welded C(T) specimens.

7.4.2 CRACK GROWTH PREDICTIONS

Crack growth predictions for the wedge-loaded specimens at mid-thickness, made using FE simulations with damage modelling, are compared to experimental measurements in Figure 7.20. The lower bound crack length predictions for WC(T)3 and WC(T)4 using the maximum ε_f closely matched the experimental measurements. Whereas for WC(T)5, the best estimate crack length prediction using the mean ε_f closely matched the test data.

The FE simulations predicted creep crack initiation to occur at up to 113 h after heating the specimen to 550°C, whereas the PD data indicated crack growth occurred immediately after the specimen was heated. During the early stages of the FE analyses damage accumulated ahead of the crack tip. The rate of damage accumulation was greatest in the regions of high stress triaxiality and therefore initiation occurred ahead of the crack tip. This is shown by the sudden change in crack length in the FE results. The crack then grew towards the pre-crack and deeper into the specimen.

In the FE simulation crack growth was modelled by reducing the load carrying capacity of the damaged elements. As the crack extended and as creep strains accumulated, stress redistribution and relaxation were predicted by the simulation. Hence the magnitude of the residual stresses ahead of the crack tip reduced and a decreasing crack growth rate was predicted.

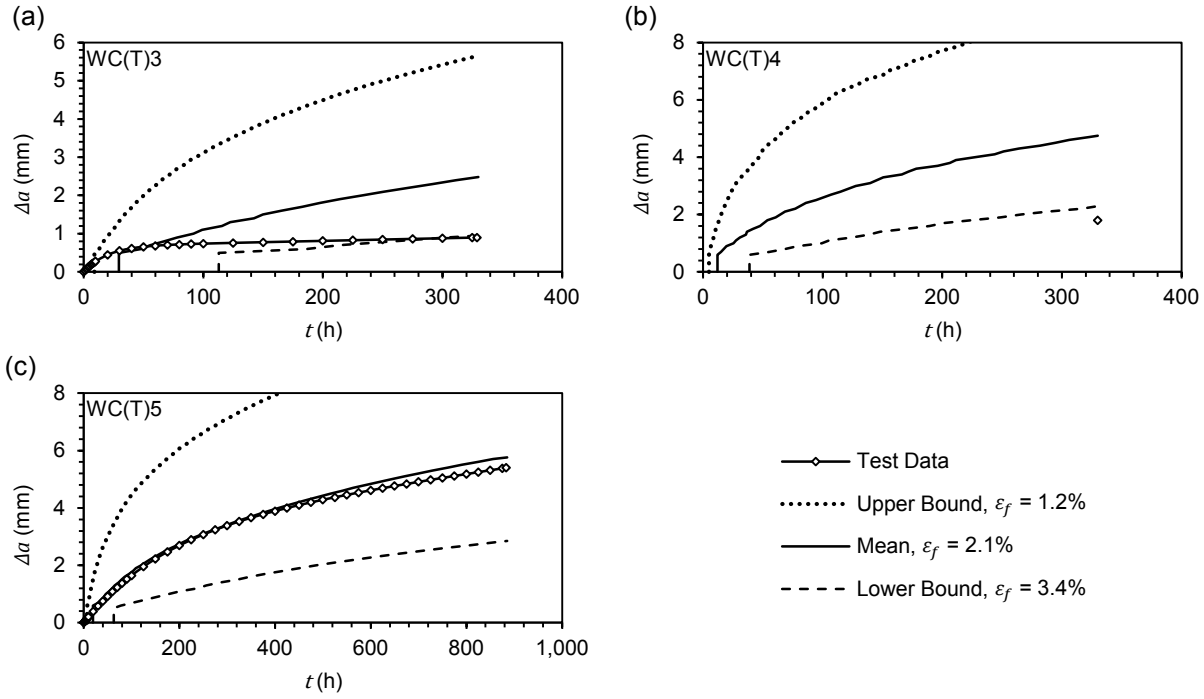


Figure 7.20 Comparison of crack growth predictions from FE simulations with experimental measurements in wedge-loaded C(T) specimens: (a) WC(T)3 (b) WC(T)4 and (c) WC(T)5

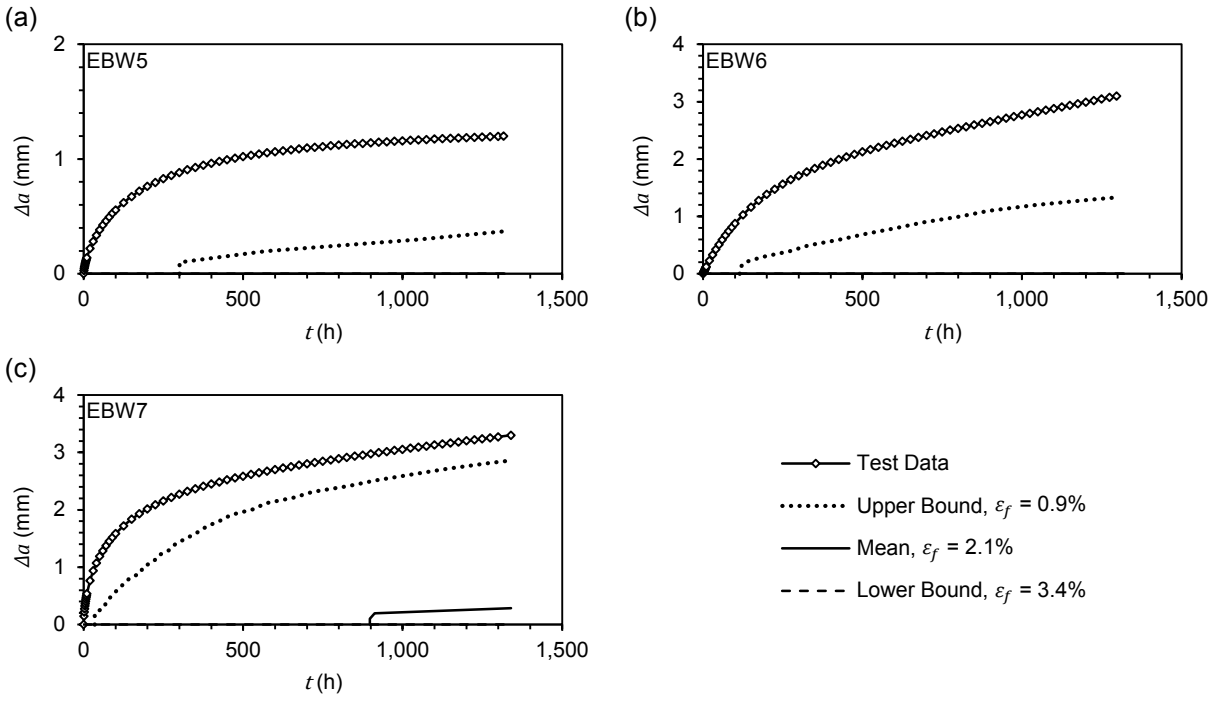


Figure 7.21 Comparison of crack growth predictions from FE simulations with experimental measurements in EB welded C(T) specimens: (a) EBW5 (b) EBW6 and (c) EBW7

Crack length predictions for the EB welded C(T) specimens, at mid-thickness of the specimen, are shown in Figure 7.21. All predictions were less than that measured experimentally. In specimens EBW5 and EBW6, crack initiation only occurred for the upper bound estimates with ε_f = 0.9%, however, the predicted crack extensions were less than half of those measured experimentally. The upper bound crack extension estimate for EBW7 was reasonably close to experimental data.

The damage models under-predict the crack growth rate in the EB welded C(T) specimens. One of the reasons for this was that the effect of plasticity on creep ductility was not included in the model. In the EB welded samples equivalent plastic strains, ε^{pl}, of up to 3% ahead of the pre-crack were predicted from the weld simulations. Dislocation pile up on grain boundaries during plastic deformation initiates voids and therefore during subsequent creep deformation the time for cavities to grow, coalesce and form micro-cracks is reduced. Furthermore plasticity generates intergranular stresses which causes high stresses around grain boundaries where triple points or precipitates cause stress concentrations. This enhances the rate of cavity nucleation [130]. This prior damage must be taken into account in the FE model either by setting the initial damage parameter to a non-zero value or by defining a plastic strain dependent creep ductility. These simulations show the importance in

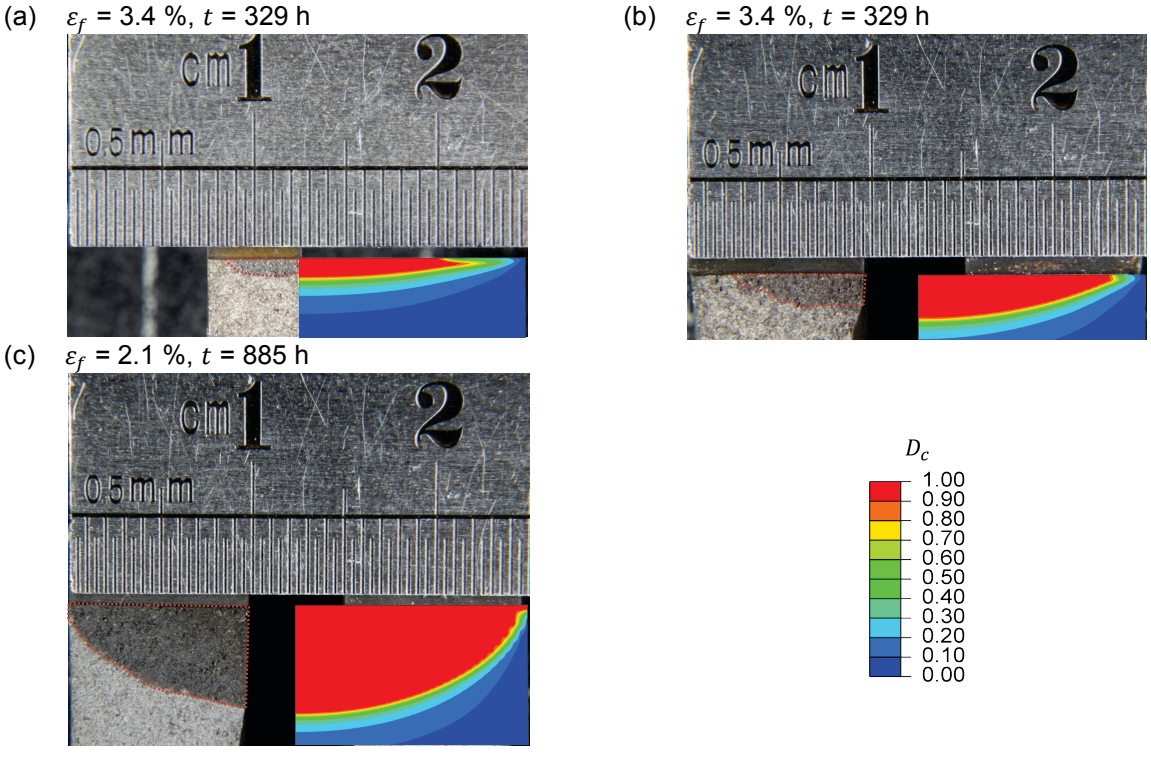


Figure 7.22 Comparison of crack profiles measured experimentally in wedge-loaded C(T) specimens with predictions using damage modelling (a) WC(T)3, (b) WC(T)4 and (c) WC(T)5

incorporating the effect of plastic strains into the damage model.

Profiles of the crack fronts at the end of the CCG simulations of the wedge-loaded and EB welded C(T) specimens are compared to experimental measurements in Figure 7.22 and Figure 7.23 respectively, where the damage parameter, D_c, is shown. A value of 1.0 indicates the element was damaged and removed from the analysis. The results presented in Figure 7.22 are for ε_f = 1.2% for WC(T)3 and WC(T)4, and ε_f = 2.1% for specimen WC(T)5 which gave the closest predictions to experimental measurements. All models provided good predictions of the shape of the crack front where very little crack growth was predicted on the outside faces of the specimen. The stress triaxialities were low in the outer regions and therefore ε_f^* was high. The shapes of the crack fronts were generally consistent with the profiles of K^S shown in Figure 4.24 and Figure 5.16 for the EB welded and wedge-loaded C(T) specimens respectively. The crack length predictions for the EB welded C(T) specimens presented in Figure 7.23 assumed ε_f = 0.9%. Figure 7.21 shows the CCG simulations for the EB welded C(T) specimens generally did not accurately predict the crack lengths observed experimentally. The profiles of the cracks also differed, where the FE simulations did not predict any crack growth towards the side faces of EBW6 and EBW7.

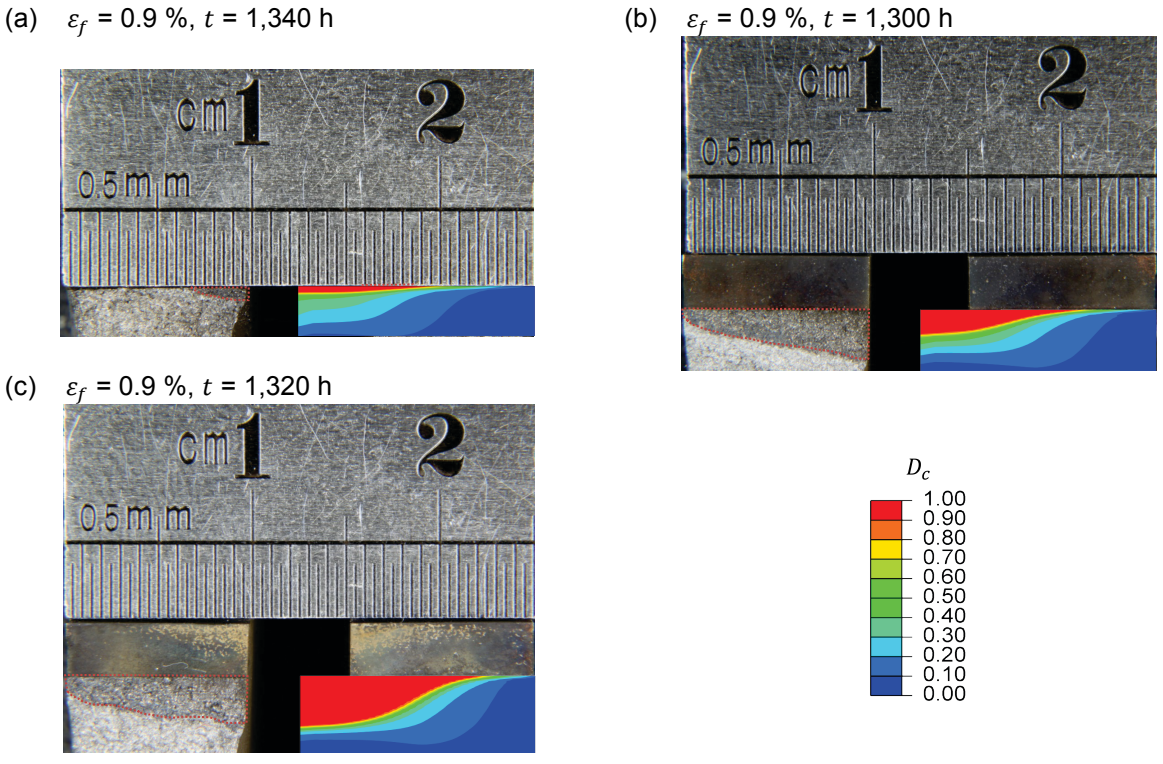


Figure 7.23 Comparison of crack profiles measured experimentally in EB welded C(T) specimens with predictions using damage modelling (a) EBW5, (b) EBW6 and (c) EBW7

7.4.3 SENSITIVITY STUDIES

The multiaxial creep ductilities predicted by the void growth models were compared in Figure 7.19 for various stress triaxialities. FE analyses of specimen WC(T)3 were conducted using Cocks and Ashby's model (2.21) and Spindler's model (2.22), and are compared in Figure 7.24. The mean value of ε_f = 2.1% was assumed for both analyses.

FE simulations with both void growth models predicted similar crack lengths. The analysis which used Spindler's model predicted a slightly shorter initiation time for WC(T)3. In this specimen the principal stresses were large ahead of the crack tip, initially $\sigma_1/\sigma_{eq} \approx 2.3$. Therefore Spindler's model predicted lower ε_f^* in comparison to Cocks and Ashby's model. In general both models predicted similar results and therefore only one void growth model was considered for damage simulations of the remaining C(T) specimens tested which are presented in Section 7.4.2.

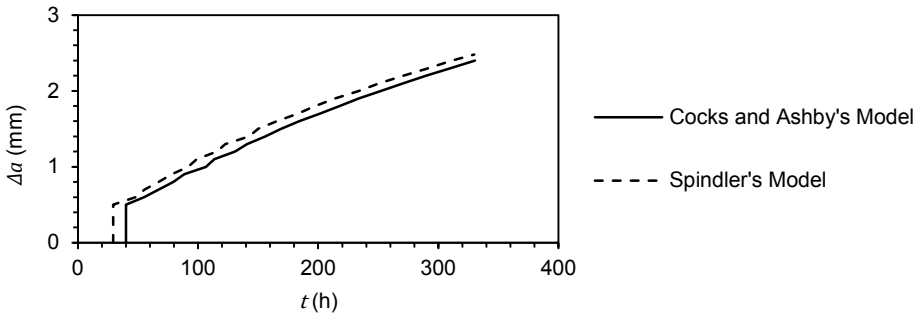


Figure 7.24 Comparison of crack extension prediction in specimen WC(T)3 using different void growth models

The CCG simulation for WC(T)3 was analysed using various mesh densities ahead of the crack tip to determine the influence of element size on crack growth. Elements with cross sectional area of 50 × 50 (μm)^2 and 100 × 100 (μm)^2 were used for this study. The mesh with 100 × 100 (μm)^2 elements was also analysed with reduced and full integration options in ABAQUS. The crack growth rates for WC(T)3 where a mean value of ε_f was assumed are shown in Figure 7.25.

The initiation time for the three models presented in Figure 7.25 were similar showing the mesh was sufficiently refined to determine the accumulation of creep damage before crack initiation. Once the crack started to grow and propagate through the specimen, a dependency with mesh size was observed. Crack propagation was modelled by effectively removing elements by reducing the load carrying capacity to insignificant values. Hence, the

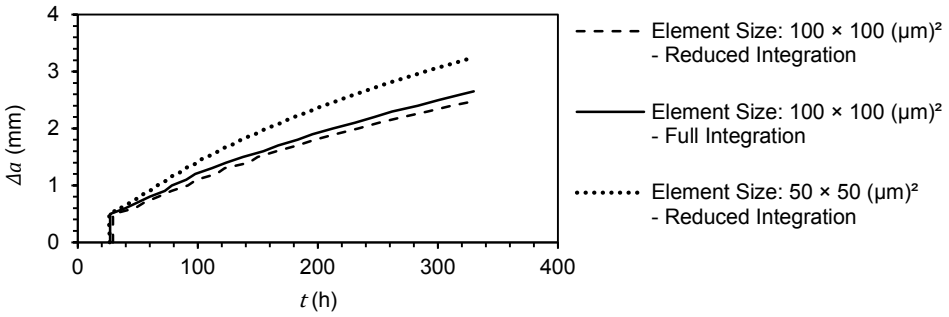


Figure 7.25 Comparison of crack length prediction in specimen WC(T)3 using different mesh densities and integration schemes

crack tip radius was approximately equal to the element size. In the model with 50 × 50 (μm)^2 elements, the stress concentration effect of the crack caused larger crack tip stresses in comparison to the models with 100 × 100 (μm)^2 sized elements and hence faster rates of crack growth were predicted. Where full integration was used, integration points were located closer to the crack tip compared to the corresponding elements with reduced integration and as a result the stresses were greater at these points. Hence the full integration scheme also caused faster crack growth although this effect was small. It is unclear which mesh size produced the most accurate crack growth predictions as using an increasingly finer mesh would also lead to an increasing crack growth rate. An element size of 100 × 100 (μm)^2, which was of the order of the grain size of the material, was selected for this study which is consistent with that used by Oh et al. [127]. The reduced integration scheme was used to minimise run times for these analyses which were up to 32 h using eight cores.

7.5 DISCUSSION

CCG predictions made using $C(t)$ determined from the R5 procedure, assuming limited crack growth, generally provided conservative crack length predictions. The extent of conservatism was dependent on whether elastic-creep or elastic-plastic-creep properties were assumed and also whether upper or lower bound crack growth properties were assumed. Crack growth estimates with elastic-creep deformation were overly conservative where predicted crack lengths were up to 10 times larger than those measured experimentally. This was due to the large $C(t)$ estimated at short times which resulted in initially high crack growth rates. By including plasticity, the values of $C(t)$ at short times were reduced and allowed more accurate crack growth predictions to be made. However the predictions were sensitive to the accuracy of the plasticity model. When making assessments using the $C(t)$ estimation methodology presented in the R5 procedure, care must be taken

that the extent of plasticity is not over-estimated as this could make the predictions non-conservative.

Crack growth predictions made using $C(t)$ estimates and damage modelling were both sensitive to the CCG properties assumed. These properties were defined using $\dot{a}$-C^* trends or creep ductilities, ε_f, which were determined from experimental data published in literature. The experimental crack growth measurements were generally between the upper and lower bound CCG estimates for the wedge-loaded C(T) specimens, predicted using $C(t)$ estimates and damage modelling. However, the upper bound crack extension estimates were up to 10 times larger than the lower bound. Examination of the microstructure surrounding the cracks in the C(T) specimens, presented in Chapter 6, showed a large variation in grain size between the specimens. All of these specimens were extracted from different regions of the same ex-service steam header component. When making component lifetime assessments, the microstructure of a component is usually unknown. For conservatism, the smallest values of ε_f or the upper bound $\dot{a}$-C^* fit should be used to predict crack growth but this could lead to very conservative crack growth estimates.

Experimental crack growth measurements for the EB welded C(T) specimens were close to the upper bound predictions made using the $C(t)$ estimates and those made using damage modelling were non-conservative. This was due to the weld induced plasticity ahead of the crack tip which caused a reduction in creep ductility. The presence of this plasticity was not accounted for in both of the crack growth prediction methods. This supports the observations by Turski et al. [3] where the plasticity induced in the pre-compressed C(T) specimens influenced the crack growth rate. Further work is needed to develop both of these assessment approaches to include the effect of prior plasticity on crack growth rates. This is important for carrying out lifetime assessments for components in service, as reheat cracking is a concern in welded components where weld induced plasticity reduces the creep ductility of the material.

In general, the analysis presented in Section 7.3 shows the crack growth estimates using the reference stress methodology in R5 Volume 4/5 Appendix A3 are in good agreement with the experimental data and hence validate this new approach. Use of elastic-plastic-creep material properties is recommended to determine accurate $C(t)$ predictions at short times. Furthermore upper bound crack growth properties should be used to take into

account reduction in creep ductility which may be caused by plasticity or microstructure variability in the component.

Stress relaxation predictions were made using various creep deformation laws with FE simulations. None of the models could accurately predict the extent of stress relaxation for all of the uniaxial constant-displacement test data available at 550°C. However, the predictions were in reasonable agreement with experimental measurements after approximately 1,000 h. Stress relaxation predictions for the C(T) specimens, which were under multiaxial conditions, were significantly different from the ND experimental measurements. The experimentally measured reduction in stress magnitude for WC(T)3 and EBW5 were approximately twice that predicted by the creep deformation models. Further work is needed to validate the creep deformation models for stress relaxation under uniaxial conditions and subsequently this needs to be extended for multiaxial conditions. The performance of the creep deformation models influence the magnitude of the stresses that are predicted in the C(T) specimens by the FE model. In turn this affects the extent of crack growth predicted by the damage models which are a function of the equivalent stress, stress triaxiality and creep strain rate.

7.6 SUMMARY

Creep deformation models were used to predict the extent of stress relaxation in the C(T) specimens which were compared to ND measurement data. The models predicted less stress relaxation than the experimental measurements.

Crack growth predictions were made using $C(t)$ estimated by following the approach in the new revision of the R5 procedure, in combination with $\dot{a}$-C^* trends that were published in literature for CCG tests under primary loading conditions. The CCG predictions using the new approach to determine $C(t)$ were consistent with the experimental data. Estimates of crack extensions in the C(T) specimens were also made using damage modelling. Whilst the predictions were in good agreement with the experimental measurements for the wedge-loaded C(T) specimens, the extent of crack-growth was under-estimated for the EB welded C(T) specimens. The damage models need to include the effects of prior plastic strains which reduce the creep ductility of the material to improve predictions. In both approaches for estimating CCG, crack growth predictions were sensitive to the variation in creep ductilities observed in ex-service Type 316H stainless steel.

8 CONCLUSIONS AND FUTURE WORK

8.1 CONCLUSIONS

Fracture mechanics specimens with residual stresses were fabricated to enable CCG testing to be conducted under secondary and combined loading conditions. In the wedge-loaded C(T) specimen an over-sized wedge was inserted into a C(T) specimen modified with a tapered mouth such that the geometrical misfit between the wedge and the specimen induced residual stresses. This specimen design has previously been used to perform tests to determine crack arrest toughness, in this study the specimen design was uniquely used to perform CCG tests. Three specimens of this design were fabricated for CCG testing which had large initial crack driving forces, where K^s varied from 36.0 MPam$^{1/2}$ to 43.6 MPam$^{1/2}$ between the specimens. C(T) specimens were also made from EB welded blocks such that the weld residual stresses caused crack growth. The initial stress intensity factor due to these residual stresses was determined as K^s = 22.2 MPam$^{1/2}$. Both of these specimens were used to perform CCG tests and to validate CCG assessment methodologies in the new revision of the R5 procedure, for secondary and combined loading.

The wedge-loaded C(T) specimen was shown to have limited plastic deformation across the ligament of the specimen. Beyond 1 mm from the crack tip, the plastic strains were predicted to be less than 0.2%. It was shown that the plastic deformation in the wedge-loaded C(T) specimen was far less than the EB welded C(T) specimen and other C(T) specimen designs with self-contained residual stresses published in the literature. Hence, the wedge-loaded C(T) specimen developed in this study was shown to be an ideal design for CCG testing under secondary loading conditions, where the crack growth rate could be investigated without the influence of variable plasticity ahead of the crack tip. However the wedge-loaded C(T) specimen could only be used for testing under secondary loading conditions, an alternate design was required for combined loading. Whilst the EB welded C(T) specimens had up to 3% plasticity ahead of the crack tip, this was shown to be less than that in other C(T) specimens with self-contained residual stresses. Hence the EB welded C(T) specimen design, which was developed in this study, was suitable for conducting tests under combined loading conditions.

CCG tests under secondary loading conditions published in the literature and performed in this study on ex-service Type 316H stainless steel in the as-received material condition showed limited or no crack growth. For cracks to initiate and grow due to relaxing

residual stresses, the creep ductility of the material needs to be sufficiently low. To ensure crack growth occurred in the specimens tested in this study, the creep ductility of the material was reduced by pre-compressing the material to 8% plastic strain. Compression was performed on rectangular blocks such that the plastic deformation was consistent across the sample and therefore the creep ductility was also uniformly reduced. Hence, in CCG tests using C(T) specimens fabricated from these blocks, the crack growth rates were assumed to be independent of the plastic strains induced during pre-compression and due to the residual stresses alone. Cracks extensions between 0.9 and 5.4 mm were attained in the wedge-loaded C(T) specimens and 1.2 mm in a EB welded C(T) specimen tested under secondary loading conditions. This was significantly greater than that observed for specimens made of material in the as-received condition, where many tests have been performed in various studies under secondary loads where little of no crack growth was observed. This confirmed the pre-conditioning process was necessary to obtain significant crack extensions from CCG testing under secondary loading, to enable crack growth assessments to be made.

The recent revision of R5 Volume 4/5 Appendix A3 presents a new methodology to determine $C(t)$ under combined loading conditions. Comparison of the experimental crack length measurements with predictions made using the new methodology shows this approach provides conservative estimates of crack growth for the test conditions considered. It was shown that at short times $C(t)$ predictions were sensitive to the extent of plastic deformation assumed in the specimens. It was also shown that the crack growth predictions were overly conservative when no plasticity was assumed, with crack extensions up to 10 times greater than the experimental measurements. There was also a significant difference between upper bound and lower bound CCG predictions which incorporated the variability in creep ductilities of the material. By including plastic strains in the analysis and using the upper bound creep crack growth material properties, the predictions were conservative and only up to three times larger than the experimental measurements for the wedge-loaded C(T) specimens.

CCG predictions in the EB welded C(T) specimens using the elastic-plastic-creep $C(t)$ estimates and upper bound crack growth data were close to the experimental measurements. However, the prediction was non-conservative for one of the test specimens (EBW6) where 2.6 mm of crack growth was predicted however 3.1 mm was experimentally measured. The weld induced plasticity reduced the creep ductility of the material and hence contributed to increasing the crack growth rate under creep conditions. Therefore, when

conducting crack growth assessments in material that has been plastically deformed, the reduction in creep ductility must be incorporated.

Damage models using a ductility exhaustion approach developed using FE simulations were also used to predict CCG. The models provided good predictions of CCG for the wedge-loaded C(T) specimens. The analyses were conservative and predicted crack lengths that were within a factor of three greater than the experimental measurements. However, crack extension predictions for the EB welded C(T) specimens using damage modelling were non-conservative. One of the reasons for this was that the influence of plasticity on CCG was not accounted for. Furthermore, the creep deformation models used in the FE simulations were shown to under predict the extent of stress relaxation in the specimens. The extent of stress relaxation predicted by the FE models was less than half of that measured experimentally by neutron diffraction. This reduced the accuracy of the damage models which require accurate creep deformations to be predicted. Therefore, further work is required to develop the creep deformation and damage models to determine accurate crack growth predictions under secondary and combined loading.

During the development of these specimens, extensive residual strain and stress measurements were made to quantify the residual stresses induced and to validate supporting numerical simulations of the fabrication processes. Neutron diffraction, slitting and the contour method were performed on the EB welded C(T) specimens. Longitudinal weld residual stresses at mid-thickness and near the weld were measured to be 450 MPa and 650 MPa by the contour method and neutron diffraction respectively. Slitting measures average stresses through the thickness of the component, these measurements appeared to be consistent with the neutron diffraction measurements. It was considered that plastic deformation of the cut surfaces occurred during sectioning, as the specimen was clamped in a non-ideal manner to enable slitting to be performed. This inelastic deformation contributed to reducing the accuracy of the contour method measurements near the weld region. However the accuracy of the measurements may also be improved by increasing the sampling frequency of cut surface deformation profile and subsequently reducing the size of the FE mesh to carry out the numerical analysis.

Numerical simulations of the fabrication of both specimen designs were developed. Detailed weld simulations were required for the EB welded C(T) specimens. These were created using the weld modelling guidelines included in a recent issue of the R6 procedure [27]. The temperature predictions were in excellent agreement with the experimental

thermocouple measurements, whilst the residual stresses predicted in the EB welds were in good agreement with the experimentally measured residual stresses. In this study the R6 weld modelling guidelines were successfully applied for the case of EB welding.

The numerical simulations were also used to determine the initial stress intensity factors due to the secondary loads, K^s. The FE software ABAQUS had recently been updated to allow J-integral evaluation where residual stresses were present. This feature was used to evaluate K^s in 3D analyses and the results were validated using a method based the superposition principle to calculate K^s. It was shown that the modified J-integral expression included in recent versions of ABAQUS may be used to accurately determine K^s in 3D analyses.

8.2 FUTURE WORK

A limited number of tests were conducted in this study to prove the concept of the novel C(T) specimen designs. Inconsistent crack extensions were observed which was partially due to the variability of crack growth material properties inherent to the test material. More tests should be conducted for each specimen to confirm the crack extension measurements. These tests should also be conducted for various lengths of time as short term tests can validate predictions of crack initiation and long term tests can prove the arrest of crack growth due to stress relaxation.

Furthermore, difficulties in mounting the wedge-loaded C(T) specimens inside the furnace were encountered during this study. The effect of resistive heating due to the DCPD measurement technique on CCG testing of C(T) specimens with residual stresses should be investigated. Alternatively tests should be conducted such that the resistive heating effect of the DCPD method does not cause significant temperature changes. An alternative method may be used to measure the crack growth rate which minimises the local heating effects, such as the alternating current potential drop (ACPD) technique [131]. The wedge-loaded C(T) specimen is an ideal design for performing a large number of tests to investigate crack initiation under secondary loading as many specimens, under the same load conditions, can be placed in series in an autoclave. Specimens may be removed sequentially such that destructive testing may be used to verify crack initiation. Measurements from the DCPD technique showed apparent crack growth very early in tests performed in this study, however such measurements are likely to be due to creep deformation of the specimen. By conducting a large number of tests for various durations the effect of crack growth and creep

deformation on the PD voltage may be separated to improve interpretation of DCPD data. In addition a constant-displacement test should be conducted on a C(T) specimen using a servo-controlled testing rig, where the applied displacement is consistent with the mouth opening displacement a wedge-loaded C(T) specimen. This would enable the crack growth rates to be compared between the two test methods, which are expected to be the same.

The assessment methodology in R5 Volume 4/5 Appendix A3 was applied for small crack extensions only. Assessments should be made for large crack extensions where $C(t)$ is defined as a function of the crack length. Long term tests with the wedge-loaded C(T) specimens would enable these assessments to be made.

Residual stresses were measured in the wedge-loaded C(T) specimens before and after thermal soaking. Creep deformation models were used predict the extent of stress relaxation in the specimens using FE analyses however the extent of stress relaxation was under-predicted. Further studies should be carried out using wedge-loaded C(T) specimens with blunt notches, which would inhibit cracking, to assess stress relaxation under multiaxial stress conditions.

Crack growth predictions were made for the wedge-loaded and EB welded C(T) specimens using damage modelling based on a ductility exhaustion approach. Further creep damage models using life fraction rules should also be investigate. The damage models could be extended to include the effect of plasticity on CCG to improve the accuracy of crack growth estimates.

9 REFERENCES

1. Coleman, M. C., Miller, D. A. and Stevens, R. A., *Reheat Cracking and Strategies to Assure Integrity of Type 316 Welded Components*, in *Integrity of High Temperature Welds*, 1998, London, Professional Engineering Publishing Limited, pp. 169-180.
2. EDF Energy Nuclear Generation Ltd., *R5: Assessment Procedure for the High Temperature Response of Structures*, EDF Energy Nuclear Generation Ltd.,, Issue 3 Revision 001, 2012.
3. Turski, M., Bouchard, P. J., Steuwer, A. and Withers, P. J., *Residual stress driven creep cracking in AISI Type 316 stainless steel,* Acta Materialia, 2008, **56**(14), pp. 3598-3612.
4. Bhadeshia, H. and Honeycombe, R., *Steels: Microstructure and Properties: Microstructure and Properties*, 2011: Elsevier Science.
5. Lemaitre, J. and Chaboche, J.-L., *Mechanics of Solid Materials*, 1994: Cambridge University Press.
6. Aird, C., Smith, M., Kapadia, P., Venkata, K. A. and Muransky, O., *Round Robin Prediction of Residual Stresses in the Edge-Welded Beam R6 Validation Benchmark Problem*, in *ASME 2013 Pressure Vessels and Piping Conference*, 2013, American Society of Mechanical Engineers, pp. V06BT06A088-V06BT06A088.
7. Webster, G. A. and Ainsworth, R. A., *High Temperature Component Life Assessment*, 1st ed, 1994, London: Chapman and Hall.
8. Frost, H. J. and Ashby, M. F., *Deformation-mechanism maps: the plasticity and creep of metals and ceramics*, 1982: Pergamon Press.
9. Webster, G. A., Davies, C. M., Skelton, R. P. and Nikbin, K. M., *Comparison of R5 Volume 4/5 Procedures for Determining Incubation Periods in Type 316H Stainless Steel*, REPORT ME 115/01, 2008.
10. RCC-MR, *Design and Construction Rules for Mechanical Components of FBR Nuclear Island*, AFCEN, Paris, Section I - Subsection Z : Technical Appendix A3, 1985.
11. Chen, B., Smith, D. J., Flewitt, P. E. J. and Spindler, M. W., *Constitutive equations that describe creep stress relaxation for 316H stainless steel at 550C,* Materials at High Temperatures, 2011, **28**(3), pp. 155-164.
12. Garofalo, F., Richmond, O., Domis, W. F. and von Gemmingen, F., *Paper 30: Strain-Time, Rate-Stress and Rate-Temperature Relations during Large Deformations in Creep,* Proceedings of the Institution of Mechanical Engineers, Conference Proceedings, 1963, **178**(1), pp. 1-31-1-39.
13. Douglas, J., Dennis, R. and Spindler, M., *Development of an advanced creep model for Type 316 stainless steel*, in *Eighth Int. Conf. on Creep and Fatigue at Elevated Temperatures*, 2007, San Antonio, Texas.
14. Cocks, A. C. F. and Ashby, M. F., *Intergranular Fracture During Power-Law Creep under Multi-Axial Stress,* Metal Science, 1980, **14**, pp. 395–402.
15. Spindler, M. W., *The Multiaxial Creep Ductility of Austenitic Stainless Steels,* Fatigue and Fracture of Engineering Materials and Structures, 2004, **27**(4), pp. 273–282.
16. Chevalier, M., *The Reliability of Degrading Structural Systems Operating at High Temperature*, EngD Thesis, Faculty of Engineering, University of Bristol, 2013.
17. Holt, P. and Spindler, M., *A practical application of continuum damage mechanics to plant integrity assessment*, in *Proceedings of the Symposium on Elasticity and Damage in Solids Subject to Microstructural Change, Newfoundland*, 1996, pp. 455-465.
18. Mehmanparast, A., Davies, C. M., Dean, D. W. and Nikbin, K. M., *The influence of pre-compression on the creep deformation and failure behaviour of Type 316H stainless steel,* Engineering Fracture Mechanics, 2013, **110**(0), pp. 52-67.

19. Mehmanparast, A., Davies, C. M., Dean, D. W. and Nikbin, K., *Material pre-conditioning effects on the creep behaviour of 316H stainless steel,* International Journal of Pressure Vessels and Piping, 2013, **108–109**, pp. 88-93.
20. Tada, H., Paris, P. C. and Irwin, G. R., *The Stress Analysis of Cracks Handbook*, 1985, Saint Louis: Paris Productions & (Del Research Corp.).
21. Anderson, T. L., *Fracture Mechanics: Fundamentals and Application*, 1991, Boston: CRC Press.
22. Rice, J. R., *A Path Independent Integral and the Approximate Analysis of Strain Concentration by Notches and Cracks,* Journal of Applied Mechanics, Transactions of the ASME, 1968, **35**, pp. 379–386.
23. Hutchinson, J. W., *Singular Behaviour at the End of a Tensile Crack in a Hardening Material,* Journal of the Mechanics and Physics of Solids, 1968, **16**(1), pp. 13–31.
24. Rice, J. R. and Rosengren, G. F., *Plane Strain Deformation Near a Crack Tip in a Power Law Hardening Material,* Journal of the Mechanics and Physics of Solids, 1968, **16**(1), pp. 1–12.
25. Riedel, H. and Rice, J. R., *Tensile Cracks in Creeping Solids*, in *Fracture Mechanics Twelfth Conference*, 1980, St-Louis, ASTM STP 700, American Society for Testing and Materials, pp. 112–130.
26. Withers, P. J. and Bhadeshia, H. K. D. H., *Residual stress. Part 1 Measurement techniques,* Materials Science and Technology, 2001, **17**(4), pp. 355.
27. EDF Energy Nuclear Generation Ltd., *R6: Assessment of the Integrity of Structures Containing Defects*, EDF Energy Nuclear Generation Ltd, R6 Revision 4, 2011.
28. Sherry, A. H., Da Fonseca, J. Q., Goldthorpe, M. R. and Taylor, K., *Measurement and modelling of residual stress effects on cracks,* Fatigue & Fracture of Engineering Materials & Structures, 2007, **30**(3), pp. 243-257.
29. O'Dowd, N. P., Nikbin, K. M., Wimpory, R. C., Biglari, F. R. and O'Donnell, M. P., *Computational and Experimental Studies of High Temperature Crack Initiation in the Presence of Residual Stress,* Journal of Pressure Vessel Technology, 2008, **130**(4), pp. 041403-7.
30. Nezhad, H. Y., O'Dowd, N. P., Davies, C. M., Nikbin, K. M. and Wimpory, R. C., *Study of creep relaxation behaviour of 316h austenitic steels under mechanically induced residual stress*, in *ASME 2011 Pressure Vessels and Piping Conference*, 2011, American Society of Mechanical Engineers, pp. 197-204.
31. Nezhad, H. Y., *Effect of Prior Deformation on Creep Behaviour of AISI 316H Austenitic Stainless Steels*, Materials and Surface Science Institute, Department of Mechanical, Aeronautical and Biomedical Engineering, University of Limerick, 2012.
32. Nadri, B., Bouchard, P. J., Smith, M., Truman, C. E. and Smith, D. J., *Modelling and Statistical Treatment of Residual Stress Distributions in an Edge Welded Stainless Steel Beam,* Strain, 2011, **47**(6), pp. 505-517.
33. Turski, M., *High Temperature Creep Cavitation Cracking Under the Action of Residual Stress in 316H Stainless Steel*, Ph.D. Thesis, Faculty of Science and Engineering, Materials Science Centre, University of Manchester, 2004.
34. Dai, H., Kelleher, J. F. and Withers, P. J., *Crack Tip Behaviour in Residual Stress Field: Finite Element Modelling and Neutron Diffraction Measurements*, in *ASME 2011 Pressure Vessels & Piping Division Conference*. 2011, ASME: Baltimore, Maryland, USA
35. Mahmoudi, A. H., Hadidi-Moud, S., Truman, C. E. and Smith, D. J., *A Numerical and Experimental Investigation into the Generation of Residual Stress in Fracture Specimens Using Local Compression*, in *ECF 15 - Advanced Fracture Mechanics for Life and Safety Assessments*, 2004, Sweden.

36. Mahmoudi, A. H., Stefanescu, D., Hossain, S., Truman, C. E., Smith, D. J. and Withers, P. J., *Measurement and Prediction of the Residual Stress Field Generated by Side-Punching,* Journal of Engineering Materials and Technology, 2006, **128**(3), pp. 451-459.
37. Mahmoudi, A. H., Truman, C. E. and Smith, D. J., *Using local out-of-plane compression (LOPC) to study the effects of residual stress on apparent fracture toughness,* Engineering Fracture Mechanics, 2008, **75**(6), pp. 1516-1534.
38. Hossain, S., Truman, C. E. and Smith, D. J., *Generation of residual stress and plastic strain in a fracture mechanics specimen to study the formation of creep damage in type 316 stainless steel,* Fatigue & Fracture of Engineering Materials & Structures, 2011, **34**(9), pp. 654-666.
39. Leggatt, R. and Kamath, M., *Residual Stresses in 25mm Thick Weld Metal COD Specimens in the As-welded and Locally Compressed States*, 1981: Welding Institute.
40. Leggatt, E. H., *Preparation of Aluminium Wide Plate Specimen: Deposition of EB Welds and Measurement of Residual Stresses*, TWI, Cambridge, UK, 1992.
41. Sharples, J. K., Harrison, M., May, K. A., Chivers, T. C. and Smith, E., *The Effect of Residual Stresses on Fracture Behaviour,* Pressure Vessel Integrity ASME, PVP, 1993, **250**, pp. 105-113.
42. Davies, C. M., Hughes, D., Wimpory, R. C., Dean, D. W. and Nikbin, K. M., *Measurements of Residual Stresses in 316 Stainless Steel Weldments*, in *ASME 2010 Pressure Vessels & Piping Division / K-PVP Conference*, July 18–22, 2010, Bellevue, Washington, USA, ASME.
43. Shirahatti, A., Truman, C. and Smith, D., *Experiments to Determine the Influence of Residual Stress and Elastic Follow-Up on Creep Crack Initiation*, in *ASME 2013 Pressure Vessels and Piping Conference*, 2013, American Society of Mechanical Engineers.
44. Shirahatti, A. M., Y. Wang, C. E. Truman and Smith, D. J., *Prediction of Creep Crack Initiation under the Interaction between Long Range Residual Stress and Applied Load*, in *13th International Conference on Fracture, June 16-21, 2013, Beijing, China*, 2013.
45. Lei, Y., O'Dowd, N. and Webster, G., *Fracture mechanics analysis of a crack in a residual stress field,* International Journal of Fracture, 2000, **106**(3), pp. 195-216.
46. Beardsmore, D. W., *JEDI: A Code for the Calculation of J for Cracks Inserted in Initial Strain Fields and the Role of J and Q in the Prediction of Crack Extension and Fracture*, in *ASME 2008 Pressure Vessels and Piping Conference*, 2008, American Society of Mechanical Engineers, pp. 955-966.
47. James, P. M., Hooton, D. G., Madew, C. J. and Sherry, A. H., *Predictions of elastic–plastic crack driving force and redistribution under combined primary and secondary stresses – Part 1: Analytical investigation,* International Journal of Pressure Vessels and Piping, 2013, **101**(0), pp. 101-112.
48. Stevens, M. J., Dennis, R. J., Bottomley, I. J. M. and Bradford, R. A. W., *Modelling the manufacturing history, through life creep-fatigue damage and limiting defect sizes of a pipework joint using finite element based methods,* International Journal of Pressure Vessels and Piping, 2013, **108–109**(0), pp. 13-27.
49. ABAQUS, *Version 6.11*. 2011, Dassault Systèmes.Hibbit, Karlsson, and Sorensen HKS Inc
50. Shih, C. F., Moran, B. and Nakamura, T., *Energy release rate along a three-dimensional crack front in a thermally stressed body,* International Journal of Fracture, 1986, **30**(2), pp. 79-102.
51. Li, F. Z., Shih, C. F. and Needleman, A., *A comparison of methods for calculating energy release rates,* Engineering Fracture Mechanics, 1985, **21**(2), pp. 405-421.

52. Paris, P. C., Gomez, M. P. and Anderson, W. E., *A rational analytic theory of fatigue,* The trend in engineering, 1961, **13**(1), pp. 9-14.
53. Ainsworth, R., Neale, B. and Price, R., *Fracture behaviour in the presence of thermal strains*, in *IMechE Conference, London*, 1978, pp. 197-204.
54. Lei, Y., *J-integral evaluation for cases involving non-proportional stressing,* Engineering fracture mechanics, 2005, **72**(4), pp. 577-596.
55. Boulay, A., Pellet, L., Bargellini, R. and Lei, Y., *Calculation of Elastic Fracture Mechanics Parameters Accounting for Residual Stresses*, in *ASME 2013 Pressure Vessels and Piping Conference*, 2013, American Society of Mechanical Engineers, pp. V06AT06A010-V06AT06A010.
56. Bueckner, H. F., *The propagation of cracks and the energy of elastic deformation,* Transactions of the American Society of Mechanical Engineers, 1958, **80**, pp. 1225-1230.
57. Webster, G. A., Ed.,, *Polycrystalline Materials — Determination of Residual Stresses by Neutron Diffraction*, ISO/TTA3 Technology Trends Assessment, Geneva, 2001.
58. ISO, *Polycrystalline Materials: Determination of Residual Stresses by neutron Diffraction, ISO/TTA 3*. 2001, International Organization for Standardization: Geneva, Switzerland
59. Hutchings, M. T., *Introduction to the characterization of residual stress by neutron diffraction*, 2005: Taylor & Francis.
60. Schajer, G. S., *Practical Residual Stress Measurement Methods*, 2013: Wiley.
61. Prime, *Measuring residual stress and the resulting stress intensity factor in compact tension specimens,* Fatigue & Fracture of Engineering Materials & Structures, 1999, **22**(3), pp. 195-204.
62. Schindler, H.-J. and Bertschinger, P., *Some Steps Towards Automation of the Crack Compliance Method to Measure Residual Stress Distributions*, in *Proceedings of the 5th International Conference on Residual Stress*, 1997, Linköping.
63. Fett, T. and Munz, D., *Stress intensity factors and weight functions*, 1997: Computational Mechanics Publications.
64. Prime, M. B., *Cross-Sectional Mapping of Residual Stresses by Measuring the Surface Contour After a Cut,* Journal of Engineering Materials and Technology, 2001, **123**(2), pp. 162-168.
65. Hosseinzadeh, F., Kowal, J. and Bouchard, P. J., *Towards good practice guidelines for the contour method of residual stress measurement,* Journal of Engineering (Online only), 2014.
66. Prime, M. B. and Kastengren, A. L., *The contour method cutting assumption: error minimization and correction*, in *Experimental and Applied Mechanics, Volume 6*, 2011, Springer, pp. 233-250.
67. Sutton, M., Wolters, W., Peters, W., Ranson, W. and McNeill, S., *Determination of displacements using an improved digital correlation method,* Image and vision computing, 1983, **1**(3), pp. 133-139.
68. ARAMIS User Handbook, GOM mbH, Braunschweig, Germany, 2001.
69. Chu, T. C., Ranson, W. F. and Sutton, M. A., *Applications of digital-image-correlation techniques to experimental mechanics,* Experimental Mechanics, 1985, **25**(3), pp. 232-244.
70. Pan, B., Qian, K., Xie, H. and Asundi, A., *Two-dimensional digital image correlation for in-plane displacement and strain measurement: a review,* Measurement science and technology, 2009, **20**(6), pp. 062001.
71. Hild, F. and Roux, S., *Digital image correlation*, 2012: Wiley-VCH, Weinheim.
72. Davies, C. M., Wimpory, R. C., Dean, D. W., Webster, G. A. and Nikbin, K. M., *Effect of Residual Stresses on Crack Growth in 316H Steel Weldments*, in *3rd International*

Conference on Integrity of High Temperature Welds, 24th–26th April, 2007, 1 Carlton House Terrace, London, UK,D.J. Allen, et al., IOM Communications, pp. 333–344.
73. Withers, P. J. and Bhadeshia, H. K. D. H., *Residual Stress. Part 2–Nature and Origins,* Materials science and technology, 2001, **17**, pp. 366.
74. Masubuchi, K., *Residual Stresses and Distortion in Welds*, in *Encyclopedia of Materials: Science and Technology (Second Edition)* K.H.J. Buschow, et al., Editors, 2005, Elsevier, Oxford, pp. 1-6.
75. Goldak, J. A. and Akhlaghi, M., *Computational welding mechanics*, 2005: Springer.
76. Lindgren, L.-E., *Finite element modeling and simulation of welding. Part 2: Improved material modeling,* Journal of thermal stresses, 2001, **24**(3), pp. 195-231.
77. ASTM, *E1457-13: Standard Test Method for Measurement of Creep Crack Growth Times and Rates in Metals*, in *Annual Book of ASTM Standards*, Vol. 03.01, 2013, ASTM International.
78. Kapadia, P., Davies, C. M., Dean, D. W. and Nikbin, K. M., *Numerical Simulation of Residual Stresses Induced in Compact Tension Specimens using Electron Beam Welding*, in *ASME 2012 Pressure Vessels & Piping Division Conference*. 2012, ASME: Toronto, Ontario, Canada
79. Davies, C. M., Dean, D. W., Mehmanparast, A. N. and Nikbin, K. M., *Compressive Pre-Strain Effects on Creep and Crack Growth Behaviour of 316H Stainless Steel*, in *ASME 2010 Pressure Vessels & Piping Division / K-PVP Conference*. 2010, ASME: Bellevue, Washington, USA2010
80. Schultz, H., *Electron Beam Welding*, 1994: Woodhead Publishing.
81. Toloczko, M. B., LUCAS, G. E., ODETTE, G. R., STOLLER, R. E. and HAMILTON, M. L., *An investigation of microstructures and yield strengths in irradiated austenitic stainless steels using small specimen techniques,* ASTM special technical publication, 1996(1270), pp. 902-918.
82. Sakanashi, Y., Gungor, S. and Bouchard, J., *Measurement of local creep properties in stainless steel welds,* 2012.
83. Mehmanparast, A. N., *The Influence of Inelastic Damage on Creep, Fatigue and Fracture Toughness*, Mechanical Engineering Department, Imperial College London, 2012.
84. Pirling, T., Bruno, G. and Withers, P. J., *SALSA—A new instrument for strain imaging in engineering materials and components,* Materials Science and Engineering: A, 2006, **437**(1), pp. 139-144.
85. Hofmann, M., Schneider, R., Seidl, G. A., Rebelo-Kornmeier, J., Wimpory, R. C., Garbe, U. and Brokmeier, H. G., *The new materials science diffractometer STRESS-SPEC at FRM-II,* Physica B: Condensed Matter, 2006, **385–386, Part 2**(0), pp. 1035-1037.
86. Boin, M., Wimpory, R. C. and Randau, C., *Improving Beamtime Efficiency for Residual Stress Neutron Experiments*, in *Materials Science Forum*, 2014, 777, Trans Tech Publ, pp. 7-11.
87. Withers, P., Preuss, M., Steuwer, A. and Pang, J., *Methods for obtaining the strain-free lattice parameter when using diffraction to determine residual stress,* Journal of Applied Crystallography, 2007, **40**(5), pp. 891-904.
88. Holden, T. M., Suzuki, H., Carr, D. G., Ripley, M. I. and Clausen, B., *Stress measurements in welds: Problem areas,* Materials Science and Engineering: A, 2006, **437**(1), pp. 33-37.
89. Traore, Y., Paddea, S., Bouchard, P. J. and Gharghouri, M. A., *Measurement of the Residual Stress Tensor in a Compact Tension Weld Specimen,* Experimental Mechanics, 2013, **53**(4), pp. 605-618.

90. Richter-Trummer, V., Moreira, P. M. G. P., Ribeiro, J. and de Castro, P. M. S. T., *The contour method for residual stress determination applied to an AA6082-T6 friction stir butt weld*, in *Materials Science Forum*, 2011, 681, Trans Tech Publ, pp. 177-181.
91. Murugan, N. and Narayanan, R., *Finite element simulation of residual stresses and their measurement by contour method,* Materials & Design, 2009, **30**(6), pp. 2067-2071.
92. Johnson, G., *Residual Stress Measurements Using the Contour Method*, School of Materials, University of Manchester, 2008.
93. Prime, M., Sebring, R., Edwards, J., Hughes, D. and Webster, P., *Laser surface-contouring and spline data-smoothing for residual stress measurement,* Experimental Mechanics, 2004, **44**(2), pp. 176-184.
94. ABAQUS, *Version 6.10*. 2010, Dassault Systèmes.Hibbit, Karlsson, and Sorensen HKS Inc
95. Vlamis, P., *Finite Element Simulation and Validation of Welding Processes and Residual Stress Predictions*, Mechanical Engineering, Imperial College London, 2013.
96. Smith, M. C., Smith, A. C. and Wimpory, R., *A review of the NeT Task Group 1 residual stress measurement and analysis round robin on a single weld bead-on-plate specimen,* International Journal of Pressure Vessels and Piping, 2014.
97. Muránsky, O., Smith, M. C., Bendeich, P. J., Hosseinzadeh, F. and Edwards, L., *Numerical analysis of retained residual stresses in C(T) specimen extracted from a multi-pass austenitic weld and their effect on crack growth,* Engineering Fracture Mechanics, 2014.
98. Smith, R. M., *FEAT-WMT: Weld-Modelling Tool User Guide*, 2011.
99. Goldak, J., Chakravarti, A. and Bibby, M., *A new finite element model for welding heat sources,* Metallurgical and Materials Transactions B, 1984, **15**(2), pp. 299-305.
100. Lundbäck, A. and Runnemalm, H., *Validation of three-dimensional finite element model for electron beam welding of Inconel 718,* Science and Technology of Welding and Joining, 2005, **10**, pp. 717-724.
101. Siegel, R., *Thermal Radiation Heat Transfer, Fourth Edition*, 2001: Taylor & Francis.
102. Muránsky, O., Hamelin, C. J., Smith, M. C., Bendeich, P. J. and Edwards, L., *The effect of plasticity theory on predicted residual stress fields in numerical weld analyses,* Computational Materials Science, 2012, **54**(0), pp. 125-134.
103. Keinänen, H., *VORSAC Task 2.5.4: Isotropic-Kinematic Hardening Models*, Espoo, Finland, VTT Manufacturing Technology Report VALC663, 1999.
104. Smith, M. C., Nadri, B., Smith, A. C., Carr, D. G., Bendeich, P. J. and Edwards, L. E., *Optimisation of Mixed Hardening Material Constitutive Models for Weld Residual Stress Simulation Using the NeT Task Group 1 Single Bead on Plate Benchmark Problem,* ASME Conference Proceedings, 2009, **2009**(43697), pp. 303-318.
105. Smith, M. C., *Development of mixed istotropic-kinematic material hardening models for finite element simulation of austenitic steel welds*, British Energy Report, E/REP/BDBB/0092/AGR/06,Revision 000, 2006.
106. ABAQUS, *A Novel Approach to Annealing Using ABAQUS - ABAQUS Behaviour with soft annealing*,V2.1, 2006.
107. ASTM, ASTM International, *E1221-12a: Standard Test Method for Determining Plane-Strain Crack-Arrest Fracture Toughness, KIa, of Ferritic Steels*,
108. Special Metals Corporation, *NIMONIC ® Alloy 115*, 2004.
109. Kapadia, P., Zhou, H., Davies, C. M., Wimpory, R. C. and Nikbin, K. M., *Simulating Residual Stresses using a Modified Wedge-Loaded Compact Tension Specimen*, in *ASME 2013 Pressure Vessels & Piping Division Conference*. 2013, ASME: Paris, France

110. Avallone, E. A. and Baumeister, T., *Marks' Standard Handbook for Mechanical Engineers*, 1996: McGraw-Hill.
111. Goodman, A. M., *Development of constitutive equations for computer analysis of stainless steel components,* Nuclear Engineering and Design, 1984, **83**(3), pp. 349-354.
112. McLennon, D. R. and Allport, L., *Measurement of Creep Crack Incubation and Creep Crack Growth Rates*, British Energy Generation Limited, E-REP-BBGB-0047-GEN-09, 2011.
113. Ritchie, R. O., Thompson, A.W, *On Macroscopic and Microscopic Analyses for Crack Initiation and Growth Toughness in Ductile Alloys,* Metallurgicac Transcations A, 1985, **16A**, pp. 236-238.
114. Nabarro, F. R. N. and de Villiers, F., *Physics Of Creep And Creep-Resistant Alloys*, 1995: Taylor & Francis.
115. Dogan, B., Ceyhan, U., Nikbin, K. M., Petrovski, B. and Dean, D. W., *European Code of Practice for Creep Crack Initiation and Growth Testing of Industrial Specimens,* Journal of ASTM International, 2006, **3**(2), pp. 20.
116. Webster, G. A., Davies, C. M. and Nikbin, K. M., *Assessment of Creep Crack Growth due to Stress Relief,* International Journal of Solids and Structures, 2010, **47**(7-8), pp. 881-886.
117. Davies, C. M., Dean, D. W., Nikbin, K. M. and O'Dowd, N. P., *Interpretation of Creep Crack Initiation and Growth Data for Weldments,* Engineering Fracture Mechanics, 2007, **74** (6).
118. Moin, P., *Fundamentals of Engineering Numerical Analysis*, 2010: Cambridge University Press.
119. Spindler, M., *RE: Test Data in CREEP2007-26152*,email to P. Kapadia, 4th September 2012 2012.
120. Frost, H. J. and Ashby, M. F., *Deformation Mechanism Maps*, 1982, Oxford: Pergamont press.
121. Chen, B., Flewitt, P. E. J., Cocks, A. C. F. and Smith, D. J., *A review of the changes of internal state related to high temperature creep of polycrystalline metals and alloys,* International Materials Reviews, 2014.
122. Foster, A. D., Copeland, T. J., Cox, C. J., Hall, P. W., Watkins, M. A., Wright, R. and Lin, J., *Error analysis and correction in the slab method for determining forming forces,* International Journal of Mechanical Engineering Education, 2009, **37**(4), pp. 304-317.
123. Chen, B., Flewitt, P. E. J. and Smith, D. J., *Microstructural sensitivity of 316H austenitic stainless steel: Residual stress relaxation and grain boundary fracture,* Materials Science and Engineering: A, 2010, **527**(27–28), pp. 7387-7399.
124. Moran, B. and Shih, C. F., *Crack tip and associated domain integrals from momentum and energy balance,* Engineering Fracture Mechanics, 1987, **27**(6), pp. 615-642.
125. Kim, Y.-J., *Contour integral calculations for generalised creep laws within abaqus,* International Journal of Pressure Vessels and Piping, 2001, **78**(10), pp. 661-666.
126. Lei, Y., *FE Creep Analysis of a Single-Edge-Cracked Plate under Combined Primary and Secondary Loading*, EDF Energy Nuclear Generation, E/REP/BBGB/0056/GEN/09, 2013.
127. Oh, C.-S., Kim, N.-H., Kim, Y.-J., Davies, C., Nikbin, K. and Dean, D., *Creep failure simulations of 316H at 550°C: Part I – A method and validation,* Engineering Fracture Mechanics, 2011, **78**(17), pp. 2966-2977.
128. Davies, C. M. and Mehmanparast, A. N., *Creep Crack Growth Modelling in 316H Stainless Steel*, in *Advanced Materials Modelling for Structures*, Vol. 19, H. Altenbach and S. Kruch, Editors, 2013, Springer Berlin Heidelberg, pp. 109-120.

129. Bradford, R. A. W., *Finite element modelling of reheat cracking initiation in austenitic weldments*, in *IMECHE CONFERENCE TRANSACTIONS*, 1998, 6, MECHANICAL ENGINEERING PUBLICATIONS, pp. 287-298.
130. Auzoux, Q., Allais, L., Caës, C., Monnet, I., Gourgues, A. F. and Pineau, A., *Effect of pre-strain on creep of three AISI 316 austenitic stainless steels in relation to reheat cracking of weld-affected zones,* Journal of Nuclear Materials, 2010, **400**(2), pp. 127-137.
131. Merah, N., *Detecting and measuring flaws using electric potential techniques,* Journal of Quality in Maintenance Engineering, 2003, **9**(2), pp. 160-175.
132. Dassault Systemes Support, *SR00201886 Potential bug found in Abaqus*,email to P. Kapadia, 1st July 2014.
133. Ford, H., *Advanced Mechanics of Materials*, 2nd Edition ed, 1977: Wiley.
134. Brocks, W., Scheider, I. and Geesthacht, G.-F., *Numerical aspects of the path-dependence of the j-integral in incremental plasticity,* 2001.
135. Brocks, W. and Olschewski, J., *On J-dominance of crack-tip fields in largely yielded 3D structures,* International Journal of Solids and Structures, 1986, **22**(7), pp. 693-708.
136. Cook, R. D., Malkus, D. S., Plesha, M. E. and Witt, R. J., *Concepts and applications of finite element analysis,* 2002.

A VALIDATION OF METHODS TO EVALUATE K^s

A.1 INTRODUCTION

A FE test model is presented where an analytical solution for the stress intensity factor due to secondary loads, K^s, was determined and compared to the value of K^s found from the J-integral, superposition and slitting approaches described in the Section 2.5. Various modelling assumptions were tested on this simple problem to determine the best practice for analysing more complicated models of fracture specimens with residual stresses.

The evaluation of K_J^s using the J-integral approach was performed using elastic and elastic-plastic material models, furthermore the elastic-plastic analyses were solved using the small-strain and large-strain assumptions in the ABAQUS solver. Each of these methods were tested to determine which methods provided path-independent values of J.

In the superposition approach, crack face loads were applied on nodal locations and on element surfaces to investigate whether the K^s solution was sensitive the load application method.

A.2 SPECIMEN GEOMETRY AND LOADING CONDITION

Stress intensity factors were determined for an edge cracked plate which had a residual stress distribution that was defined by a cosine function, as shown in Figure A.2. The geometry and loading condition was selected such that the residual stress distribution ahead of the crack was similar to that in the EB welded C(T) specimen. For this simple test case, an analytical solution of K was available and was used to validate the three approaches.

The stress intensity factor, K, for this test load case is determined by [20]:

$$K = \sigma_0\sqrt{\pi a}\left[\frac{1.122 - 4\left(\frac{a}{b}\right)^3}{1 + 2\left(\frac{a}{b}\right)^2} + 1.5\frac{a}{b}\left(0.375 - \frac{a}{b}\right)\left(1 - \frac{a}{b}\right)^3\right] \quad \text{(A-1)}$$

where a is the crack length in a plate of with width, b, which are selected to be 3.5 mm and 25 mm respectively. This analytical solution has an accuracy of 1% [20].

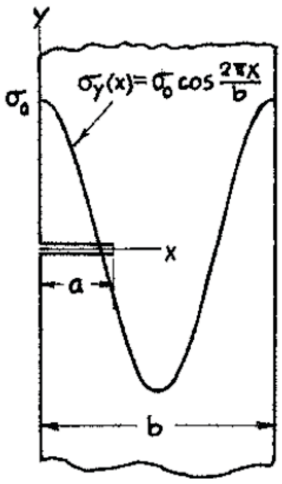


Figure A.2 Edge cracked plate with residual stresses defined by a cosine curve (image from [20])

The stress, σ_0, defines the stress distribution using:

$$\sigma = \sigma_0 \cos\left(\frac{2\pi x}{b}\right) \tag{A-2}$$

The uncracked plate was modelled in 2D assuming plane strain conditions and is shown in Figure A.1(a). The simulation modelled half of the plate geometry with a plane of symmetry defined along the crack line. The x-displacement of a single node was constrained to prevent rigid body motion. For the model of the cracked plate, the symmetry boundary condition on the crack face was removed as shown in Figure A.1(b).

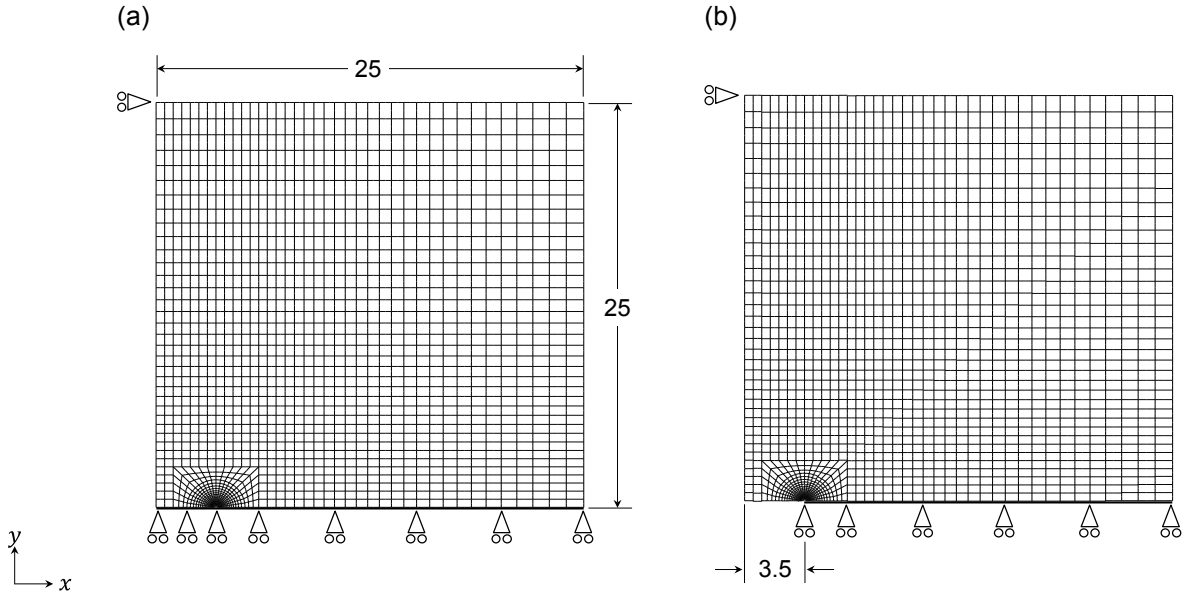


Figure A.1 Geometry and boundary conditions on edge cracked plate with contour integral mesh (a) before crack insertion (b) after crack insertion

The element type was selected to be CPE8R where plane strain was assumed and eight noded elements were used with reduced integration. The elements were attributed a thickness of 25 mm. In the models where K^S was determined using contour integrals a focused mesh was used in the crack region where the element length was 5 μm at the crack tip as shown in Figure A.3. The contour integrals were evaluated over 36 contours up to 2.5 mm from the crack tip. The crack tip was meshed using quadratic quadrilateral elements which had collapsed sides such that the nodes along one side of the element were at the same location in the beginning of the analysis. As the crack mouth opened the nodes moved apart to model crack tip blunting.

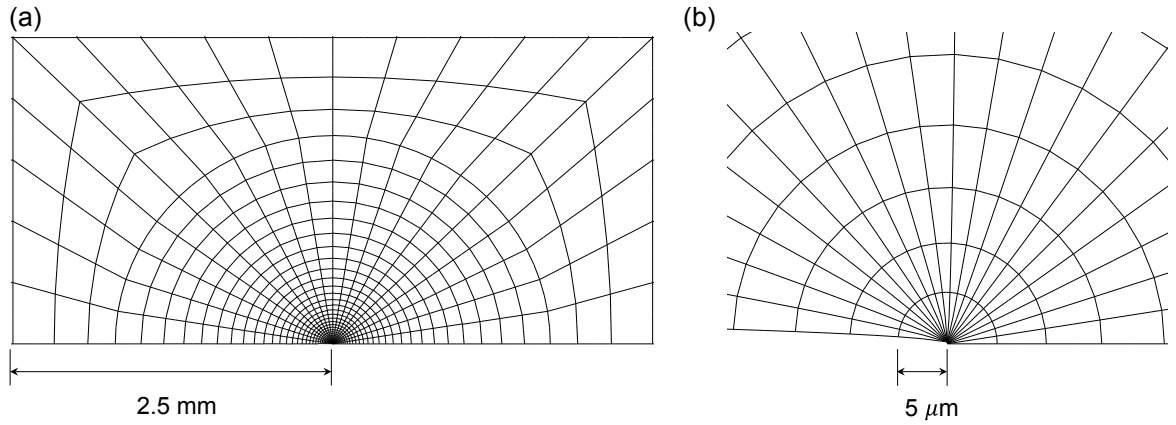


Figure A.3 (a) Focused mesh showing the contour domains around the crack tip (b) Deformed mesh near the crack tip

The initial stress was imposed in the FE model of the uncracked plate using the *INITIAL CONDITION option in ABAQUS with the user subroutine SIGINI. At the beginning of the analysis σ_{yy} was defined using (A-2) with σ_0 = 200 MPa and the components σ_{xx} and σ_{xy} were initialised as zero. In the first step of the FE analysis no additional loads or constraints were applied such that these initial stresses redistributed to reach equilibrium.

These analyses used simple elastic and elastic-plastic material models based on Type 316H stainless steel at room temperature with isotropic hardening. The Young's modulus and Poisson's ratio are 195.6 GPa and 0.294 respectively, and the elastic-plastic model was defined using the true stress and plastic strain data presented by Nadri et al. [32].

The stresses, σ_{yy}, determined at various stages of the J-integral analysis are shown in Figure A.4. Figure A.4(a) shows the stresses after the residual stresses were induced by the user subroutine (Step Time = 0), which redistribute to Figure A.4(b) to satisfy equilibrium

(Step Time = 1). Further stress redistribution took place when the crack was inserted as shown in Figure A.4(c), (Step Time = 2). The stresses component σ_{yy} along the crack line, in the uncracked plate, at these various stages of the analysis are shown in Figure A.5. As the initial stresses redistribute to reach equilibrium the stress magnitudes reduce and are closely defined by a peak stress of 194 MPa in the analytical profile in (A-2).

The analytical solution for K is found to be 21.6 ± 0.2 MPam$^{1/2}$ using equation (A-1) and an initial peak stress, σ_0, of 194 MPa.

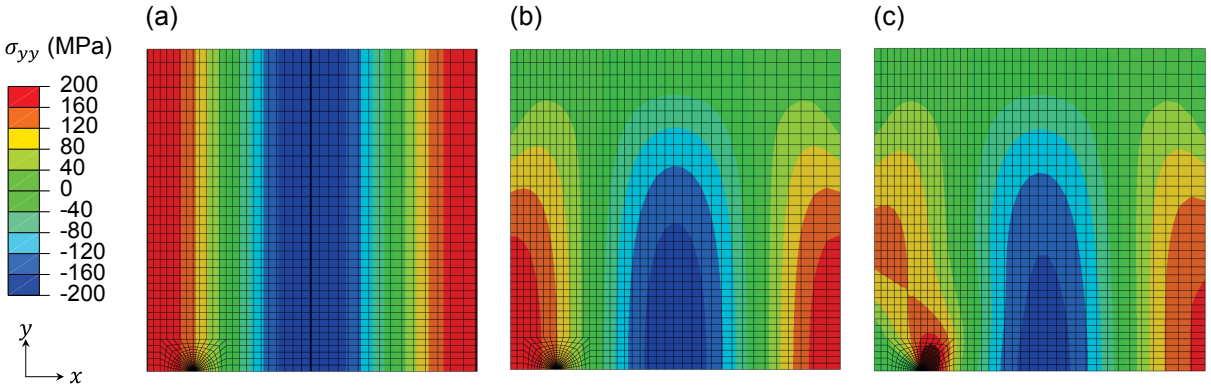


Figure A.4 Stress, σ_{yy}, in MPa (a) imposed on uncracked plate, (b) in uncracked plate after equilibrium is reached (c) after edge crack insertion

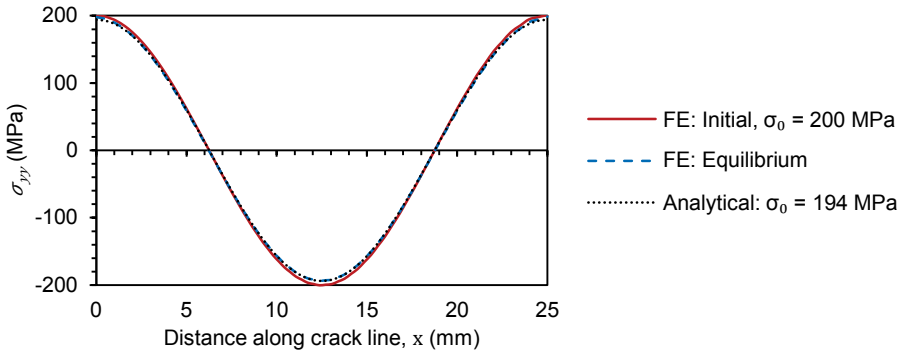


Figure A.5 Stresses along the crack line in the direction normal to the crack face

A.3 THE *J*-INTEGRAL APPROACH

To assess the J-integral with the presence of residual stresses the uncracked plate, shown in Figure A.4(b), was defined as the initial state using the RESIDUAL STRESS STEP option in the *CONTOUR INTEGRALS keyword. The symmetry boundary condition on the crack face of the specimen was then removed to introduce the crack as shown in

Figure A.4(c). The constraint was removed on all nodes simultaneously. If the crack was introduced incrementally, by sequentially removing the boundary condition of each node, the crack tip stresses would induce plasticity at each crack position and a plastic wake would have been formed along the crack faces. This plasticity reduces the crack driving force which results in non-conservative estimates of J [28].

Analyses were performed using elastic and elastic-plastic material models, furthermore the elastic-plastic models were run with small strain and large strain assumptions to determine which produced path-independent values of J.

A fault was encountered in the ABAQUS software which affected the J-integral solution. When residual stress fields were defined in a model using the SIGINI user-defined subroutine (i.e. using the *INITIAL CONDITIONS, type=STRESS, USER keyword) or transferred from another analysis (i.e. with the *MAP SOLUTION keyword), J was path dependent. However when the residual stresses were generated by modelling the stress inducing process or by copying from another analysis using the *INITIAL CONDITIONS, TYPE=STRESS, FILE=*oldjobname*.odb keyword, J was path independent. This was reported to the ABAQUS support team and after investigation it was found that a bug existed where a fix would be implemented in a future release (bug report number: BR10000162554) [132]. This fault affected the analysis of the test model as the residual stresses were initialised using the SIGINI user-subroutine and also affected the EB weld simulation detailed in Chapter 4 as the results were transferred using the *MAP SOLUTION keyword. As a work-around an intermediate step was introduced in the analyses where the stresses were copied to an identical model using the *INITIAL CONDITIONS, TYPE=STRESS, FILE=*oldjobname*.odb keyword. The results of the test model shows path independent values of J were obtained using this procedure as shown in Figure A.6.

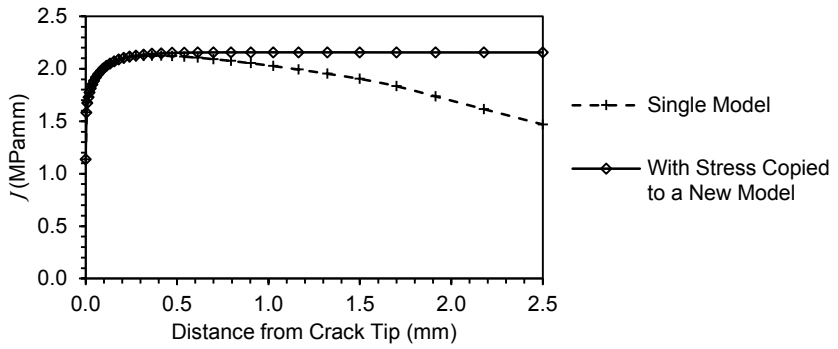


Figure A.6 J-integral for edge cracked plate with residual stresses showing path independence where stresses are copied to a new model

Stress intensity factors were determined from J using (2.45) and are shown in Figure A.7 as a function of distance from the crack tip and contour domain number. The models with elastic-plastic material properties were analysed using small strain and large strain assumptions. The elastic analysis converged to K_J^s = 21.3 MPam$^{1/2}$ at the second contour domain, this value is close to the analytical solution. The elastic-plastic analyses also provided predictions close to the analytical solution (K_J^s = 21.5 MPam$^{1/2}$), however converged to a path independent value at larger distances from the crack tip.

The solutions from both elastic-plastic models converged at contour domain number 25 which was 0.61 mm from the crack tip. The equivalent plastic strains, ε^{pl}, around the crack are shown in Figure A.8 and the nodes in contour domain 25 are highlighted, the

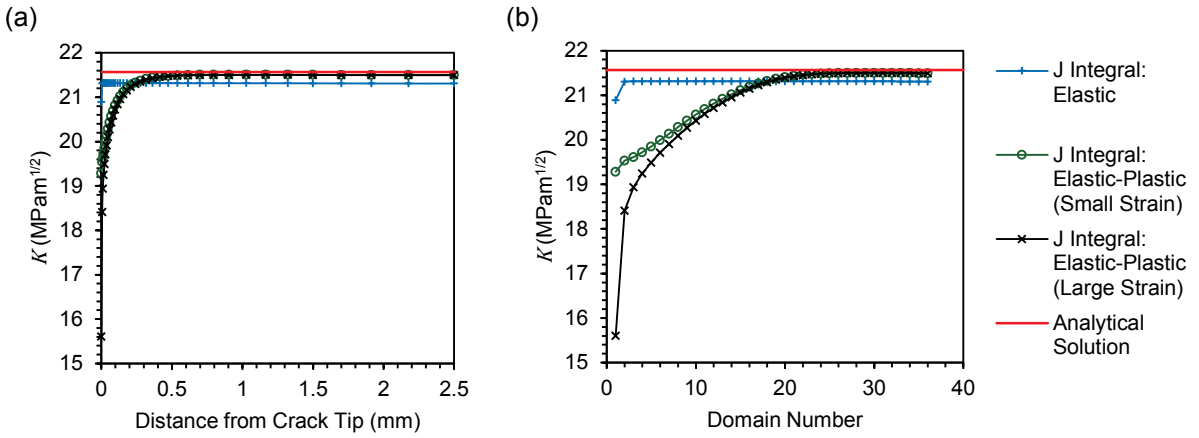


Figure A.7 Stress intensity factor solutions for edge cracked plate under residual stress field determined using the J-integral as a function of (a) distance from the crack tip (b) domain number of the contour integral

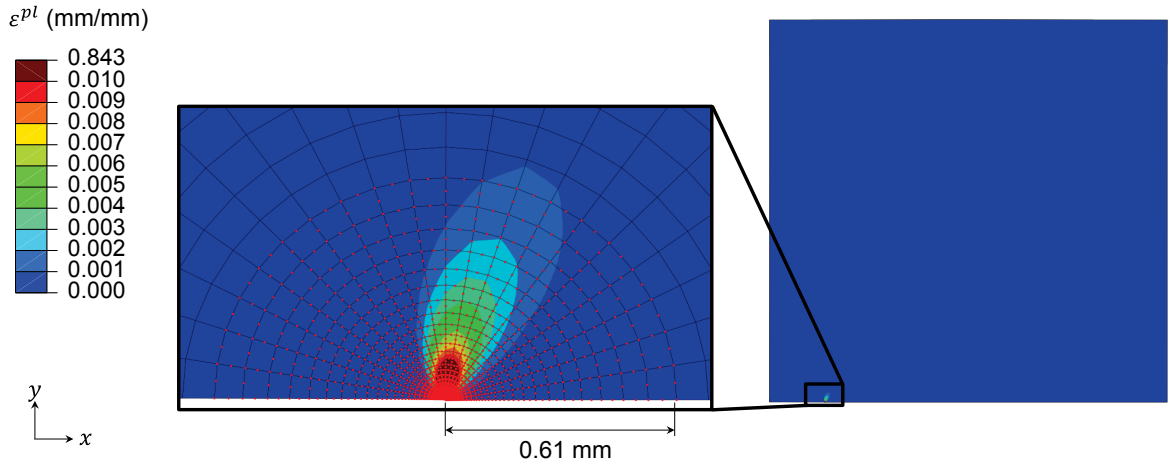


Figure A.8 Equivalent plastic strains (in mm/mm) near the crack tip of the edge cracked plate with residual stresses, the nodes for contour domain 25 are highlighted

results shown are for the analysis with the large strain assumption. Hence the J-integral becomes path independent when the contour domain extends beyond the plastic zone which is where ε^{pl} > 0.1%.

The edge cracked plate modelled with elastic-plastic material properties was analysed using both small and large strain theory. In general, the strain tensor is computed using a series expression which include second order terms. Such terms are required to define large strains accurately. For the small strain approximation, second order terms within the definition of strain are assumed to be negligible. In general the small strain approximation is valid for strains less than 1% [133, p121]. Using this simplification, the strain field in the FE solution may be derived based on the original configuration of the body. For the large strain formulation the strains are derived based on the deformed shape of the body [49]. For this method, the stiffness matrix needs to be reassembled for every increment in the analysis, hence the large-strain analyses are computationally more expensive.

The effect of the small and large strain assumption on evaluating the J-integral under primary load conditions was investigated by Brocks et al. [134]. It was found that the J-integral in small strain analyses converged to become path independent at domains significantly closer to the crack tip in comparison to large strain analyses. As more deformation occurs with the large strain assumption, crack tip blunting is more pronounced and therefore the contour domain must be large enough to contain this region of crack tip plasticity.

In primary load conditions, the plastic zone size is limited to a small region around the crack tip. Therefore use of the small strain assumption does not affect the global response of the component and can be made for such loading conditions. In the EB welded C(T) specimens investigated in this study significant plastic deformation occurs throughout the specimen as the residual stresses are induced and requires large strain theory to be used in the corresponding FE analyses. Once large strain theory is used to determine the residual stresses induced, it must also be used for all subsequent steps of the analysis. Therefore the evaluation of J-integrals under residual stress dominated load conditions must be performed using the large strain assumption and its use has been validated by the edge cracked plate model.

ABAQUS does not recommend the use of focused meshes for large strain analyses as severe deformation can occur near the crack tip which can lead to numerical difficulties in the

analysis [49]. However a study by Brocks et al. [135] has shown that singular elements around crack tip regions are compatible with large-strain analyses and has validated J-integrals under primary load conditions with this assumption.

Figure A.7 shows the near crack tip K values from the J-integral analysis with the small strain assumption are slightly larger than those when the large strain assumption is used. This indicates the stress singularity is more pronounced in the crack tip region for the small strain analysis. This is expected as more crack tip blunting occurs in the large strain analysis and hence the stresses reduce. As the size of the J-integral domain increases and encompasses the crack tip plastic zone to become path independent, both deformation theories converge to give the same solution.

A.4 THE SUPERPOSITION APPROACH

The superposition analysis was performed using the geometry of the cracked plate shown in Figure A.9(a). Loads were applied to the crack face of the edge cracked plate and K was evaluated using contour integrals in ABAQUS. The applied loads were extracted from the J-integral FE analysis after the initial stresses had reached equilibrium in the uncracked plate, as shown in Figure A.4(b). Two methods of load application in ABAQUS were investigated where the crack face loads were applied using concentrated nodal forces and distributed surface loads.

The nodal forces were obtained from the reaction forces along the crack face of the uncracked plate, i.e. the stresses in Figure A.4(b), and were applied as concentrated forces (*CLOAD) on the corresponding nodes in the edge cracked plate, as shown in Figure A.9(b). The forces along the crack face nodes are shown in Figure A.11(a). The force distribution is

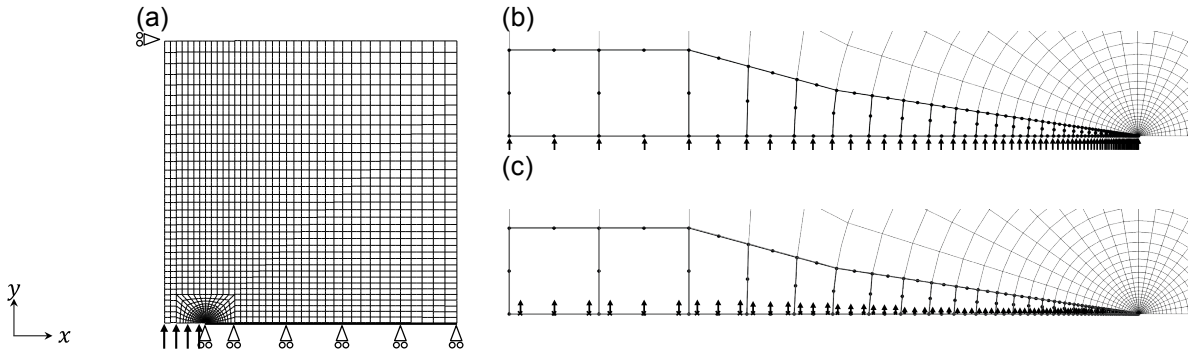


Figure A.9 (a) Loading conditions on the edge crack plate for K evaluation using the superposition method, (b) load application using concentrated forces on nodes and (c) load application using distributed load on surface

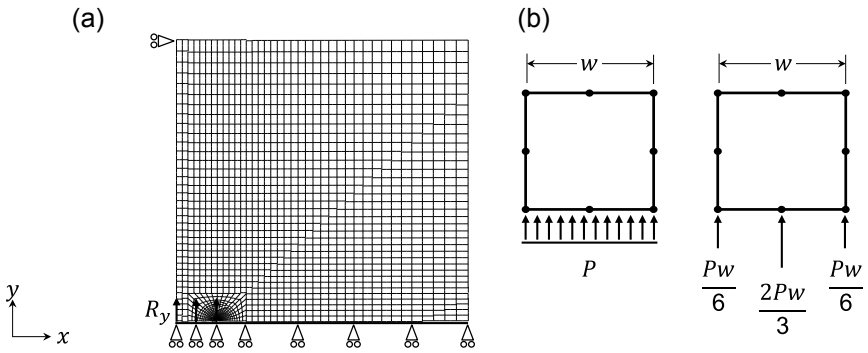


Figure A.10 (a) Uncracked plate showing location of reaction forces extracted for the superposition method (b) allocation of uniform distributed load to nodes on an 8 noded 2D element

not a smooth profile across the nodes as the mid-sided and corner nodes have weighting factors of (2/3) and (1/6) respectively as shown in Figure A.10(b) [136, p113]. To validate these reaction forces, stresses were obtained by dividing these loads by the weighting factors and the element surface area, which are shown in Figure A.11(b). The resulting stresses followed the same distribution as the applied stress, however were slightly smaller in magnitude which is due to the redistribution of residual stresses.

In the second approach the stresses normal to crack growth were extracted from the J-integral analysis and applied as a distributed pressure load on the element faces on the crack line in the superposition analysis, as shown in Figure A.9(c). The distributed load (*DSLOAD) was applied as a non-uniform pressure on the crack face using the DLOAD user-subroutine and the UEXTERNALDB subroutine was used to store the stress data. The pressure was applied at integration points on the surface of the elements [49]. These surface integration points are shown in Figure A.12 and are different from the points within the volume of the element that are used to numerically integrate the stiffness matrix. The exact

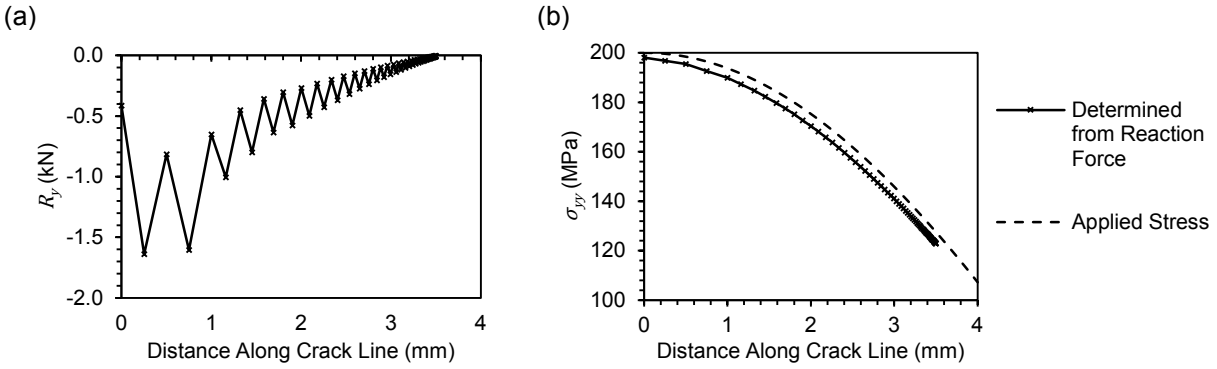


Figure A.11 (a) Reaction forces, R_y, on uncracked plate to be applied to the crack face in the superposition method (b) Stress, σ_{yy}, determined from the reaction forces compared to the applied stress

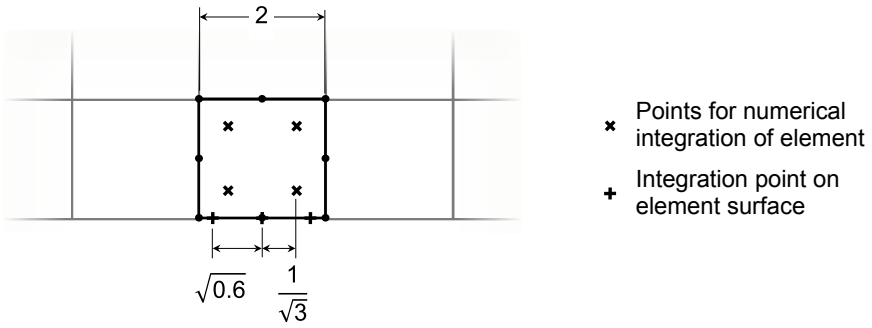


Figure A.12 Integration points on a quadratic element (8-noded) with reduced integration

locations of the surface integration points are not stated in the ABAQUS documentation, the integration point locations were found using a single element test model. For quadratic elements which have eight nodes, the location of the surface integration points along the element face are found to match the gauss point locations of 3rd order elements [136, p210], irrespective of whether full or reduced integration is used for the numerical integration of the element stiffness matrix.

For the superposition model of the edge cracked plate using a distributed load, the crack face pressure could be obtained in two ways: the analytical expression of the stress distribution, equation (A-2), or the extraction of stresses from the FE analysis of the uncracked plate. The second approach required extrapolation of the stress output at element integration points to the surface integration points and therefore was less accurate than the first approach which was considered exact. However for general loading conditions, such as the EB welded C(T) specimens with residual stresses, an analytical solution was not available and extrapolation of stresses to the element surface was required. The accuracy of these two approaches was investigated using the edge cracked plate test model. A simplistic way of calculating the pressure at the element surface was to use the average of the stresses at the nodes on the surface of the element and therefore a constant pressure was applied across each element surface. This method involves extrapolation of stresses which introduces inaccuracies, however it was easy to implement in the *DLOAD user-subroutine as knowledge of the order of integration points across the element surface was not required. The crack face pressure determined using the analytical solution and extrapolation of stresses are shown in Figure A.13. The analytical expression was solved using σ_0 = 194 MPa to take into account redistribution of the residual stresses.

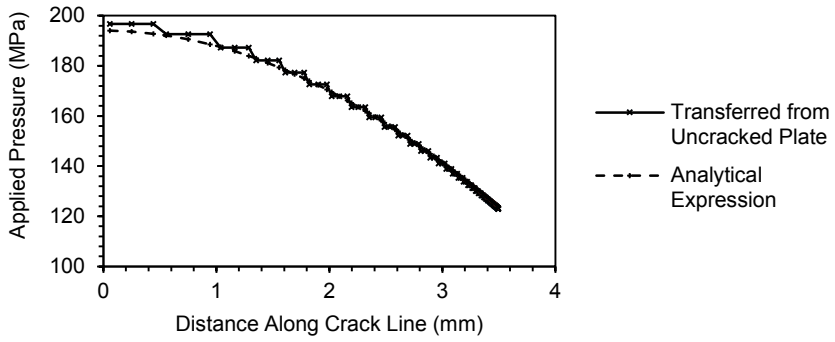


Figure A.13 Comparison of non-uniform pressure applied to the crack face of edge crack plate determined analytically and by transferring stresses interpolated from the uncracked plate FE analysis

These analyses used element type CPE8R and an identical mesh to the J-integral analysis. This ensured the element and node numbering remained consistent between the two models, allowing results to be easily transferred. Three FE models of the edge cracked plate were analysed to determine K using the superposition approach:

1. Concentrated loads at the crack face nodes were determined from reaction forces in the uncracked plate FE analysis
2. Distributed pressure load on the crack face surface was defined by an analytical expression
3. Distributed pressure load on the crack face surface was extrapolated from the uncracked plate FE analysis.

Stress intensity factors determined from each of these analyses are shown in Figure A.14 as a function of distance from the crack tip and the contour domain number, and are compared to the analytical solution of K. Both analyses using the distributed pressure

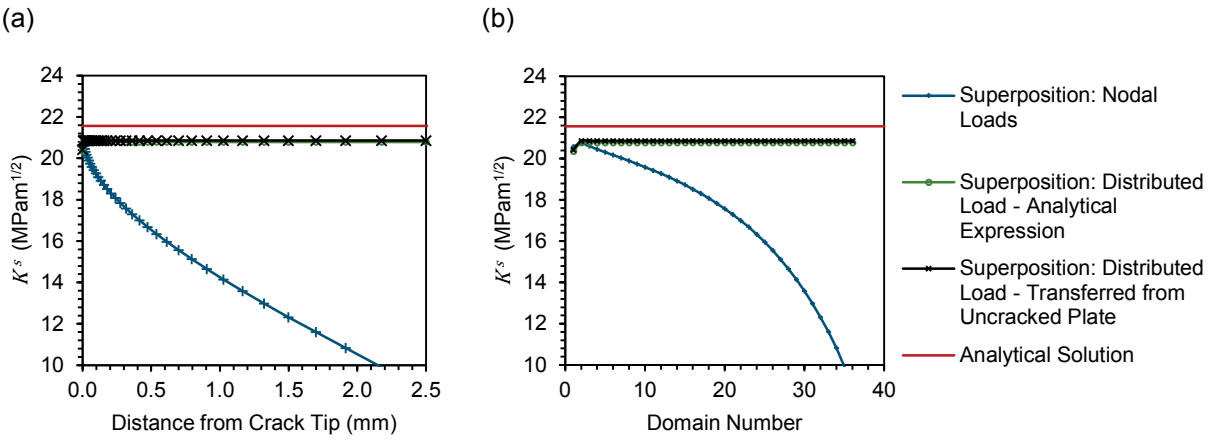


Figure A.14 Stress intensity factor solutions for edge cracked plate under residual stress field determined using the superposition approach as a function of (a) distance from the crack tip (b) domain number of the contour integral

loads produced path independent values of K which are in close agreement with each other. The stress intensity factors, K, determined using the analytically defined pressure distribution and the pressure distribution interpolated from the uncracked plate were 20.7 MPam$^{1/2}$ and 20.8 MPam$^{1/2}$ respectively. Therefore the error in K when extrapolating and averaging stresses over element faces was judged to be small.

The model using the concentrated nodal loads did not produce path independent results. The value of K at the second contour domain was close to the analytical expression and matched the distributed load analyses, however K reduced as the size of the domain increased. The deformation and stress distribution in all the superposition analyses were the same and therefore should produce the same values of K. It is considered that this path dependence occurred as ABAQUS treated the nodal loads as crack face tractions in the evaluation of the contour integral. However the crack face tractions are assumed to be zero in the formulation of the J-integral which is used by ABAQUS to determine K [49].

A.5 THE SLITTING APPROACH

The numerical simulation of the slitting method was performed by progressively introducing a crack into the plate after the residual stresses had redistributed and reached equilibrium by removing the symmetry boundary condition constraint of successive nodes. The crack was propagated through the entire width of the specimen such that K was determined for each crack position, similar to the study by Prime [61]. A uniform mesh was used in the plate where all the elements, of type CPE8R, along the crack plane had equal length. The strain extrapolated to the node at the back face of the plate during crack insertion was used to determine K using (2.50).

The strain on the back face of the specimen is shown in Figure A.15(a). As the crack was incrementally inserted, the crack mouth opened and compressive strains were induced at the back face. The strain profile was differentiated to obtain the distribution in Figure A.15(b). This calculation was performed by fitting a second order polynomial successively to sets of three data points such that piecewise functions were obtained which were easily differentiated. This followed the approach in ASTM E1457-13 [77].

The influence function, $Z(a)$, is determined using the formulae presented by Schindler and Bertschinger [62] for a beam with a crack. Using (2.50), K was calculated for each

incremental crack length and is shown in Figure A.16. For a crack length of 3.5 mm, K = 21.4 MPam$^{1/2}$, which is in very close agreement to the analytical solution.

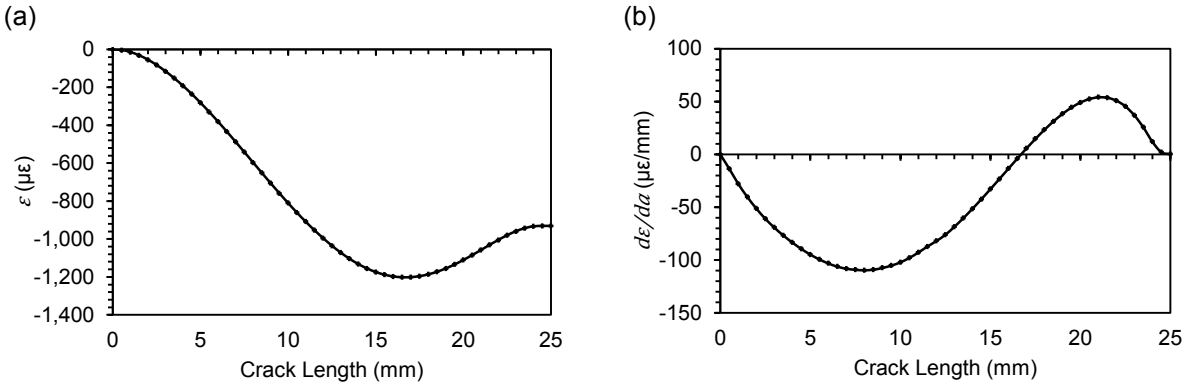


Figure A.15 (a) Back face strain on plate with residual stresses during incremental crack insertion and (b) incremental strain per incremental crack length

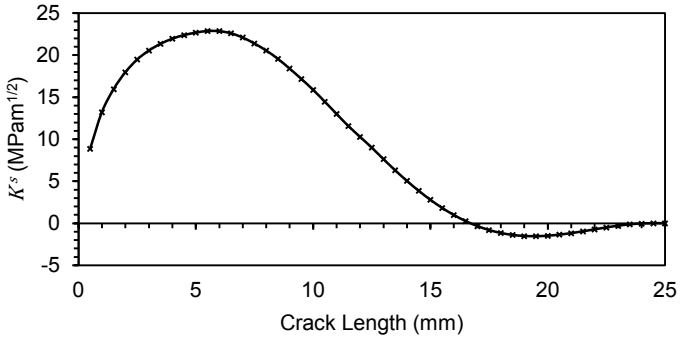


Figure A.16 Stress intensity factor, K, in the plate with sinusoidal residual stress distribution for incremental crack lengths determined using a simulation of the slitting method

A.6 SUMMARY FOR EDGE CRACKED PLATE

The various approaches for determining K were applied to the simple problem of the edge cracked plate with a sinusoidal residual stress distribution. Each of the approaches closely matched the analytical solution, as shown in Table A.1, and therefore the various approaches to determine K were validated. The methods were used to calculate K for FE simulations of C(T) specimens which have residual stresses induced by EB welding. The following recommendations were made from this study to ensure accurate estimates of K:

- The contours used to determine the J-integrals must be large enough to enclose the crack tip plasticity region, which is defined as ε^{pl} > 0.1%
- J-integrals may be evaluated for small strain or large strain analyses

- A fault exists in the ABAQUS software for analyses that use the *MAP SOLUTION keyword. The stresses must be copied to another model using *INITIAL CONDITIONS, TYPE=STRESS, FILE=*oldjobname*.odb keyword to obtain path independent J-integral solutions
- In the superposition approach, crack face loads must be applied as distributed pressure loads using *DLOAD and the user subroutine DSLOAD, and not using concentrated nodal loads (*CLOAD)
- The average stress through the volume of an element, from an uncracked body, may be assumed to be the crack face pressure when transferring stresses for the superposition approach

Table A.1 Stress intensity factors, K^s, determined for the edge cracked plate with residual stresses using various approaches

Method	K^s **(MPam$^{1/2}$)**
Analytical Solution	21.7
J-Integral	21.5
Superposition Approach	20.8
Slitting Approach	21.4